Quantum Optical Nonlinearity of a Single Molecule Strongly Coupled to a Microcavity

DISSERTATION

Der Naturwissenschaftlichen Fakultät
der Friedrich-Alexander-Universität Erlangen-Nürnberg
zur Erlangung des Doktorgrades
Dr. rer. nat.
vorgelegt von

André Pscherer
aus Nürnberg

Lehrstuhl für Experimentalphysik
Friedrich-Alexander-Universität Erlangen-Nürnberg
und
Max-Planck-Institut für die Physik des Lichts

Als Dissertation genehmigt
von der Naturwissenschaftlichen Fakultät
der Friedrich-Alexander-Universität Erlangen-Nürnberg

Tag der mündlichen Prüfung: 15.03.2024

Gutachter: Prof. Dr. Vahid Sandoghdar
Prof. Dr. Richard Warburton

Abstract

Achieving near-deterministic photon-emitter and photon-photon interactions is one of the main challenges in constructing large-scale quantum networks. Because of the finite scattering cross-section and branching ratio of emitters existing up to date, it is not possible to achieve this goal without the fabrication of photonic structures around the emitter. In this work, we employ a tunable Fabry-Pérot microcavity with a finesse as high as $\mathscr{F} = 24\,000$, which selectively enhances the coherent 0-0 zero-phonon line (00ZPL) of a single dibenzoterrylene (DBT) molecule in an anthracene crystal.

Due to the small cavity mode volume of only $V = 4.4\,\lambda^3$, we achieve high coupling rates up to $2g = 2\pi \cdot 1.54\,\mathrm{GHz}$ between single cavity photons and molecular excitations. This exceeds both the cavity loss rate ($\kappa = 2\pi \cdot 1.3\,\mathrm{GHz}$) and the free-space emission rate of the molecule ($\gamma = 2\pi \cdot 0.04\,\mathrm{GHz}$). We report the first spectroscopic observation of a single molecule strongly coupled to a cavity and find a cooperativity of $C = 45$. The transmission spectrum of the coupled system shows two polariton peaks separated by a dip with transmission $T < 1\,\%$. We furthermore perform ringdown measurements which elucidate the dynamics of the energy transfer between cavity and molecule. This marks the first measurement of a single molecule undergoing single-photon Rabi oscillations.

As photon-emitter interactions are highly efficient in this system, we utilize its nonlinearity to mediate photon-photon interactions. Saturating the molecule increases the transmission through the common resonance, reaching $T = 50\,\%$ with a mean photon number as low as $\bar{n} = 0.40$ in the cavity. In a pump-probe configuration, we benchmark the performance of our system as a high-contrast all-optical switch at the level of single photons. As this nonlinearity is quantum in origin, we inspect the photon statistics of the transmitted light and find an intensity autocorrelation value of $g^{(2)}(0) = 252$ due to the strong selective suppression of single photons. In addition, we show that symmetric two-frequency excitation leads to four- and even six-wave-mixing sidebands in the emitted spectrum.

Lastly, we present spectrally tailored dichroic cavity mirrors with a finesse of $\mathscr{F} = 10\,000$, which transmit Stokes-shifted fluorescence of the molecule. The detected rate of fluorescence light is proportional to the excited state population of the molecule. This additional information enables several new experiments, three of which we evaluate the feasibility of: Firstly, the direct access to the excited-state population can be used to test the prediction that a two-level system, our molecule, can exhibit steady-state inversion when coupled to a high-finesse cavity. Secondly, it is possible to detect cavity-mediated coupling between two molecules by exciting

a two-photon transition at the average resonance frequency of the molecules. This gives rise to a resonance which can be observed in the excited-state population, but not in the cavity transmission. Thirdly, we estimate the cavity parameters necessary to resolve the quantization of the AC Stark shift. This would allow us to detect the photon statistics inside the cavity.
The results in this thesis benchmark the ability of single molecules to mediate interactions between single photons. This represents a major step towards the realization of a network of quantum emitters connected via a quantum photonic channel.

Zusammenfassung

Nahezu deterministische Photonen-Emitter- und Photonen-Photonen-Wechselwirkungen zu erzielen ist eine der größten Herausforderungen beim Aufbau großflächiger Quantennetzwerke. Aufgrund des begrenzten Streuquerschnitts und Zerfalls-Verzweigungsverhältnisses der bis dato existierenden Emitter ist es nicht möglich, dieses Ziel ohne die Fertigung photonischer Strukturen um den Emitter zu erreichen. In dieser Arbeit verwenden wir einen verstimmbaren Fabry-Pérot-Mikroresonator mit einer Finesse von bis zu $\mathscr{F} = 24\,000$, der selektiv die kohärente 0-0-Null-Phononen-Linie (00ZPL) eines einzelnen Dibenzoterrylen-Moleküls (DBT) in einem Anthracenkristall verstärkt.

Aufgrund des kleinen Resonator-Modenvolumens von nur $V = 4.4\,\lambda^3$ erreichen wir hohe Kopplungsraten bis zu $2g = 2\pi \cdot 1.54\,\mathrm{GHz}$ zwischen einzelnen Resonator-Photonen und Anregungen des Moleküls. Diese übersteigen sowohl die Resonator-Verlustrate ($\kappa = 2\pi \cdot 1.3\,\mathrm{GHz}$) als auch die freie Emissionsrate des Moleküls ($\gamma = 2\pi \cdot 0.04\,\mathrm{GHz}$). Wir präsentieren die erste spektroskopische Beobachtung eines einzelnen Moleküls, das stark an einen Resonator gekoppelt ist, und ermitteln eine Kooperativität von $C = 45$. Das Transmissionsspektrum des gekoppelten Systems weist zwei durch die Polaritonen verursachte Maxima auf, die durch ein Minimum mit einer Transmission $T < 1\,\%$ getrennt sind. Darüber hinaus führen wir Ringdown-Messungen durch, die die Dynamik des Energietransfers zwischen Resonator und Molekül aufzeigen. Dies ist die erste Messung eines einzelnen Moleküls, das Einzelphotonen-Rabi-Oszillationen ausführt.

Da Photonen-Emitter-Wechselwirkungen in diesem System sehr effizient sind, nutzen wir seine Nichtlinearität um Photonen-Photonen-Wechselwirkungen zu vermitteln. Wird das Molekül gesättigt, erhöht sich die Transmission durch die gemeinsame Resonanz und erreicht $T = 50\,\%$ bereits mit einer mittleren Photonenzahl $\bar{n} = 0.40$ im Resonator. In Pump-Probe-Experimenten testen wir die Leistungsfähigkeit unseres Systems als optischer Schalter mit hohem Kontrast auf Einzelphotonen-Ebene. Da diese Nichtlinearität quantenmechanischen Ursprungs ist, untersuchen wir die Photonenstatistik des transmittierten Lichts und finden aufgrund der stark selektiven Unterdrückung von 1-Photonen-Zuständen einen Intensitätsautokorrelationswert von $g^{(2)}(0) = 252$. Darüber hinaus zeigen wir, dass Anregung mit zwei symmetrisch um die Resonanz des Moleküls verstimmten Lasern zu Seitenbändern im Emissionsspektrum führt, die von Vier- und sogar Sechs-Wellen-Mischungs-Prozessen stammen.

Abschließend präsentieren wir spektral maßgeschneiderte dichroitische Resonatorspiegel mit einer Finesse von $\mathscr{F} = 10\,000$, die die Stokes-verschobene Fluoreszenz des Moleküls

transmittieren. Die Detektionsrate des Fluoreszenzlichts ist proportional zur Population des angeregten Zustands des Moleküls. Dieser zusätzliche Informationskanal ermöglicht mehrere neue Experimente, von denen wir drei auf ihre Durchführbarkeit prüfen: Erstens kann der direkte Zugang zur Population der angeregten Zustände genutzt werden, um die theoretische Vorhersage zu testen, dass ein Zwei-Niveau-System, unser Molekül, im stationären Zustand eine Populations-Inversion aufweisen kann, wenn es an einen Resonator mit hoher Finesse gekoppelt ist. Zweitens ist es möglich, eine durch den Resonator vermittelte Kopplung zwischen zwei Molekülen nachzuweisen, indem ein Zwei-Photonen-Übergang bei der Durchschnittsresonanzfrequenz beider Moleküle angeregt wird. Dies führt zu einer Resonanz, die sich durch die Population des angeregten Zustands beobachten lässt, nicht aber durch die Resonator-Transmission. Drittens schätzen wir die Resonatorparameter ab, die erforderlich sind um die Quantisierung der AC Stark-Verschiebung aufzulösen. Dies würde es uns ermöglichen, die Photonenstatistik im Inneren des Resonators zu erfassen.
Die Ergebnisse dieser Arbeit zeigen, dass einzelne Moleküle in der Lage sind, Wechselwirkungen zwischen einzelnen Photonen zu vermitteln. Dies ist ein wichtiger Schritt auf dem Weg zur Realisierung eines Netzwerks bestehend aus Quantenemittern, die über einen quantenphotonischen Kanal miteinander verbunden sind.

Contents

1 Introduction

"Two photons met each other in free space. What happened? Nothing, they just waved." This joke portrays the absence of interaction between photons in vacuum. Making them interact requires them to sense each other's presence, for example by the photon-number-dependent response of a material. This intensity-nonlinearity is a well-characterized property of macroscopic materials, but too weak to mediate interactions between individual photons [1]. Hence, nonlinear effects are typically observed under intense laser illumination. Most have been experimentally observed only since the invention of the laser [2], for example second-harmonic generation [3], the Kerr effect [4], spontaneous parametric down-conversion [5, 6] or the AC Stark shift [7]. The nonlinear response of matter originates from the nonlinearity of its constituents – atoms and molecules. In other words, even a single quantum emitter enables experiments showing many facets of its nonlinearity [8, 9]: Rabi oscillations [10], emission of the Mollow triplet [11, 12], stimulated emission [13] or two-photon absorption [14, 15], to name just a few.

In these proof-of-principle experiments, the proportion of the photons interacting with each other is very low. This is because a single photon has a low probability of interacting with a single emitter. The probability of two photons simultaneously undergoing an interaction with the emitter is accordingly even lower [8]. There are various approaches to increasing the interaction probability: If the spatial waveform of the photon matches the dipolar emission pattern [16, 17] and the temporal waveform is the inverse of spontaneous emission [18], an atom can deterministically absorb an incoming photon. A practical implementation of this is technically difficult. Alternatively, one can reduce the group velocity of a photon significantly within a photonic crystal waveguide. The hereby increased emitter-photon interaction time enables a nearly-deterministic coupling [19]. Another approach is to use plasmonic nanoantennas to concentrate light within a few nm^3. This increases the absorption and emission rate by orders of magnitude and therefore significantly enhances the interaction probability [20]. Our approach is to embed the emitter in a tunable micro-Fabry-Pérot cavity [21], in which the light is concentrated in a μm^3 volume over an extended period of time.

Previously, an interaction probability of $\beta = 93\,\%$ of light with a single molecule was shown in this system [22].

Building upon this, we recently reached the strong-coupling regime of light-matter interaction [23]. Our experimental platform, therefore, is among the first to show strong light-matter coupling with a single molecule, alongside one demonstration with a plasmonic nano-antenna [24]. In the latter case, strong coupling was achieved at room temperature. However, the coherent light-matter interaction is limited to a few femtoseconds due to the inherently high dephasing rate. Coherent strong coupling of an individual quantum emitter to a cavity is a particularly pertinent regime for studying the quantum nature of light-matter interaction and has previously been achieved with other emitters, such as atoms [25], quantum dots [26] and nitrogen vacancy centers in diamond [27]. The cavity protects the emitter from decoherence caused by interaction with the environment [28, 29], similarly to the box around Schrödinger's cat [30]. Within the cavity, photons can be coherently absorbed and re-emitted several times, analogously to Rabi oscillations in the semiclassical treatment of light-matter interaction. However, the Rabi frequency is quantized [31]. It is proportional to the square root of the number of photons in the cavity. The strong coupling between the emitter and the cavity transfers the photon-number nonlinearity of the emitter to the cavity, turning it into an anharmonic oscillator. The energy level scheme, called the Jaynes-Cummings ladder [29], enables the overall system to respond in a photon-number dependent manner. This effect can be utilized, for example, to create a stream of single photons via photon blockade [32, 33], or to create N-photon bundles [34].

The ability to mediate an interaction between beams of light efficiently is often essential in constructing optical circuit components – the building blocks of optical computers or routers [35–38]. The earliest experiments paving this road explored a power-hysteresis effect in cavities filled with Kerr-nonlinear media or saturable absorbers, namely optical bistability [39–41]. However, the optical power required to reach the bistable regime in ensembles [42] or bulk materials [43, 44] is macroscopic, in the order of several mW. Although reducing the mode volume and choosing materials with stronger nonlinearity [45–47] reduces the power requirements, for applications in quantum communication and quantum information processing [48–50] it is crucial to reach the nonlinear regime with single photons. A single quantum emitter behaves nonlinearly with ~ 1 photon in the cavity if β is close to 1. Proof-of-principle demonstrations were performed using single atoms [51–56], quantum dots [57–61] and color centers in diamond [62–64]. High switching contrast is important to avoid signal degradation in a cascade of switches. The strength of our system lies in its remarkably high contrast, attributable to low decoherence rates.

We explored different nonlinear optical effects, with efficiencies boosted by the strong light-matter interaction. With a mean photon number of $\bar{n} \sim 1$ inside the cavity, we can saturate the molecule, rendering it transparent to a second beam, thus realizing a single-photon switch. We furthermore investigated the qualitatively different response of the molecule to different photon numbers. This property can be utilized for photon number sorting [65]. Moreover, we

showed that the nonlinearity of the molecule can mediate four-wave-mixing processes at the level of individual photons.

In this thesis, we first explain the photophysics of the molecule, the properties of cavities and the interaction of a single emitter with the cavity field in Chapter 2. We introduce a consistent mathematical framework describing all of our experiments and describe our simulations therein. In Chapter 3 we introduce the key components of our experimental setup and essential experimental methods. In Chapter 4 we present the first experimental demonstration of strong coupling between a single molecule and a Fabry-Pérot cavity, while Chapter 5 discusses the nonlinear optical measurements mentioned in the previous paragraph. We elaborate on three concrete experimental ideas, which are feasible within the near future in Chapter 6, before closing the thesis with a brief summary and a broader outlook in Chapter 7.

2 Theoretical Background

2.1 Organic Molecules in Solid State

Organic molecules have been used in a variety of optical settings ranging from the demonstration of fundamental effects [12, 66, 67] to dye lasers [68], superresolution microscopy [69, 70] and single-molecule quantum optics [71, 72]. Essential to this diversity are the many different types and sizes of organic molecules, with optical transitions over a broad spectral range from 200 to 800 nm [73]. This work focuses on single polyaromatic hydrocarbons (PAHs) embedded in organic crystals. More specifically, we use dibenzoterrylene (DBT) doped anthracene crystals. Both DBT and anthracene resemble cut-out pieces of graphene and are therefore also referred to as nanographenes [74]. Fig. 2.1 shows their chemical structure.

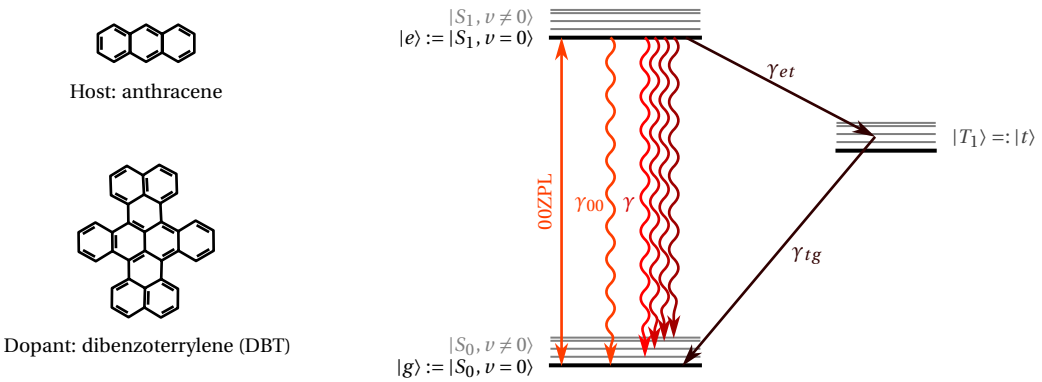

Figure 2.1: Left: The chemical structure of anthracene and DBT. Right: The relevant energy levels and transitions of DBT.

At liquid helium temperatures (4.2 K) DBT molecules yield optical transitions with lifetime-limited linewidths of 30–40 MHz [75]. Moreover, within the crystal the molecules are photostable. Hence, the same molecule can be used over months for optical experiments.

The energy levels of DBT (Fig. 2.1) involve the electron orbitals, electron spin and movement of the nuclei. When the molecule is excited from the ground state $|S_0\rangle$ into the next higher singlet state $|S_1\rangle$, it can decay

- into the ground state $|g\rangle := |S_0, v = 0\rangle$ by emitting a photon. This transition is called 0-0 zero-phonon line (00ZPL). We denote the transition rate by γ_{00}. For DBT in anthracene the wavelength of photons emitted via the 00ZPL is 785 nm.
- into the electronic ground state with a quantized excitation of one or more modes of vibration $|S_0, v \neq 0\rangle$. The photon emitted in this process has less energy than a photon emitted from the 00ZPL transition. The vibration decays into crystal phonons within a few picoseconds [76]. We denote the overall decay rate from the $|S_1\rangle$ to the $|S_0\rangle$ states by γ. The branching ratio $\alpha_{00} = \frac{\gamma_{00}}{\gamma}$ is given by the Franck-Condon principle [77]. In free space, it is $\alpha_{00} \approx 33\,\%$ [78], but it was previously shown [22] that this ratio can be increased to 95 % by a frequency-selective Purcell-enhancement (see Ch. 2.3.6).
- into the triplet state $|T_1\rangle$ via inter-system crossing (ISC). From there it can further decay into the ground state either by emitting a phosphorescence photon or by internal conversion. The transition rate in γ_{et} and out of the triplet state γ_{tg} are several orders of magnitude smaller than γ [75]. This is because these transitions are spin-forbidden in an ideal unperturbed system, and only weakly allowed in a real molecule. Depending on how much the local environment of the molecule distorts its shape, the ISC rates vary among different individual molecules [79]. Despite being very low, the ISC rate plays a role in the saturation behavior of the molecule, as will be explained in Ch. 2.4.

Working with single molecules [80, 81] requires the density of molecules to be very low in the spatial and spectral domains. Defects in the crystal individualize the nanoenvironment around the molecules, shifting the energy levels, which gives rise to a spread in the transition frequencies, called inhomogeneous broadening [82]. We typically work with samples exhibiting $\sim 10^2$ molecules over a few hundred gigahertz within one diffraction-limited volume.

2.2 Cavities

Generally, an optical cavity is a structure which concentrates light in three dimensions [28]. Various geometries are possible: ring resonators [83, 84], whispering gallery mode resonators [85, 86], photonic crystal cavities [87–89] and Fabry-Pérot cavities [90–92]. In this work, a Fabry-Pérot cavity is used, but the concepts explained here can be generalized to other types of cavities.

2.2.1 Mirror Coating

In a Fabry-Pérot cavity light is concentrated between two mirrors with a spacing of length L. The mirrors can be made out of metal. The light does not penetrate deep into the metal mirror,

therefore the mode volume can be very small [93]. Furthermore, as it is only a single layer it is easy to produce. However, the reflectivity of a metal mirror is limited by absorption. This is why high-reflectivity mirrors consist of multiple layers of dielectric materials alternating between high and low refractive indices. If the optical thickness of each layer i is a quarter wavelength, $n_i d_i = \lambda/4$, the partial reflections from each interface interfere constructively, making this *Bragg mirror* highly reflective for the wavelength λ. Other layer thickness combinations allow the reflectivity spectrum to be tailored to specific applications, including dichroic mirrors, chirped mirrors and shortpass/longpass/bandpass/notch filters [94].

Reflectivities of dielectric mirrors up to 99.999 84 % have been reported [95]. A more convenient metric to express the reflectivity R is the finesse

$$\mathscr{F} = \frac{\pi\sqrt{R}}{1-R}. \tag{2.1}$$

In a cavity consisting of two mirrors with reflectivity R, the light undertakes on average $\mathscr{F}/2\pi$ round-trips before it leaks out or is absorbed.

2.2.2 Eigenmodes

Given the shape of the mirrors, one can find the eigenmodes of the cavity. Mathematically, this corresponds to the eigensystem question: "Which initial field distribution leads to the very same field distribution after propagating a full round-trip through the cavity?" [96, 97]. For spherical mirrors of radii r_1, r_2 this question can be answered analytically: It is the set of Laguerre-Gauß beams.[1] The modes are stable, if the distance between the mirrors L fulfils the following condition [99]

$$0 < \left(1 - \frac{L}{r_1}\right)\left(1 - \frac{L}{r_2}\right) < 1. \tag{2.2}$$

For plano-concave cavities, such as those used in this work, $r_1 = \infty$ and $r_2 = R_0 > 0$. We can calculate the mode using the boundary condition that its wavefronts match the mirror shapes. The wavefront radius of curvature at a distance z from the beam waist is

$$R(z) = z\left(1 + \left(\frac{z_R}{z}\right)^2\right), \tag{2.3}$$

with the Rayleigh range z_R. The beam waist ($z = 0$) must be at the flat mirror, because only here is the wavefront flat: $R(0) \to \infty$. The other beam parameters are fixed by the second mirror at $z = L$. To match its radius of curvature, $R(L)$ must equal R_0, hence

$$z_R = \sqrt{(R_0 - L)\,L}. \tag{2.4}$$

[1] More generally, for elliptical mirrors the eigenmodes are Hermite-Gauß modes. If the semi-axes of the ellipse are equal (it is a sphere), the Hermite-Gauß modes H_{mn} and H_{nm} become degenerate, i.e. resonant for the same cavity length L. At these common resonances, the Hermite-Gauß modes hybridize into Laguerre-Gauß modes. If the finesse of the cavity is high enough, one can resolve individual Hermite-Gauß modes [98].

2.2.3 Resonance

A beam of wavenumber $k = \frac{2\pi}{\lambda}$ is on resonance with the cavity, if the phase it acquires during one round-trip Φ is an integer multiple of 2π. The round-trip phase [93]

$$\Phi = 2kL + 2\psi(L) - \phi_1 - \phi_2 \tag{2.5}$$

consists of three contributions: The phase due to propagation $2kL$, the Guoy phase $\psi(L)$ for each half round-trip and the phase shift upon reflection from the mirrors $-\phi_1 - \phi_2$. With the Guoy phase

$$\psi(L) = -(m+1)\arcsin\sqrt{\frac{L}{R_0}} \tag{2.6}$$

one can numerically solve

$$q \cdot 2\pi = 2kL - 2(m+1)\arcsin\sqrt{\frac{L}{R_0}} - \phi_1 - \phi_2 \tag{2.7}$$

for the length L of the mode with longitudinal mode number q and transversal mode number m. We use this relation to determine q experimentally, as described in Appendix I. Fig. 2.2 shows the relation for our experimental parameters.

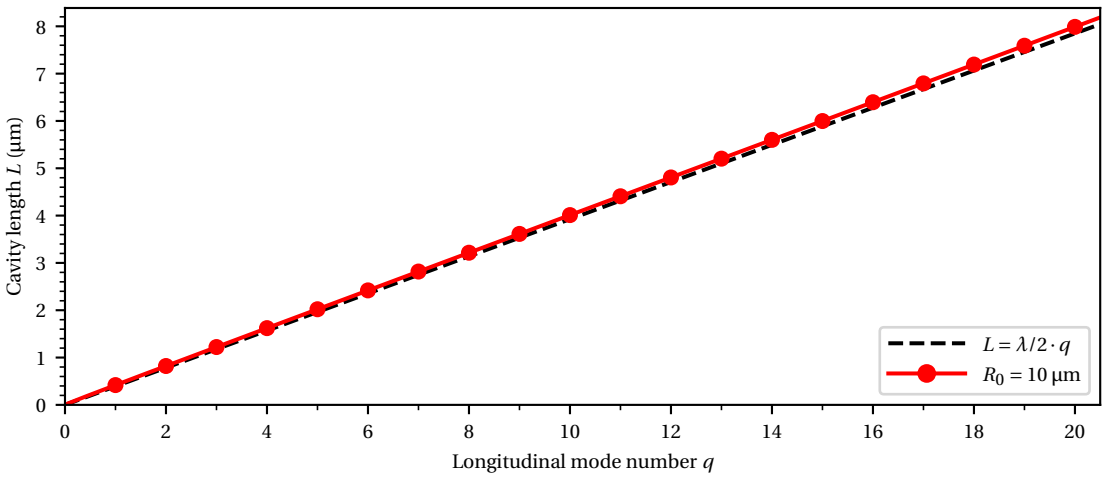

Figure 2.2: Red: The cavity length L as a function of the longitudinal mode number q for the fundamental mode ($m = 0$) of wavelength $\lambda = 785$ nm in a cavity with mirror radius $R_0 = 10$ µm. The black dashed line shows the cavity length in the absence of the Guoy phase (Eq. 2.6), or for $R_0 \to \infty$. For simplicity, we assume the reflection phases of the mirrors to be $\phi_1 = \phi_2 = 0$ to assign $q = 0$ to the mode of length $L = 0$. If the reflection phase is $\phi_1 = \phi_2 = \pi$, the $L = 0$ mode is $q = 1$ using the convention from Eq. 2.7.

2.2.4 Mode Volume

The mode volume V specifies how much the cavity concentrates the light. It is defined as

$$V = \frac{\iiint u(\vec{r})\mathrm{d}^3\vec{r}}{\max[u(\vec{r})]}, \tag{2.8a}$$

where

$$u(\vec{r}) = \varepsilon(\vec{r})\left|\vec{E}(\vec{r})\right|^2 \tag{2.8b}$$

is the energy density of the mode considered, with $\vec{E}(\vec{r})$ being the electric field strength and $\varepsilon(\vec{r})$ the electric permittivity at position $\vec{r}$. The integration runs over all space, but practically the field is confined between the two mirrors. For short cavities $L = \mathcal{O}(\lambda)$ the field within the mirror coating also contributes significantly. The mode volume V is the amount of space homogeneously filled with the highest energy density in the cavity, $\max[u(\vec{r})]$, which contains the same total energy as the cavity mode $\iiint u(\vec{r})\mathrm{d}^3\vec{r}$. For a standing-wave Gaussian beam with beam waist w_0 the mode volume in a cavity of length L is [100]

$$V = \frac{\pi}{4}{w_0}^2 L. \tag{2.9}$$

We note that in [100] Eq. (12.56), the mode volume is twice as large. This is because the authors consider a travelling wave. In a standing wave, as in our Fabry-Pérot cavity, the energy is concentrated in half as much volume because of the interference between the forward and backward propagating beams.

To provide some exemplary numbers, we compare our microcavity with the filter cavity used in Chapters 5.2 & 5.4. The microcavity consists of a planar mirror and a curved mirror with a radius of curvature $R = 10\,\mu\mathrm{m}$ (see Ch. 3.1.1). Neglecting the field penetration into the mirror coatings, a distance of $L = 2.5\,\mu\mathrm{m}$ between the mirrors results in a mode waist of $w_0 = 1.0\,\mu\mathrm{m}$ for a wavelength of $\lambda = 785\,\mathrm{nm}$. This mode has a volume of $V = 2.1\,\mu\mathrm{m}^3$. The filter cavity is a confocal cavity consisting of two spherical mirrors with radii of curvature $R = 2\,\mathrm{cm}$, which are $L = 2\,\mathrm{cm}$ apart. The beam waist of this mode is $w_0 = 50\,\mu\mathrm{m}$. Therefore, the mode volume measures $V = 0.039\,\mathrm{mm}^3$.

2.3 Interaction of a Single Emitter with the Cavity Field

So far, the system has been described classically. However, if a quantum emitter is introduced into the cavity, a description using the Schrödinger equation is necessary to account for all quantum effects. The state $|\psi(t)\rangle$ describes the state of the molecule and the field in the cavity. The basis vectors of this Hilbert space are denoted by $|g/e, n\rangle$, where the first part describes the state of the emitter (g for the ground, e for the excited state) and n is the number of photons in the cavity.

2.3.1 Jaynes-Cummings Hamiltonian

The Hamiltonian of the system is [29]

$$\hat{H} = \hat{H}_E + \hat{H}_F + \hat{H}_I, \tag{2.10a}$$

where

$$\hat{H}_E = \hbar\omega_e |e\rangle \langle e| =: \hbar\omega_e \hat{\rho}_{ee} \tag{2.10b}$$

is the energy if the emitter,

$$\hat{H}_F = \hbar\omega_c \left(\hat{a}^\dagger \hat{a} + \frac{1}{2}\right) \tag{2.10c}$$

is the energy of the field in the cavity and

$$\hat{H}_I = -\hat{\vec{d}} \cdot \hat{\vec{E}}(\vec{r}) \tag{2.10d}$$

is the interaction energy of the electric field $\hat{\vec{E}}$ with the emitter at position $\vec{r}$ in dipole approximation [101]. ω_e and ω_c are the transition frequency of the molecule and the resonance frequency of the cavity, respectively. The electric field operator $\hat{\vec{E}}(\vec{r})$ can be written in terms of the creation $\hat{a}^\dagger$ and annihilation $\hat{a}$ operators of the cavity mode:

$$\hat{\vec{E}}(\vec{r}) = -\sqrt{\frac{\hbar\omega_c}{2\varepsilon_0 V}} \left(\vec{f}(\vec{r})\hat{a} + \vec{f}^*(\vec{r})\hat{a}^\dagger\right), \tag{2.11}$$

in which $\vec{f}(\vec{r})$ is a unitless function which accounts for the spatial distribution of the field [29]. The dipole operator is [101]

$$\hat{\vec{d}} = \vec{d}_{eg} \left(|g\rangle \langle e| + |e\rangle \langle g|\right) =: \vec{d}_{eg} \left(\hat{\sigma}_- + \hat{\sigma}_+\right), \tag{2.12}$$

in which $\vec{d}_{eg}$ is the dipole matrix element for the emitter's transition. For DBT in anthracene its amplitude is 13.1 Debye ($\approx 4.37 \cdot 10^{-29}\,\mathrm{C\,m}$) [102] times the square root of the free-space branching ratio $\sqrt{\alpha_{00}}$. Defining

$$g(\vec{r}) := -\sqrt{\frac{\omega_c}{2\hbar\varepsilon_0 V}} \vec{d}_{eg} \cdot \vec{f}(\vec{r}) \tag{2.13}$$

we can write the interaction Hamiltonian (Eq. 2.10d) as

$$\hat{H}_I = \hbar \left(\hat{\sigma}_- + \hat{\sigma}_+\right) \left(g\hat{a} + g^* \hat{a}^\dagger\right) = \hbar g \left(\hat{\sigma}_- \hat{a} + \hat{\sigma}_- \hat{a}^\dagger + \hat{\sigma}_+ \hat{a} + \hat{\sigma}_+ \hat{a}^\dagger\right), \tag{2.14}$$

where the phase of the dipole is chosen such that g is real and positive [101]. The operator $\hat{\sigma}_- \hat{a}^\dagger$ describes the emitter transitioning from the excited into the ground state while a photon in the cavity is created, while $\hat{\sigma}_+ \hat{a}$ describes removing a photon while exciting the emitter.

The other two terms describe the simultaneous creation of a photon and an excitation of the emitter, or their annihilation, respectively. These energy nonconserving terms play a minor role if $g \ll \omega_c$ and are therefore neglected in the rotating-wave approximation [29].

As can be seen from the Schrödinger equation

$$\partial_t |\psi(t)\rangle = -i\frac{\hat{H}}{\hbar}|\psi(t)\rangle, \tag{2.15}$$

the vacuum energy of the cavity field $\frac{1}{2}\hbar\omega_c$ (Eq. 2.10c) only contributes a global phase $e^{-i\omega_c t/2}$, and therefore does not affect observables. Hence, we omit it and arrive at the Jaynes-Cummings Hamiltonian [103]

$$\frac{\hat{H}}{\hbar} = \omega_e \hat{\rho}_{ee} + \omega_c \hat{a}^\dagger \hat{a} + g\left(\hat{\sigma}_- \hat{a}^\dagger + \hat{\sigma}_+ \hat{a}\right). \tag{2.16}$$

2.3.2 Single-Photon Rabi Oscillations

As an example of the dynamics imposed by this Hamiltonian, we solve the Schrödinger equation for the initial state $|\psi(0)\rangle = |g,1\rangle$; with the emitter in the ground state and one photon in the cavity. We denote a general state

$$|\psi(t)\rangle = c_p(t)|g,1\rangle + c_e(t)|e,0\rangle. \tag{2.17}$$

This describes a superposition of one excitation consisting of a photon with probability amplitude c_p and an excitation of the emitter with probability amplitude c_e. The normalization $|c_p(t)|^2 + |c_e(t)|^2 = 1$ must be satisfied for all times t. Because the Hamiltonian conserves the number of excitations in the system, the amplitudes for all other basis vectors of the Hilbert space remain 0. Substituting this expansion into the Schrödinger equation results in

$$\partial_t\left(c_p(t)|g,1\rangle + c_e(t)|e,0\rangle\right) = -i\left(\left(\omega_e c_e(t) + g c_p(t)\right)|e,0\rangle + \left(\omega_c c_p(t) + g c_e(t)\right)|g,1\rangle\right), \tag{2.18a}$$

which can be separated into

$$\begin{cases} \partial_t c_p(t) = -i\left(\omega_c c_p(t) + g c_e(t)\right) \\ \partial_t c_e(t) = -i\left(\omega_e c_e(t) + g c_p(t)\right). \end{cases} \tag{2.18b}$$

For the given initial conditions $c_p(0) = 1, c_e(0) = 0$ the solution to these coupled differential equations is

$$\begin{aligned} c_p(t) &= \exp\left(-i\frac{\omega_c+\omega_e}{2}t\right)\left(\frac{i(\omega_c-\omega_e)}{\Omega_1}\sin\left(\frac{\Omega_1}{2}t\right) + \cos\left(\frac{\Omega_1}{2}t\right)\right) \\ c_e(t) &= -\frac{2ig}{\Omega_1}\exp\left(-i\frac{\omega_c+\omega_e}{2}t\right)\sin\left(\frac{\Omega_1}{2}t\right), \end{aligned} \tag{2.19}$$

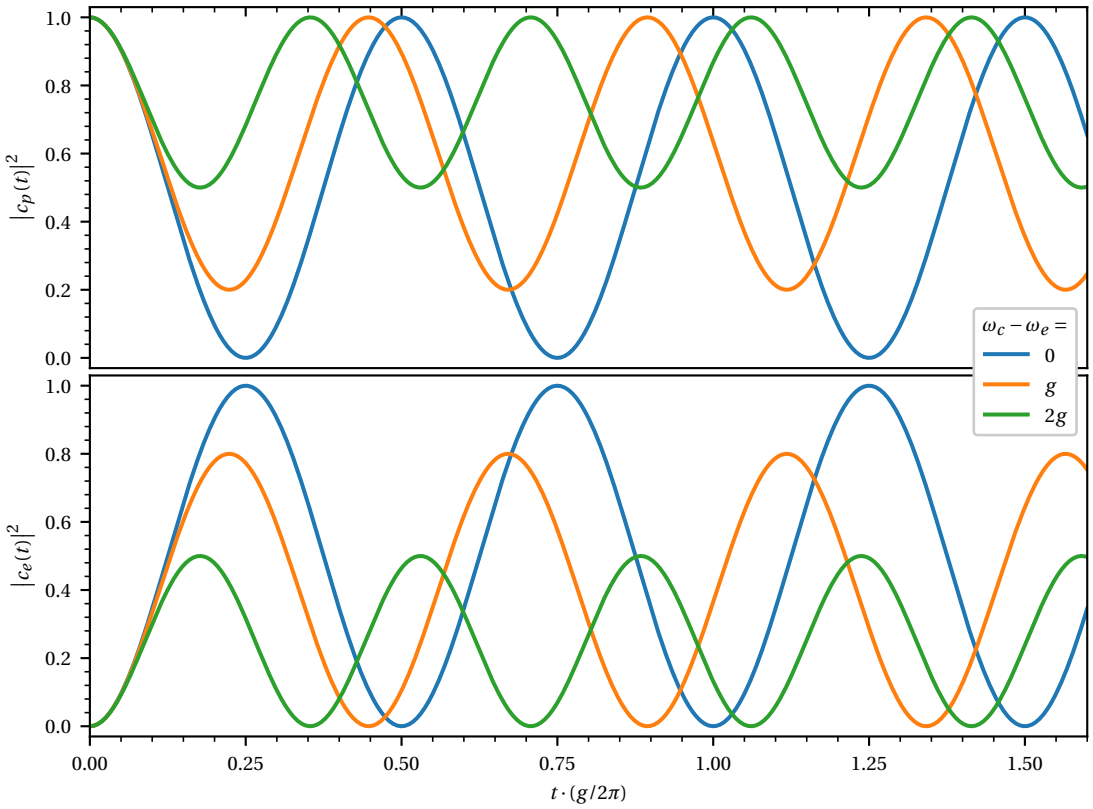

Figure 2.3: Single-photon Rabi oscillations for various cavity-emitter detunings $\omega_c - \omega_e$ after the system is initialized in the state $|\psi(0)\rangle = |g,1\rangle$.

where $\Omega_n = \sqrt{n(2g)^2 + (\omega_c - \omega_e)^2}$ is used.[2] In Fig. 2.3 the evolution of the probabilities of finding a photon in the cavity $\left|c_p(t)\right|^2$ and finding the emitter in the excited state $\left|c_e(t)\right|^2$ are plotted against time t. If the cavity and emitter are resonant $\omega_e = \omega_c$, the photon is completely absorbed and re-emitted with a period of $2\pi/2g$. Analogously to the Rabi oscillations occurring in the semiclassical theory of light-matter interaction, $2g$ is called the *single-photon Rabi frequency* (or vacuum Rabi frequency). If the cavity and emitter are detuned relative to each other, the Rabi oscillations occur with reduced amplitude at a higher frequency Ω_1. More generally, an n-photon state in the cavity drives the emitter into Rabi oscillations of frequency Ω_n, which is called the *generalized n-photon Rabi frequency*.

2.3.3 Polaritons

These dynamics show that the product states of emitter and cavity field are not eigenstates of the Hamiltonian, except for the trivial case of $|g,0\rangle$. The eigenstates for $n \geq 1$ excitations, called *polaritons*, are superpositions of excitations of the emitter and the cavity field. They are given by [101]

[2] A general solution for the case of n excitations is given in chapter 6.2.1 of [104].

$$
\begin{aligned}
|n+\rangle &= \sin\theta_n |g,n\rangle + \cos\theta_n |e,n-1\rangle \\
|n-\rangle &= \cos\theta_n |g,n\rangle - \sin\theta_n |e,n-1\rangle
\end{aligned}
\tag{2.20}
$$

and have energies of

$$
E_{n\pm} = \hbar\left((n-1)\omega_c + \frac{\omega_c + \omega_e \pm \Omega_n}{2}\right). \tag{2.21}
$$

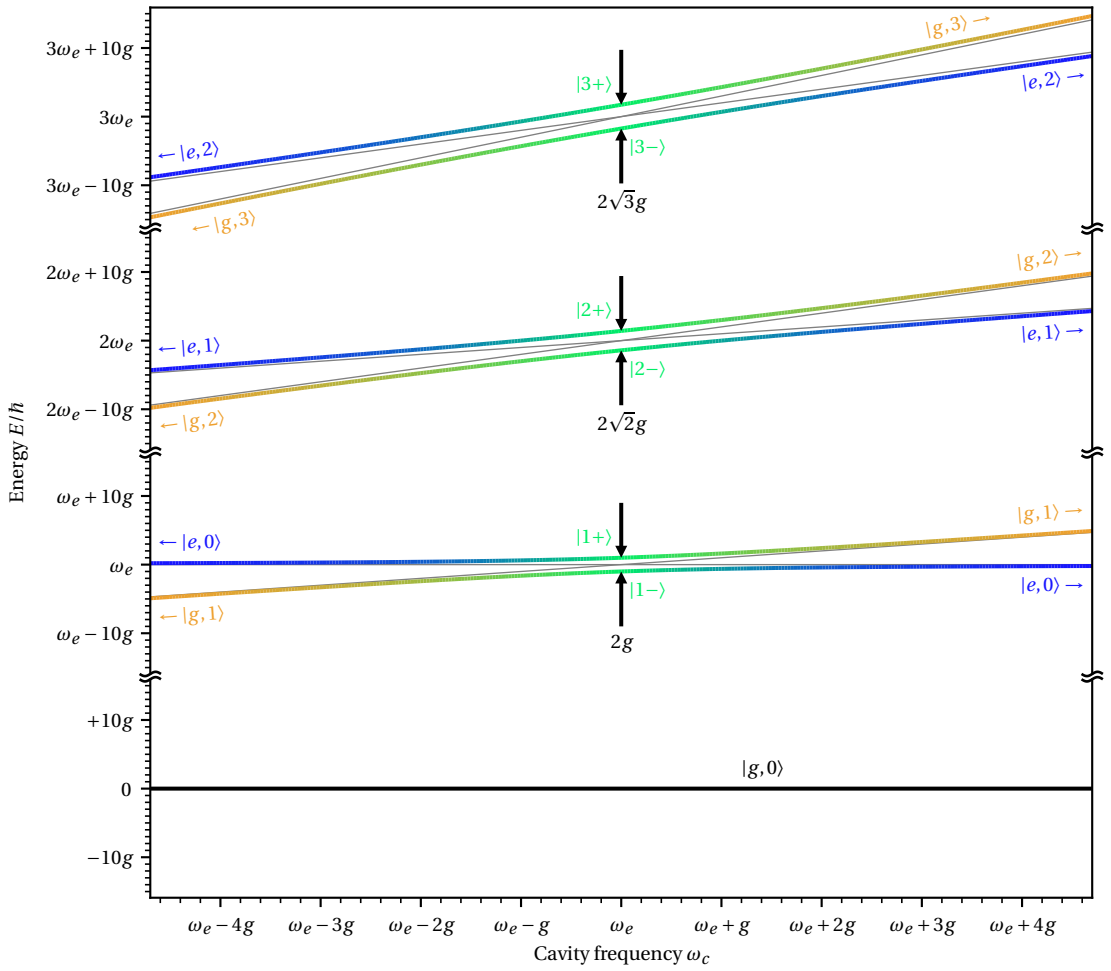

Figure 2.4: Energy levels of a two-level emitter of fixed frequency ω_e coupled to a cavity of frequency ω_c. The thin grey lines show the energies of uncoupled states. The thick colored lines show the energies for a single-photon Rabi frequency of $2g$. Their colors encode the proportion of the state in which the emitter is excited $|e,n-1\rangle$, as given by Eq. 2.20.

The mixing angle $\theta_n \in [0, \pi/2]$, also called *Stückelberg angle*, is given by

$$\tan 2\theta_n = -\frac{2\sqrt{n}g}{\omega_c - \omega_e}. \tag{2.22}$$

Fig. 2.4 shows the energies of the polaritons as a function of the cavity frequency ω_c. On resonance $\omega_c = \omega_e$, the mixing is maximal $\theta_n = \frac{\pi}{4}$. In this case, the energy splitting is minimal

$$E_{n+} - E_{n-} = 2\sqrt{n}\hbar g. \tag{2.23}$$

In the limit of high detuning $|\omega_c - \omega_e| \gg 2\sqrt{n}g$ the energy eigenstates converge to the uncoupled states $|g, n\rangle$ and $|e, n-1\rangle$.

2.3.4 Losses and Driving

So far, the cavity and emitter have been considered a closed system without connection to the environment. In a real experiment the emitter does not only interact with the cavity mode, but also with a continuum of free-space modes, resulting in a decay into non-cavity modes at a rate γ. Moreover, the cavity mirrors do not reflect 100 % of the light. With mirror reflectivities R_1, R_2 every round-trip a fraction of $(1 - R_1 R_2)$ of the energy is lost by outcoupling through the mirrors or by absorption or scattering. This leads to an energy loss rate of

$$\kappa = \frac{-\ln(R_1 R_2)}{t_{\mathrm{RT}}}, \tag{2.24}$$

where t_{RT} is the round-trip time in the cavity [105]. These two loss mechanisms couple the system under observation to the environment. We do not explicitly model the environment, hence the system is generally described as a mixed state ρ, which evolves according to the Lindblad equation [106, 107]

$$\partial_t \rho = -i\left[\frac{\hat{H}}{\hbar}, \rho\right] + \mathscr{L}_\gamma(\rho) + \mathscr{L}_\kappa(\rho). \tag{2.25a}$$

with the Lindblad terms

$$\mathscr{L}_\gamma(\rho) = \gamma\left(\hat{\sigma}_-\rho\hat{\sigma}_+ - \frac{1}{2}\left(\hat{\sigma}_+\hat{\sigma}_-\rho + \rho\hat{\sigma}_+\hat{\sigma}_-\right)\right) = \gamma\left(\hat{\sigma}_-\rho\hat{\sigma}_+ - \frac{1}{2}\left(\hat{\rho}_{ee}\rho + \rho\hat{\rho}_{ee}\right)\right) \tag{2.25b}$$

and

$$\mathscr{L}_\kappa(\rho) = \kappa\left(\hat{a}\rho\hat{a}^\dagger - \frac{1}{2}\left(\hat{a}^\dagger\hat{a}\rho + \rho\hat{a}^\dagger\hat{a}\right)\right). \tag{2.25c}$$

2.3.5 Damped Single-Photon Rabi Oscillations

To describe the lossy cavity-emitter system, we follow the approach in [108], chapter 13.3.1. The density matrix can be decomposed into two parts

$$\rho(t) = \rho_0(t) + \rho_1(t), \tag{2.26}$$

where

$$\rho_0(t) = P_{\text{emitted}}(t)\,|g,0\rangle\langle g,0| \tag{2.27a}$$
$$\rho_1(t) = |\psi(t)\rangle\langle\psi(t)|\,. \tag{2.27b}$$

$P_{\text{emitted}}(t)$ is the probability that the system has decayed to the ground state $|g,0\rangle$ by time t via either of the two decay channels. $|\psi(t)\rangle$ is a pure state

$$|\psi(t)\rangle = c_p(t)\,|g,1\rangle + c_e(t)\,|e,0\rangle\,, \tag{2.28}$$

describing the coherent evolution within the 1-excitation subspace. The difference to Eq. 2.17 is that $|\psi(t)\rangle$ is not normalized, but instead $\left|c_p(t)\right|^2 + |c_e(t)|^2 + P_{\text{emitted}} = 1$. The differential equations for the coefficients $c_p(t)$, $c_e(t)$

$$\begin{cases} \partial_t c_p(t) = -i\left(\omega_c c_p(t) + g c_e(t)\right) - \frac{\kappa}{2} c_p(t) \\ \partial_t c_e(t) = -i\left(\omega_e c_e(t) + g c_p(t)\right) - \frac{\gamma}{2} c_e(t) \end{cases} \tag{2.29}$$

show damping at rates $\frac{\kappa}{2}$ and $\frac{\gamma}{2}$ additionally to the unitary dynamics of the lossless system (cf. Eq. 2.18b). Starting with the emitter in the excited state $c_e(0) = 1$, the solution to Eq. 2.29 is

$$\begin{aligned} c_p(t) &= -\frac{2ig}{\tilde{\Omega}_1} \exp\left(\left(-i\frac{\omega_c+\omega_e}{2} - \frac{\kappa+\gamma}{4}\right)t\right) \sin\left(\frac{\tilde{\Omega}_1}{2}t\right) \\ c_e(t) &= \exp\left(\left(-i\frac{\omega_c+\omega_e}{2} - \frac{\kappa+\gamma}{4}\right)t\right)\left(\cos\left(\frac{\tilde{\Omega}_1}{2}t\right) + i\frac{\tilde{\delta}}{\tilde{\Omega}_1}\sin\left(\frac{\tilde{\Omega}_1}{2}t\right)\right). \end{aligned} \tag{2.30a}$$

This describes Rabi oscillations with a complex frequency $\tilde{\Omega}_1$ damped at a rate $\frac{\kappa+\gamma}{2}$. The complex Rabi frequency takes detuning and losses into account:

$$\tilde{\Omega}_1 = \sqrt{(2g)^2 + \tilde{\delta}^2} \tag{2.30b}$$

with

$$\tilde{\delta} = (\omega_c - \omega_e) - i\frac{\kappa-\gamma}{2}. \tag{2.30c}$$

Fig. 2.5 shows the evolution of the photon $|c_p(t)|^2$ and excited state population $|c_e(t)|^2$ for various damping rates in the resonant case $\omega_c = \omega_e$. The Rabi oscillations are exponentially

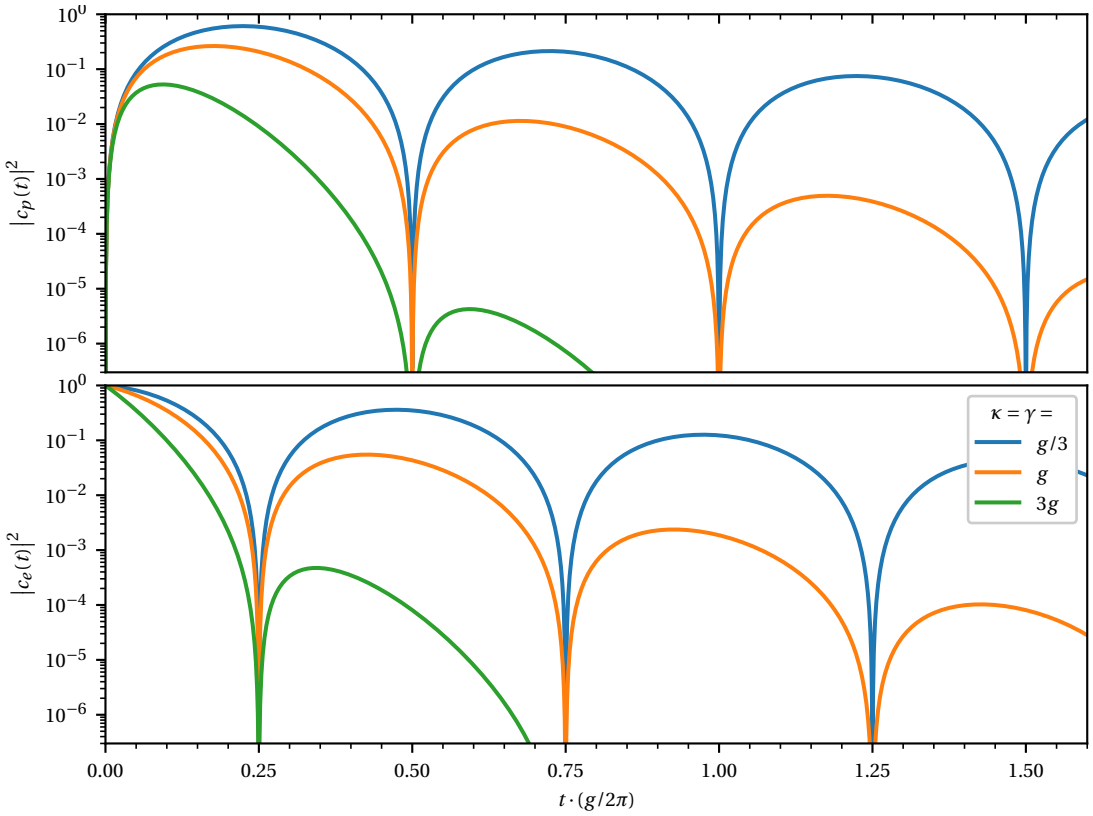

Figure 2.5: Single-photon Rabi oscillations damped equally due to cavity outcoupling at rate κ and free-space emission at rate γ.

damped at a rate $(\kappa+\gamma)/2$. If the Rabi oscillation dominates the dynamics, a photon in the cavity can interact multiple times with the emitter before it leaks out of the cavity. Therefore, this regime is called the *strong coupling* regime.

We note that the strong coupling regime can also be defined by the exceptional point of the complex Rabi frequency [109]. For a resonant cavity $\omega_c = \omega_e$, the complex Rabi frequency (Eq. 2.30b) is imaginary provided $4g < \kappa - \gamma$. For g higher than the exceptional point $g_{\text{ex}} = (\kappa-\gamma)/4$, the system is said to be in the strong coupling regime and $\tilde{\Omega}_1$ is real.

2.3.6 Purcell Effect

In the bad cavity limit ($\kappa \gg g, \gamma$) photon reabsorption does not play a role, but the cavity does enhance the interaction between the emitter and the electromagnetic field of the cavity mode, as in the previous chapters. This is indicated by an increased decay rate of the excited state. For $g \ll |\tilde{\delta}|$ the ratio $\tilde{\delta}/\tilde{\Omega}_1$ approaches 1. We can therefore use Euler's formula to write the

wavefunction coefficient for the excited state $c_e(t)$ in Eq. 2.30a as

$$c_e(t) = \exp\left(\left(-i\frac{\omega_c+\omega_e}{2} - \frac{\kappa+\gamma}{4}\right)t\right)\exp\left(i\frac{\tilde{\Omega}_1}{2}t\right). \tag{2.31}$$

Next, we Taylor-expand $\tilde{\Omega}_1$ around $g = 0$ and obtain

$$\tilde{\Omega}_1 = \sqrt{(2g)^2+\tilde{\delta}^2} = \sqrt{\tilde{\delta}^2} + \frac{2g^2}{\sqrt{\tilde{\delta}^2}} + \mathcal{O}(g^4) \approx \tilde{\delta} + \frac{2g^2}{\tilde{\delta}}. \tag{2.32}$$

Some terms in the exponent cancel with the $\tilde{\delta}$ giving

$$\begin{aligned} c_e(t) &= \exp\left(\left(-i\frac{\omega_c+\omega_e}{2} - \frac{\kappa+\gamma}{4} + i\frac{\omega_c-\omega_e}{2} + \frac{\kappa-\gamma}{4} + \frac{ig^2}{(\omega_c-\omega_e) - i\frac{\kappa-\gamma}{2}}\right)t\right) \\ &= \exp\left(\left(-i\omega_e - \frac{\gamma}{2} + \frac{ig^2}{(\omega_c-\omega_e) - i\frac{\kappa-\gamma}{2}}\right)t\right). \end{aligned} \tag{2.33}$$

Together with $\kappa - \gamma \approx \kappa$ the probability of finding the emitter in the excited state

$$\begin{aligned} |c_e(t)|^2 &= \exp\left(\left(-\gamma + \frac{ig^2}{(\omega_c-\omega_e) - i\frac{\kappa}{2}} - \frac{ig^2}{(\omega_c-\omega_e) + i\frac{\kappa}{2}}\right)t\right) \\ &= \exp\left(\left(-\gamma - \frac{4g^2}{\kappa}\frac{\left(\frac{\kappa}{2}\right)^2}{(\omega_c-\omega_e)^2 + \left(\frac{\kappa}{2}\right)^2}\right)t\right) \end{aligned} \tag{2.34}$$

decays exponentially at the free-space decay rate γ plus an additional rate

$$\gamma_{\text{cav}} = \frac{4g^2}{\kappa}\frac{\left(\frac{\kappa}{2}\right)^2}{(\omega_c-\omega_e)^2 + \left(\frac{\kappa}{2}\right)^2} \tag{2.35}$$

due to the cavity. The Purcell factor F_P is the ratio of cavity-induced to free-space decay rates:

$$F_P := \frac{\gamma_{\text{cav}}}{\gamma} = \frac{4g^2}{\kappa\gamma}\frac{\left(\frac{\kappa}{2}\right)^2}{(\omega_c-\omega_e)^2 + \left(\frac{\kappa}{2}\right)^2}. \tag{2.36}$$

The Purcell factor can alternatively be explained in terms of enhancing the density of modes and concentrating their electric field within the cavity volume [110]. This is evident when the Purcell factor is expressed by the cavity properties alone. We can write the free-space spontaneous emission rate

$$\gamma = \frac{\left|\vec{d}_{eg}\right|^2 {\omega_e}^3}{3\pi\varepsilon_0\hbar c^3} \tag{2.37}$$

and the coupling g (see Eq. 2.13) in terms of the transition dipole moment $\vec{d}_{eg}$. If the emitter is in the field maximum of the cavity mode, resonant with the cavity $\omega_e = \omega_c$ and its transition

dipole moment parallel to the mode polarization $\vec{d}_{eg} \parallel \vec{E}$, the Purcell factor is

$$F_P = \frac{4g^2}{\kappa\gamma} = \frac{4}{\kappa} \frac{\frac{\omega_c}{2\hbar\varepsilon_0 V}\left|\vec{d}_{eg}\right|^2}{\frac{\left|\vec{d}_{eg}\right|^2 {\omega_c}^3}{3\pi\varepsilon_0\hbar c^3}} = \frac{3}{4\pi^2}\left(\frac{\lambda}{n}\right)^3 \frac{Q}{V} \tag{2.38a}$$

$$= \frac{6}{\pi^3}\left(\frac{\lambda}{n}\right)^2 \frac{\mathscr{F}}{{w_0}^2}, \tag{2.38b}$$

where we introduce the quality factor $Q = \omega_c/\kappa$. To maximize the Purcell factor, a cavity must have a high finesse $\mathscr{F}$ and the cavity mode must be strongly focused to achieve a small mode waist w_0. We would also like to note that the Purcell factor depends neither on the linewidth of the emitter γ nor on the length of the cavity L. This means, for a given Gaussian beam defined by its waist w_0 and wavelength λ, one could place a wavefront-matched curved mirror at any distance from the beam waist (see Fig. 2.6) and obtain the same Purcell factor. This only a thought experiment, because the mirror radius r_2 depends on the distance from the waist z, as in Eq. 2.3.

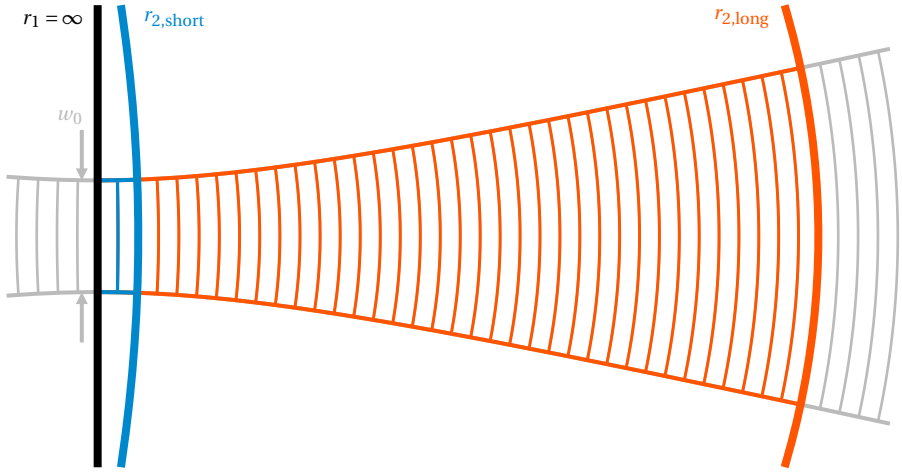

Figure 2.6: Thought experiment: Constructing a cavity for a given Gaussian beam. A flat mirror ($r_1 = \infty$) is placed at the beam waist, and a curved mirror of radius r_2 is placed at a distance z from the waist. The radius r_2 is chosen to match the wavefront curvature $R(z)$ of the beam (see Eq. 2.3). The figure shows two cavities with vastly different lengths. Despite the different mode volumes V, both cavities have the same Purcell factor F_P.

The cooperativity C can be used to assess the purity of interaction of the emitter with the cavity compared to its interaction with the environment. For an ideal two-level system, the cooperativity is the same as the Purcell factor for a resonant cavity

$$C := \frac{4g^2}{\kappa\gamma}. \tag{2.39}$$

However, for emitters with several decay channels from $|e\rangle$ to $|g\rangle$, there is a difference: While for the cooperativity the decay rate γ in the denominator means the overall decay rate of all channels, for the Purcell factor only the resonantly enhanced transition is taken into account. In our case, the cavity is tuned in resonance with the 00ZPL of DBT, which constitutes $\alpha_{00} = \frac{\gamma_{00}}{\gamma} \approx \frac{1}{3}$ of the overall free-space decay rate. The cooperativity $C = \alpha_{00} F_P$ is therefore one third of the Purcell factor. To achieve a high cooperativity, emitters with a high branching ratio α_{00} are preferred.

A similar measure is the beta-factor β, which specifies the ratio of light emitted into the cavity mode $C\gamma$ compared to the overall decay rate $\gamma + C\gamma$

$$\beta = \frac{C\gamma}{\gamma + C\gamma} = \frac{C}{1+C}. \tag{2.40}$$

Hence, a high β implies that the emitter interacts with nearly every photon in a cavity, making linear and nonlinear light-matter interactions much more likely than without a cavity. In our experiments, we find a cooperativity of up to 45. Since in the strong coupling regime a photon can be emitted and reabsorbed several times, we note that the definition of the beta factor does not apply here. Furthermore, we have assumed that the spontaneous emission rate into non-cavity modes γ is the same as in free space. This is not generally the case [111, 112], but a reasonable approximation in our case, because the cavity covers only a small solid angle.

2.3.7 Laser Driving

The previous examples illustrate the dynamics of the cavity-emitter system starting from a given initial state. In our experiments, we create these states by coupling one or two laser beams into the cavity. The lasers can be pulsed, as in the experiments described in Ch. 4.2, or continuous-wave as in all other experiments. Here, we explain how the laser driving is included in the model.

The laser drives the cavity with a strength $\Xi(t)$, analogously to the description of the semiclassical Rabi frequency drive on a two-level system. This adds

$$\hat{H}_L(t) = \hbar\left(\Xi(t)\,\hat{a}e^{i\omega_L t} + \Xi^*(t)\,\hat{a}^\dagger e^{-i\omega_L t}\right) \tag{2.41}$$

to the Hamiltonian. To remove the phase rotating at ω_L we switch to a rotating frame, in which the overall Hamiltonian reads

$$\frac{\hat{H}(t)}{\hbar} = (\omega_e - \omega_L)\,\hat{\rho}_{ee} + (\omega_c - \omega_L)\,\hat{a}^\dagger\hat{a} + g\left(\hat{\sigma}_+\hat{a} + \hat{\sigma}_-\hat{a}^\dagger\right) + \Xi(t)\,\hat{a} + \Xi^*(t)\,\hat{a}^\dagger. \tag{2.42}$$

A. Auffèves-Garnier *et al.* [113] show that under certain approximations an analytic solution is possible. These approximations include correlations between cavity and emitter being

negligible and the corresponding operators becoming factorizable, for example

$$\left\langle \hat{\rho}_{ee}\hat{a}\right\rangle = \left\langle \hat{\rho}_{ee}\right\rangle \left\langle \hat{a}\right\rangle . \tag{2.43}$$

This is a close approximation for a weakly coupled system, in which a photon emitted into the cavity has negligible back-action onto the emitter. However, in the *strong coupling* regime, defined by said back-action, the operators cannot generally be separated. There are exceptions in the cases of extremely strong $\Xi \to \infty$ and extremely weak driving $\Xi \to 0$. In the former, the fraction of the photons the emitter can interact with approaches 0. Hence, observables such as the transmission through the cavity T approach the case without an emitter. They can therefore be described accurately by the model. More importantly for our experiments in Ch. 4.1, in the case of weak driving, the population of the excited state of the emitter is very small, as are the correlations to the cavity. This model therefore shows close agreement with the full numerical model we explain in Ch. 2.4, but with the advantage of analytical expressions for the transmission and reflection spectra. Therefore, we review its main results.[3] It is possible to calculate the field transmission coefficient t of the system

$$t(\omega_L,\omega_c,\omega_e) = t_0(\omega_c-\omega_L)\left(-1+\frac{1}{1+\frac{2i(\omega_e-\omega_L)+\gamma}{\frac{4g^2}{\kappa}t_0(\omega_c-\omega_L)}}\right) \tag{2.44a}$$

with the field transmission coefficient of the empty cavity

$$t_0(\omega_c-\omega_L) = \frac{1}{1+i\frac{\omega_c-\omega_L}{\kappa/2}}. \tag{2.44b}$$

The intensity transmission coefficient is the absolute value of the the field transmission coefficient squared

$$T(\omega_L,\omega_c,\omega_e) := \frac{I_{\text{trans}}}{I_{\text{in}}} = \left|t(\omega_L,\omega_c,\omega_e)\right|^2 \tag{2.45}$$

where I_{trans} is the rate of transmitted, and $I_{\text{in}} = (2\Xi)^2/\kappa$ the rate of incident, photons. If the cavity is resonant with the emitter $\omega_c = \omega_e$, and if $\gamma \ll g,\kappa$, the transmission spectrum simplifies to

$$T(\omega_L,\omega_c=\omega_e) = \frac{1}{1+\left(\frac{2g^2}{\kappa(\omega_e-\omega_L)}-\frac{\omega_e-\omega_L}{\kappa/2}\right)^2}. \tag{2.46}$$

Its maxima are at $\omega_c \pm g$, the energies of the first polaritons, therefore the single-photon Rabi frequency can be identified in a measured spectrum from the separation of the maxima. Fig. 2.7a) shows the transmission spectrum of a single emitter according to Eqns. 2.45 & 2.44

[3] We note that in Ref. [113] κ denotes the *field* decay rate, which is half our κ, the rate at which the *intensity* inside the cavity decays. Furthermore, some quantities have different symbols. Our g is their Ω, our γ is their γ_{at}, our rate of incident photons I_{in} is denoted $|b_{\text{in}}|^2$ in their paper.

for a range of cavity frequencies around the emitter frequency. The case $\omega_c = \omega_e$ is shown in Fig. 2.7b), together with the resonance frequencies of the polaritons.

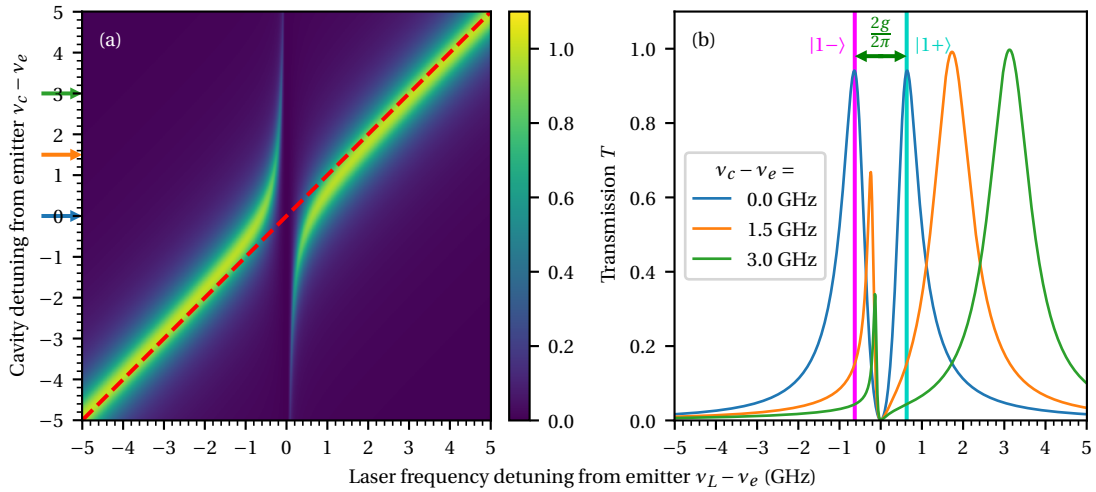

Figure 2.7: (a) The transmission through the cavity-emitter system as a function of the laser and cavity detuning calculated for the weak-excitation limit [113] for $g/2\pi = 0.63\,\text{GHz}$, $\kappa/2\pi = 1.28\,\text{GHz}$ and $\gamma/2\pi = 0.04\,\text{GHz}$. (b) Some cross-sections through the 2D spectrum for constant cavity frequencies ν_c indicated by the correspondingly colored arrows in (a).

While this model describes the weak-excitation experiments presented in Ch. 4.1 accurately, the approximation (Eq. 2.43) does not hold in the strong coupling regime at intermediate driving strengths, when the photon number in the cavity is on the order of 1. This is the regime, in which the nonlinear experiments (Ch. 5) take place. To be able to compare our experimental results with the theoretical predictions in this regime and to conceptualize relevant measurements, we formulated a numerical model, described in the next section.

2.4 General Theoretical Model and Simulations

The model is intended to describe all experimental situations consistently. Additionally, it should allow us to include the specifics of our system. We therefore employ simulations carried out with the Python package QuTiP [114, 115], which offers convenient handling of quantum states and operators as well as eigenvalue and differential equation solvers.

In addition to the two Lindblad terms used in the general model (Eq. 2.25), for our molecule we must account for the effect of the long-lived triplet state (see Chapter 2.1). One extra Lindblad term

$$\mathcal{L}_{\gamma_{et}}(\rho) = \gamma_{et}\left(|t\rangle\langle e|\,\rho\,|e\rangle\langle t| - \frac{1}{2}\left(|e\rangle\langle e|\,\rho + \rho\,|e\rangle\langle e|\right)\right) \tag{2.47a}$$

accounts for the incoherent transition from the excited state to the triplet state $|e\rangle \rightarrow |t\rangle$ at a rate γ_{et} and another one

$$\mathscr{L}_{\gamma_{tg}}(\rho) = \gamma_{tg}\left(|g\rangle\langle t|\rho|t\rangle\langle g| - \frac{1}{2}\left(|t\rangle\langle t|\rho + \rho|t\rangle\langle t|\right)\right) \tag{2.47b}$$

for the incoherent transition from the triplet into the ground state $|t\rangle \rightarrow |g\rangle$ at a rate γ_{tg}. Although the decay in and out of the triplet state is much slower (tens to hundreds of kHz [79]) than the other dynamics in the molecule, they change the dynamics noticeably. While the molecule is in the triplet state, it is far from resonance with the laser or the cavity. Hence, the cavity behaves as if the molecule was not there. In the limit of driving the molecule very strongly $\Xi(t) \rightarrow \infty$, the molecule spends $1\Big/\left(2\frac{\gamma_{tg}}{\gamma_{et}}+1\right)$ of the time in the triplet state.

We note that we do not include the energy of the triplet state in the Hamiltonian, because all transitions in and out of the triplet state are incoherent and therefore a term of the form $E_t|t\rangle\langle t|$ commutes with the Hamiltonian: $\left[\hat{H}, |t\rangle\langle t|\right] = 0$.

The Hilbert space $\mathscr{H}$ is the tensor product of the Hilbert spaces of the molecule $\mathscr{H}_{\text{mol}}$ and the cavity $\mathscr{H}_c$. While $\mathscr{H}_{\text{mol}}$ is 3-dimensional (basis vectors $|g\rangle$, $|e\rangle$ and $|t\rangle$), $\mathscr{H}_c$ is infinite-dimensional (basis vectors $\left\{|n\rangle \middle| n \in \mathbb{N}_0\right\}$). The size of the simulated Hilbert space must be finite. The number of computational steps to find the eigenvalues of a matrix scales with the third power of the size of the matrix [116]. As such the optimal size is the smallest possible Hilbert space for which the errors are small. This depends heavily on the concrete experimental parameters and the observables of interest. A Hilbert space with too few dimensions results in photon-number dependent nonlinear behavior of the cavity, which is the same behavior we would like to observe in the molecule. To ensure we do not introduce artificial nonlinearities to the simulation, we increase the size of the Hilbert space to the point where additional dimensions change the density matrix only by a value comparable to the floating-point precision. Fig. 2.8 compares the photon number statistics for an empty driven cavity for two different sizes N_c of the Hilbert space. For this simple situation, there is an analytic steady-state solution $|\psi\rangle_{ss}$ – a coherent state $|\alpha\rangle$ builds up in the cavity:

$$|\psi\rangle_{ss} = |\alpha\rangle = \exp\left(-\frac{|\alpha|^2}{2}\right)\sum_{n=0}^{\infty}\frac{\alpha^n}{\sqrt{n!}}|n\rangle \tag{2.48a}$$

It has a Poissonian photon number distribution [104]

$$P(n) = |\langle n|\alpha\rangle|^2 = \exp\left(-|\alpha|^2\right)\frac{|\alpha|^{2n}}{n!}. \tag{2.48b}$$

Its amplitude α is $\Xi^*/\left(\frac{i}{2}\kappa - (\omega_c - \omega_L)\right)$ (see Eq. B.15). In the nonlinear optical experiments described in Ch. 5, the photon number in the cavity can be high ($> 10^1$). To describe these situations accurately and simulate beyond the experimental parameters, requires large Hilbert spaces, which would slow down the simulations drastically. In the following we explain how

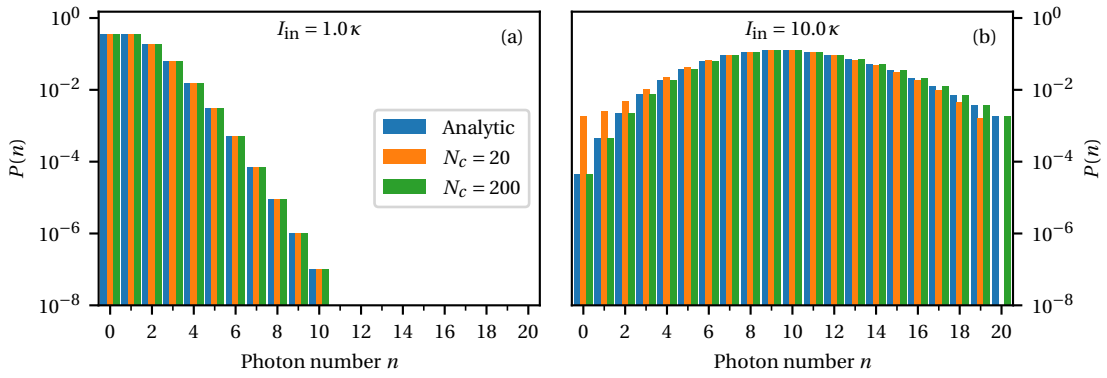

Figure 2.8: The photon number distribution of a cavity without emitter. (a) For a mean photon number of $|\alpha|^2 = 1.0$, a 20-dimensional photonic Hilbert space describes the situation accurately. (b) For a higher laser power leading to $|\alpha|^2 = 10$ photons in the cavity, this is insufficient. High photon number states can evolve in ways which take them outside the Hilbert space, for example $\hat{a}^\dagger|19\rangle \sim |20\rangle$ is not captured. Therefore, the low-dimensional simulation computes too little population of the high Fock states and too much population of the low Fock states.

to simulate the molecule-cavity system accurately without power-dependent Hilbert space dimensionality.

Single-photon emitters can only absorb or emit one photon at a time. Therefore, their influence on a strong coherent state is limited. The left column of Fig. 2.9 compares the photon number statistics of a driven cavity-molecule system with the Poissonian statistics of the state $|\alpha(t)\rangle$ which builds up in the absence of the molecule. The difference between them is small, especially when the laser power is high. On displacing the photonic state by the amplitude $\alpha(t)$, what remains is purely the effect of the molecule. As the molecule can only absorb or emit one photon at a time and photons leave the cavity at a rate κ, they require many fewer Hilbert space dimensions to be computed accurately. The photon number statistics in this *vacuum picture* [117] are shown in the right column of Fig. 2.9.

The transformation is detailed in Appendix B. We call the transformed density matrix ρ_v and the transformed Hamiltonian is given by

$$\frac{\hat{H}_v}{\hbar} = (\omega_e - \omega_L)\,\hat{\rho}_{ee} + (\omega_c - \omega_L)\,\hat{a}^\dagger\hat{a} + g\left(\hat{\sigma}_+\left(\hat{a} + \alpha(t)\right) + \hat{\sigma}_-\left(\hat{a}^\dagger + \alpha^*(t)\right)\right). \tag{2.49}$$

The Lindblad terms are not changed, because the molecular states are not affected by the transformation and the nonclassical state of light created by the molecule decays at the same rate κ as the rest of the light. Comparing this Hamiltonian with the non-transformed Hamiltonian (Eq. 2.42), we note that the driving of the cavity mode $\Xi(t)\hat{a} + \Xi^*(t)\hat{a}^\dagger$, which indirectly affects the molecule, is now replaced by a direct drive of the molecule $g\,(\hat{\sigma}_+\alpha(t) + \hat{\sigma}_-\alpha^*(t))$ due to the coherent state of amplitude $\alpha(t)$. Coherent states are eigenstates of the electric field

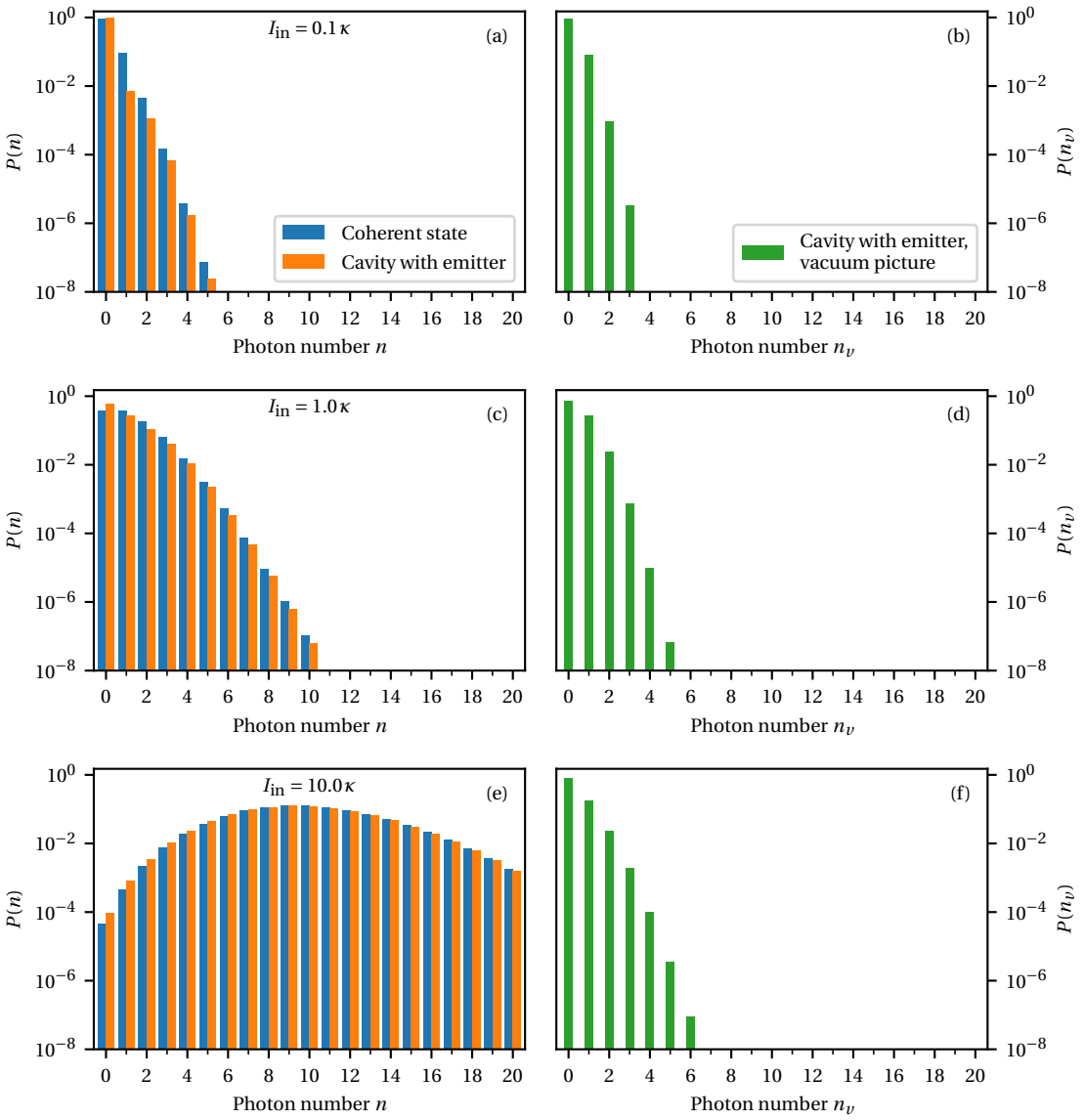

Figure 2.9: Left column: The probabilities $P(n)$ of finding n photons in the cavity. Without an emitter, a coherent state builds up in the the cavity (see Eq. 2.48). In the presence of an emitter, the photon number distribution changes slightly, but closely resembles a Poissonian distribution. Right column: In the vacuum picture, we simulate the deviation from the coherent state. Because the molecule only scatters one photon at a time, its influence on the deviation is limited. Hence, even at high excitation power only few dimensions in the photonic part of the Hilbert space are necessary for an accurate description of the state. In this simulation, we used $g/2\pi = 0.63\,\mathrm{GHz}$, $\kappa/2\pi = 1.28\,\mathrm{GHz}$ and $\gamma/2\pi = 0.04\,\mathrm{GHz}$.

operator and therefore the connection between the classical and quantum description of light [118]. Therefore, the Hamiltonian is the same as if the molecule was driven directly with a classically modelled beam of Rabi frequency $\Omega_\alpha(t) = g\alpha(t)$, as illustrated in Fig. 2.10. Only in

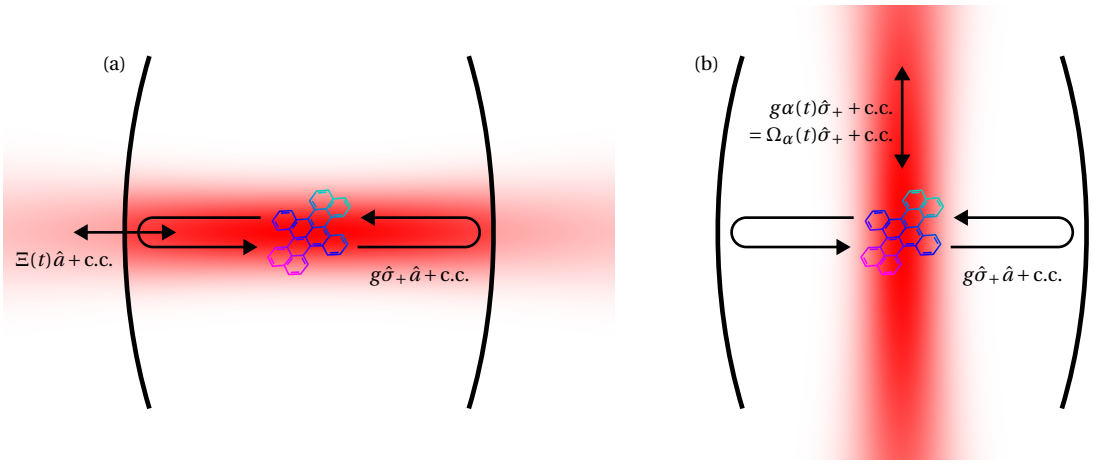

Figure 2.10: Comparison of the regular driven Jaynes-Cummings model (Eq. 2.42) and its vacuum picture transformed version (Eq. 2.49). (a) In the regular Hamiltonian, the cavity mode is populated by the laser driving term $\Xi(t)\hat{a}+\text{c.c.}$, where c.c. stands for complex conjugated. In the absence of the molecule, this would create a coherent photonic state $|\alpha(t)\rangle$ in the cavity. A molecule interacts with and modifies this state by means of the term $g\hat{\sigma}_+\hat{a}+\text{c.c.}$. (b) For the molecule, this situation is equivalent to a free-space laser driving with Rabi frequency $\Omega_\alpha(t)$ plus its interaction with the photons it emitted into the cavity.

measurements of the total cavity field (or the field leaking out of the cavity) does one need to account for the coherent part.

Note that the vacuum picture is not an approximation, but an exact transformation. In the following subsections we explain how concrete experimental measurements are modeled. To summarize, the general equation of motion in the vacuum picture is

$$\begin{aligned}\partial_t\rho_v = -i\Big[&(\omega_e-\omega_L)\,\hat{\rho}_{ee}+(\omega_c-\omega_L)\,\hat{a}^\dagger\hat{a}+g\left(\hat{\sigma}_+\left(\hat{a}+\alpha(t)\right)+\hat{\sigma}_-\left(\hat{a}^\dagger+\alpha^*(t)\right)\right),\rho_v\Big]\\&+\kappa\left(\hat{a}\rho_v\hat{a}^\dagger-\frac{1}{2}\left(\hat{a}^\dagger\hat{a}\rho_v+\rho_v\hat{a}^\dagger\hat{a}\right)\right)\\&+\gamma\left(\hat{\sigma}_-\rho_v\hat{\sigma}_+-\frac{1}{2}\left(\hat{\rho}_{ee}\rho_v+\rho_v\hat{\rho}_{ee}\right)\right)\\&+\gamma_{et}\left(|t\rangle\langle e|\,\rho_v\,|e\rangle\langle t|-\frac{1}{2}\left(|e\rangle\langle e|\,\rho_v+\rho_v\,|e\rangle\langle e|\right)\right)\\&+\gamma_{tg}\left(|g\rangle\langle t|\,\rho_v\,|t\rangle\langle g|-\frac{1}{2}\left(|t\rangle\langle t|\,\rho_v+\rho_v\,|t\rangle\langle t|\right)\right).\end{aligned}\tag{2.50}$$

2.4.1 Steady State

To compute the reflection and transmission spectra of the cavity-molecule system, we use the steady-state solver `steadystate` of QuTiP. Since the laser is tuned over the spectral features much slower than the dynamics of the system, we can approximate the system to be in the

steady state $\rho_{v,ss}$ at any laser frequency ω_L. To find $\rho_{v,ss}$ QuTiP solves the equation

$$0 \stackrel{!}{=} \partial_t \rho_{v,ss} = \hat{\hat{\mathrm{L}}} \rho_{v,ss}, \tag{2.51}$$

in which $\hat{\hat{\mathrm{L}}}\rho_{v,ss}$ is the right-hand side of Eq. 2.50, written with the Liouvillian superoperator $\hat{\hat{\mathrm{L}}}$ [114]. In other words, the steady state $\rho_{v,ss}$ is the eigenstate of the Liouvillian $\hat{\hat{\mathrm{L}}}$ with eigenvalue 0. If $N = N_{\mathrm{mol}} \cdot N_c$ is the number of dimensions of the Hilbert space $\mathscr{H} = \mathscr{H}_{\mathrm{mol}} \otimes \mathscr{H}_c$ describing the state of the molecule and the cavity, the density matrix $\rho_{v,ss}$ has N^2 entries. The Liouvillian $\hat{\hat{\mathrm{L}}}$ is therefore represented as an $N^2 \times N^2$ matrix. Finding the eigenvalues of this matrix has a computational complexity of $\mathscr{O}\left(\left(N^2\right)^3\right)$ [116]. This is the bottleneck in computing the transmission/reflection spectrum. Then the transmitted photon flux

$$I_{\mathrm{t}} = \kappa \left\langle \left(\hat{a}^\dagger + \alpha^*\right)\left(\hat{a} + \alpha\right) \right\rangle \tag{2.52}$$

is obtained from the steady state density matrix. It is the energy loss rate of the cavity κ multiplied by the total number of photons in the cavity $\langle (\hat{a}^\dagger + \alpha^*)(\hat{a} + \alpha) \rangle$. Note that the total number of cavity photons is not only $\langle \hat{a}^\dagger \hat{a} \rangle$, because ρ_v does not contain the coherent light due to the laser. Leaving the coherent part out is a convenient way to inspect solely the light scattered into the cavity mode by the molecule or to model the situation depicted in Fig. 2.10b).

In some cases we do not detect purely the transmitted light, since it interferes with coherent light of amplitude β. For example, the reflection of the cavity is a superposition of the light leaking out of the cavity with the coherent light reflected from the first mirror of the cavity. Even in the cross-polarized detection scheme (see Ch. 3.4.2) some back-reflected light is not eliminated by the polarizer and interferes with the light from the cavity. These situations can conveniently be described by adding the complex amplitudes of the coherent cavity field α and the additional coherent field β

$$I_{\mathrm{int}} = \kappa \left\langle \left(\hat{a}^\dagger + \left(\alpha + \frac{\beta}{\sqrt{\kappa}}\right)^*\right)\left(\hat{a} + \left(\alpha + \frac{\beta}{\sqrt{\kappa}}\right)\right) \right\rangle. \tag{2.53}$$

The factor $\sqrt{\kappa}$ arises from the fact that the field of strength α is *inside* the cavity, while the interfering field has the amplitude β *outside* the cavity.

In addition to the transmission and reflection of the laser light, we can observe the population of the excited state of the molecule by detecting the red-shifted fluorescence (see Ch. 6.1). The emission rate is proportional to $\langle \hat{\rho}_{ee} \rangle$.

2.4.2 Time Evolution

While we usually measure expectation values in the steady state, in the ringdown experiments (Ch. 4.2) we observe the evolution of the system after preparation by a short laser pulse. We use a Hamiltonian with time-dependent $\alpha(t)$ (see Eq. B.22) to describe the effect of the laser

pulse. Using QuTiP's `mesolve` we solve Eq. 2.50 for the evolution of $\rho_v(t)$. This allows us to find the time-dependence of expectation values, for example for the transmitted light $I_t(t)$.

2.4.3 Emission Spectrum

To compute the emission spectrum of our system, as in the four-wave mixing experiments (Ch. 5.4), we use the Wiener-Khinchin theorem [119]. This states that the emission spectrum $S(\omega)$ is the Fourier transform of the (unnormalized) first-order correlation function $G^{(1)}(\tau)$:

$$S(\omega) = \int_{-\infty}^{\infty} G^{(1)}(\tau) e^{-i\omega\tau} \mathrm{d}\tau \tag{2.54a}$$

$$G^{(1)}(\tau) \sim \left\langle \hat{a}^\dagger(t+\tau)\hat{a}(t) \right\rangle \tag{2.54b}$$

The expectation value in Eq. 2.54b is calculated using the quantum regression theorem [104]

$$\begin{aligned} \left\langle \hat{A}(t+\tau)\hat{B}(t) \right\rangle &= \mathrm{Tr}[\hat{A}(t+\tau)\hat{B}(t)\rho] = \mathrm{Tr}[\hat{A}(t+\tau)\left(\hat{B}\rho(t)\right)] \\ &= \mathrm{Tr}[\hat{A}\hat{\mathscr{U}}(t;t+\tau)\left(\hat{B}\rho(t)\right)\hat{\mathscr{U}}^\dagger(t;t+\tau)], \end{aligned} \tag{2.55}$$

with $\hat{\mathscr{U}}(t;t+\tau)$ the time-evolution operator from t to $t+\tau$. In our simulations, this is implemented by first computing the steady state of the system ρ_{ss}, evolving the product $\hat{a}\rho_{ss}$ over a time τ (using QuTiP's `mesolve`), multiplying by $\hat{a}^\dagger$ from the left and then taking the trace. According to Eq. 2.54a, we must calculate $G^{(1)}(\tau)$ for all values of τ. However, calculating it for $\tau \geq 0$ is sufficient due to the Hermitian symmetry $G^{(1)}(-\tau) = G^{(1)}(\tau)^*$. In practice, however, it suffices to calculate a discrete spectrum $S(\omega)$ with enough samples to resolve all spectral features. The spectral resolution $d\nu$ and span $\nu_{\max}$ are reciprocally related to the span of τ-values $\tau_{\max}$ and the temporal resolution $d\tau$:

$$d\nu = \frac{1}{2\tau_{\max}} \tag{2.56a}$$

$$\nu_{\max} = \frac{1}{2\,d\tau}. \tag{2.56b}$$

We also use the quantum regression theorem to simulate $g^{(2)}(\tau)$, as for Ch. 5.3. In detail, we use

$$\begin{aligned} g^{(2)}(\tau) &\sim \left\langle \hat{a}^\dagger(t)\hat{a}^\dagger(t+\tau)\hat{a}(t+\tau)\hat{a}(t) \right\rangle = \mathrm{Tr}[\hat{a}^\dagger(t)\hat{a}^\dagger(t+\tau)\hat{a}(t+\tau)\hat{a}(t)\rho] \\ &= \mathrm{Tr}[\hat{a}^\dagger(t+\tau)\hat{a}(t+\tau)\left(\hat{a}\rho(t)\hat{a}^\dagger\right)] = \mathrm{Tr}[\hat{a}^\dagger\hat{a}\hat{\mathscr{U}}(t;t+\tau)\left(\hat{a}\rho(t)\hat{a}^\dagger\right)\hat{\mathscr{U}}^\dagger(t;t+\tau)]. \end{aligned} \tag{2.57}$$

This means we evolve the product $\hat{a}\rho_{ss}\hat{a}^\dagger$ over a time τ, multiply it by the photon number operator $\hat{a}^\dagger\hat{a}$ and then take the trace.

2.4.4 Two-Frequency Excitation

In some experiments, we use two laser beams of different frequencies, as in the switching (Ch. 5.2) or four-wave mixing experiments (Ch. 5.4). When modeling these situations, there is no rotating frame in which the Hamiltonian $\hat{H}_v$, in particular the coherent state amplitude $\alpha(t)$, is time-independent. Hence, the system does not converge towards a steady state $\rho_{v,ss}$. The explicit form of the time dependence of $\alpha(t)$ is calculated in Appendix B.3. However, it varies periodically with a frequency $\Delta\nu$, corresponding to the detuning between the two lasers. Instead of a time-independent steady state, the system converges to a stationary state $\rho_{v,st}(t)$, which changes over time, but repeats itself after one period $T = 1/\Delta\nu$: $\rho_{v,st}(t+T) = \rho_{v,st}(t)$. The measured emission spectra are the average over the emission of all states during a period. Therefore, the definition of $G^{(1)}(\tau)$ in Eq. 2.54b must be modified by averaging over all possible starting times t within one period

$$G^{(1)}(\tau) \sim \frac{1}{T}\int_0^T \left\langle \hat{a}^\dagger(t+\tau)\hat{a}(t)\right\rangle \mathrm{d}t. \tag{2.58}$$

3 Experimental Platform

This chapter describes the specific experimental methods and the setup used to perform the measurements presented in Ch. 4 & 5. The first part deals with the production and characterization of the key component of the setup – the cavity mirrors. Next, we describe the growth of DBT doped anthracene crystals. After illustration of the cryogenic assembly, the functional units of the optical setup are explained. The last part contains a description of the feedback loop used to stabilize the cavity length and how its error signal is used in the data analysis.

3.1 Mirrors

3.1.1 Substrates

The cavity consists of a flat and a spherical dielectric mirror. The substrate of the flat mirror is a $10 \times 10 \times 0.17\,\mathrm{mm}^3$ borofloat glass coverslide. To facilitate approaching the curved mirror to distances below 1 µm, even in the presence of relative tilt, its substrate must have a small footprint. This was realized in two ways: (i) by using the end facet of an optical fiber as substrate or (ii) by grinding the front facet of a cylindrical gradient index (GRIN) lens.

Optical Fiber

The end facet of a single-mode fiber is a suitable substrate for curved mirrors. A recent review on this type can be found in [120]. A depression for the curved mirror is FIB machined in the center of the fiber to allow a part of the cavity mode to couple to the mode propagating in the fiber core. Accurate positioning on the Ø 125 µm end facet relative to the fiber core is difficult, because the FIB machine does not provide optical access to the sample. Hence, the coupling efficiency can be low.[1] For the fiber used in the experiments described in Ch. 4 & 5, the coupling efficiency was so low that we employed a cross-polarization detection scheme,

[1] The effect of misalignment is analyzed in detail in [121, 122].

as described in Ch. 3.4. More details about the fabrication of the fiber mirrors can be found in [123].

GRIN Lenses

We purchased Ø 2 mm GRIN lenses (GT-LFRL-200-025-50-NC, Grintech GmbH) as substrates for the curved mirrors. A Ø 30–50 µm pedestal was machined on the front facet by ultrasound-assisted diamond turning (UPT Optik Wodak GmbH). Then, several near-spherical depressions were milled into the pedestal by focused ion-beam (FIB) machining (see Fig. 3.2). Fig. 3.1 sketches the shape of a GRIN lens with a single curved mirror. The GRIN lens mode matches the cavity mode with a collimated free-space beam, similar to [124], where a GRIN fiber is spliced at the end of a single-mode fiber to mode-match the fiber output and cavity modes.

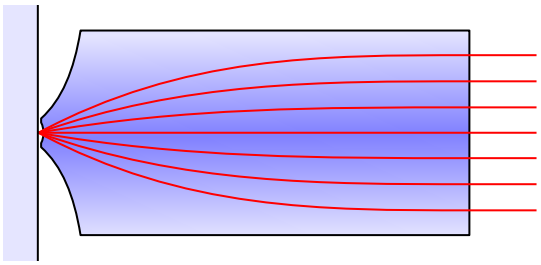

Figure 3.1: The GRIN lens as substrate for the curved mirror collimates the light outcoupled from the cavity mode. The proportions are not to scale.

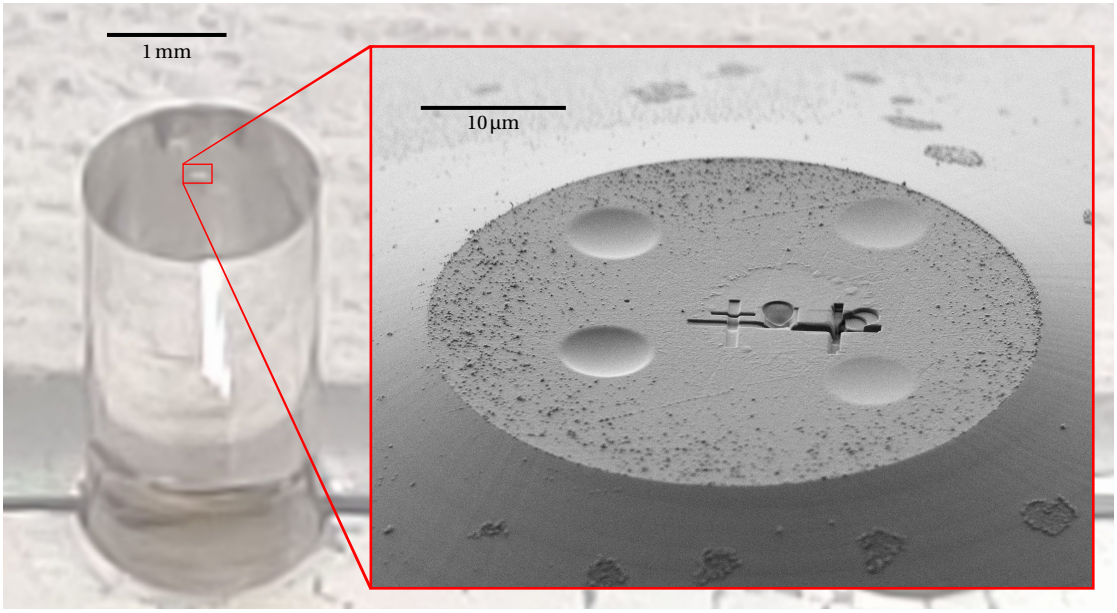

Figure 3.2: Photograph of an uncoated GRIN lens in the holder for the coating machine. The inset is a scanning electron microscope image of the pedestal. Four micromirrors with different geometry and some alignment markers are FIB-machined into the pedestal. This GRIN lens still has many particles from the diamond turning process on the front facet. The GRIN lenses sent for coating were cleaned in an ultrasonication bath.

Curved Mirror Profile

The FIB machine (ORION NanoFab, Carl Zeiss Microscopy Deutschland GmbH) accelerates and focuses gallium ions into the sample to remove material with high precision [125]. Compared to the common technique of CO_2 laser ablation [126, 127], it can produce very small mirrors, down to a radius of curvature (ROC) of 2.6 µm while keeping the root-mean-square surface roughness below 5 nm [93]. The shape of the depression is controlled by the dose of gallium ions. Fig. 3.4 shows a cross-section through the FIBbed structure. It is a spherical depression with a ROC of 10 µm or 15 µm and a depth t of 493 nm or 303 nm, respectively. To reduce the risk of internal-stress-induced cracks in the coating, the edges are smoothed with a radius r_s between 2–7 µm (see Fig. 3.3). For mirrors of this size, the surface roughness is < 0.4 nm [22].

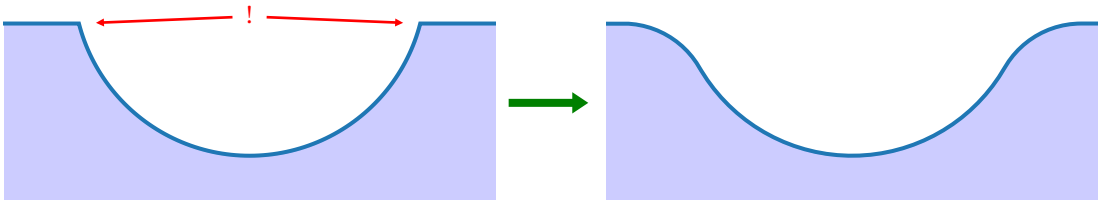

Figure 3.3: Principle of the edge smoothing. The profile in Fig. 3.4 shows a smoothed profile with the actual aspect ratio.

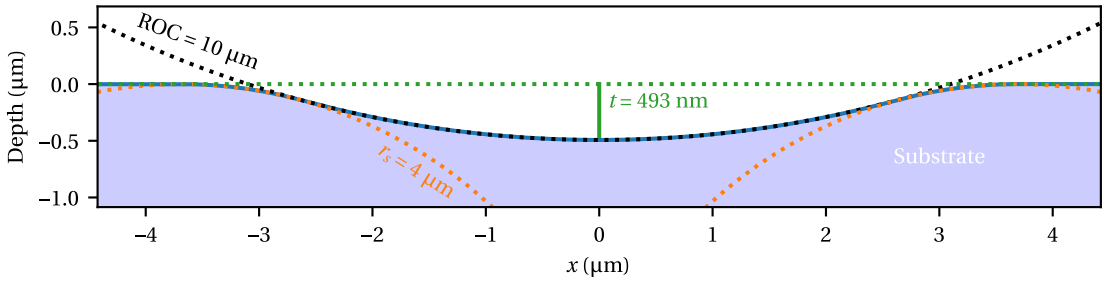

Figure 3.4: Profile of the micromirrors: The shape is defined by its ROC, the depth t and the smoothing radius r_s.

3.1.2 Coating

The substrates are then sent to Laseroptik GmbH, who coat them with multiple layers of dielectric materials by ion beam sputtering [128]. The mirrors consist of a total of 25 layers, alternating between Nb_2O_5 with a refractive index of 2.27 and SiO_2 with a refractive index of 1.48 at $\lambda = 785$ nm. Each layer has an optical thickness of a quarter wavelength, such that all partial reflections at the layer interfaces interfere constructively. This type of mirror is also called *distributed Bragg reflector* (DBR) or *Bragg mirror*.

The reflectivity of this stack is 99.994 % at an angle of incidence (AOI) of 0°, corresponding to a finesse of 57 000. Experimentally, we found a finesse between 20 000 and 50 000. This is due to

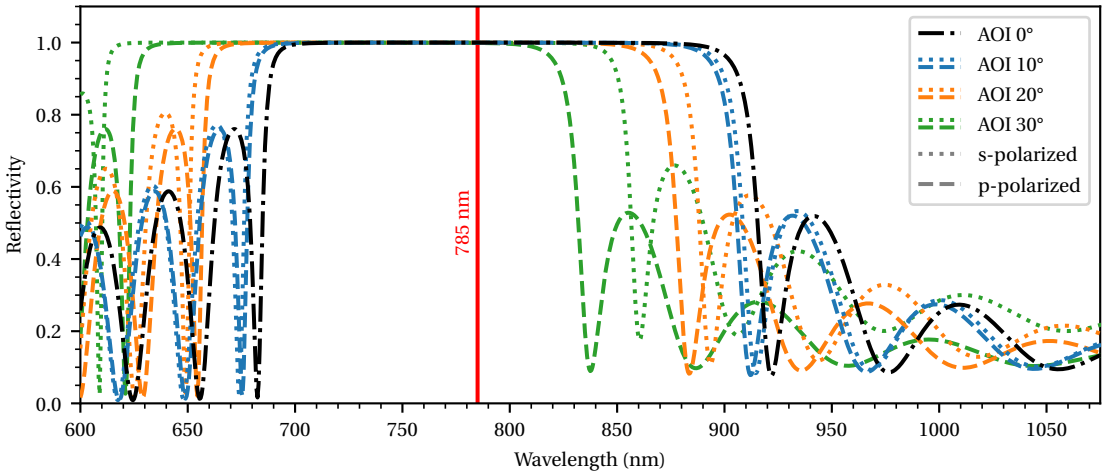

Figure 3.5: The reflectivity spectrum of the Bragg mirrors for different AOI and polarizations, simulated with the transfer matrix method [129].

several factors: Firstly, the cavity mode is a Gaussian beam with a divergence θ between 10° and 16°, depending on the longitudinal mode. Therefore, some parts of it experience the coating under a different AOI. For tilted incidence, the reflectivity spectrum is blue-shifted (see Fig. 3.5), so that the reflectivity for these partial waves is lower. Fig. 3.6 shows the AOI dependence of the reflectivity at $\lambda = 785\,\text{nm}$. The Fresnel coefficients depend on the polarization of the incident light. A focused Gaussian beam contains both, s- and p-polarized light, as explained in Fig. 3.7. As Fig. 3.6 shows, the divergence of the beam does not have a strong effect on the reflectivity of the Bragg mirror, because the large majority of power hits the mirror at an angle where the reflectivity is almost the same as for 0° AOI. In contrast, for the mirrors described in Ch. 6.1, this consideration plays an important role in the design.

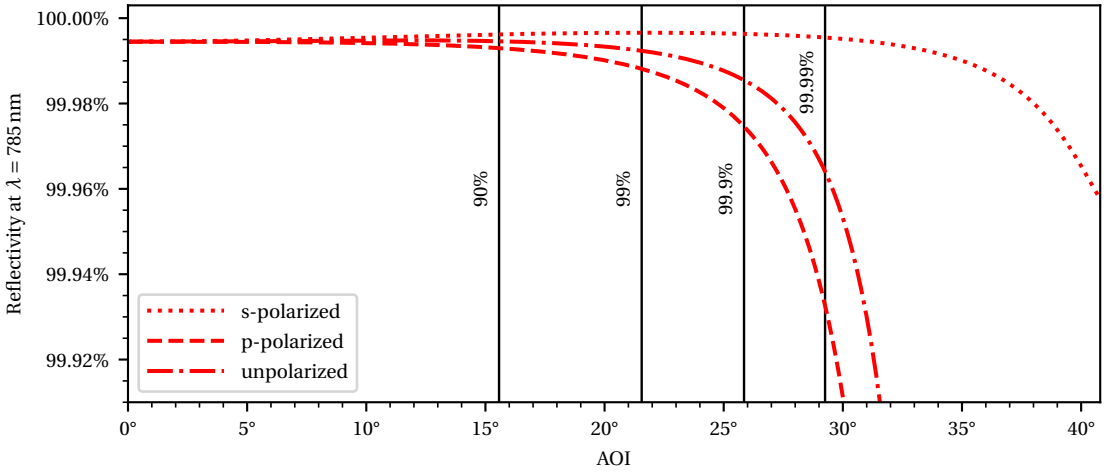

Figure 3.6: The AOI dependence of the Bragg mirror reflectivity for the 00ZPL wavelength $\lambda = 785\,\text{nm}$. The vertical lines indicate the fraction of power contained in a beam of divergence $\theta = 15°$ up to their corresponding AOI.

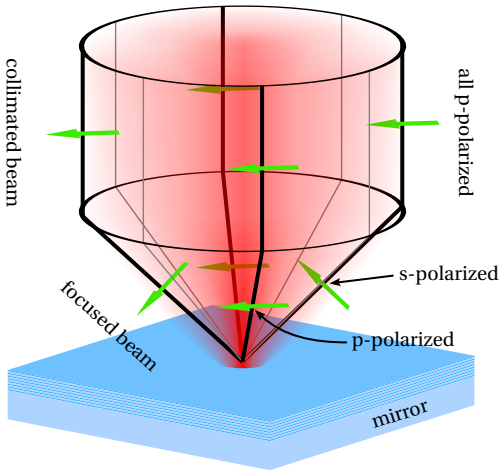

Figure 3.7: A linearly polarized laser beam is focused on a mirror. Each partial ray is polarized orthogonal to its propagation direction. Hence, half of the power in the beam hits the mirror as s-polarized, the other half as p-polarized [130]. This need to be considered in the calculation of the Fresnel coefficients.

Secondly, the finesse is reduced due to clipping losses [127]: The Gaussian beam extends spatially beyond the finite area covered by the curved mirror. A partial ray which is reflected off a part of the curved mirror outside the spherical region, walks off the cavity and is therefore lost. Thirdly, additional sources of loss reduce the effective reflectivity of the mirrors. This can be scattering from particles within the cavity mode or from surface roughness. Additionally, the light can be absorbed within the coating layers, but for Bragg-design mirrors, the role of absorption is small, because among all layer sequences it has the lowest field penetration depth [131].

3.2 Anthracene Crystals

DBT doped anthracene crystals are grown from supersaturated vapor [132] and then transferred onto the flat cavity mirror (see previous section).

The growth apparatus is sketched in Fig. 3.8a). First, a DBT:anthracene stock solution with a DBT concentration between 50 and 500 ppm is created by melting the two constituents together in a closed vial. After the stock solution has cooled down, we insert tens to a few hundreds of milligrams of it into a 50 mL pear-shaped flask, together with a cleaned coverglass. The flask is connected to a pump and a supply of dry nitrogen. To remove water and oxygen, the flask is flushed 3 times with nitrogen [133]. At the end of the last flushing cycle, we set the pressure to 500–1000 mbar. We found the influence of the pressure to be insignificant compared to the influence of other factors, such as the heating time or the amount of raw material. The stock solution is heated with a heatgun set to 300 °C directly underneath the vial. 10 s after the stock solution has melted, the heatgun is switched off and the system is left to cool down to room temperature. During the cooling thin crystals form on the coverslide, the flask walls and in the atmosphere. To optimally collect the crystals formed in the atmosphere, the coverslide lies horizontally inside the flask as shown in Fig. 3.8b). The coverglass with the crystals is carefully taken out of the vial, then we gently lay a flat cavity mirror on it, to pick

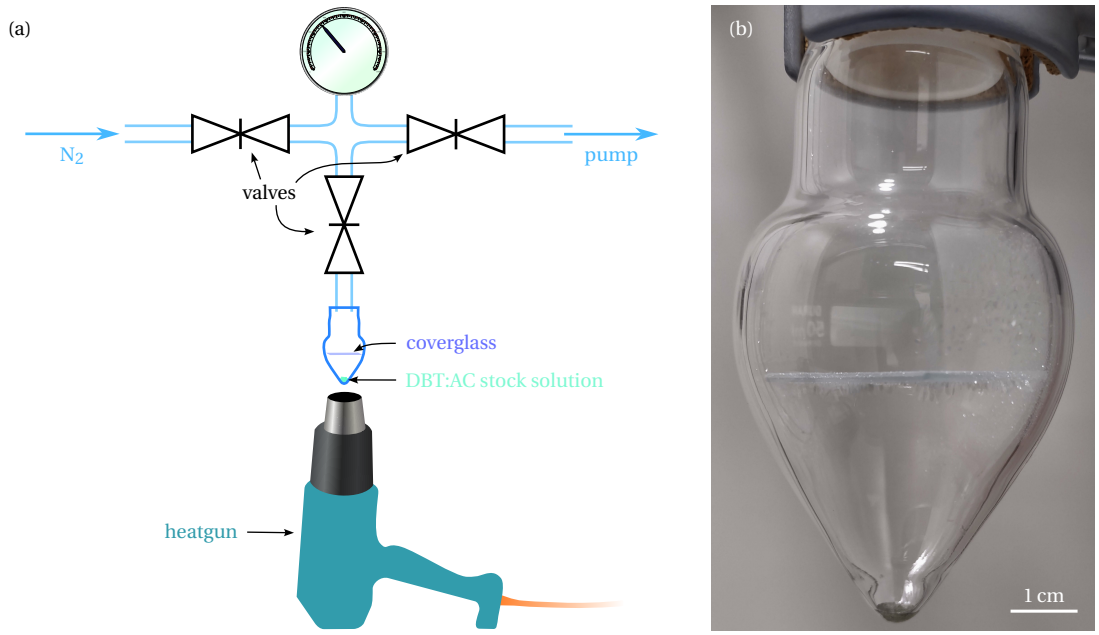

Figure 3.8: (a) Sketch of the setup to control the pressure and temperature during the crystal growth. See text for the procedure. (b) The coverslide inside the flask after crystal growth. Anthracene crystals up to several millimeters in size grew on the bottom side.

up some loose crystals. Some excess crystals which are not properly attached to the mirror surface can be blown away with nitrogen from a nozzle.

We then inspect the crystals on the mirror with a white-light cross-polarization microscope. Our experiments require crystals thick enough to have a field maximum of the cavity mode within them ($\gtrsim 200\,\mathrm{nm}$) and thin enough to allow the two cavity mirrors to be brought close enough together to have negligible clipping losses ($\lesssim 2\,\mu\mathrm{m}$). Additionally, a transversal size larger than $50\,\mu\mathrm{m}$ facilitates the manual alignment of the cavity (see Ch. 3.3 and Appendix H).

The thickness of the crystals can be estimated using their color in the cross-polarization image (see Fig. 3.9), which originates from their birefringence. The refractive index for light polarized along the a-axis is $n_a = 1.55$ and $n_b = 1.775$ along the b-axis [134]. If light of wavelength λ passes through the crystal, its polarization component along the a-axis acquires a different phase than the polarization component along the b-axis. Passing through the crystal twice, in the reflection geometry shown in Fig. 3.9a), the polarization state changes, such that a fraction

$$\left(2\cos\theta\sin\theta\cdot\sin\left(2\pi\left(n_b-n_a\right)\frac{d}{\lambda}\right)\right)^2 \tag{3.1}$$

of the reflected intensity is polarized orthogonally to the incident beam (see Appendix C.1). θ is the angle between the incident polarization and the b-axis. For a given crystal thickness d,

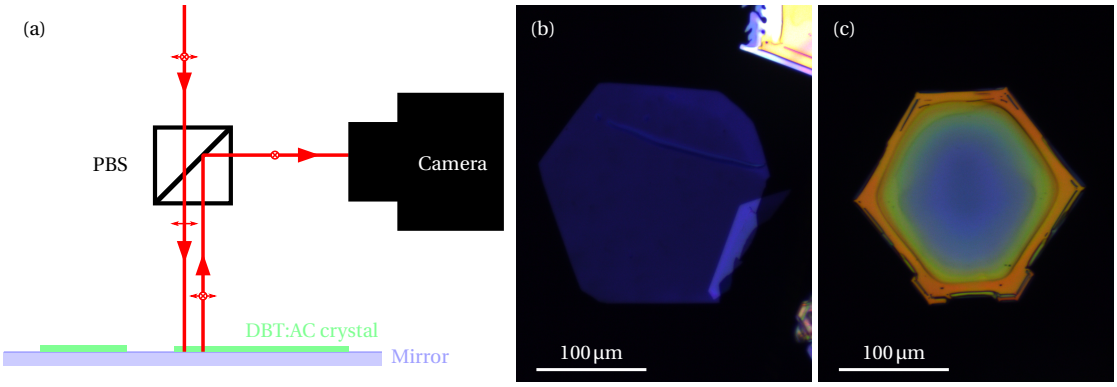

Figure 3.9: Cross-polarization inspection of the crystals. (a) Simplified beam path of the cross-polarization microscope: Light is (y-)polarized by passing through a polarizing beamsplitter (PBS). When traversing the anthracene crystal, it changes its polarization. Only light of the opposite (x-)polarization is used to image the crystals on the camera. (b) A very thin crystal appearing in faint blue. (c) A crystal with a thickness gradient.

the wavelength with maximum transmission through the cross-polarizer is therefore

$$\lambda_{\max} = 4\,(n_b - n_a)\,d \approx 0.9\,d. \tag{3.2}$$

The transmission through the faint blue crystal in Fig. 3.9b) is dominated by blue light. The thickness is therefore clearly less than 400 nm. Cross-polarization colors ranging from blue to orange in the crystal in Fig. 3.9c) reveal that its thickness increases towards the edge.

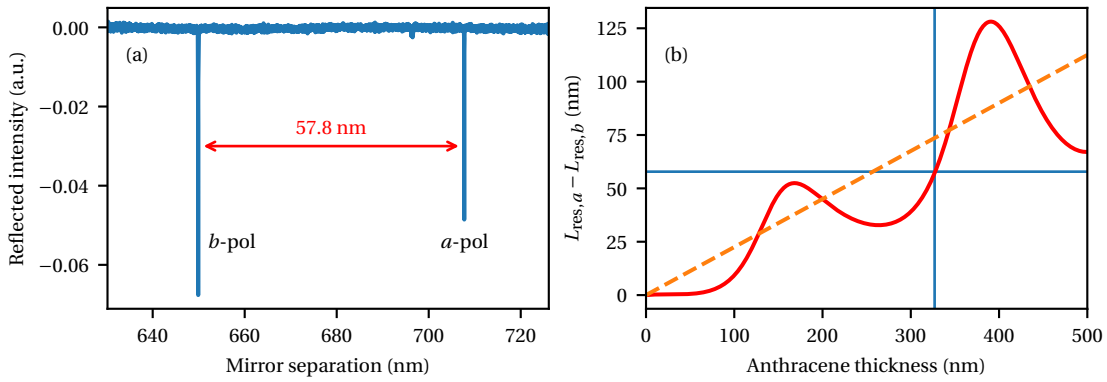

Figure 3.10: (a) A scan of the cavity length over the resonance lengths of the a- and b-modes in a $d = 327\,\mathrm{nm}$ thick crystal on a dichroic mirror (see Ch. 3.1.2). (b) The thickness can be determined by the polarization mode splitting. Without taking the interference between the anthracene crystal and the mirror layers into account (Eq. 3.3, orange dashed line), the crystal appears to be $d = 257\,\mathrm{nm}$ thick. Treating the crystal together with the mirror, the situation can be modeled by the transfer matrix method [129] (red line).

After a suitable crystal has been placed on a flat mirror and aligned within the cavity mode (see Ch. 3.3), we can determine its local thickness from the polarization mode splitting of the cavity. In an empty cavity, the resonance condition (Eq. 2.7) is independent of the polarization of the light, i.e. the polarization modes are degenerate.[2] The birefringent crystal changes the optical round-trip length of the cavity differently for light polarized along the a- and b-axes. Hence, the resonance condition for a- and b-polarized light is fulfilled at different physical mirror distances $L_{\mathrm{res},a/b}$. We can measure the difference in resonance lengths $L_{\mathrm{res},a} - L_{\mathrm{res},b}$ by scanning the cavity length and detecting the resonances (see Fig. 3.10a). Considering only the optical path length in one round-trip, we can deduce a crystal thickness of

$$d = \frac{L_{\mathrm{res},a} - L_{\mathrm{res},b}}{n_b - n_a} \approx 4.4\left(L_{\mathrm{res},a} - L_{\mathrm{res},b}\right). \tag{3.3}$$

This simple model neglects multiple reflections within the anthracene layer and their interference with the mirror. For a rigorous treatment, the effect of the anthracene crystal must be included in the properties of the flat mirror [136]. This leads to oscillatory behavior of the polarization mode splitting when the thickness of the crystal is varied (see Fig. 3.10b).

For our measurements, we couple the spectroscopy lasers to the b-mode, because the transition dipole moment of DBT is aligned with the b-axis [137].

3.3 Cryogenic Setup

3.3.1 Cryostat

The anthracene crystal and the cavity are cooled to 4.2 K within a bath cryostat (10002, CryoVac). It is the same as in D. Wang's dissertation [123]. The sample chamber is in thermal contact with a liquid helium tank. Around it is an isolation layer in contact with another liquid helium tank. To reduce the evaporation rate of the helium, there is a third cryogenic layer around it, which is in contact with a liquid nitrogen tank. The outermost layer is at room temperature. The layers are separated from each other by an isolation vacuum.

3.3.2 Cryostat Insert

In the sample chamber, the cryostat insert stands on a Maxwell kinematic coupling on the baseplate. To minimize the influence of vibrations transferred to the cavity via the sample rod, it is decoupled by a balls-and-rods system (see Fig. 3.11). The insert hosts an aspheric lens for coupling light into the cavity. It can be moved with a piezoelectric slip-stick nanopositioner (PSN) (attocube ANPx51) along the optical axis to adjust the focus. The flat mirror adheres to a ring piezo (PD080.30, PI Piezotechnology) mounted on a PSN (attocube ANPz51), which can

[2] In high-finesse cavities one can sometimes resolve a polarization mode splitting without crystals. This is caused by the ellipticity of the mirror and/or stress-induced birefringence of the coating [135]. But its effect is negligible compared to that of the crystal.

move vertically. This enables us to move different crystals on the flat mirror through the cavity mode. The alignment along the horizontal direction must be performed manually during the assembly outside the cryostat (see Appendix H). The curved mirror is mounted on a ring piezo, which is mounted on a horizontally moving PSN (attocube ANPx51). This allows us to coarsely

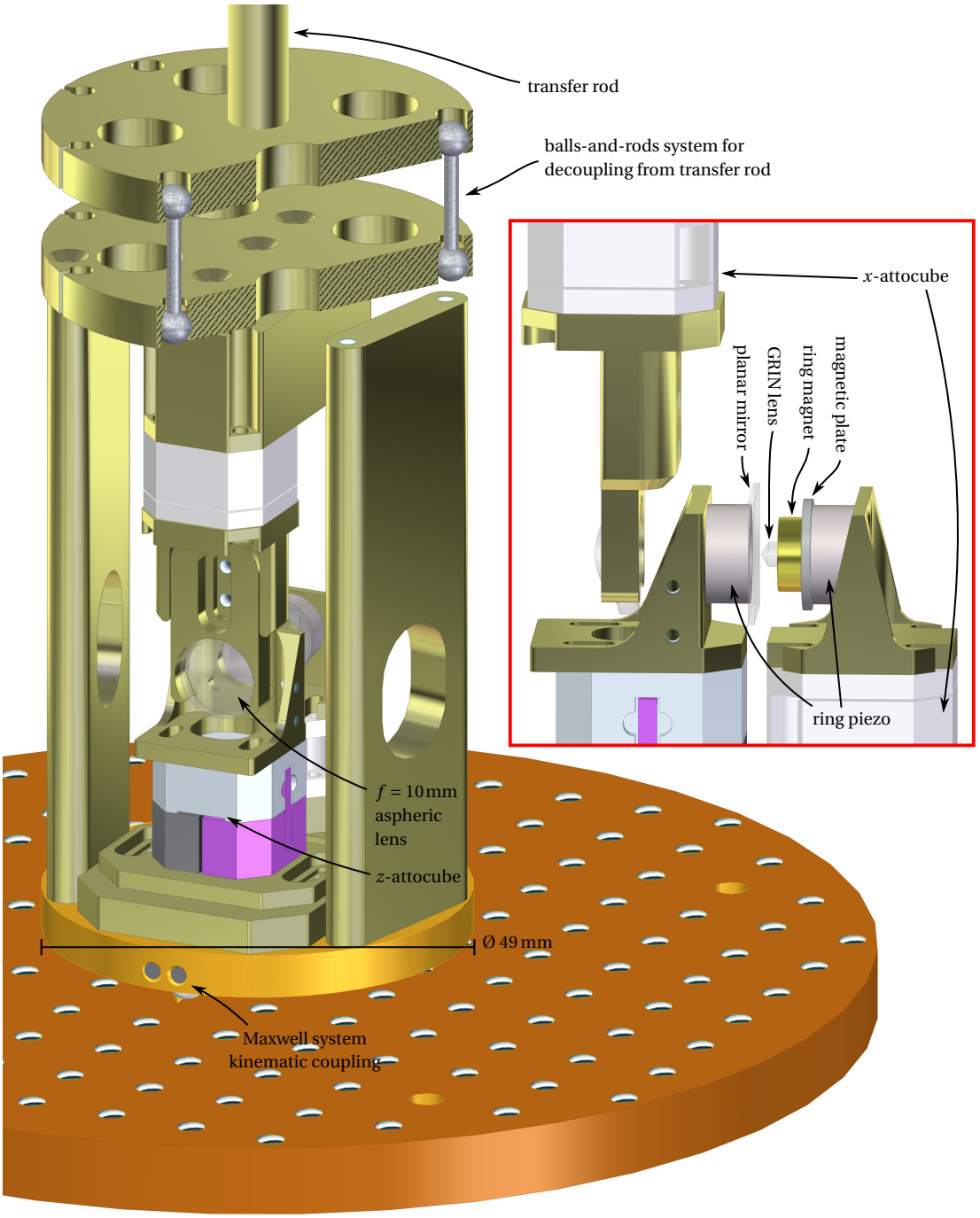

Figure 3.11: The cryostat insert. The inset shows the GRIN lens cavity.

approach or retract the curved mirror. If the substrate for the curved mirror is a fiber (see Ch. 3.1.1), another aspheric lens is mounted after the curved mirror to for in-/outcoupling of light from this side. The GRIN lenses are both, substrate for the curved mirror and coupling optics (see Fig. 3.1). The ring piezos on the mirrors allow continuous fine scanning and locking (see Ch. 3.5) of the cavity length.

3.4 Optical Setup

The optical setup is sketched in Fig. 3.12. Four optical paths start on the table with light coupling out of a fiber (outcouplers O_{pump}, O_{probe}, O_{lock}, O_{curv}). Which laser is connected to which outcoupler depends on the measurement and is mentioned in the individual chapters 4, 5 & 6. Each path has a laser-line filter to remove unwanted light created in the fiber, a linear polarizer, a half-wave plate (HWP), a quarter-wave plate (QWP), neutral density (ND)

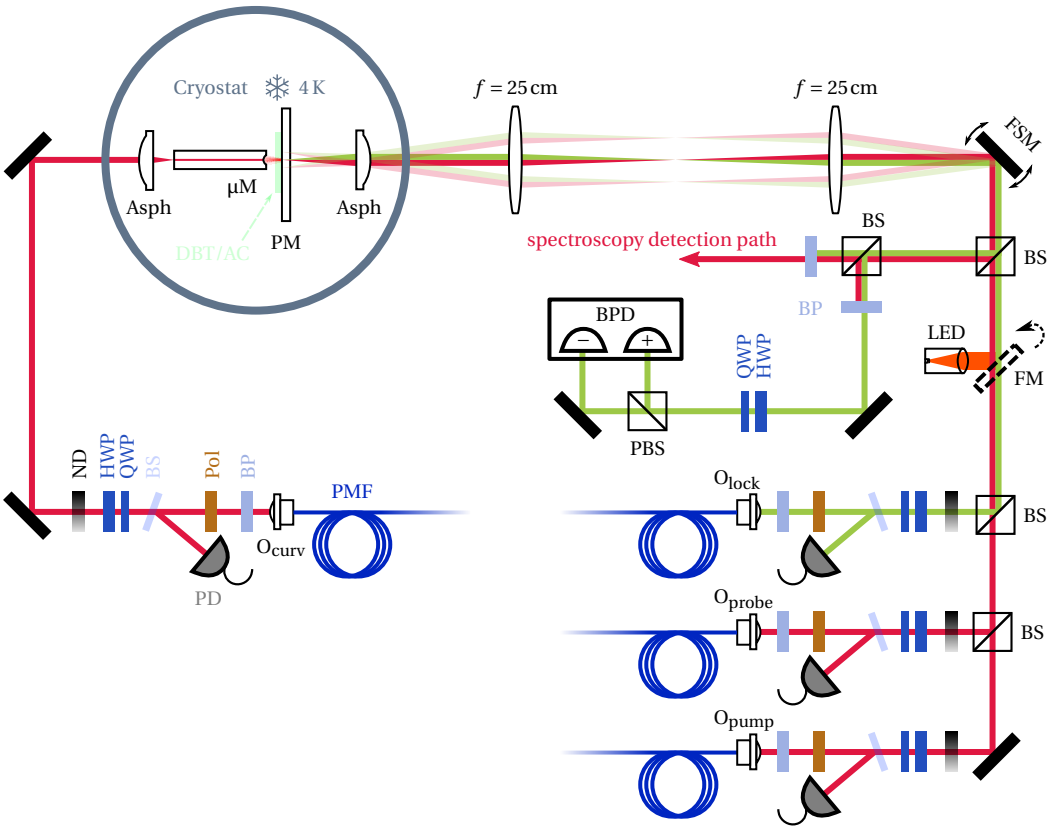

Figure 3.12: The optical setup. Asph: aspheric lens, BP: bandpass filter, BPD: balanced photodiode, BS: beamsplitter, FM: flip mirror, FSM: fast steering mirror, HWP: half-wave plate, LED: light-emitting diode, µM: micromirror, ND: neutral-density filter, O_i: fiber outcoupler, PBS: polarizing beamsplitter, PD: photodiode, PM: planar mirror, PMF: polarization-maintaining single-mode fiber, Pol: linear polarizer, QWP: quarter-wave plate.

filters and a beam sampler with a photodiode. The photodiode is part of a feedback loop to stabilize the intensity. A proportional-integral-differential controller (PID) monitors the photodiode signal and corrects the laser intensity by controlling the modulation amplitude of an acousto-optic modulator (AOM), as shown in Fig. 3.13. The pump, probe and lock paths merge and access the cavity from the flat mirror side, while the fourth path comes from the curved mirror side.

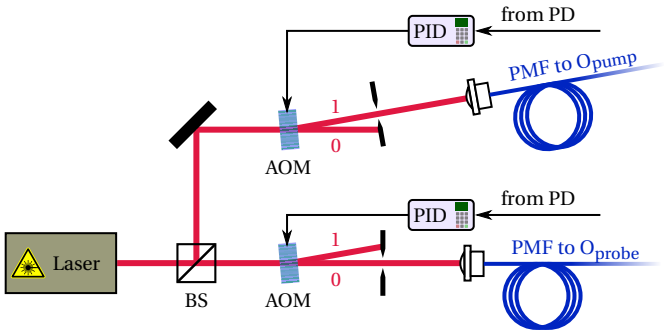

Figure 3.13: Preparation of the pump and probe beam. AOM: acousto-optic modulator, BS: beamsplitter, O_i: fiber outcoupler (see Fig. 3.12), PD: photodiode (see Fig. 3.12), PID: proportional-integral-differential controller, PMF: polarization-maintaining single-mode fiber.

3.4.1 Lock Detection Path

Light coming from the flat mirror side of the cavity reaches the detection path through a 30:70 (R:T) beamsplitter and is separated into a lock detection and spectroscopy detection path. Using appropriate laser-line filters around 760 nm and 785 nm we ensure a clean separation of the signals. The lock beam's polarization is adjusted with a HWP and a QWP and then split by a polarizing beamsplitter (PBS) onto the two detectors of a balanced photodiode (OE-200, Femto Messtechnik GmbH). The locking scheme is explained in Ch. 3.5.

3.4.2 Cross-Polarization Detection

The spectroscopy detection path (see Fig. 3.15) starts with a HWP, QWP and a linear polarization filter for cross-polarized detection. This method is used to detect a transmission-like signal in reflection. The birefringence of the anthracene crystal splits the resonance of the cavity into a mode polarized along the a- and a mode polarized along the b-axis of the crystal (see Ch. 3.2). Since the dipole moment of DBT in anthracene aligns with the b-axis [137], we tune the length of the cavity such that a b-polarized mode is resonant with the molecule of interest. The laser, also around the resonance frequency, is sent into the cryostat with a polarization at 45° relative to the b-axis. Half of its intensity couples into the cavity, interacts with the molecule and then leaks out through both mirrors. The waveplates in the spectroscopy detection path are set such that the linear polarizer removes the polarization component

parallel to the incident light. This means that one half of the light coming out on the flat mirror side is transmitted through the polarizer. As this light has been in the cavity, the detected intensity is proportional to the transmitted intensity.

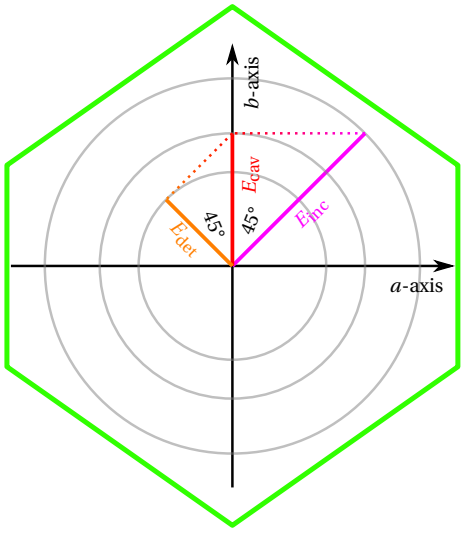

Figure 3.14: The cross-polarization axes. The green hexagon indicates the orientation of the anthracene crystal. E_{inc}: incident electric field vector, E_{cav}: electric field vector within the cavity, E_{det}: electric field vector after the cross-polarizer.

3.4.3 Spectroscopy Detection Box

The rest of the spectroscopy detection path is enclosed in a box to reduce stray light (see Fig. 3.15). First, the light passes through a confocal pinhole, then we can direct it to various detectors: A sCMOS camera (Orca Flash 4.0, Hamamatsu Photonics), an APD (SPCM AQRH-14, Excelitas Technologies Corp.), a photodiode (PDA36A, Thorlabs Inc.) or a Hanbury Brown & Twiss (HBT) setup with two fast APDs (PDM100, Micro Photon Devices S.r.l.). Additionally, we can filter the light through a scannable Fabry-Pérot cavity (Tropel 240, 7.5 GHz FSR, 30 MHz

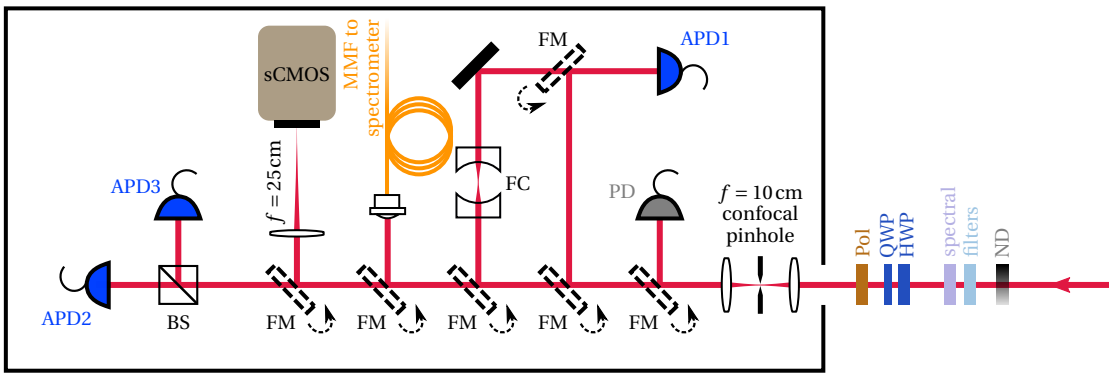

Figure 3.15: The spectroscopy detection path. APD: avalanche photodiode, BS: beamsplitter, FC: filter cavity, FM: flip mirror, HWP: half-wave plate, MMF: multi-mode fiber, ND: neutral-density filter, PD: photodiode, Pol: linear polarizer, QWP: quarter-wave plate, sCMOS: scientific complementary metal-oxide-semiconductor camera.

FWHM) or couple it into a fiber and guide it into a spectrometer (Andor Kymera-328i-B2-SIL, Oxford Instruments).

3.5 Lock

A high-finesse cavity is extremely sensitive to changes in the cavity length. At a finesse of 24 000, as in the experiments described in Ch. 4 & 5, the FWHM of the transmission peak in a cavity length scan is 16 pm. Mechanical vibrations cause the cavity length to fluctuate during the measurement and thereby wash out the detected signals.

3.5.1 Hänsch-Couillaud Locking Scheme

We utilize the birefringence of the anthracene crystal for a Hänsch-Couillaud lock [138]. This scheme requires that only one polarization component of the incoming beam couples to the cavity. Our system fulfills this requirement because of the polarization mode splitting due to the birefringent crystal (see Ch. 3.2). The lock laser is sent to the cavity with a polarization at 45° relative to the cavity mode. For the lock we can use either, the a- and the b-mode, whichever is within the lock laser scan range while a b-polarized mode is resonant with the molecule of interest. If we have the choice, we preferably lock to an a-mode, because the cross-polarizer then suppresses the lock laser, in addition to the spectral filter. We lock the cavity at $\lambda_{\text{lock}} = 760\,\text{nm}$ with an external cavity diode laser (DL Pro, Toptica Photonics AG). When using the dichroic cavity mirrors introduced in Ch. 6.1 we use a wavelength between 975 nm and 1005 nm from a Ti:sapphire laser (Matisse 2 TS, Sirah Lasertechnik GmbH).

The Hänsch-Couillaud locking scheme is based on measuring the phase difference between the polarization component which couples to the cavity and the directly reflected light. Using

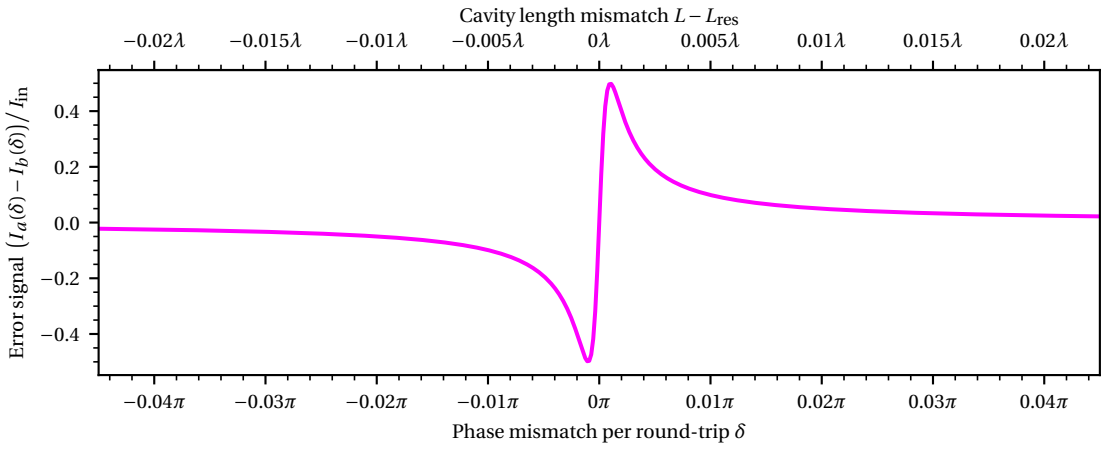

Figure 3.16: The error signal for a Hänsch-Couillaud lock on a cavity mode of finesse $\mathscr{F} = 1000$ as a function of the cavity detuning.

a quarter-wave plate (QWP) and a polarizing beamsplitter (see Fig. 3.12), the phase difference is converted to an intensity difference $I_a - I_b$ between the two detectors of the balanced photodiode[3]

$$I_a - I_b = I_{\text{in}} \frac{T R \sin\delta}{(1-R)^2 + 4R\sin^2\left(\frac{\delta}{2}\right)} \tag{3.4}$$

(see Fig. 3.16). I_{in} is the incident intensity and T and R are the transmissivity and reflectivity of the mirrors, respectively. The detuning in this equation is given in units of phase mismatch per round-trip $\delta = 2\pi\,(L - L_{\text{res}})\,/\,\lambda$.

The error signal $\text{Err}(t) := I_a(t) - I_b(t)$ is fed into a PID (PID 110, Toptica Photonics AG or SIM960, Stanford Research Systems). The output voltage is then applied to the ring piezo on the flat mirror side. Although the bandwidth of the balanced photodiode at the used amplification is 50 kHz, we set the PID gains such that the feedback only compensates for slow (< 30 Hz) vibrations. Mechanical resonances between 100–2000 Hz (see Fig. 3.17) cause the feedback to be 180° out of phase, leading to an amplification of the vibration, if the PID bandwidth is too high. A standard PID feedback loop therefore cannot dampen the resonant vibrations.

We therefore took several measures to keep the excitation of the vibrations low. To isolate the cryostat insert from external acoustic noise, it is decoupled from the transfer rod by a balls-and-rods system, as shown in Fig. 3.11. The cryostat is surrounded by 2 layers of noise insulation foam (Basotect G+, Flexolan GmbH) and 1 layer is glued to the laboratory doors.

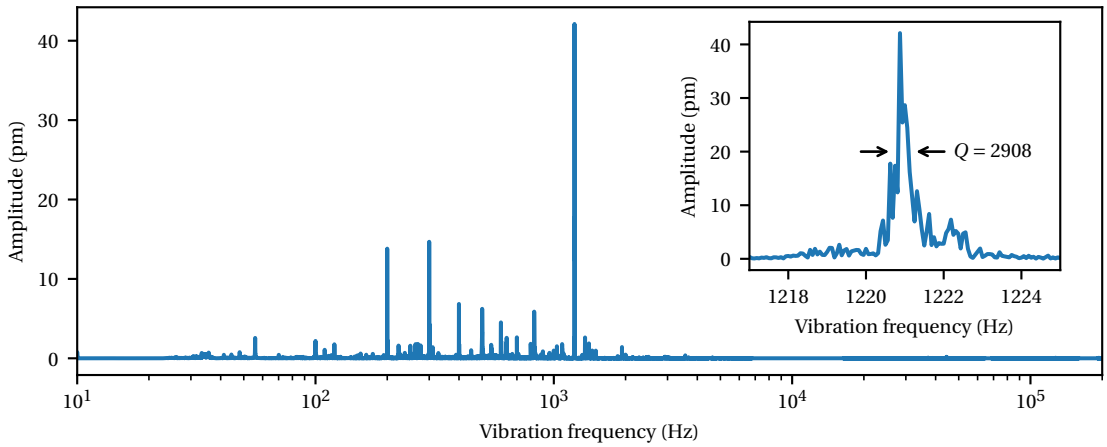

Figure 3.17: The spectrum of the error signal, revealing several sharp peaks. The inset shows a closeup of the most prominent vibration mode. Note that this vibration spectrum is extracted from the measurement shown in Fig. 3.18, with the error signal linear with respect to the cavity length change, facilitating the conversion from error signal (V) to vibration amplitude (pm).

[3]The derivation and a sketch of the setup are detailed in [138]. However, the resulting equation for the error signal therein (Eq. 6; corresponding to Eq. 3.4 here) is missing the "+" in the denominator.

All lasers with chillers are located in another room and all other noisy electronic devices are enclosed in a sound isolated network rack (Logilink W15D67G, 2direct GmbH). The turbo pump for the isolation vacuum of the cryostat is located on the ground floor of the building and damped by massive concrete blocks, while our experimental setup is in the basement. To minimize vibrations originating within the cryostat, we adjust the filling schedule. Boiling liquid nitrogen causes strong vibrations, therefore we only fill it in the evening. The amount is chosen such that the nitrogen tank empties in the morning before we start measurements. The helium tanks are also filled in the evening. This ensures that they reach an equilibrium state overnight. Furthermore, the needle valve connecting the two tanks is adjusted to be nearly closed. It then warms to $\sim 60\,\mathrm{K}$, creating a helium bubble between the tip and seat which prevents helium flow even if the pressure between the tanks is not perfectly equal.

In addition to these measures, one could employ more sophisticated feedback loops capable of overcoming the resonances [139]. Furthermore, a stiffer cryostat insert mechanically decoupled from the internal vibrations of the cryostat would reduce the amplitude of vibrations of the cavity [140–142].

3.5.2 Synchronized Detection

Instead of implementing a more complicated locking scheme to dampen the vibrations at the mechanical resonance frequencies, we record the error signal at a rate of 1 Mega-sample per second (1 MS/s) and use it in the data analysis. We synchronize the data acquisition with the error signal recorded by a DAQ card (USB6363, National Instruments). Because the bandwidth of the error signal is limited to 50 kHz by the balanced photodiode, we smoothen the data via a moving average over $10\,\mu\mathrm{s}$ to reduce the effect of noise. After shifting the data tracks relative to each other to account for their relative delays (see Appendix D), we distribute them into bins depending on the error signal. Effectively, this means that we extract data for different cavity detunings from one dataset (see Fig. 3.18) and therefore acquire 2D spectra such as that shown in Fig. 2.7. For the experiments presented in Ch. 4 & 5, we focus on the situation when the cavity is on resonance with the molecule. We therefore only use data from moments in which the error signal is within a narrow range around the voltage indicating resonance V_0. The experiments described in Ch. 6 detect features which appear in the dispersive regime, when the cavity is detuned relative to the molecule. We can then use the full dataset, as in Fig. 3.18, to identify these features in the dispersive regime and confirm that they disappear at zero detuning.

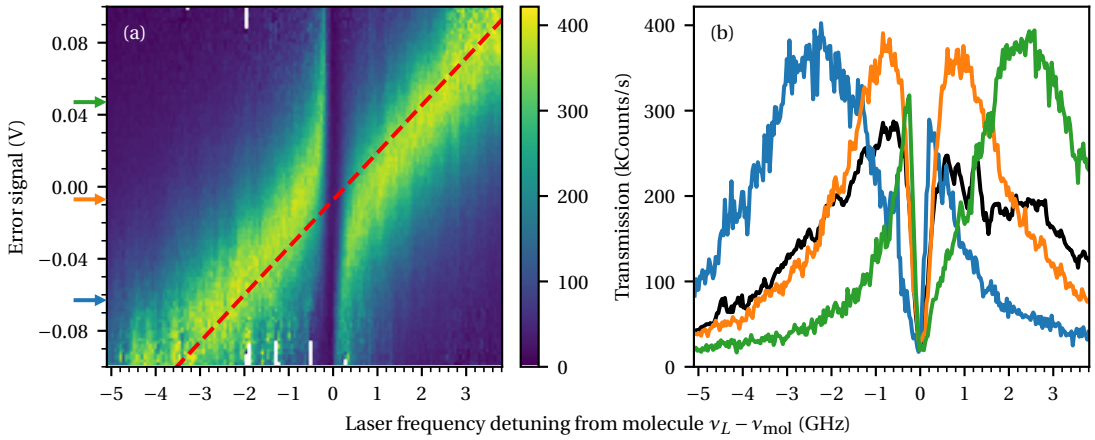

Figure 3.18: The transmission spectrum as a function of the error signal. (a) 2D histogram of the transmission through the cavity, binned over the error signal and the laser frequency. The red dashed line indicates the translation between cavity resonance frequency and error signal. The finesse of the mode used for the lock is low, such that the error signal fluctuates only within its approximately linear range, far from the turning points around resonance (see Fig. 3.16). (b) Three transmission spectra for different values of the error signal, indicated by the colored arrows in (a). The detunings of the cavity relative to the molecule are −2 GHz (blue), 0 GHz (orange) and +2 GHz (green), respectively. The overall spectrum, averaged over all error signal values, is plotted in black.

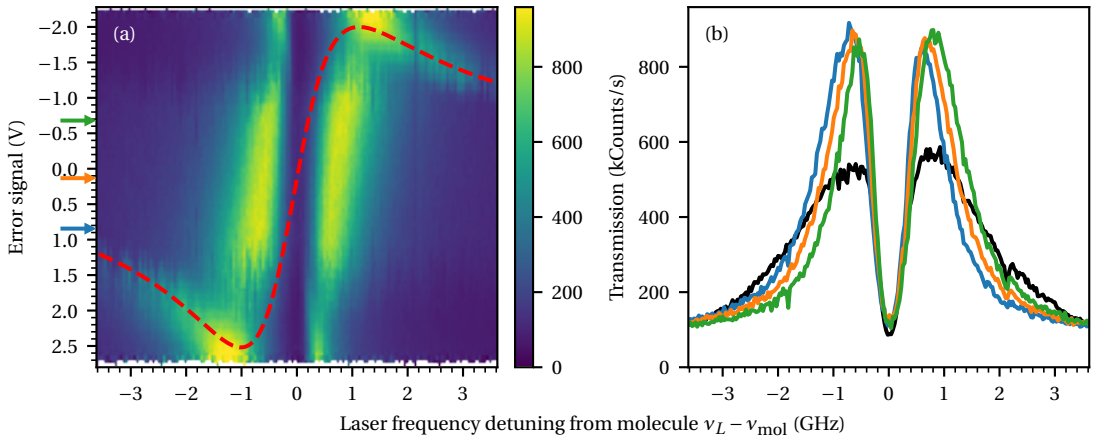

Figure 3.19: Same as Fig. 3.18, but with the cavity locked to a high-finesse mode. (a) The cavity vibrations cause the error signal to fluctuate beyond the turning points. Hence, when the error signal lies outside [−1 V, +1 V], we cannot identify the cavity resonance frequency uniquely. (b) However, within a small range, it is possible to select the cavity resonance frequency. The cavity-molecule detunings are −0.2 GHz (blue), 0 GHz (orange) and +0.2 GHz (green).

4 Strong Coupling

If an emitter exchanges a single photon with a photonic structure faster than the photon is lost, they are strongly coupled to each other [143]. In the strong coupling regime, the energy eigenstates of the molecule and the cavity hybridize into polariton states (see Ch. 2.3.3), which we detect in the spectral domain in Ch. 4.1. If the composite system is initialized by an excitation of either the molecule or the cavity, the excitation is exchanged back and forth between them (see Ch. 2.3.5). We experimentally explore these oscillations in Ch. 4.2. The results presented in Chapters 4 & 5 were obtained using a cavity consisting of two Bragg mirrors (see Ch. 3.1.2), with an optical fiber as the substrate for the curved mirror (see Ch. 3.1.1).

The content of this and the next chapter was published in *Single-Molecule Vacuum Rabi Splitting: Four-Wave Mixing and Optical Switching at the Single-Photon Level* by A. Pscherer, M. Meierhofer, D. Wang, H. Kelkar, D. Martín-Cano, T. Utikal, S. Götzinger and V. Sandoghdar, Phys. Rev. Lett. **127**, 133603 (2021).

4.1 Vacuum Rabi Splitting

To detect the hybridization of energy levels, we use the following experimental configuration: One beam from the spectroscopy laser is coupled into the cavity from the planar mirror side. We detect light leaving the cavity on the same side. Using crossed polarizations (see Ch. 3.4.2), the intensity detected on the APD is proportional to the transmission through the cavity. To minimize the effect of the mechanical vibrations of the cryostat insert, we employ the synchronized detection technique described in Ch. 3.5.2. The detected photon count rate C_{det} is corrected for the photons hitting the APD within the deadtime of $T_d = 87.3\,\mathrm{ns}$ (see Appendix E). Furthermore, we subtract the incoherent background caused by the locking laser.[1] Scanning the spectroscopy laser frequency across the cavity reveals a Lorentzian profile with FWHM of $\kappa/2\pi = 1.28\,\mathrm{GHz}$ (see Fig. 4.1b)). This is the lifetime-limited linewidth of the cavity, as we confirmed by ring-down measurements (see Ch. 4.2). Together with a FSR of

[1] The locking laser at $\lambda_{\mathrm{lock}} = 760\,\mathrm{nm}$ creates red-shifted light in the cavity, some of which is transmitted through the $785 \pm 5\,\mathrm{nm}$ laser-line filter in the detection path. The origin of this light is unknown.

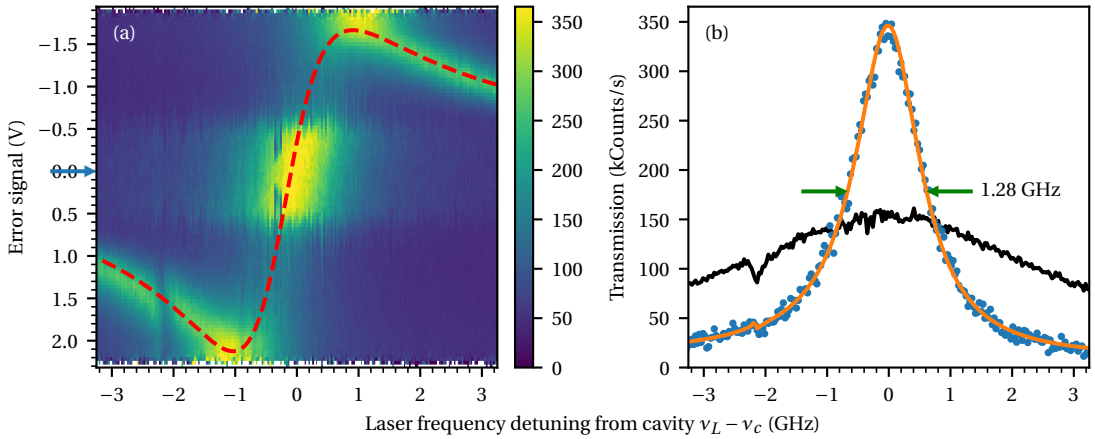

Figure 4.1: The transmission spectrum of the cavity without a molecule. (a) 2D histogram over the transmission binned over the laser frequency and the error signal. The red dashed line shows the relation between the cavity frequency ν_c and the error signal. Between $[-0.5, 0.5]$ V error signal the apparent transmission through the cavity in this measurement is higher than for error signal values outside this range. These error signal values correspond to two different possible cavity frequencies, hence the corresponding transmission spectra are averaged over both detunings. (b) The spectrum for an error signal of $V_0 = 0$ V (blue + orange fit) compared to the vibrationally broadened spectrum with a FWHM of 5.0 GHz (black). The extinction dip at $\nu_L = \nu_c - 2.1$ GHz is due to a weakly coupled molecule.

31.09 THz [123], this gives a finesse of $\mathscr{F} = 2.4 \cdot 10^4$, or a Q factor of $3.0 \cdot 10^5$. Without the synchronized detection technique (see Ch. 3.5.2), the linewidth measured in this way would be broadened, because the cavity changes its resonance frequency during the measurement. In addition, the apparent linewidth changes from one measurement to another, because the amplitude of the mechanical vibrations in the cryostat depends on many factors, such as the levels of cryogenic liquid in the tanks of the cryostat and the temperature of the needle valve.

Knowing the lifetime-limited linewidth of the cavity is particularly important when it interacts with a molecule. κ is not the spectroscopically measured linewidth, but it determines how fast photons leave the cavity. As shown in Ch. 3.5, the vibrations of the cavity are in the kHz range – much slower than the optical transition of the molecule. At any given time, the molecule therefore interacts with a cavity of certain frequency, and at a later time it interacts with a cavity of a different frequency. If, in contrast, the broadened linewidth corresponded to the energy loss rate κ, the molecule would interact with a lossier cavity and therefore exhibit different behavior.

Fig. 4.2b) shows the measured transmission spectrum through the cavity-molecule system, when the 00ZPL is resonant with the bare cavity resonance frequency. From a fit to the model described in Ch. 2.4.1 we extract $2g/2\pi = 1.54$ GHz and $\kappa/2\pi = 1.31$ GHz. The cavity is resonant with the molecule at an error signal of $V_0 = -0.29$ V. A small amount of vibrational broadening remains in this measurement, even after selecting this error signal value in the

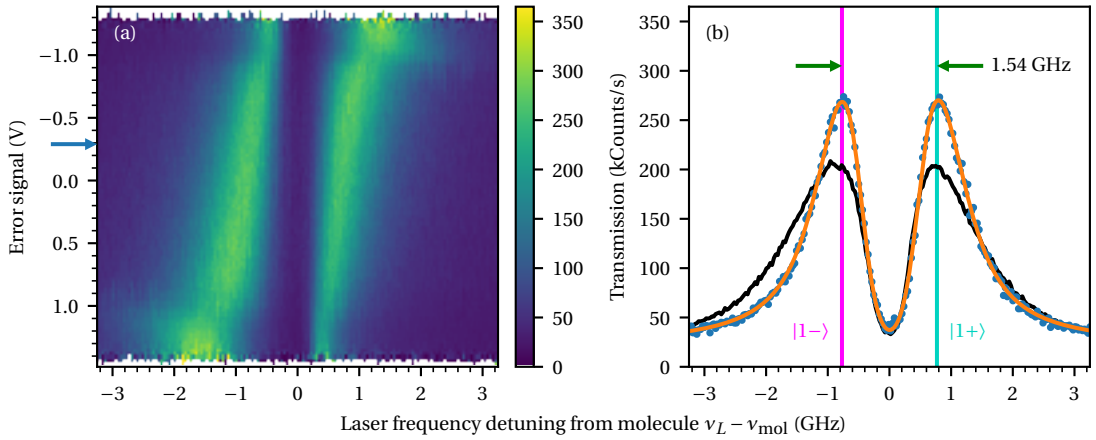

Figure 4.2: The transmission spectrum of the cavity strongly coupled to a molecule. (a) 2D histogram over the transmission binned over the laser frequency and the error signal. (b) The spectrum for an error signal of $V_0 = -0.29\,\mathrm{V}$ (blue + orange fit) compared to the vibrationally broadened spectrum (black). The vertical lines indicate the transition frequencies from the ground state $|g,0\rangle$ to the first polaritons $|1\pm\rangle$.

data analysis. The broadening can be described by a Gaussian distribution of cavity resonance frequencies ν_c with a FWHM of 0.90 GHz. Together with a free-space decay rate of the molecule of $\gamma/2\pi = 0.04\,\mathrm{GHz}$, we obtain a cooperativity of $C = 45$. Since the energy exchange rate between molecule and cavity is higher than the energy loss rate of the cavity $2g > \kappa$, this molecule is in the strong coupling regime. In the next section, we investigate the energy exchange dynamics in the time-domain.

4.2 Vacuum Rabi Oscillations

In a microcavity, the dominant damping of the Rabi oscillations is due to the losses of the cavity $\kappa \sim 1/t_{\mathrm{RT}}$ because of the short round-trip time t_{RT}. Reaching the strong coupling regime therefore requires the single-photon Rabi frequency $2g$ to exceed the cavity decay rate κ. One way to achieve this is to use emitters with a large transition dipole moment $\vec{d}_{eg}$, since $g \sim |\vec{d}_{eg}|$. This led to the first demonstration of strong coupling with quantum dots [26, 92] in the spectral domain. As the energy exchange rates of these systems lies in the tens of GHz range, the dynamics are too fast to observe directly. Our system achieves strong coupling due to the high finesse of our cavity and the correspondingly low κ. This allows us to resolve single-photon Rabi oscillations with low-timing-jitter single-photon detectors.

We perform ring-down measurements to observe the time-evolution of the cavity. We couple 7 ps pulses from a Ti:sapphire laser into the cavity and detect the light leaking out of the cavity with a fast APD (see Ch. 3.4.3). Ideally, the photon detection probability, as a function of the delay after the excitation pulse, is directly proportional to the number of photons in the cavity. However, the detection electronics respond with a non-constant delay, washing out the

temporal dynamics of the investigated system. This is described by the instrument response function (IRF): If a photon hits the APD at time $t = 0$, the IRF describes the probability distribution of times at which the photon is registered by the timetagger (PicoHarp 300, PicoQuant GmbH). This is partially due to noise and the binning in the time tagger[2], but mostly due to processes in the APD. The exact time when an electrical pulse is generated depends on where in the APD the photon is absorbed. APDs tailored for low timing jitter have a thin active area (1–2 µm) to minimize the spread in travel times for charge avalanches. This allows the FWHM of the IRF to be as narrow as 38 ps in our case. Some photons pass through the active area and are absorbed below it. The charges created this way diffuse and eventually reach the active area, leading to a pulse delayed by the more widely distributed diffusion time. This gives rise to the slowly decaying exponential tail [145, 146]. The IRF of our detection system is shown in Fig. 4.3. The probability distribution of registering a photon is given by the convolution of the IRF with the emission probability distribution intrinsic to the process, such as exponentially decaying Rabi oscillations.

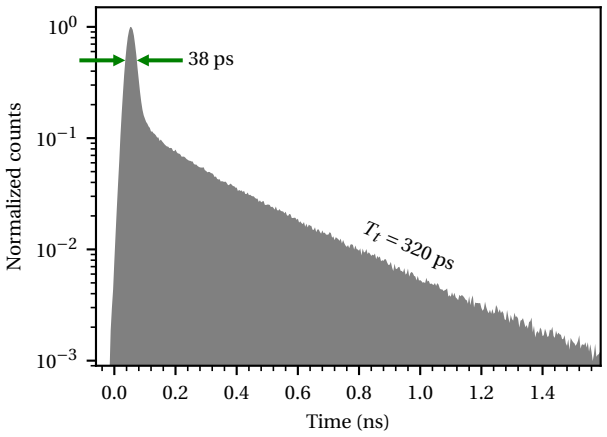

Figure 4.3: The IRF of the fast APD: A Gaussian peak with a FWHM of 38 ps is followed by an exponential decay e^{-t/T_t} with a time constant T_t = 320 ps. Each contribution contains approximately half of the detected photons.

First, we investigate the decay rate of the cavity when it is off-resonant from any molecule. The 7 ps laser pulses are spectrally much broader than the cavity, hence only a fraction of the light enters the cavity, while most of it is reflected. This would lead to a strong background in our measurements, even with the cross-polarization technique described in Ch. 3.4.2. We therefore send the pulses into the cavity from the curved mirror side (see the optical path starting with O_{curv} in Fig. 3.12), through the fiber. Start-stop histograms are then recorded with a timetagger, with the "start" signal coming from the intra-resonator photodiode of the pulsed laser and the "stop" signal is the detection of a photon on the fast APD.

Fig. 4.4 shows the start-stop histogram. We observe an exponential decay of the intensity with a rate $\kappa = 2\pi \cdot 1.28$ GHz, convolved with the instrument response function (IRF) of the APD (see Fig. 4.3). This confirms the value obtained in the spectral domain. It corresponds to a photon lifetime in the cavity of $1/\kappa = 125$ ps. Note that this measurement is not influenced by the cavity vibrations, because the leakage rate of the cavity does not change within a detuning

[2] We use the PicoHarp 300 with a specified single-channel timing precision of 20 ps (FWHM) [144]. Of the measured IRF with 38 ps FWHM we can therefore attribute $\sqrt{(38\,\text{ps})^2 - (20\,\text{ps})^2} = 32$ ps to the APD.

of a few GHz. We can therefore use the whole dataset instead of restricting it to a narrow range of error signal values. This is the reason for the high signal to noise ratio of the empty cavity decay curve compared to the decay curve of the coupled system in Fig. 4.4.

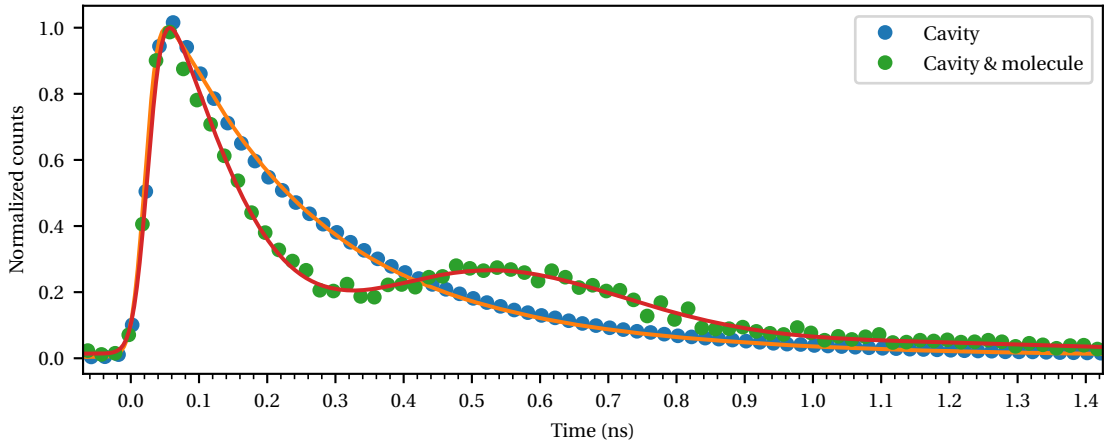

Figure 4.4: The start-stop histograms of the ringdown measurements. The solid lines are fits of the physical model (Ch. 2.4.2) convolved with the IRF. See Fig. 4.5 for the comparison to the pure theory.

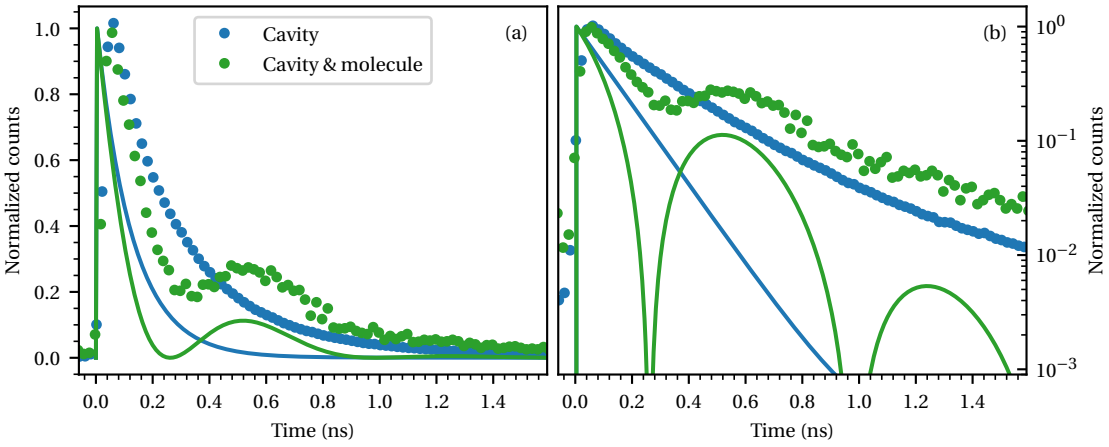

Figure 4.5: The measured start-stop histograms (dots) and the pure theory (without IRF; solid lines) curves, calculated with the parameters extracted from the fits, on a linear (a) and a logarithmic axis (b).

Second, we tune the cavity in resonance with the molecule described in the previous section. The ringdown measurement now reveals oscillations with an exponentially decaying amplitude. When the pulse impinges on the cavity, it first excites the cavity mode. Hence, immediately after the excitation pulse, the start-stop histogram is highest. The photon then excites the molecule, such that after half a Rabi cycle, the remaining energy is stored in the molecule. Because of the absence of cavity photons, the histogram shows a minimum at that time. During another half Rabi cycle the molecule re-emits the excitation into the cavity. This

leads to another maximum in the histogram. The cycle repeats, but with decaying amplitude, because the excitation leaks out of the cavity at a rate κ and out of the molecule at a rate γ. We ensure that each pulse excites $\ll 1$ photon, such that we can neglect contributions from 2 or more photons to the detected signal. A fit of the model described in Ch. 2.4.2 convolved with the IRF reveals a single-photon Rabi frequency $2g/2\pi = 1.53\,\text{GHz}$ and a cavity decay rate of $\kappa = 2\pi \cdot 1.31\,\text{GHz}$. In this measurement, the Rabi oscillations wash out after 1½ cycles because of the slowly decaying tail of the IRF (see Fig. 4.3).

The cavity vibrations must be considered for this measurement. To synchronize the timetags of the start-stop measurement with the cavity error signal, we send TTL pulses from the DAQ card to the marker inputs of the timetagger. From the same dataset, we can choose error signal values corresponding to a detuned cavity. Fig. 4.6a) shows the complete 2D histogram and b) shows individual cross-sections corresponding to different cavity detunings. As predicted by the theory (Eqns. 2.19 & 2.30), the contrast decreases and the effective Rabi frequency Ω_1 increases with detuning.

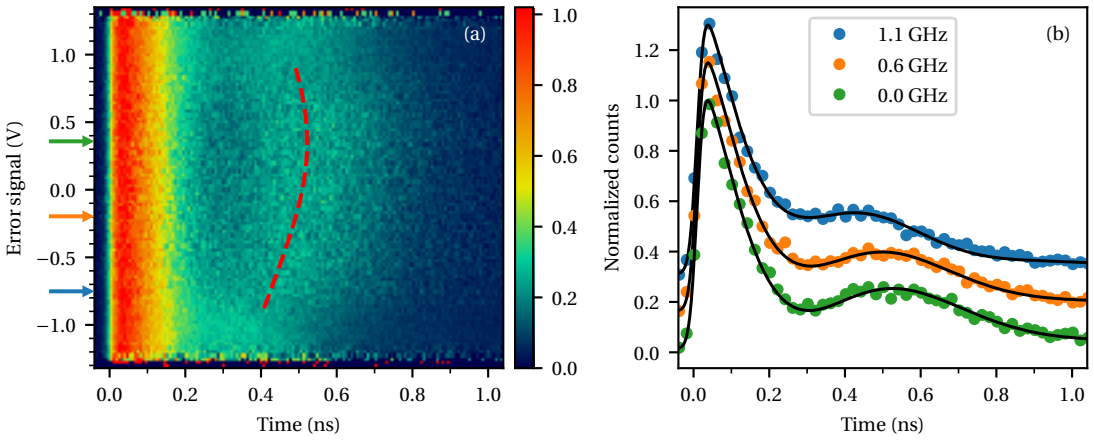

Figure 4.6: Single-photon Rabi oscillations for different cavity-molecule detunings. (a) 2D histogram. The red dashed line marks the time after which 1 Rabi cycle is finished. (b) 1D histograms for detunings 0, 0.6 and 1.1 GHz, respectively. They are vertically shifted to assist visualization.

To model a measurement, we could deconvolve the IRF from the measured data and then fit the physical model to the result. The issue with this method is that convolution is not perfectly reversible over a finite dataset, and the deconvolved signal can be very noisy, because both the experimentally measured IRF and data are noisy to begin with [116]. Instead, we convolve our physical model with the IRF and then fit it to the measured data. This is how the fits in Fig. 4.4 & 4.6 were calculated. Fig. 4.5 compares the measured data to the physical model without the effect of the IRF.

To summarize, we performed the first measurements with a single molecule strongly coupled to a Fabry-Pérot cavity. We provided evidence for this in the spectral domain by observing pronounced Rabi splitting, as well as in the temporal domain by resolving single-photon Rabi

oscillations. Having demonstrated the efficient interaction between the molecule and single photons, in the following chapter we use the molecule to mediate photon-photon interactions effectively.

5 Nonlinear Optical Experiments at the Level of Single Photons

The anharmonicity of the energy level spacing of atoms or molecules causes them to behave qualitatively differently from a linear harmonic oscillator. A laser resonantly driving the molecule from its electronic ground state into its first excited state is far off-resonant from driving it further into the second excited state. This is why it is justified to treat our emitters as two-level systems, which undergo stimulated emission rather than transitioning into a higher state. This is the fundamental reason behind all nonlinear effects shown in this chapter. We begin with an investigation of the saturation behavior of the molecule (Ch. 5.1), which happens at the level of single photons in the cavity, due to the high interaction efficiency. We then use this low saturation threshold to saturate the molecule with one laser beam to make it transparent to another one, realizing an efficient all-optical switch (Ch. 5.2). In chapter 5.3 we realize the quantum version of a switch, in which the molecule-cavity system only transmits photons pairwise. Lastly, we analyze how photons of new frequencies originate in four-wave mixing processes (Ch. 5.4).

The content of this and the previous chapter was published in *Single-Molecule Vacuum Rabi Splitting: Four-Wave Mixing and Optical Switching at the Single-Photon Level* by A. Pscherer, M. Meierhofer, D. Wang, H. Kelkar, D. Martín-Cano, T. Utikal, S. Götzinger and V. Sandoghdar, Phys. Rev. Lett. **127**, 133603 (2021).

5.1 Saturation

The nonlinearity of our system is revealed on saturating it by increasing the laser power. We record spectra in the same experimental configuration as in Ch. 4.1, i.e. using cross-polarized detection (Ch. 3.4.2) synchronized with the lock (Ch. 3.5.2) and correcting for APD deadtime (Eq. E.1c) and incoherent background. When we scan the laser frequency across the common resonance of the molecule and cavity with low power, we find two transmission maxima due to the transitions from the ground state $|g,0\rangle$ to the first polaritons $|1-\rangle$ and $|1+\rangle$. The molecule used in this experiment shows a single-photon Rabi splitting of $2g/2\pi = 1.26\,\mathrm{GHz}$

in a $\kappa/2\pi = 1.28\,\mathrm{GHz}$ broad cavity. Fig. 5.1 shows the spectrum on a logarithmically scaled vertical axis, together with spectra measured at higher laser powers.

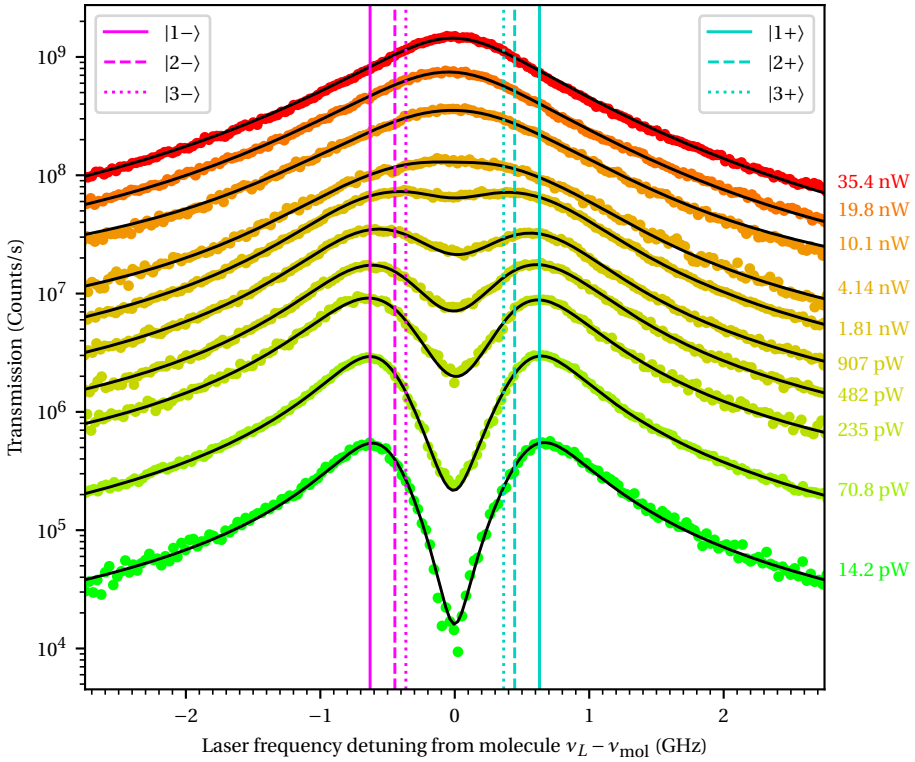

Figure 5.1: Transmission through the cavity on resonance with a molecule. The colored numbers on the right-hand side indicate how much laser power was coupled to the cavity in the respective spectra. The power corresponding to one photon per cavity lifetime is 2.04 nW. Vertical lines are drawn at the resonance frequencies of the n-photon transitions $|g,0\rangle \rightarrow |n\pm\rangle$ (see Fig. 5.2 and explanation in the text). For excitation power $\geq 235\,\mathrm{pW}$ we inserted a calibrated ND filter in the detection path, which attenuated the intensity by a factor of 22.45 ± 0.32; for power $\geq 4.14\,\mathrm{nW}$ it was attenuated by a factor of 323 ± 18.

The double-peaked low-power spectrum gradually turns into the single-peaked spectrum of an empty cavity as the laser power increases. As mentioned in the introduction to this chapter, the reason for this behavior is that the molecule is a two-level system: It can only absorb one photon at a time – a subsequent photon arriving within the lifetime of the excited state stimulates the re-emission of the first photon, effectively keeping the number of photons in the beam constant. Hence, the higher the rate of incident photons, the less the effect of the molecule on the fraction of transmitted photons.
In the strong coupling regime, the energy eigenstates are not the uncoupled states of the molecule and the cavity, but the polaritons (see 2.3.3). We can equivalently describe the saturation behavior in this basis. At low laser power, incident photons usually encounter the molecule-cavity system in the ground state $|g,0\rangle$. When the laser is resonant with the transition to the first polaritons $|1\pm\rangle$, the photons can excite the system. In the transmission

spectrum, this results in a peak at these frequencies $\omega_c \pm g$. With increasing laser power, the chances of a second photon arriving at the cavity before the first excitation has leaked out of the system increases. It is possible that the energy to excite the system into the second polariton $\hbar\left(2\omega_c \pm \sqrt{2}g\right)$ is shared between two photons, leading to a resonance at the laser frequency $\omega_L = \omega_c \pm g/\sqrt{2}$. Analogously, when the laser is tuned to $\omega_L = \omega_c \pm g/\sqrt{n}$, the energy of n photons excites the system into the nth polariton $|n\pm\rangle$. The higher n, the closer the resonance frequency to that of the empty cavity. Fig. 5.2 illustrates these transitions for $n \in \{1,2,3\}$. Deeper in the strong coupling regime, when the width of the polaritons $\left((2n-1)\kappa+\gamma\right)/2$ is less than the separation of the different n-photon resonance frequencies, it is possible to resolve discrete resonances. They appear as additional transmission peaks as the laser power increases, seen, for example, in Fig. 3.3d of the dissertation of D. Najer [147] or very clearly in a transmon qubit [148]. For our system parameters, the resonances are not resolved. Instead, the gap in the transmission spectrum between the first polaritons $|1\pm\rangle$ is continuously filled, making the spectrum increasingly similar to that of the empty cavity. The spectrum taken at a power of 1.81 nW shows that the transmission maxima are not at the single-photon resonance.

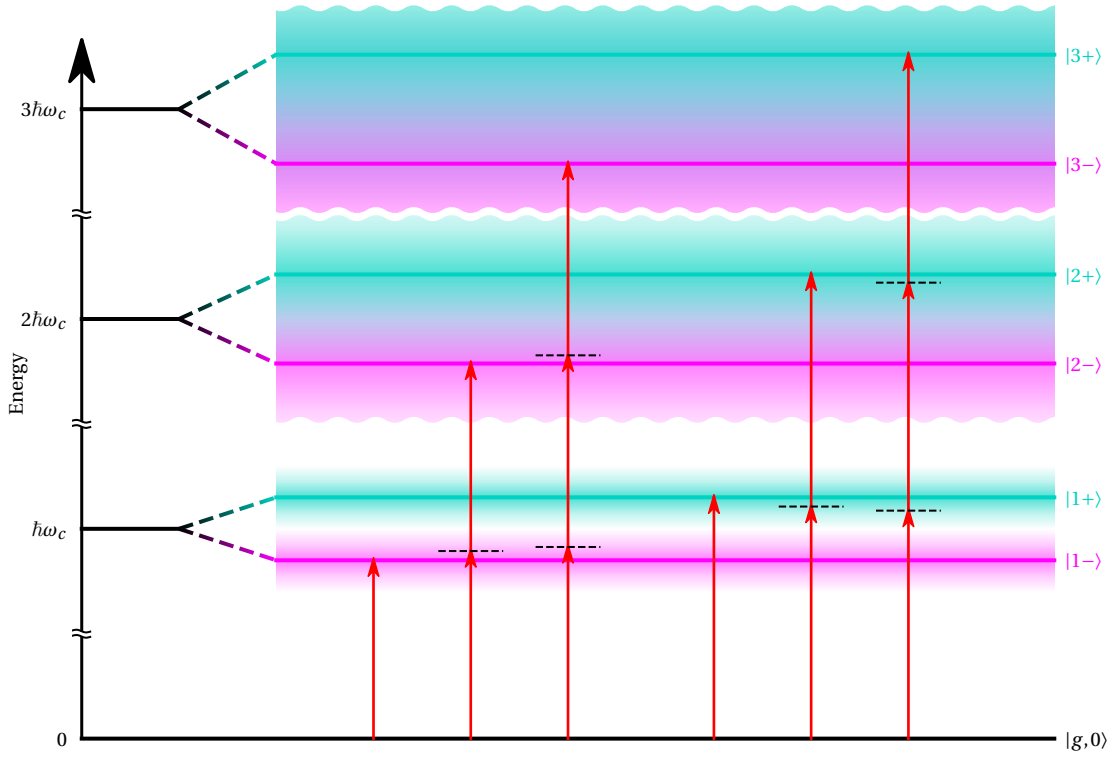

Figure 5.2: 1-, 2- and 3-photon transitions into the upper and lower polaritons $|n\pm\rangle$. The sharp purple and turquoise lines indicate the energy of the lower and upper polaritons, respectively. The color gradients indicate their linewidths.

Qualitatively, the transmission through the common resonance of cavity and molecule is very low as long as the excitation is kept weak. In the limit of infinite power, the transmission goes

to 1. We can quantify this by extracting the transmission from each spectrum in Fig. 5.1. Doing so involves the following steps: First, we fit the model described in Ch. 2.4.1 to the spectrum. Here, we leave g and κ as free fit parameters for the lowest power and use their resulting values as fixed parameters in the fits of the higher power data. This reduces the uncertainty in the fit, because the effect of the molecule on the spectrum is small at high powers. Second, we extract the coherent cross-polarization background α_{cp} from the fit and subtract it from the data. As the absolute transmitted countrate $C_{\mathrm{trans,\,mol}}$ we take the average countrate in a window of $[-50,+50]$ MHz around the molecule frequency ν_{mol}. Third, we calculate the countrate transmitted in the absence of the molecule at the same power $C_{\mathrm{trans,\,cav}}$ by evaluating the fit model with the coupling strength g set to 0. As a result, we find the normalized transmission through the cavity-molecule system to be the ratio

$$T = \frac{C_{\mathrm{trans,\,mol}}}{C_{\mathrm{trans,\,cav}}}. \tag{5.1}$$

Fig. 5.3 shows the normalized transmission extracted this way as data points of the same color as the corresponding spectra in Fig. 5.5. The blue line shows the theory curve assuming that the decay rates in and out of the triplet state are equal $\gamma_{et} = \gamma_{tg}$. We note that these rates vary from molecule to molecule and we do not know them for the molecule used in this experiment. However, it suffices to know their ratio, since this determines how much population is shelved in the triplet state $|t\rangle$. Fig. 5.4 shows a comparison between theoretical transmission curves with γ_{et}/γ_{tg} ranging from 10^{-1} to 10^{+1}. The slower the molecule relaxes from the triplet state

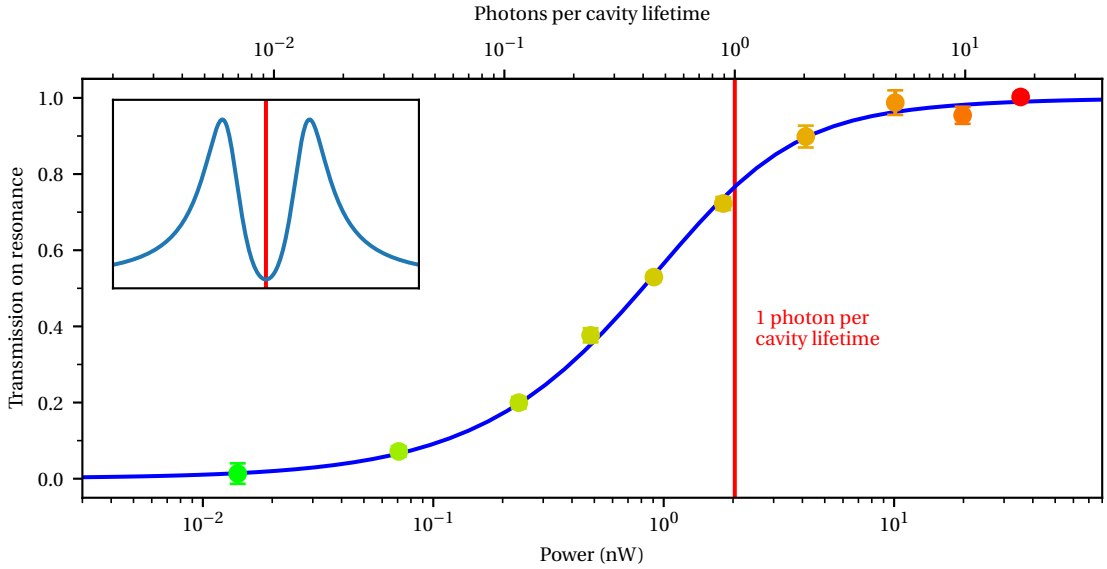

Figure 5.3: Normalized transmission through the cavity-molecule system. At an excitation power of 1 photon per cavity lifetime the transmission is $T = 77\,\%$. The inset illustrates the spectral configuration for this measurement: The laser probes the transmission through the common resonance of molecule and cavity.

to the ground state (γ_{tg}) compared to the rate at which it transitions from the excited state into the triplet state (γ_{et}), the higher the average transmission at intermediate excitation power. This is because the molecule spends more time in the triplet state. During that time, the molecule does not interact with the cavity and therefore transmits light as if there was no molecule.

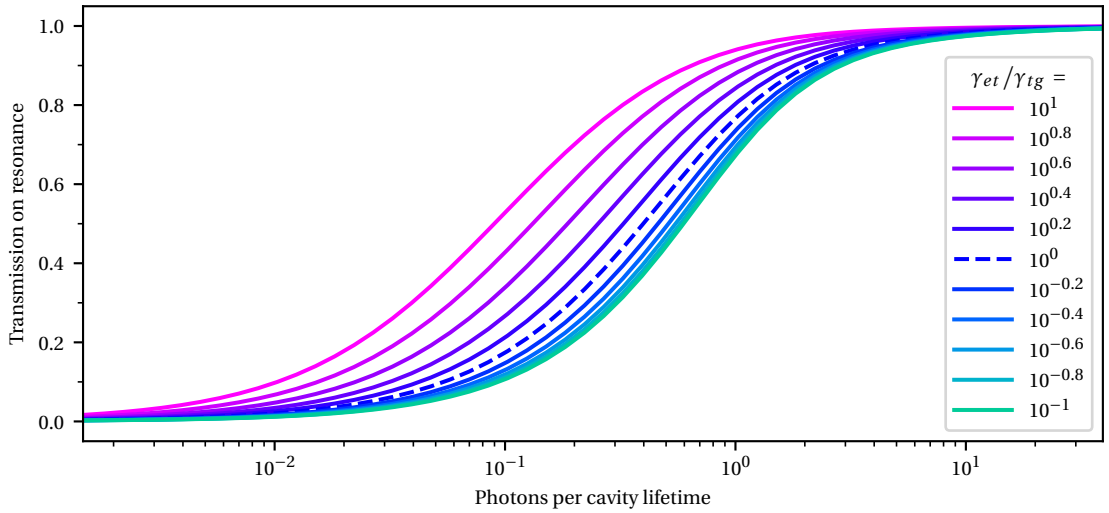

Figure 5.4: Theoretical saturation of the transmission for different ratios γ_{et}/γ_{tg}. The molecule behaves like a two-level system in the limit $\gamma_{et} \ll \gamma_{tg}$.

In order to benchmark the low power required for our system to behave nonlinearly, we now quantify the degree of saturation as assessed using different quantities. We therefore define different versions of the saturation parameter, analogous to the saturation parameter S_{2LS} describing saturation in a two-level system in free space. On resonant excitation, the saturation parameter is [101]

$$S_{2LS} := \frac{2\Omega^2}{\Gamma^2} = \frac{1}{\frac{1/2}{\rho_{ee}} - 1}, \tag{5.2}$$

where Ω is the free-space Rabi frequency and Γ is the free-space emission rate of the two-level system. We cannot straightforwardly transfer this definition to our system. While we have an analog to the Rabi frequency $\Omega_\alpha = g\alpha$ (see Ch. 2.4), the emission rate of the molecule is not clearly defined because in the strong coupling regime, the decay of the molecule's excited state population is not monotonic, as demonstrated in Ch. 4.2. Instead, we can use the population of the excited state ρ_{ee} to quantify the saturation. Eq. 5.2 normalizes the excited state population to its value in the limit of infinite laser power $\rho_{ee}(\Omega \to \infty)$, which is 1/2 in the case of a two-level system. In contrast to that, our system reaches a steady-state population of $\rho_{ee}(I_{in} \to \infty) = \gamma_{tg} / (\gamma_{et} + 2\gamma_{tg})$. Defining

$$S_{\rho_{ee}}(I_{in}) := \frac{1}{\frac{\rho_{ee}(I_{in}\to\infty)}{\rho_{ee}(I_{in})} - 1}, \tag{5.3a}$$

our system reaches a saturation parameter of $S_{\rho_{ee}} = 1$ for 0.24 photons per cavity lifetime $I_{\text{in}} = 0.24\,\kappa$ (see red curve in Fig. 5.5). Alternatively, one can use the normalized excited state population $p_e := \rho_{ee}/(\rho_{ee} + \rho_{gg})$ and define

$$S_{p_e}(I_{\text{in}}) := \frac{1}{\frac{1}{2p_e(I_{\text{in}})} - 1} \tag{5.3b}$$

(see green curve in Fig. 5.5). The threshold of $S_{p_e} = 1$ is reached for $I_{\text{in}} = 0.32\,\kappa$. We would like to note that the definitions 5.3a and 5.3b result in negative values in the regime of an incident power of ~ 2 photons per cavity lifetime, because $\rho_{ee}(I_{\text{in}} \approx 2\kappa) > \rho_{ee}(I_{\text{in}} \to \infty)$. We discuss this population inversion effect in Ch. 6.2. A third possibility is to define the saturation parameter using the directly measured transmission through the cavity T. It rises monotonically from $T(I_{\text{in}} \to 0) = (1 + C)^{-2}$ to $T(I_{\text{in}} \to \infty) = 1$ with the rate of incident photons I_{in}. Then,

$$S_T(I_{\text{in}}) := \frac{T(I_{\text{in}}) - T(I_{\text{in}} \to 0)}{1 - T(I_{\text{in}})} \tag{5.3c}$$

reaches $S_T = 1$ when the transmission is halfway between 1 and $T(I_{\text{in}} \to 0)$. This is the case for 0.40 photons per cavity lifetime.

Fig. 5.5 plots the three described quantities, together with the absolute value of the coherence term $|\rho_{eg}|$ (orange). It is proportional to the dipole moment and therefore a measure of the amount of coherently scattered light. It reaches its maximum value at $I_{\text{in}} = 0.31\,\kappa$.

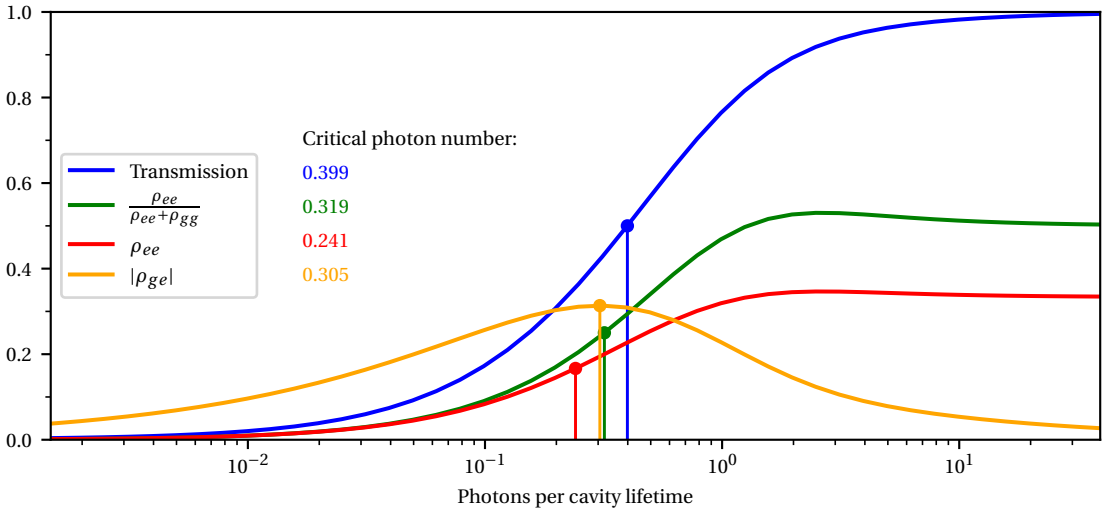

Figure 5.5: Different quantities indicating saturation. The dots and vertical lines indicate the threshold when the corresponding saturation parameter (Eqns. 5.3) reaches 1. These graphs are simulated for the system parameters measured in the experiment: $g/2\pi = 0.63\,\text{GHz}$, $\kappa/2\pi = 1.28\,\text{GHz}$, $\gamma/2\pi = 0.04\,\text{GHz}$ and $\gamma_{et} = \gamma_{tg}$.

In the Purcell regime (Ch. 2.3.6) it is common to compare the rate of incident photons I_{in} to the Purcell-enhanced excited-state decay rate $\gamma_{\text{cav}} = \frac{4g^2}{\kappa}$, instead of the energy loss rate of the cavity κ. One then finds that the rate of photons per emitter lifetime to reach a saturation parameter of $S_{\text{2LS}} = 1$ approaches 1/4 in the limit of $\beta \to 1$ [22, 113].

In conclusion, we have demonstrated the nonlinear transmission through the cavity-molecule system due to saturation. The observed behavior matches the theoretical model elaborated in Ch. 2.4.1 closely, including the low photon number required for the onset of saturation. Furthermore, we would like to highlight that the molecule remained stable despite the high rates of photon absorption and emission in these experiments. This would lead to severe excitation-induced spectral diffusion [149–152] in many other solid-state systems.

5.2 High-Contrast All-Optical Switching

Motivated by the high dynamic range of transmission experienced by the laser beam in the previous chapter, we now explore the nonlinearity from a different angle – mediating an interaction between different laser beams. The transmission of one beam is controlled by the presence of another one, as in a logical `AND` gate.

We perform pump-probe experiments, in which a pump laser drives the system into a particular state while a weak probe laser is used to acquire information about the system without perturbing it significantly. In our case, the probe laser is on resonance with the molecule and the cavity, to assess the transmission through them, and the pump laser saturates the system, thereby increasing its transmission. The excitation is the same as in the previous chapters (excitation through the planar mirror, using the cross-polarization scheme described in Ch. 3.4.2), except that we combine the probe and pump beams via a beamsplitter before coupling them into the cavity (see Ch. 3.4). In order to measure the transmission of the probe beam in the presence of the up to 800 times stronger pump beam, the pump beam is detuned by $\Delta\nu = +300\,\text{MHz}$ from the probe and we use a Fabry-Pérot cavity with a linewidth of 30 MHz (FWHM) in the detection path (see Ch. 3.4.3) to separate the two beams. The inset of Fig. 5.6 shows the frequencies of the two lasers relative to a low-power transmission spectrum of the cavity with molecule. The filter cavity is scanned around the probe frequency in linear ramps of 10 s duration to acquire the spectrum of the transmitted light convolved with the Lorentzian line shape of the filter cavity. The scan voltage is sampled synchronously with the APD counts and the error signal for the postprocessing described in Ch. 3.5.2. Each ramp is then fitted with a double-Lorentzian plus background

$$\tilde{T}(V) = \frac{A_{\text{probe}}}{1 + \left(\frac{V - V_{\text{probe}}}{w}\right)^2} + \frac{A_{\text{pump}}}{1 + \left(\frac{V - (V_{\text{probe}} + k\Delta\nu)}{w}\right)^2} + B \tag{5.4}$$

to account for the probe, pump and incoherent light. $k = 0.78\,\text{V/GHz}$ is the conversion factor between the voltage applied to the scanning piezo of the filter cavity and the change in its

resonance frequency; $w = 10.4\,\mathrm{mV}$ is the HWHM of the Lorentzians on the voltage axis. Fig. 5.6 shows an example ramp from the measurement with the highest pump power $P_{\mathrm{pump}} = 9.2\,\mathrm{nW}$. Although the tail of the Lorentzian from the pump beam spans the probe Lorentzian, we can extract the amplitude of the probe peak A_{probe} with confidence.

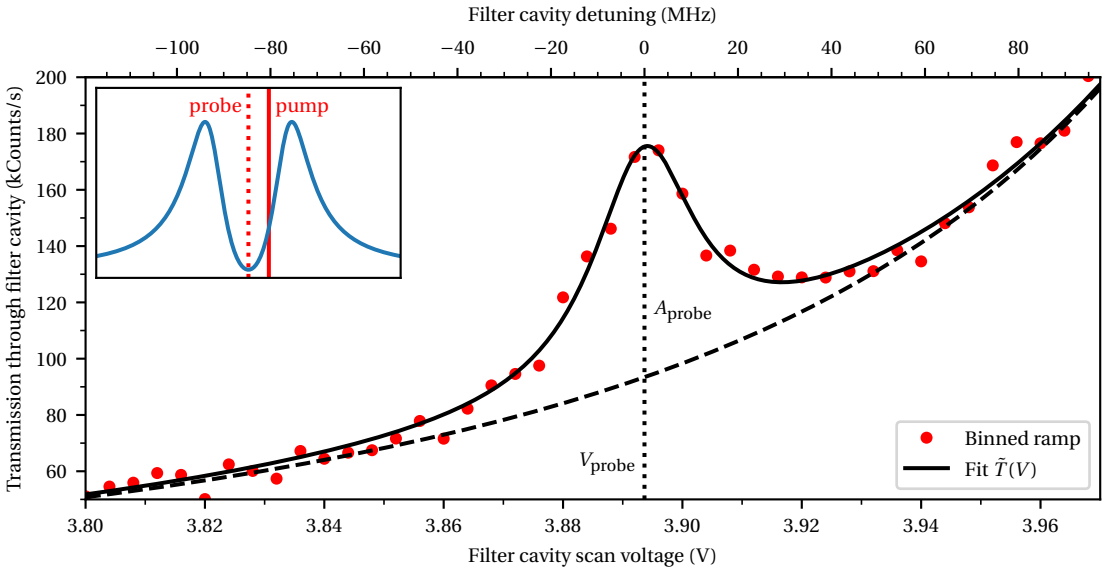

Figure 5.6: Example filter cavity ramp at pump power $P_{\mathrm{pump}} = 9.2\,\mathrm{nW}$. The quantity of interest, A_{probe}, is the height of the Lorentzian centered at V_{probe} above the residual signal from pump and background (dashed line).

The extracted amplitude A_{probe} is then normalized to the amount of light which would be transmitted through an empty cavity at the same probe power D_{direct}. Therefore, we record a transmission spectrum with only the probe beam in the same way as in Chapters 4.1 & 5.1 shortly before the pump-probe measurement, referred to as "normalization spectrum" in the following. We correct this spectrum for the APD deadtime, subtract the incoherent background and then fit each laser scan ramp of it with the model described in Ch. 2.4.1. We can calculate the rate of photons transmitted through the empty cavity D_{direct} by evaluating the fit model with g set to 0. The normalized probe transmission is then $T_{\mathrm{probe}} = A_{\mathrm{probe}}/(\eta_{\mathrm{cav}} D_{\mathrm{direct}})$, where $\eta_{\mathrm{cav}} = 9.7\,\%$ is the calibrated peak transmission through the filter cavity. Two refinements make this normalization more accurate: Taking (i) the contribution from the cross-polarization background and (ii) the cavity length jitter remaining after the postprocessing into account.

For (i), we use the fit of the normalization spectrum to decompose the transmission countrate through the empty cavity into the actual transmission through the empty cavity D'_{direct} and the cross-polarization background $\mathrm{CP}_{\mathrm{direct}}$

$$D_{\mathrm{direct}} = D'_{\mathrm{direct}} + \mathrm{CP}_{\mathrm{direct}}. \tag{5.5a}$$

The cross-polarization contribution also contributes to the amplitude of the Lorentzian at the probe frequency, in addition to the actual probe transmission through the cavity and filter cavity A'_{probe}, hence

$$A_{\text{probe}} = A'_{\text{probe}} + \eta_{\text{cav}}\text{CP}_{\text{direct}}. \tag{5.5b}$$

The more accurate normalized probe transmission is therefore

$$T_{\text{probe}} = \frac{A'_{\text{probe}}}{\eta_{\text{cav}} D'_{\text{direct}}} = \frac{A_{\text{probe}}/\eta_{\text{cav}} - \text{CP}_{\text{direct}}}{D'_{\text{direct}}}. \tag{5.5c}$$

This decomposition is particularly important for measurements at low pump power, when the actual probe transmission through the cavity is very low, i.e. the contribution from the cross-polarization background is relatively high.

The issue with (ii) is that despite the synchronized detection and postprocessing the mapping between error signal and cavity resonance frequency has a residual uncertainty, for reasons we do not know at the time of writing. This means that the transmission through the cavity is averaged over a range κ_{vib} of detunings. Therefore, the average transmission is lower than for a fixed-frequency cavity, as demonstrated by the example in Fig. 4.1. If the residual uncertainty was the same in each measurement, we could calibrate it once and take it into account in the data analysis. In practice, however, it varies between 0 and 0.9 GHz between measurements. While it is possible to extract it from measurements in which the laser is scanned across the cavity resonance frequency, in the pump-probe experiments detailed in this chapter the laser frequency is fixed and we therefore cannot determine the residual broadening κ_{vib}. Despite this we found a correlation between κ_{vib} and the integrated noise in the error signal in the spectral range [13.5, 27] kHz. Using this, we can estimate κ_{vib} in the pump-probe measurements and correct for it.

The probe transmission for a wide range of pump powers is shown in Fig. 5.7. It ranges between 2.29 ± 0.76 % and 103.1 ± 10.5 %, where the uncertainty denotes the variation among the individual scan ramps within the measurement. Additionally, we note that there is a systematic tendency to underestimate the contribution of the cross-polarization background, because of polarization drifts between the measurements. Hence, the subtracted contribution tends to be lower than the actual background, leading to an overestimation of the probe transmission. This has a high relative impact on the probe transmission calculated at low pump power, because the transmission is very low for these measurements. A more accurate value of the probe transmission is available in the absence of the pump beam from the normalization spectra, because here we can obtain a much more accurate estimation of the cross-polarization background from the edges of the spectrum. The probe transmission in these measurements is 0.64 ± 0.32 %. The ratio between this and the maximum transmission, 22.1 ± 2.2 dB, is a marked improvement over previous experiments without a cavity [13, 153]. The low transmission in the absence of the pump beam results from the remarkably high

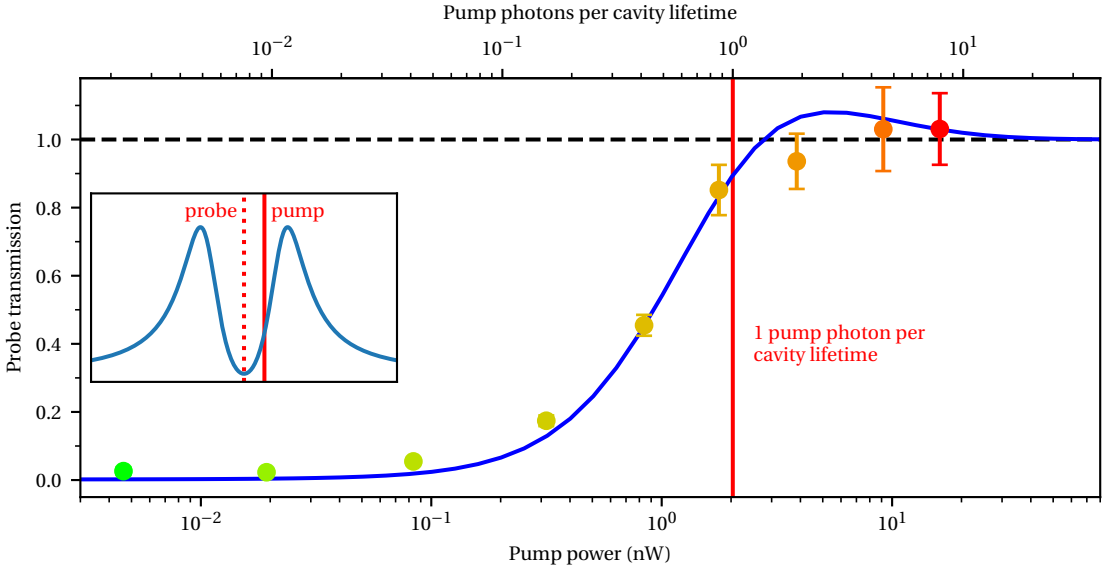

Figure 5.7: Normalized probe transmission in the presence of a $\Delta\nu = +300\,\mathrm{MHz}$ detuned pump beam. The blue curve shows the value expected from theory with the independently measured parameters $\kappa/2\pi = 1.28\,\mathrm{GHz}$, $g/2\pi = 0.63\,\mathrm{GHz}$, $\gamma/2\pi = 0.04\,\mathrm{GHz}$ and $\gamma_{et} = \gamma_{tg}$. The inset shows the frequencies of pump and probe relative to the transmission spectrum of the cavity and molecule.

cooperativity $C = 31$ of this molecule. From Eq. 2.44 we can determine the all-resonant transmission $T(\omega_L = \omega_c = \omega_{\mathrm{mol}}) = (1+C)^{-2} \approx 0.10\,\%$ in the limit of zero probe power.

The measured transmission data in Fig. 5.7 agree closely with the theoretical prediction using independently measured system parameters. The nonlinearity sets in at very low pump power, as evidenced by a 89 % probe transmission at only 1 pump photon per cavity lifetime. The theory also predicts the probe beam to be slightly amplified around $I_{\mathrm{in}} \approx 3\kappa$, which is not resolved in the data. We would like to note that the amplification in this experiment, with pump detuning $\Delta\nu = 300\,\mathrm{MHz}$, is not due to population inversion of the molecule. Inversion would occur at a different combination of pump and cavity detuning, as we elaborate in Ch. 6.2. The amplification is instead caused by coherent energy transfer from the pump to the probe beam, which can also be described as stimulated emission in the laser-dressed molecular states [117, 153, 154], also called “three-photon resonance” on page 325 in R. Boyd’s *Nonlinear Optics* [1].

Fig. 5.8 shows the probe transmission for other choices of the pump detuning $\Delta\nu$. While the effect on the maximum probe transmission is small, the threshold power shifts to higher values as the pump detuning increases. This is because the pump can saturate the molecule more efficiently if they are resonant. While the switching threshold would be slightly lower for lower pump detuning, for the experiment we chose a detuning of $\Delta\nu = 300\,\mathrm{MHz}$. As such, the threshold is low, and we are able to separate the pump and probe frequencies in the detection with a high fidelity, as shown in Fig. 5.6.

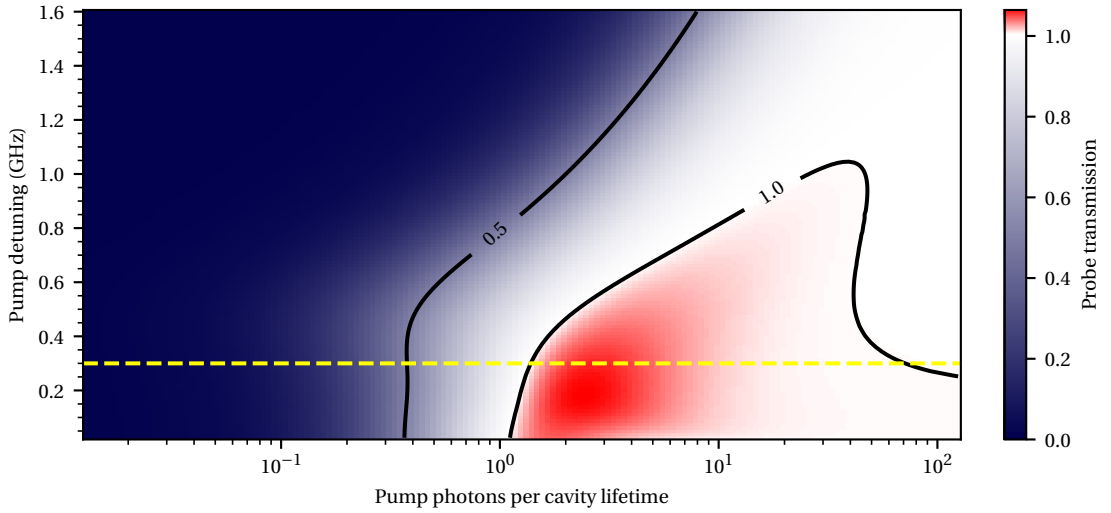

Figure 5.8: The probe transmission as a function of the pump power for a range of pump detunings. The yellow dashed line indicates the pump detuning used in the experiments $\Delta\nu = 300\,\mathrm{MHz}$.

To summarize, we have demonstrated how the saturation behavior of a single molecule can be used to realize an all-optical switch. The efficient light-matter coupling enabled by the cavity not only increases the switching contrast, but also reduces the critical number of photons required to "flip" the switch, compared to free space. However, for an ideal AND gate the two beams would be interchangeable and an increase in the power by a factor of 2 would suffice to switch the transmission from ~0 % to ~100 %. In this way, one beam is too weak to be transmitted, but both beams together saturate the molecule and are therefore transmitted. The reason this does not happen despite near-unity interaction efficiency is that the molecule's intrinsic nonlinearity manifests in its response to different photon number states $|n\rangle$ rather than to different coherent field amplitude states $|\alpha\rangle$. The coherent states in the cavity created by the probe and pump beams are superpositions of different photon number states (see Eq. 2.48) and therefore wash out the discrete behavior. In turn, this suggests that the molecule-cavity system can be used to operate on single-photon states – an essential task in quantum computation [49]. Indeed, this photon-number nonlinearity is benchmarked with a continuous-wave beam in the next chapter. Yet, constructing a quantum gate for single-photon pulses has been shown to have a fundamental fidelity limit because of the time-bandwidth problem [155, 156]: If the pulses are comparable to, or longer than, the storage time of the cavity κ^{-1}, there is the possibility that the single photons are scattered independently, i.e. without interacting. Instead, if the pulses are comparable or shorter, parts of their spectrum are filtered out because of the finite bandwidth κ of the cavity. Hence, there is a probability of them being reflected without interacting with the molecule. Rosenblum *et al.* [156] propose a solution involving a 3-level atom to increase the memory time of the system. Alternatively, the time-bandwidth limitation can be circumvented by employing a dynamically coupled cavity as a load-lock for the cavity with the two-level system [157, 158].

5.3 Photon Number Sorting

In this subchapter, we explain the quantum version of the all-optical switch described in the previous chapter. Instead of the average transmitted power, we measure correlations in the arrival times of transmitted photons. We couple a weak continuous-wave laser into the cavity and send the transmitted light to a Hanbury Brown & Twiss (HBT) setup (see Ch. 3.4.3). The arrival times of the photons are registered with a PicoHarp 300 (PicoQuant GmbH). We then compute the unnormalized intensity autocorrelation $G^{(2)}(\tau)$ by counting the absolute occurrence of arrival time differences τ between all possible pairs of photons. $G^{(2)}(\tau)$ is then normalized, to $g^{(2)}(\tau)$, using the condition that for time differences τ much longer than the memory time of the system, no correlation is expected, i.e. $g^{(2)}(\tau = \infty) = 1$. The result is shown in Fig. 5.9.

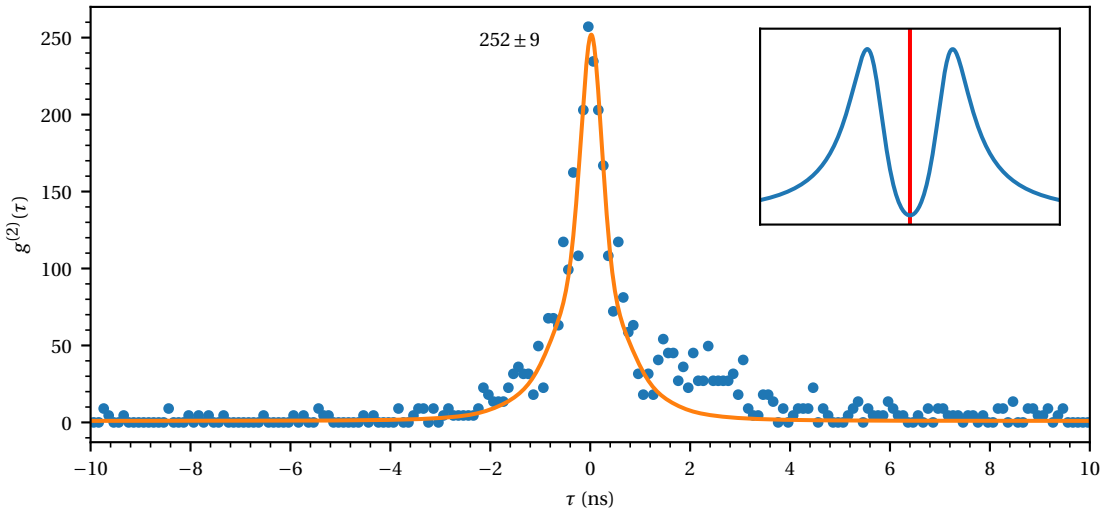

Figure 5.9: Normalized intensity autocorrelation $g^{(2)}(\tau)$ of the transmitted light. The peak around $\tau = 0$ is evidence of distinct photon bunching. Around $\tau = 2$ ns the data is systematically higher than the expectation. This is due to cross-talk between the APDs, caused by the breakdown flash of one APD sending a photon to the other APD [159]. These data points are excluded from the fit.

The value of $g^{(2)}(0)$ reaches the notably high value of 252, which is a significant increase over the value of 21 reported in our previous work [22] and other systems [54, 62, 160–164]. One can interpret the intensity autocorrelation function in terms of conditional probability as [165]

$$g^{(2)}(\tau) = \frac{P(t+\tau|t)}{P(t)}, \tag{5.6}$$

where $P(t)$ is the probability density of detecting a photon at time t and $P(t+\tau|t)$ is the conditional probability density of detecting a photon at time $t+\tau$ if another photon was detected at time t. Applied to our experiment, this means that if one photon is detected, one is 252 times more likely to detect another photon at the same time ($\tau = 0$) than with a long time difference ($\tau \to \infty$). This pronounced superbunching has its origin in the aforementioned

photon-number nonlinearity of the single-photon emitter. For an intuitive understanding, we consider the coherent state in the cavity created by the laser as a superposition of different Fock states $|0\rangle$, $|1\rangle$, $|2\rangle$, etc. (see Eq. 2.48). Because of its anharmonic energy level spacing, a molecule suppresses the single-photon component $|1\rangle$ in the cavity strongly but its response to the Fock-state components consisting of several photons is qualitatively different. Adapting the model in [166] to a single emitter [22, 123] we can find analytic expressions for the relative probability amplitudes of the 1- and 2-photon states in the cavity. The probability of finding 1 photon in the cavity is reduced to a fraction $1/(1+C)^2$ compared to a cavity without a molecule of cooperativity C. The 2-photon probability is only reduced by $(1-C)^2/(1+C)^2$. In the limit of infinite cooperativity $C \to \infty$, the 1-photon probability goes to 0, while the 2-photon probability is unaffected. The input to the cavity is randomly sampled by the coherent laser beam from the three situations

(i) 0 photons

(ii) 1 photon; the transmission is strongly suppressed

(iii) 2 photons; the transmission is almost unimpeded for high cooperativity C.

As the measurement described here is performed with a single coherent beam, the photons are indistinguishable and therefore do not have designated roles as “pump” and “probe”. We would nevertheless like to point out the parallels to the switching experiments in the previous chapter. A single photon resembles the case with only one beam (probe or pump) on, hence the transmission probability is low. Two photons correspond to both beams on, with an accordingly high transmission probability. The strongly correlated transmission is attested to by the high value of $g^{(2)}(0)$. For the molecule used in this experiment ($g/2\pi = 0.63\,\mathrm{GHz}$, $\kappa/2\pi = 1.28\,\mathrm{GHz}$, $\gamma/2\pi = 0.04\,\mathrm{GHz}$), we would therefore expect a value of

$$g^{(2)}(0) = \frac{\frac{(1-C)^2}{(1+C)^2}}{\left(\frac{1}{(1+C)^2}\right)^2} = \left(1-C^2\right)^2 = 9.2 \cdot 10^5. \tag{5.7}$$

The main reason we do not reach this high value is that we measure $g^{(2)}(\tau)$ at a finite laser power, while the aforementioned model operates in the limit of zero excitation power. Shot-noise in the coincidence histogram sets a practical limit on the lowest excitation power we can use: The rate at which two-photon coincidences are detected is proportional to the power squared. Fig. 5.10 shows how the shot noise and the effect of APD cross-talk decrease when the rate of detected photons increases. Unfortunately, the expected value of $g^{(2)}(0)$ significantly reduces even at very low incident laser power (see simulations in Fig. 5.11). Even if we increased the measurement duration to overcome the shot noise, a finite background would limit the maximally achievable value of $g^{(2)}(0)$. The strong correlation in the actual signal $g^{(2)}_{\mathrm{act}}(\tau)$ is diluted due to uncorrelated coincidences between background and signal photons, and between background and background photons. If the ratio of countrates of

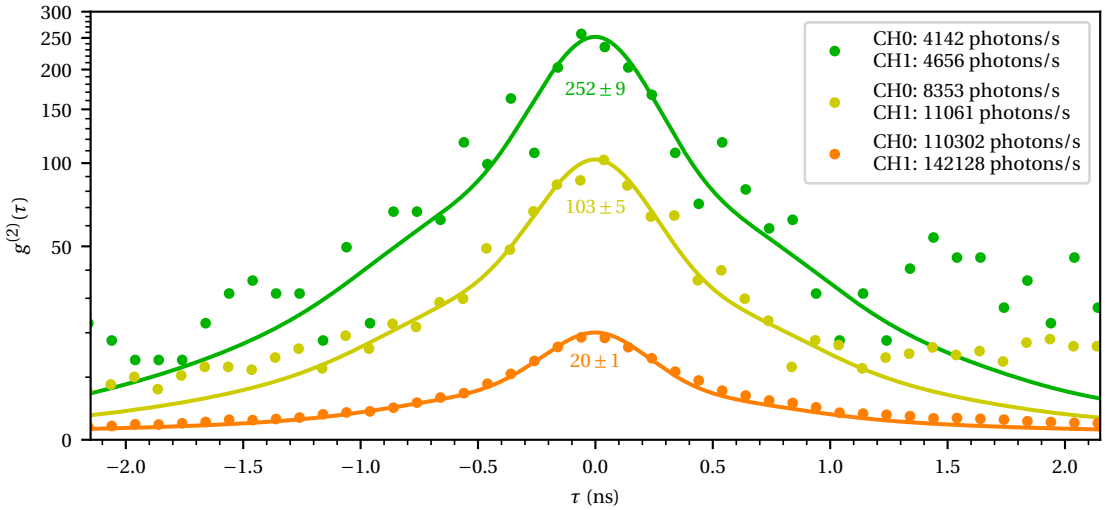

Figure 5.10: $g^{(2)}(\tau)$ for different laser powers. The countrates of the timetagger channels are listed in the legend.

background to signal is $I_{\mathrm{bg}}/I_{\mathrm{sig}} =: r_{\mathrm{bg/s}}$, we only measure (see Appendix C.2)

$$g^{(2)}_{\mathrm{meas}}(\tau) - 1 = \frac{g^{(2)}_{\mathrm{act}}(\tau) - 1}{\left(1 + r_{\mathrm{bg/s}}\right)^2}. \tag{5.8}$$

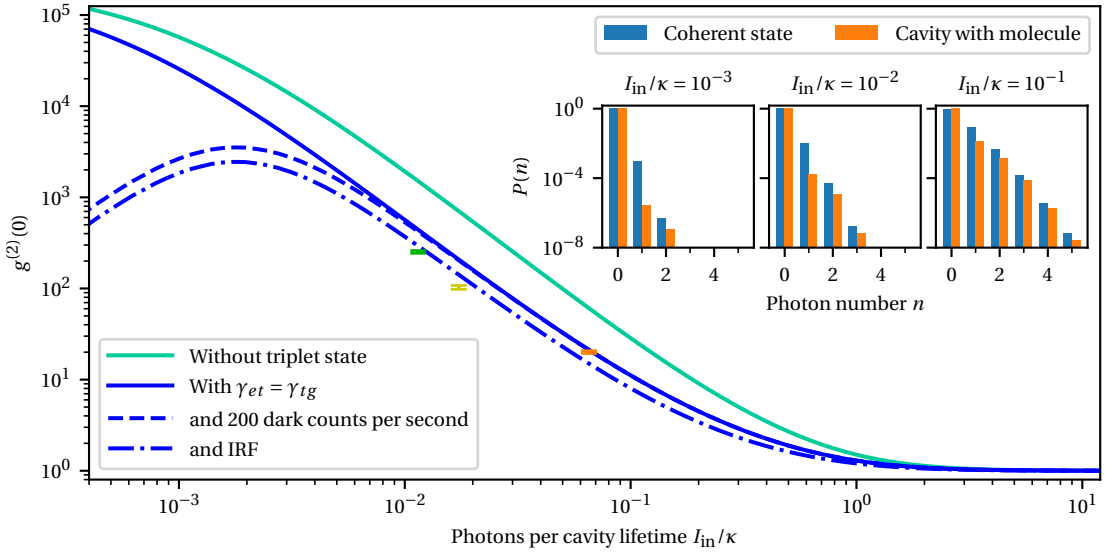

Figure 5.11: The influence of incident power, the triplet state, background/dark counts and the detector IRF on the measured value of $g^{(2)}(0)$. The data points correspond to the three measurements shown in Fig. 5.10. The inset shows the photon number statistics for three different laser powers (not corresponding to the three measurements). Higher laser power weakens the selective relative suppression of the 1-photon component.

In our experiments, we had approximately 200 photons/s background. Fig. 5.11 shows such a background affects the measured value of $g^{(2)}(0)$, especially at low power.

The triplet state of the molecule also affects the achievable $g^{(2)}(0)$: For the time that the molecule is in the triplet state, the laser fully passes through the cavity, contributing the coincidences of a coherent state $g^{(2)}_{\mathrm{coh}}(\tau) = 1$ to the histogram. Since the transmission through the empty cavity is much higher than through molecule & cavity, the accordingly higher countrate contributes a significant fraction of the overall coincidences, even if the fraction of time the molecule spends in the triplet state is small.

Lastly, we must also take the IRF of our APDs into account. The timing jitter redistributes coincidences over a longer time span, thereby reducing the height of the peak at $\tau = 0$ [167]. Fig. 5.12b) shows the theoretical $g^{(2)}(\tau)$ without the IRF. Without the timing jitter, the peak of $g^{(2)}(0)$ above 1 would be 1.44 times higher than the measured value.

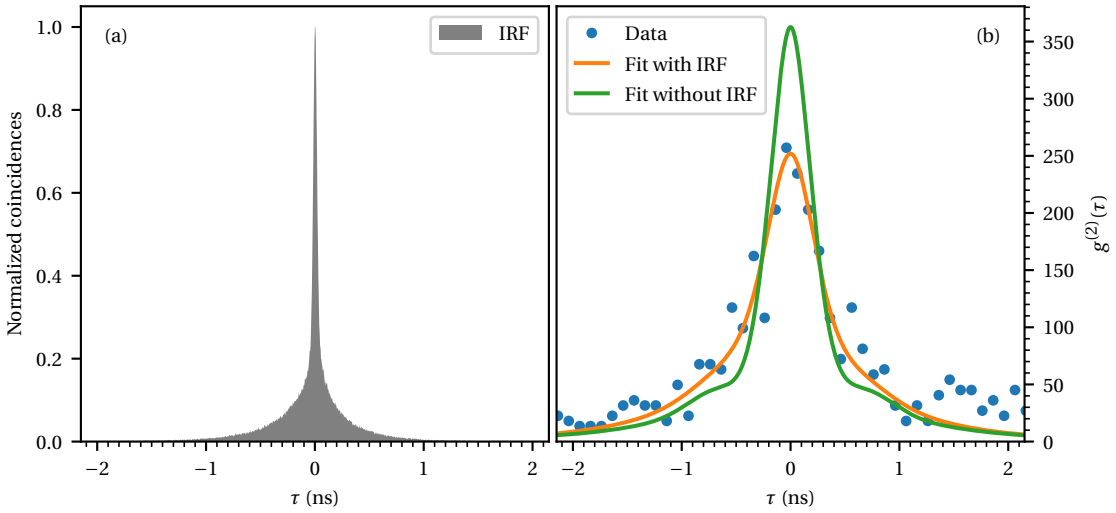

Figure 5.12: a) The IRF of both fast APDs, indicating the timing jitter of photon coincidences. b) The measurement shown in Fig. 5.9. The fit is calculated from the theoretical model (see Ch. 2.4.3) convolved with the IRF.

Taking all of the above effects into account, we expect $g^{(2)}(0)$ values which are close to those measured (see Fig. 5.11). We note that the power used in the measurements is not calibrated and may deviate from the values plotted in that figure. To minimize the effect of background, in particular from imperfect cross-polarization, we coupled the laser into the cavity from the curved mirror side through the fiber (see Fig. 3.12). The exact incoupling efficiency here is unknown, but very low. To estimate the power coupled to the cavity in the measurements shown in Fig. 5.10, we used the countrate on the fast APDs and compared it to the normalization spectra from the switching experiments, taking the relative quantum efficiencies of the APDs into account.

In this chapter, we have provided experimental evidence of the pronounced photon-number dependence of the transmission in the molecule-cavity system. The highly selective transmission of photon pairs manifests itself in a measured value of $g^{(2)}(0) = 252 \pm 9$. More generally, this photon-number nonlinearity creates photon bound states, which were recently detected in a similar system optimized for low losses [168].

5.4 Four-Wave Mixing

In this section, we focus on the interaction of laser beams of different frequencies via the nonlinearity of the molecule to generate photons of new frequencies. As in the other experiments presented in this chapter, this happens at low average photon numbers around 1 in the cavity. We generate two laser beams with a relative detuning of $\Delta\nu = 300\,\mathrm{MHz}$ (see Fig. 3.13) and couple both to the cavity (see Ch. 3.4) using the usual cross-polarization scheme (see Ch. 3.4.2). We tune the lasers such that they are symmetrically detuned from the common resonance frequency of cavity and molecule by $\pm\Delta\nu/2 = \pm 150\,\mathrm{MHz}$, as sketched in the inset of Fig. 5.13. In the detection path we direct the light through the same filter cavity with linewidth 30 MHz (FWHM) as for the switching experiments. Scanning the resonance frequency of the

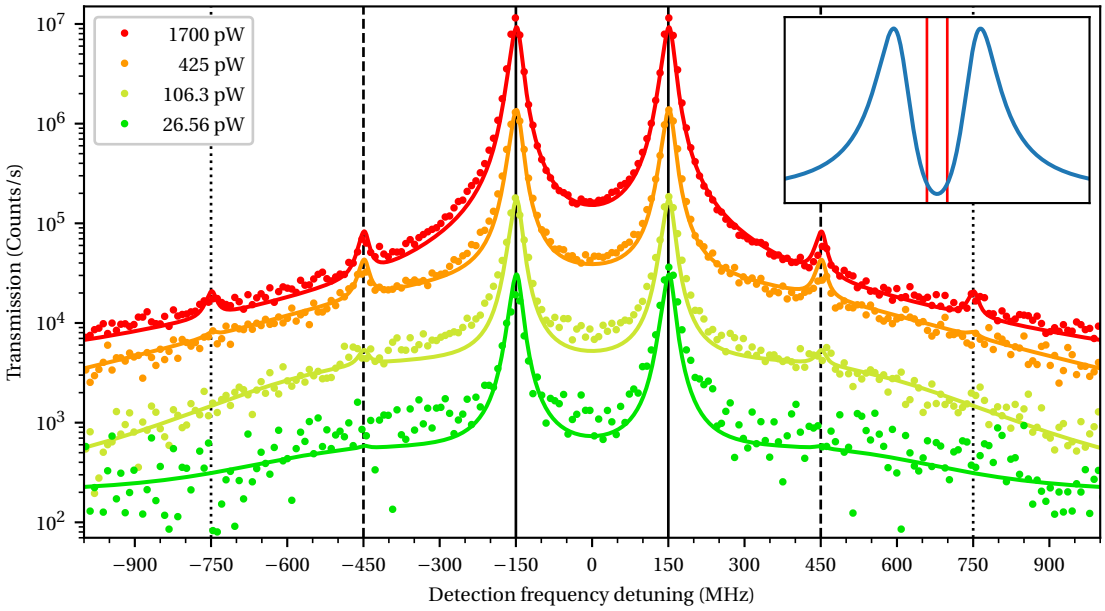

Figure 5.13: Experimental data (dots) of FWM experiments at various laser powers. The legend indicates the laser power coupled to the cavity per beam, using the calibrated incoupling efficiency of 17 %. The solid lines are purely theoretical (up to a global vertical scaling factor) and calculated from the independently determined system parameters $g/2\pi = 0.63\,\mathrm{GHz}$, $\kappa/2\pi = 1.28\,\mathrm{GHz}$, $\gamma/2\pi = 0.04\,\mathrm{GHz}$. The inset depicts the detuning of the two lasers relative to a transmission spectrum through the molecule-cavity system.

filter cavity reveals the spectrum of light leaking out of the microcavity. Fig. 5.13 shows the resulting spectra for various laser powers.

At low power, we see two peaks at the frequencies of the incident laser beams. However, as the laser power is increased, an additional pair of peaks at frequencies ±450 MHz becomes apparent. The power contained in these frequencies generated by four-wave mixing (FWM) is (1.4 ± 0.3) % of the power in the excitation frequencies for a cavity-coupled power of only 425 pW, corresponding to 0.21 photons per cavity lifetime. If we couple as much as 1.7 nW per beam into the cavity, we can see a further pair at ±750 MHz produced by a process involving at least 6 photons. The efficiency of these four- and six-photon processes is significantly higher than in a previous experiment where the lasers were strongly focused on a molecule without a cavity [153]. We further verify the origin of the side peaks in the nonlinearity of the molecule with two control experiments, shown in Fig. 5.14. If only one frequency is coupled into the cavity, we find only one peak in the emission spectrum, because it does not interact with a beam of different frequency to generate sidebands. Also, if the cavity and lasers are tuned off-resonance from any molecule, two beams do not cause additional frequencies to occur, because the cavity itself behaves linearly.

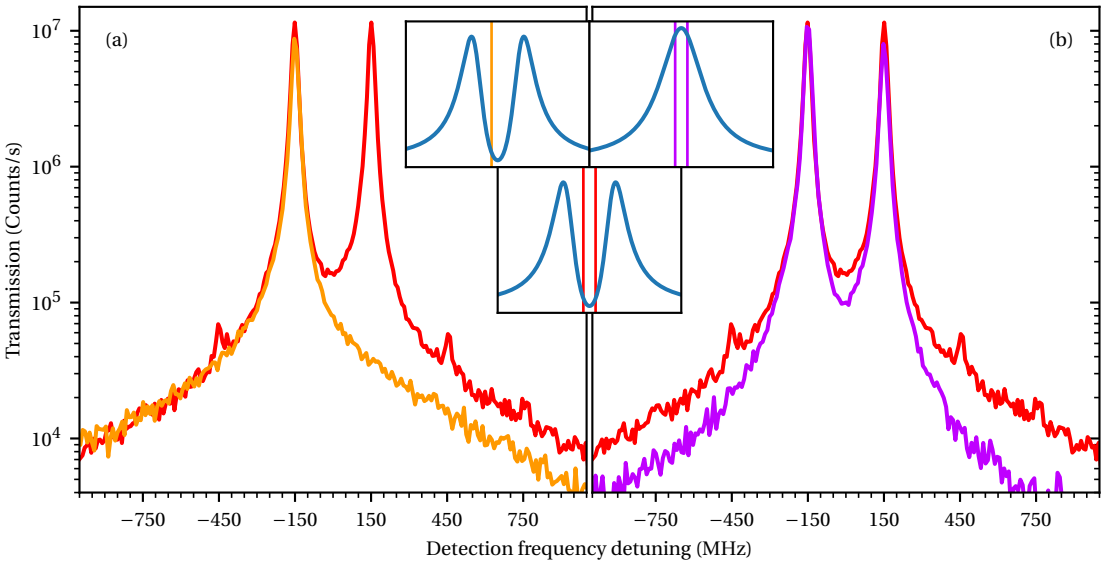

Figure 5.14: The FWM sidebands are absent when only one beam hits the molecule (a) or in the absence of a molecule (b). The insets indicate the spectral constellation of cavity, molecule and lasers. The red dataset is identical with the highest-power dataset in Fig. 5.13. The two control datasets were also recorded with 1.7 nW in each beam.

We now explain the observed phenomena from two different perspectives. In the time-domain, the two laser beams at $\pm\Delta\nu/2 = \pm 150$ MHz are equivalent to one laser beam at 0 MHz intensity-modulated as $I(t) = 4I_0 \cos^2\left(2\pi\frac{\Delta\nu}{2}t\right)$ with the beating frequency $\Delta\nu$ and the intensity of an individual beam I_0. Floquet's theorem [169] states that a periodically driven system with dissipation converges towards a stationary state in which its density matrix evolves with the

same period. In our case, this period is the inverse of the beating frequency $T = 1/300\,\mathrm{MHz}$. This condition, $\rho_{ss}(t+T) = \rho_{ss}(t)$, implies that only integer multiples of the fundamental frequency can be part of the evolution of $\rho_{ss}(t)$ [170]. In the case of a linear system, it would even be restricted to the fundamental frequency only. In a nonlinear system such as ours, higher harmonics of the beating frequency emerge through the deviation from linear behavior. Fig. 5.15 shows the evolution of the photon number in the cavity $\langle \hat{a}^\dagger \hat{a} \rangle (t)$ and the excited state population of the molecule $\langle \hat{\rho}_{ee} \rangle (t)$ for the laser powers used in the experiment. At low power, both quantities evolve sinusoidally with the beating frequency. However, as the molecule approaches saturation, it can not linearly follow the varying intracavity intensity and imprints higher harmonics onto the evolution. These higher harmonics show up as sharp peaks in the emission spectrum (Fig. 5.16). Additionally, the emission spectrum reveals a broad background from the incoherent decay of the polaritons. When this emission spectrum is convolved with the spectral response of our filter cavity (a 30 MHz FWHM Lorentzian), we obtain the theory curves in Fig. 5.13, where the incoherent background is not clearly resolved under the tails of the coherent emission peaks. One can only see *that* there is some background when comparing the situations with/without molecule, as in Fig. 5.14b).

Complementarily, the nonlinear processes can be explained in the spectral domain, by drawing the elementary processes relative to the energy levels of the nonlinear system (Fig. 5.17). This is

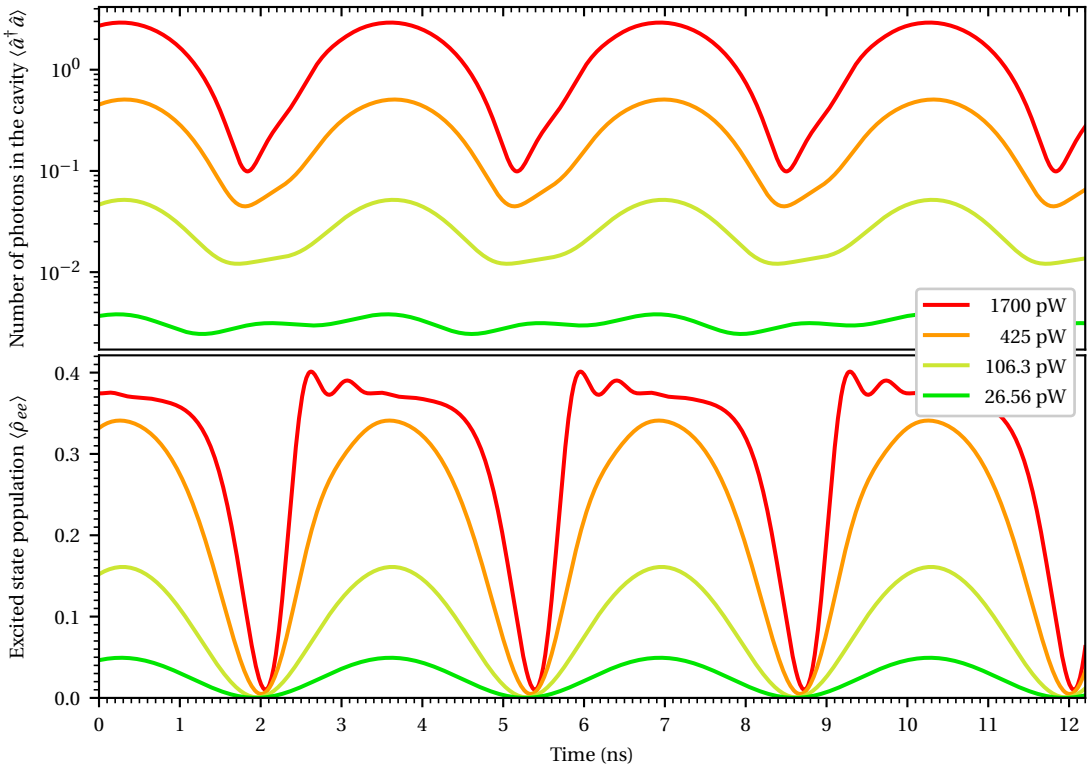

Figure 5.15: Evolution of the power inside the cavity and the excited state population during the FWM measurement.

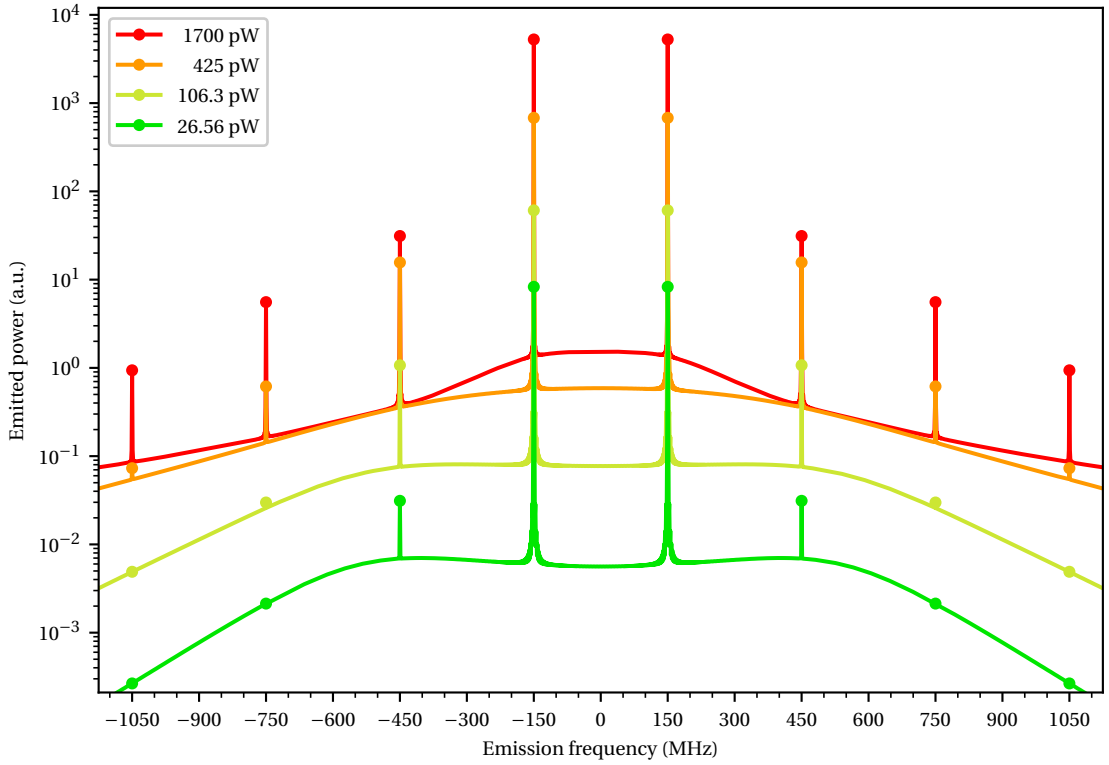

Figure 5.16: Theoretical FWM spectra without the filter cavity linewidth and background.

often done to find all possible paths which end at the same energy as they started. Additionally, this method allows one to assess how likely a process is: The further an intermediate step is from a real energy level, the lower the contribution of this process [1]. The coherence created as a result of the driving between the involved energy levels can be used to detect decoherence processes caused, for example, by phonons [171]. Furthermore, the closed-loop nature of the processes reveals insights into correlations between photons of different frequencies being created in the same process. A follow-up experiment could quantify the entanglement between photon pairs [172]. Moreover, synchronized single photons could be used to trigger a particular process with high efficiency [173]. Narrowband photon pairs from spontaneous parametric downconversion in whispering gallery mode resonators [174] could be a viable candidate.

In this chapter, we have demonstrated several experimental scenarios revealing the nonlinearity of a two-level emitter. Because of the high interaction efficiency, the nonlinear phenomena can be observed with the minimum number of photons required for the process. The data match the theoretical model very closely and we have used these simulations to provide further insights into the mechanisms behind the observations. However, being restricted to the light of the cavity mode leaking through the mirrors limits our capability to assess the dynamics within the cavity. Gaining access to the excited-state population of the molecule

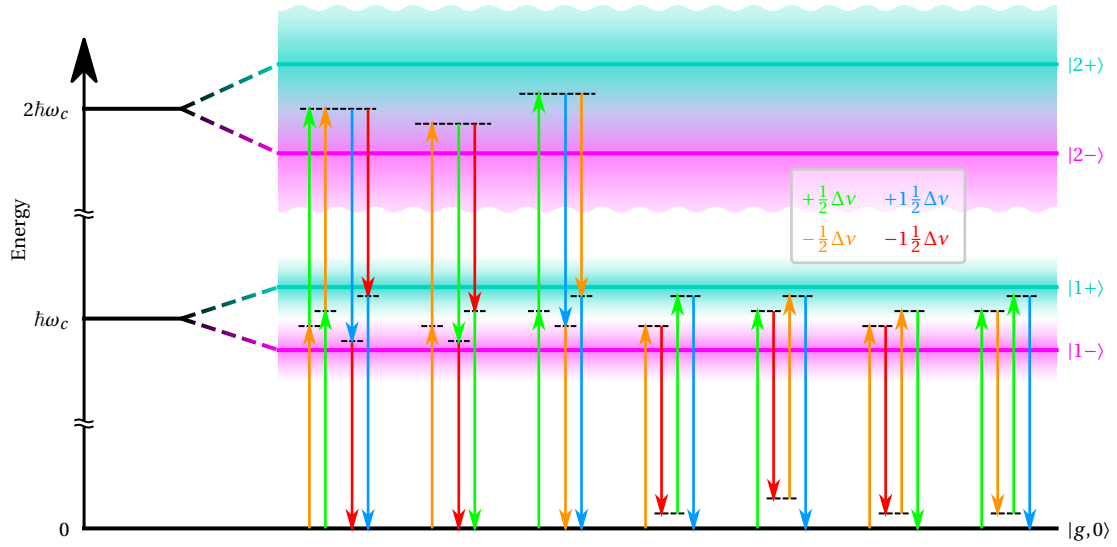

Figure 5.17: The elementary FWM processes starting and ending in the ground state $|g,0\rangle$. There are more processes starting in the polariton levels $|n\pm\rangle$. Upward arrows indicate photons being absorbed, downward arrows indicate photons being emitted from the system. The legend lists the detuning from the common resonance of molecule and cavity.

allows more direct access to the internal configuration of the cavity molecule system. In the next chapter, we propose experiments using this extra information.

6 Near-Term Future Experiments

In the previous chapters we showed the potential of DBT molecules in anthracene as a highly coherent quantum emitter in classical and quantum nonlinear experiments. Moreover, the coupling to a high-finesse microcavity allowed us to perform these experiments with high efficiency at mean photon numbers in the cavity around $\bar{n} \sim 1$. In these experiments, we used Bragg design mirrors, which are highly reflective at the wavelengths of the Stokes-shifted fluorescence of DBT (see Ch. 2.1). In Ch. 6.1, we introduce specially designed dichroic cavity mirrors with a high transmission for these wavelengths. This allows us to gain information about the excited-state population of the molecule, which is proportional to the fluorescence emission rate. Hence, instead of being limited to the excitation light scattered by the cavity-molecule system as a whole, we gain insight into the states and dynamics within this compound. The subchapters following thereafter provide examples of experiments using this additional channel. In Ch. 6.2, we explain how the coupling to a cavity mode enables a two-level system to be population-inverted in the steady-state, and how this effect can be measured in our system. In Ch. 6.3, we propose a simple way to reveal cavity-mediated coupling between two molecules. In Ch. 6.4, we explore how strong light-matter interaction gives rise to a photon-number-dependent AC Stark shift and the experimental parameters required to resolve the discretization.

6.1 Dichroic Cavity Mirrors

The dichroic coating is designed to have a transmission window for Stokes-shifted fluorescence of DBT. At the same time, the finesse at $\lambda = 785\,\mathrm{nm}$ is intended to be comparable to the finesse of the Bragg mirrors. As such, a cavity made of one Bragg and one dichroic mirror has balanced reflectivities and therefore does not lose coupling efficiency due to over- or under-coupling. To collect as much of the fluorescence spectrum as possible, the reflectivity edge must be very steep. This introduces some challenges; in particular the divergence of the mode must be taken into account, as tilted incidence shifts the spectrum towards the blue and therefore extends the transmission window closer to $\lambda = 785\,\mathrm{nm}$. We took the divergence of the mode

into account by considering the effective finesse

$$\mathscr{F}_{\text{eff}} = \frac{\pi\sqrt{R_{\text{eff}}}}{1-R_{\text{eff}}}. \tag{6.1a}$$

This is calculated using the effective reflectivity

$$R_{\text{eff}} = \int_0^{\pi/2} R(\alpha)\, p_\theta(\alpha)\, \mathrm{d}\alpha, \tag{6.1b}$$

which is the average reflectivity for all AOI α, weighted by the fraction of power $p_\theta(\alpha)$ in the Gaussian mode under this angle. Since half of the mode hits the mirror with s- and p-polarization (see Fig. 3.7), the reflectivity $R(\alpha)$ is the average of the reflectivities for both polarizations.

A typical strategy for designing a mirror with such specific requirements is to start with several DBR stacks with spacer layers between them to describe the desired spectrum approximately and then perform a numerical optimization of the layer thicknesses such that the resulting spectrum approaches the desired one as close as possible [94]. Laseroptik GmbH designed a coating (catalog number B-18605) consisting of 38 layers alternating between TiO_2 with a refractive index of 2.37 and SiO_2 with a refractive index of 1.48 at $\lambda = 785\,\text{nm}$. The optical thickness of each layer deviates from a quarter wavelength, optimized for the aforementioned spectral properties. The exact layer thicknesses are confidential. Fig. 6.1 shows the theoretical reflectivity spectrum without losses of the final design. We would like to highlight the steep reflectivity edge separating the 00ZPL wavelength $\lambda = 785\,\text{nm}$ and the fluorescence transmission window, which blue-shifts for tilted incidence. The angle-dependent reflectivity for $\lambda = 785\,\text{nm}$ (Fig. 6.2) reflects this fact. The reflectivity of the dichroic mirrors reduces more significantly with increasing AOI than the reflectivity of the Bragg mirrors (c.f. Fig. 3.6).

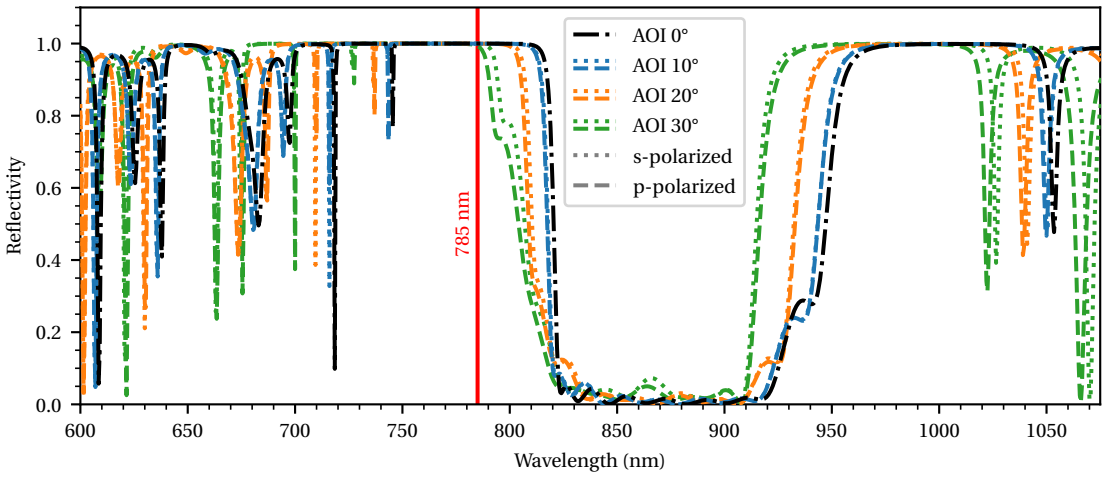

Figure 6.1: The reflectivity spectrum of the dichroic mirrors for different AOI and polarizations.

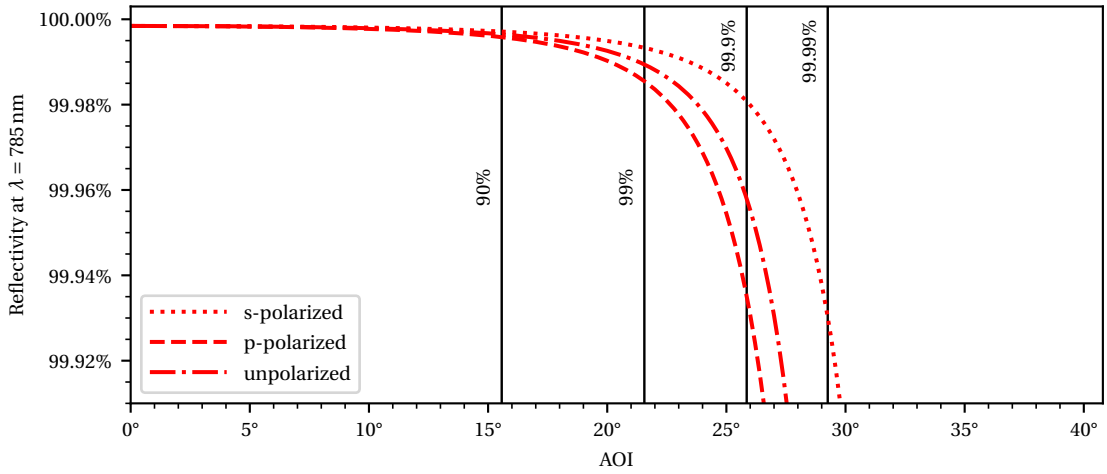

Figure 6.2: The AOI dependence of the dichroic mirror reflectivity for the 00ZPL wavelength $\lambda = 785\,\text{nm}$. The vertical lines indicate the fraction of power contained in a beam of divergence $\theta = 15°$ up to their corresponding AOI.

This angle dependence is taken into account in the effective finesse $\mathcal{F}_{\text{eff}}$, defined in Eq. 6.1a. Fig. 6.3 shows the effective finesse for the dichroic mirrors and the Bragg mirrors. The emission spectrum of an ensemble of DBT molecules inside a dichroic cavity is also shown. It reveals the characteristic emission peaks corresponding to transitions into vibrational states [75]. The design additionally results in a high reflectivity around $\lambda = 1000\,\text{nm}$, which can be used for

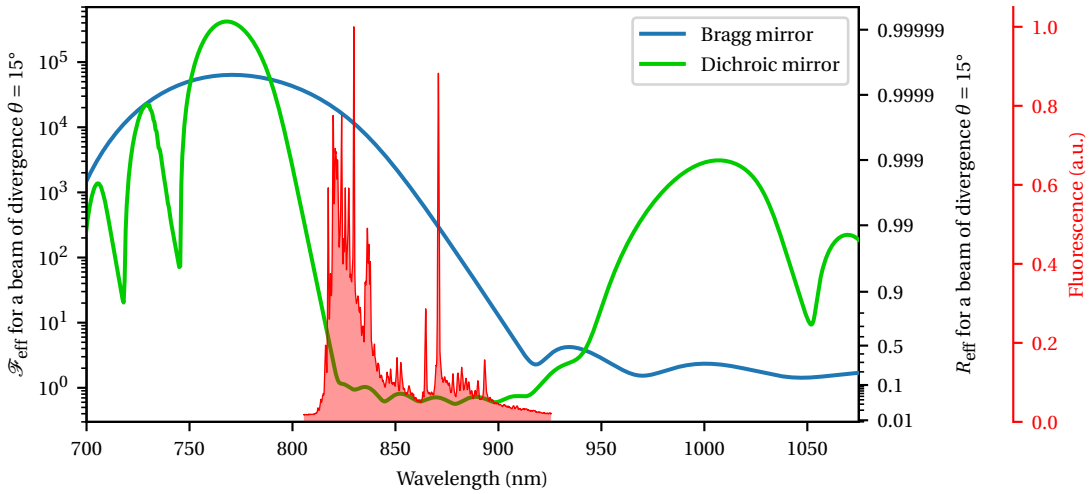

Figure 6.3: The effective finesse $\mathcal{F}_{\text{eff}}$ and effective reflectivity R_{eff} of the two mirror designs for a mode with divergence of 15°. For comparison, the emission spectrum of DBT in anthracene, measured in a dichroic cavity, is shown in red. While the Bragg design has an effective reflectivity $R_{\text{eff}} > 90\,\%$ for most of the emitted wavelengths, the dichroic mirror has a transmission window.

locking the cavity length (see Ch. 3.5) at a wavelength which can easily be separated from the fluorescence and the 00ZPL.

Experimentally, the finesse at $\lambda = 785\,\text{nm}$ reaches up to 10 000. In addition to the loss mechanisms in the Bragg-design mirrors, absorption within the coating plays a major role, because the steep edge in the reflectivity spectrum near 785 nm causes the field to penetrate further into the coating than for Bragg mirrors. While a finesse of 10 000 suffices for the experiments described in Ch. 6.3 & 6.2, the experiment in Ch. 6.4 requires a significantly higher ratio g/κ. There are ways to optimize the mirrors for higher finesse: Firstly, an anthracene crystal of given thickness can be taken into account as an additional mirror layer. This restricts the flexibility of the setup, but since most crystals show a thickness gradient (such as the one in Fig. 3.9c), it is likely that many crystals have a region with the design thickness. Secondly, the transmission window can be designed less restrictively. In the current design, the reflectivity is $< 5\,\%$ between 827–919 nm. Relaxing this condition would in turn allow a decrease in the field penetration depth at 785 nm.

We can detect single molecules in a dichroic cavity with the common fluorescence excitation spectroscopy method [81], except that the excitation happens via the cavity mode. We excite the molecules via the 00ZPL and filter out the excitation laser (see Ch. 3.4) to detect only light with wavelengths $\lambda > 800\,\text{nm}$. Scanning the excitation laser reveals several narrow resonances, corresponding to the 00ZPLs of individual molecules (see Fig. 6.4). A saturated molecule results in around 10^5 detected photons per second.

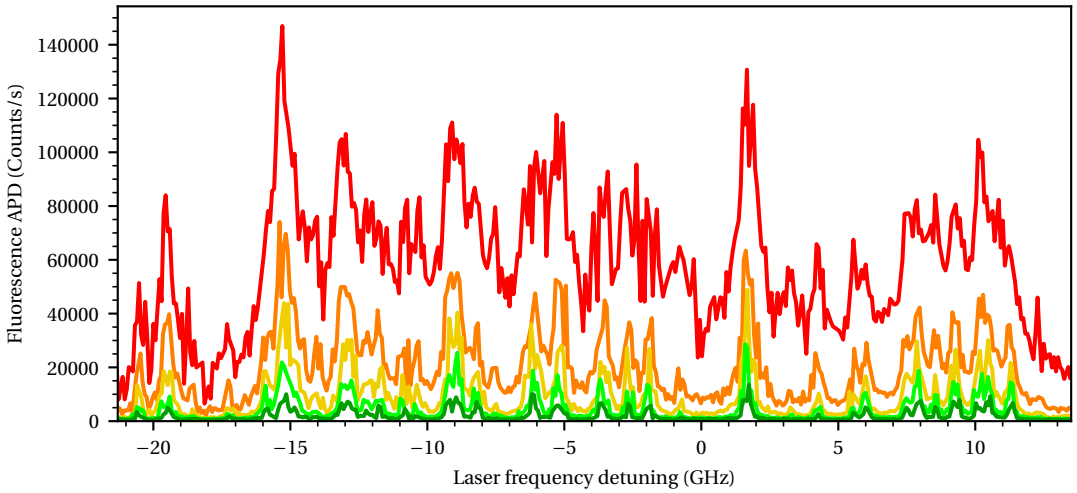

Figure 6.4: The fluorescence excitation spectrum of several molecules in a dichroic cavity. The laser power is increased by approximately a factor of 4 between the measurements. At the highest power a background emerges from many molecules in the excitation volume.

6.2 Steady-State Inversion of a Two-Level System

In the all-optical switching experiments (see Ch. 5.2) we found that the probe beam can be amplified when passing through the cavity-molecule system. To establish whether this is caused by stimulated emission from a population-inverted molecule, we simulated the excited-state population as a function of the pump power. Fig. 6.5a) shows this, together with the transmission of the probe beam. It reveals that population inversion does not occur at the pump power for which > 100 % probe transmission is observed. As detailed in Ch. 5.2, the reason for the probe amplification is multiphoton processes transferring energy from the pump to the probe beam. In contrast to this observation, we find that in a simple resonant saturation measurement, a two-level system coupled to a cavity can be inverted. However, due to energy conservation in this one-beam experiment, the transmission does not exceed 100 % (Fig. 6.5b)). Despite the fact that a two-level system cannot be inverted in its steady state, the 53 % excited state population is not an error in our simulation. In fact, this effect had already been discovered numerically in 1988 by C. M. Savage [175].

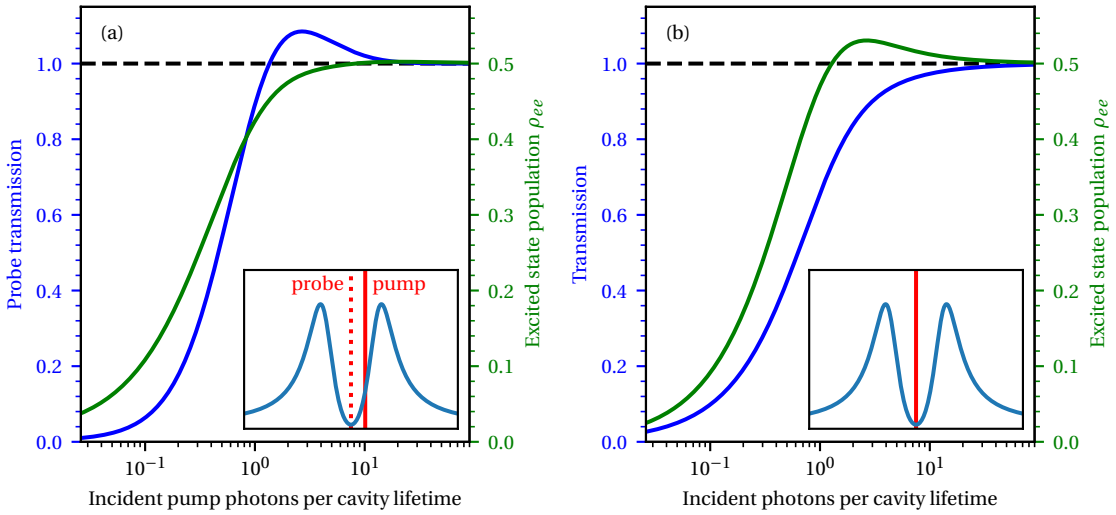

Figure 6.5: A molecule coupled to a cavity with $\{g,\kappa,\gamma\} = 2\pi \cdot \{0.63, 1.28, 0.04\}$ GHz. (a) A weak resonant probe beam interrogates the transmission through the molecule-cavity system while a $\Delta\nu = 300$ MHz detuned pump beam saturates the molecule. (b) A single resonant laser beam saturates the molecule.

These two examples show that a pump-probe experiment is not suited to unambiguously proving inversion, because it is not fully correlated with transmission through the cavity. However, the dichroic cavity mirrors (see Ch. 6.1) allow use of the fluorescence emission rate to assess the excited state population. S. Hughes & H. J. Carmichael [176] have theoretically explored the excited state population for a wide range of parameters, including the detunings between cavity, emitter and laser, and found even higher excited state populations up to 75 %. Fig. 6.6 shows 2D detuning spectra for the cavity and molecule parameters such as those in the nonlinear optics experiments (Ch. 5). We find excited-state probabilities of up to 63.4 %.

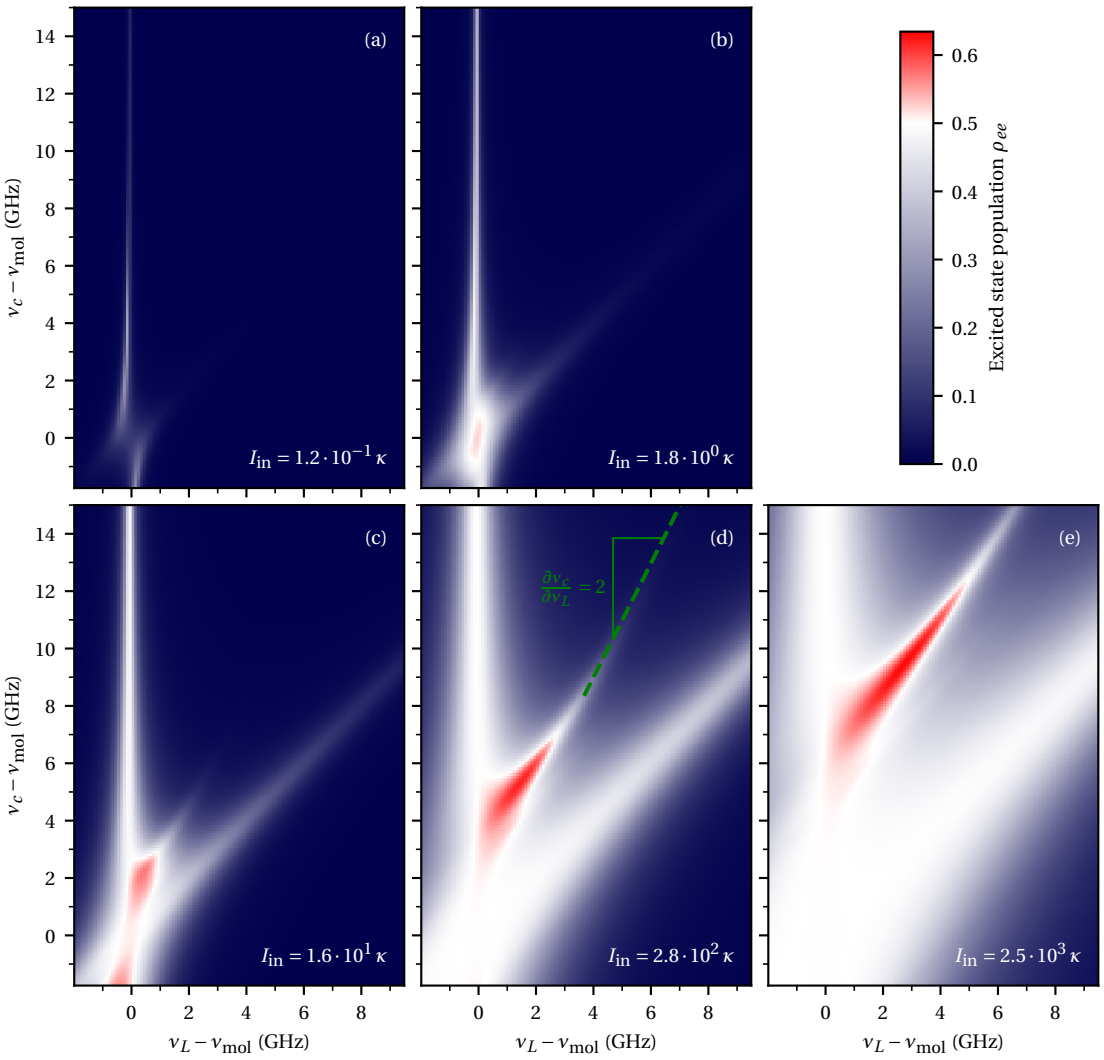

Figure 6.6: The excited state population for a cavity-coupled molecule with $\{g, \kappa, \gamma\} = 2\pi \cdot \{0.63, 1.28, 0.04\}$ GHz for different incident laser powers. The colormap is chosen such that 50 % excited state probability corresponds to the color white. Values above 50 % are red.

Notably, the inversion occurs within an elongated region of the spectrum, for which cavity and molecule are detuned from each other and the laser pumps at a frequency between the two. The slope of this region is $\partial \nu_c / \partial \nu_L \approx 2$, which suggests a two-photon process may be responsible for the inversion.

To understand how the cavity-coupled molecule can be inverted, whereas a molecule in free-space cannot, we examine the elementary processes [177]. A two-level system in free space (Fig. 6.7a)) can not be inverted, because laser driving at Rabi frequency Ω couples $|g\rangle \leftrightarrow |e\rangle$ bidirectionally, i.e. it increases the rate of stimulated absorption and emission equally. Therefore, the population between $|g\rangle$ and $|e\rangle$ can at most be balanced. The additional channel of spontaneous emission shifts the balance towards the ground state. If we add the cavity,

two more elementary processes are added: The Jaynes-Cummings interaction, in which the cavity and emitter exchange an excitation, and the decay of photons out of the cavity at rate κ. We now ascertain if one or a combination of these processes can lead to a net increase in the excited-state population. We model the system in the vacuum picture (see Ch. 2.4), in which the laser effectively drives the emitter directly and for the cavity mode we only consider the photons scattered by the emitter. As the basis, we use the states $\{|g/e,n\rangle | n \in \mathbb{N}_0\}$, which are not the energy eigenstates of the coupled system, but do form a complete basis. In the limit of high cavity-emitter detuning, they approach the energy eigenstates (see Ch. 2.3.3). Fig. 6.7b) shows how the elementary processes connect the first four states. The laser driving and the Jaynes-Cummings interaction are bidirectional, hence they do not drive the molecule into inversion. The release of cavity photons does not influence the state of the molecule, and the free-space decay of molecular excitations counteracts inversion. Next, we evaluate the effect of the second-order processes, i.e. combinations of first-order elementary processes (see Fig. 6.7c)). Combining one laser driving and one Jaynes-Cummings step results in a process connecting $|g/e,n\rangle \leftrightarrow |g/e,n+1\rangle$, hence not changing the population of the excited state. Repetitions of the same process leave the complete system unaffected. Hence, second-order processes cannot invert the molecule, either. However, there is one third-order process (Fig. 6.7d))

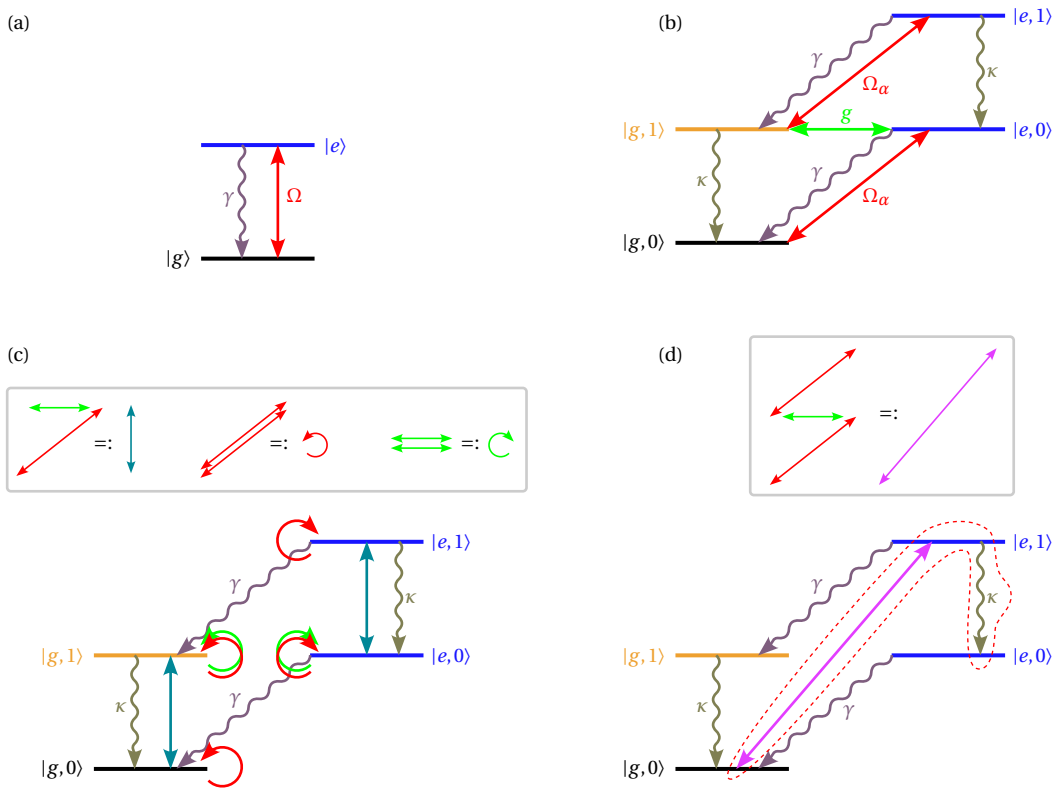

Figure 6.7: (a) Elementary processes in a laser-driven two-level system. (b) First-order, (c) second-order and (d) third-order elementary processes in the first four states of a cavity-coupled laser-driven two-level system.

which allows an effective transport of population into the excited state: A combination of two laser drive steps and one Jaynes-Cummings step. This process, by itself, is bidirectional $|g,0\rangle \leftrightarrow |e,1\rangle$. However, a subsequently emitted cavity photon brings the system into the state $|e,0\rangle$ and therefore out of reach of the reverse process.

The set of $|g,0\rangle \leftrightarrow |e,1\rangle \rightarrow |e,0\rangle$ (marked by the red dashed line in Fig. 6.7d)) is therefore similar to a three-level laser, in which the population is pumped into $|e,0\rangle$ [178]. To achieve inversion, the rate of this pumping must exceed the spontaneous emission rate γ of the two-level system. The highest inversion can be achieved when the pumping process is driven with as little activity as possible in the other, potentially population-equalizing, processes. If the cavity is far-detuned from the emitter, the rate of Jaynes-Cummings transitions is low; and if the laser is detuned from the single-photon resonance of the molecule, this process can also be suppressed. Instead, the laser is tuned in resonance with the two-photon transition $|g,0\rangle \leftrightarrow |e,1\rangle$. This explains the slope of $\partial\nu_c/\partial\nu_L \approx 2$ of the inversion feature in Fig. 6.6d): If the cavity is detuned by $\Delta\nu_c$, the laser frequency must be detuned by $\Delta\nu_c/2$ to remain resonant with the two-photon transition, as illustrated in Fig. 6.8. The offset of the inversion feature from the line $\nu_L = (\nu_{\mathrm{mol}} + \nu_c)/2$ is due to the interaction energy $2\hbar g$ and the laser-dressing of the cavity-dressed states [179].

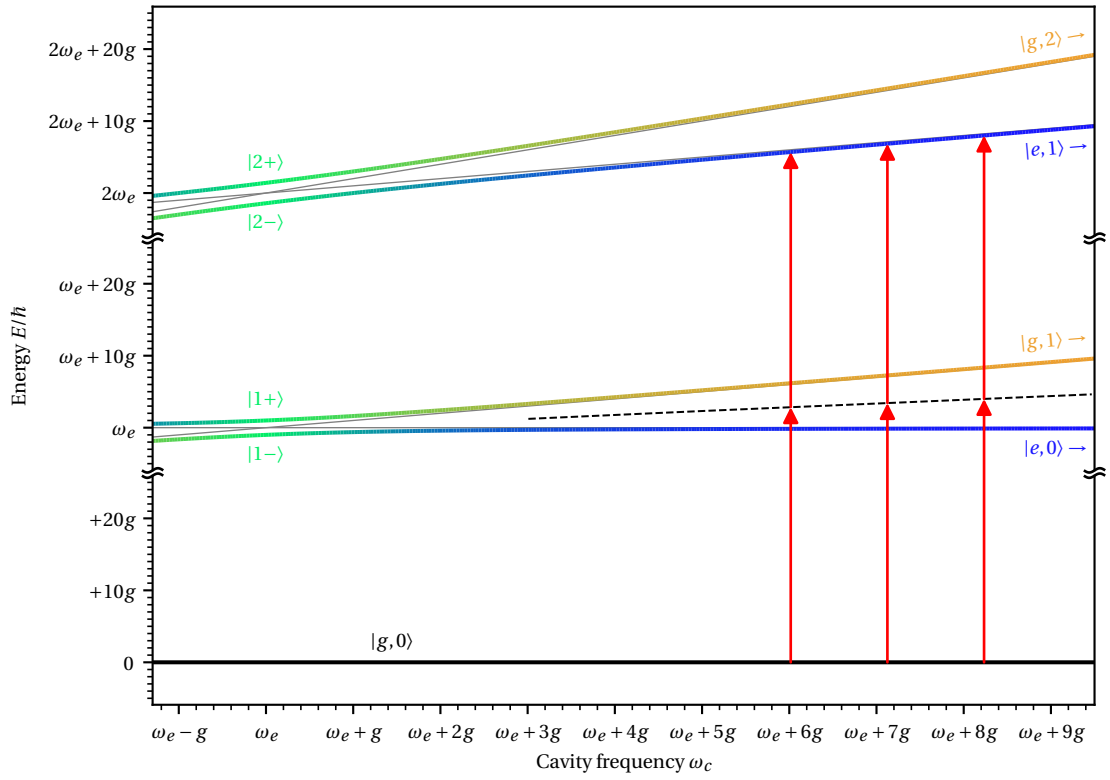

Figure 6.8: The energy levels of the detuned cavity-emitter system (cf. Fig. 2.4). A two-photon transition into the state $|2-\rangle \approx |e,1\rangle$ is detuned from the single-photon resonances $|g,0\rangle \rightarrow |e,0\rangle$ and $|g,0\rangle \rightarrow |g,1\rangle$.

Although the fluorescence countrate is proportional to the excited state population, it is not normalized, i.e. we cannot determine from a single data point whether the molecule is inverted. Therefore, we ideally record 2D spectra as in Fig. 6.6 to be able to compare the fluorescence countrate for different combinations of laser and cavity detunings. As described in Ch. 3.5.2, our data is naturally recorded in these 2D spectra. In a first test, we assembled a cavity with dichroic mirrors. The optical setup was modified from what we describe in Ch. 3.4. The curved mirror substrate was a GRIN lens (see Ch. 3.1.1). This allowed us to excite the cavity mode through the flat mirror and detect the transmission through the cavity on the curved mirror side, instead of using a cross-polarization scheme. Additionally, we collected Stokes-shifted fluorescence transmitted through the flat mirror. We find a cavity linewidth of $\kappa/2\pi = 3.9\,\mathrm{GHz}$ and identify a molecule with $g/2\pi = 0.7\,\mathrm{GHz}$ as a suitable candidate. Simulations show that

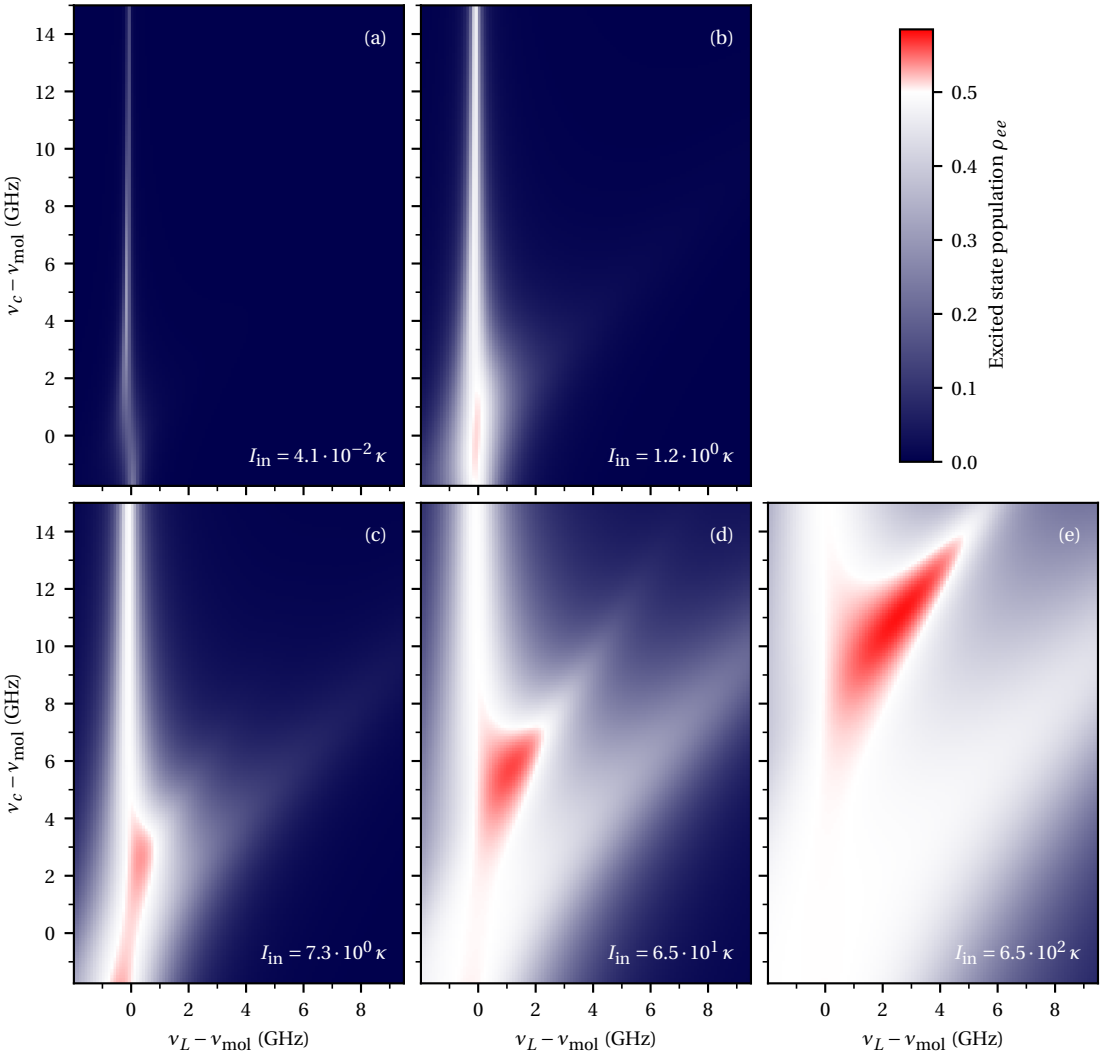

Figure 6.9: The excited state population for a cavity-coupled molecule with $\{g, \kappa, \gamma\} = 2\pi \cdot \{0.7, 3.9, 0.04\}$ GHz for different incident laser powers.

the excited state population in this system can be as high as 58.5 % (see Fig. 6.9). Fig. 6.10 shows the 2D fluorescence spectra for increasing laser powers. At high excitation power the background around $\nu_L = \nu_c$ dominates the detected fluorescence, masking any signature of inversion. The background has the same polarization and spatial profile as the fluorescence from the single molecule. The spectrum also shows a strong similarity. We therefore suggest that it originates from a phonon-wing excitation [180] of a small ensemble of DBT molecules within the cavity mode. An ideal crystal for this experiment would therefore have a significantly lower doping concentration.

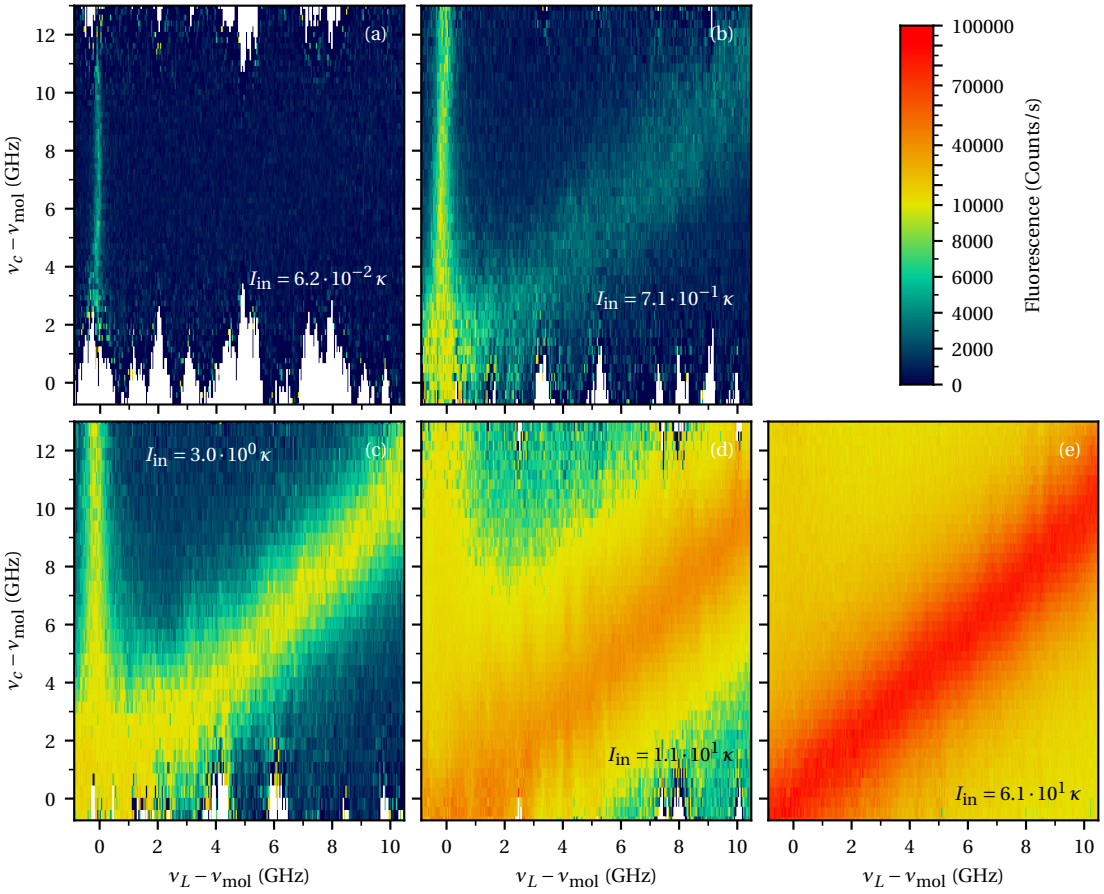

Figure 6.10: The detected fluorescence as a function of the laser frequency and the cavity frequency for different laser powers.

To conclude, this experiment highlights the difference between a two-level system in free space and a two-level system which interacts with its own nonclassical emission via a cavity. Furthermore, multi-photon transitions of this kind in an off-resonant cavity-molecule system have been proposed as a source of N-photon bundles with potential applications in quantum metrology and quantum information processing [34].

6.3 Molecule-Molecule Coupling via the Cavity Mode

Before discussing the specific case of two molecules coupled via a common cavity mode, we give a more general review of emitter-emitter coupling. Two emitters, coupled via common electromagnetic field modes, can coherently exchange energy at a rate $2J$. The Hamiltonian of this system consists of three contributions

$$\hat{H} = \hat{H}_{E,1} + \hat{H}_{E,2} + \hat{H}_{\text{coupl}}, \tag{6.2a}$$

namely the energies of the individual emitters with resonance frequencies $\omega_{e,i}$

$$\frac{\hat{H}_{E,i}}{\hbar} = \omega_{e,i}\hat{\rho}_{ee,i} \tag{6.2b}$$

and the coupling term

$$\frac{\hat{H}_{\text{coupl}}}{\hbar} = J\left(\hat{\sigma}_{-,1}\hat{\sigma}_{+,2} + \hat{\sigma}_{+,1}\hat{\sigma}_{-,2}\right). \tag{6.2c}$$

The $\hat{\sigma}$ and $\hat{\rho}_{ee}$ operators are the same as in Ch. 2.3.1 $\hat{\rho}_{ee,i} = |e_i\rangle\langle e_i|$, $\hat{\sigma}_{+,i} = |e_i\rangle\langle g_i| = \left(\hat{\sigma}_{-,i}\right)^\dagger$, except that the subscript i indicates that it acts on the ith molecule. Analogously to the hybridization between cavity and molecule (see Ch. 2.3.3), the single-excitation energy eigenstates of the coupled emitters are the dark $|D\rangle$ and superradiant state $|S\rangle$ (see Fig. 6.11)

$$\begin{aligned} |S\rangle &= \sin\theta\,|e_1 g_2\rangle + \cos\theta\,|g_1 e_2\rangle \\ |D\rangle &= \cos\theta\,|e_1 g_2\rangle - \sin\theta\,|g_1 e_2\rangle, \end{aligned} \tag{6.3a}$$

with the mixing angle $\theta \in [0, \pi/2]$ given by

$$\tan 2\theta = \frac{2J}{\omega_{e,2} - \omega_{e,1}}. \tag{6.3b}$$

For two resonant emitters $\omega_{e,1} = \omega_{e,2}$, the mixing angle is $\theta = \pi/4$ and $|S\rangle$ and $|D\rangle$ are maximally entangled states (see Fig. 6.11a)). In the emission of the superradiant state $|S\rangle$, the transition dipole moments of the two emitters interfere constructively, giving rise to an accelerated radiative decay of this state, while the transition dipoles in the dark/subradiant state interfere destructively, reducing the radiative decay rate.[1] The energies of these states are

$$\begin{aligned} E_S/\hbar &= \omega_{e,1}\sin^2\theta + \omega_{e,2}\cos^2\theta + 2J\sin\theta\cos\theta \\ E_D/\hbar &= \omega_{e,1}\cos^2\theta + \omega_{e,2}\sin^2\theta - 2J\sin\theta\cos\theta. \end{aligned} \tag{6.4}$$

[1] The modified decay rates and the coupling J can be derived from the coupling of the emitters to common modes of the electromagnetic field. R. Dicke [181] describes a situation with an arbitrary number of emitters coupled to a single mode; U. Akram *et al.* [182] describe two emitters coupled via a continuum of modes.

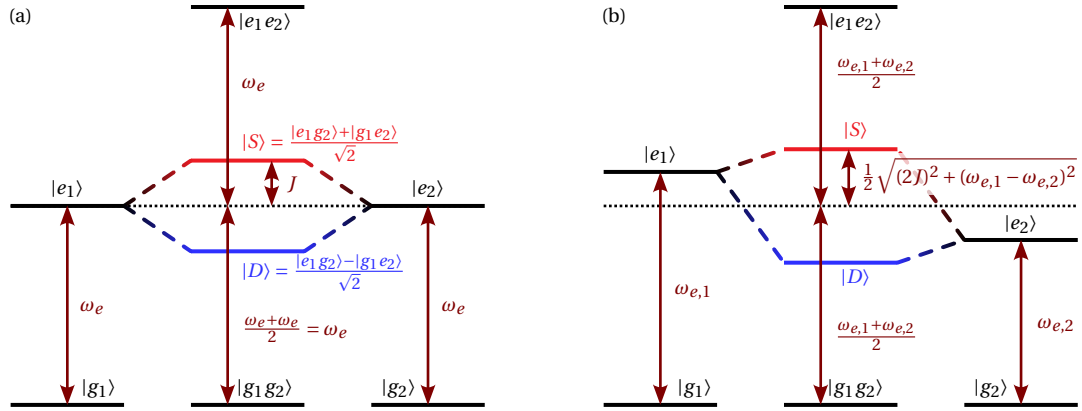

Figure 6.11: Energy levels of two emitters, interacting with coupling strength $J > 0$ for (a) resonant emitters $\omega_{e,1} = \omega_{e,2}$ and (b) detuned emitters.

The origin of the coupling can be a dipole-dipole interaction of two nearby emitters. For two emitters whose separation $\vec{r}_{12}$ is small compared to the wavelength of the light λ, the coupling rate is [183]

$$J = \frac{3}{4} \frac{\sqrt{\gamma_1 \gamma_2}}{\left(\frac{n}{c}\omega |\vec{r}_{12}|\right)^3} \left(\frac{\vec{d}_1 \cdot \vec{d}_2}{|\vec{d}_1||\vec{d}_2|} - 3 \frac{\left(\vec{d}_1 \cdot \vec{r}_{12}\right)\left(\vec{d}_2 \cdot \vec{r}_{12}\right)}{|\vec{d}_1||\vec{d}_2||\vec{r}_{12}|^2} \right), \tag{6.5}$$

where $\vec{d}_i$ is the transition dipole moment of the ith emitter. Fig. 6.12a) illustrates the situation. Practically, one rarely finds a pair of emitters, for which the coupling rate J is comparable to or higher than the radiative decay rate γ of the emitters. There are few publications, in which the near-field coupling of two molecules has been reported [184–186]. This is because the emitters must be spatially and spectrally close for the coupling to affect the spectrum significantly. Moreover, for real emitters, the branching ratio α_{00} must be taken into account. Only the emission via the 00ZPL $\gamma_{00} = \alpha_{00}\gamma$ contributes to the coupling, because all other emission pathways involve environmental degrees of freedom which dissipate quickly.

Quantitatively, in a highly doped DBT:anthracene crystal with 10^4 emitters per µm^3 each emitter has on average 10^0 emitters close enough that $|J| > \gamma$, assuming $\alpha_{00} = 1/3$. However, since their resonance frequencies $\omega_{e,i}$ exhibit an inhomogeneous distribution of typically $10^4\,\gamma$, the proportion of molecules with a spectral neighbor within $[-10\gamma, 10\gamma]$ is 10^{-3}.

However, the energy exchange need not be a near-field interaction. The field could be guided over long distances between the emitters by an optical waveguide [187]. Alternatively, the emitters can be coupled to the same cavity mode as illustrated in Fig. 6.12b). This relaxes the spatial requirement in particular: Instead of a sub-wavelength distance, as for the dipole-dipole interaction, the emitters must only be within the cavity mode. Treated rigorously, a system of two emitters coupled to a cavity mode gives rise to energy eigenstates in which the

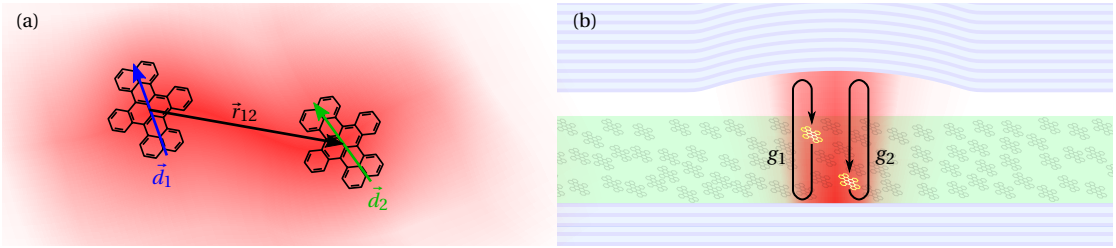

Figure 6.12: (a) Two molecules coupled via their near-field dipole-dipole interaction. (b) Two molecules individually coupled to a common cavity mode.

excitations are shared among the two emitters and the cavity, where the coefficients depend on the relative detunings and coupling strengths. Within this parameter space, rich physics is to be explored [188]. Here, we focus on a subset of these configurations, namely two emitters dispersively coupled to a cavity, meaning that the cavity is detuned from the emitters by more than the detuning between the emitters. As such, the molecules can interact with each other due to the spatial confinement of their emission by the cavity. However, because of its high detuning, the cavity mode is only weakly populated. Hence, the energy eigenstates of the coupled tripartite system approach the pure emitter states $|S\rangle$ and $|D\rangle$. Usually, as is also the case in our system, the cavity mode loses excitations at a much higher rate than the emitters $\kappa \gg \gamma$. The low weight of cavity excitations in the hybridized states is therefore beneficial. In the limit $g_i \ll |\omega_{e,i} - \omega_c|$, the Hamiltonian of the system

$$\frac{\hat{H}}{\hbar} = \omega_{e,1}\hat{\rho}_{ee,1} + \omega_{e,2}\hat{\rho}_{ee,2} + \omega_c \hat{a}^\dagger \hat{a} + g_1\left(\hat{\sigma}_{+,1}\hat{a} + \hat{\sigma}_{-,1}\hat{a}^\dagger\right) + g_2\left(\hat{\sigma}_{+,2}\hat{a} + \hat{\sigma}_{-,2}\hat{a}^\dagger\right) \tag{6.6a}$$

can be approximated to second order perturbation in $g_i/(\omega_{e,i} - \omega_c)$ to yield [189]

$$\approx \tilde{\omega}_{E,1}\hat{\rho}_{ee,1} + \tilde{\omega}_{E,2}\hat{\rho}_{ee,2} + \tilde{\omega}_c \hat{a}^\dagger \hat{a} + J\left(\hat{\sigma}_{+,1}\hat{\sigma}_{-,2} + \hat{\sigma}_{-,1}\hat{\sigma}_{+,2}\right), \tag{6.6b}$$

where $\tilde{\omega}_{E1}$, $\tilde{\omega}_{E2}$ and $\tilde{\omega}_c$ are the Lamb-shift-corrected resonance frequencies of the two emitters and the cavity. The coupling strength in the last term is

$$J = \frac{g_1 g_2}{2}\left(\frac{1}{\omega_{e,1} - \omega_c} + \frac{1}{\omega_{e,2} - \omega_c}\right). \tag{6.7}$$

Coupling two emitters via a cavity mode is routine in circuit quantum electrodynamics [191, 192], but has only recently been demonstrated in the optical domain with silicon vacancy centers (SiVs) in a diamond photonic crystal resonator [190] and with rubidium atoms in the evanescent field of a photonic crystal resonator [193]. Fig. 6.13 shows transmission spectra from the former experiment, in which the super- and subradiant states are identified. Because of the detuning-dependence of J (cf. Eq. 6.7), the subradiant state $|D\rangle$ is always the one closer to the cavity frequency. Transmission spectra with only one emitter were also recorded, by ionizing one SiV. This allows a direct comparison between the single-emitter and coupled-

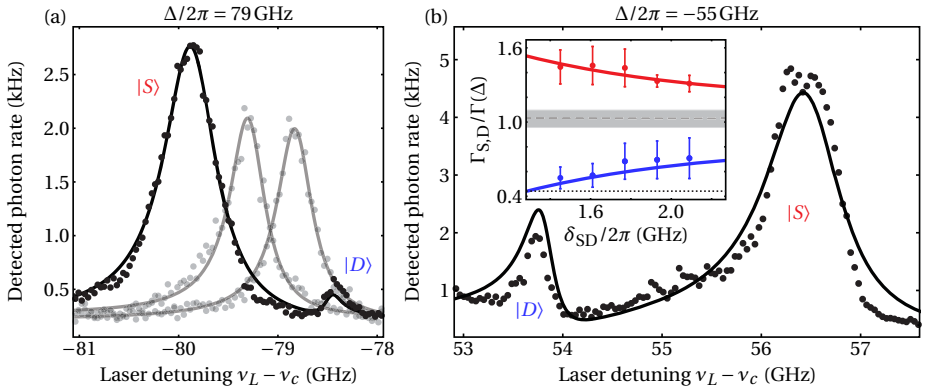

Figure 6.13: Transmission spectra of two silicon vacancy centers (SiVs) in diamond coupled to a detuned photonic crystal resonator. The individual coupling strengths and loss rates are $\{g_1 \approx g_2, \kappa, \gamma_1 \approx \gamma_2\} = 2\pi \cdot \{7.3, 30, 0.19\}$ GHz. (a) The cavity is blue-detuned by 79 GHz from the SiVs. The grey data show the transmission spectra when one of the SiVs is inactivated by ionizing it. (b) The cavity is red-detuned by 55 GHz. The inset shows the linewidths $\Gamma_{S,D}$ of the super-/subradiant states for various splittings δ_{SD} between $|S\rangle$ and $|D\rangle$. From [190] / Reprinted with permission from AAAS. Modified with permission from the author.

emitter spectra (Fig. 6.13a)). Using the triplet state $|t\rangle$ of our molecules to passivate them temporarily would allow us to perform a similar measurement, but the few µs lifetime of the triplet state makes this measurement protocol very demanding. Alternatively, the coupling could be confirmed by tuning the emitters in and out of resonance with each other [186, 194] and observing the linewidth and resonance frequency of the coupled states $|S\rangle$ and $|D\rangle$.

Here, we propose detecting the coupling via a two-photon transition $|g_1 g_2\rangle \rightarrow |e_1 e_2\rangle$ into the state where both molecules are excited simultaneously. Even though this process connects two separable states, it only works if the molecules can exchange energy via their coupling [183]. Since it is a two-photon process, it is revealed only at higher excitation power and can be identified by its saturation behavior. As demonstrated by various experiments (Ch. 5), our system is very well suited to such nonlinear optical experiments. Fig. 6.14a) shows the simulated transmission spectrum of two cavity-coupled molecules $\{g_1 = g_2, \kappa, \omega_{e,2} - \omega_{e,1}\} = 2\pi \cdot \{0.63, 1.28, 2.0\}$ GHz for different excitation powers. The two-photon resonance, equidistant between between the one-photon resonances, causes only a very shallow feature in the transmission spectrum. This is because the molecules are close to saturation when the laser power is high enough to excite the two-photon transition noticeably. Therefore, its relative effect on the transmission spectrum is very small. In a cavity made of dichroic mirrors we can additionally detect Stokes-shifted fluorescence, which is proportional to the sum of excited state probabilities $\langle \hat{\rho}_{ee,1} + \hat{\rho}_{ee,2} \rangle$. As shown in Fig. 6.14b), the two-photon resonance can be clearly identified here. Because of the low weight of the cavity mode in the hybridized states, this effect is only weakly sensitive to the cavity decay rate κ. Fig. 6.15 shows that the two-

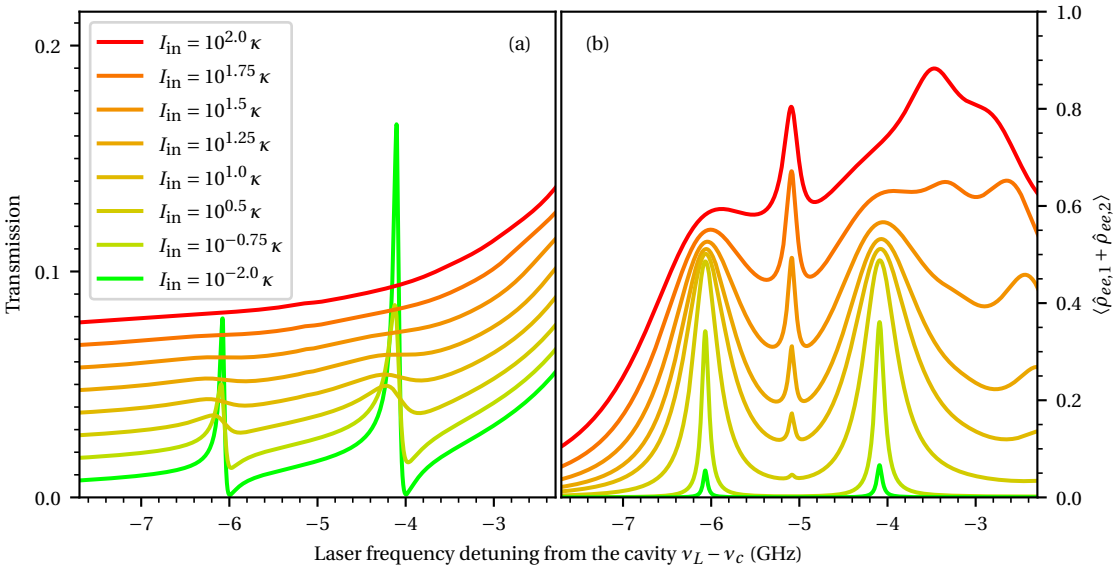

Figure 6.14: (a) Transmission spectra for two molecules detuned by $\nu_{\mathrm{mol},1} - \nu_{\mathrm{mol},2} = 2\,\mathrm{GHz}$ coupled to a cavity; $\{g_1 = g_2, \kappa, \gamma_1 = \gamma_2\} = 2\pi \cdot \{0.63, 1.28, 0.04\}$ GHz. They are vertically shifted by 0.01 relative to each other for clearer visualization. (b) Combined excited-state probability of both molecules, proportional to the overall detected fluorescence. We note that these spectra are simulated with the full Hamiltonian (Eq. 6.6a), without the dispersive approximation (Eq. 6.6b). The extra peaks on the right side of the spectrum originate from multiphoton processes, such as those described in the previous subchapter.

photon peak is still clearly resolved in a cavity three times lossier. $\kappa = 3.9\,\mathrm{GHz}$ is the linewidth of the dichroic cavity we assembled for a first test.

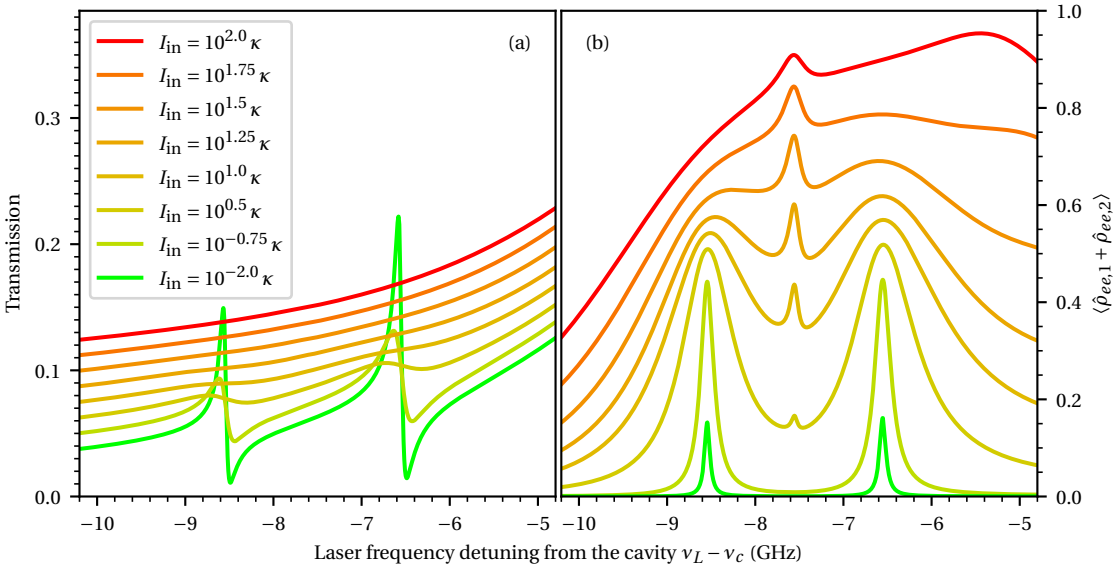

Figure 6.15: Same as Fig. 6.14, but with $\kappa/2\pi = 3.9\,\mathrm{GHz}$.

This test uses the same experimental configuration as described in the previous subchapter. However, for this initial test, the doping concentration of the anthracene crystal was too low, such that the closest candidate for molecule-molecule coupling was a pair of molecules with $\{g_1, g_2, \kappa, \omega_2 - \omega_1\} = 2\pi \cdot \{0.36, 0.5, 3.9, 2.4\}$ GHz. The coupling between them is too low to resolve the two-photon resonance. At the time of writing, however, we have verified our ability to grow crystals with significantly higher doping by increasing the temperature of the DBT-anthracene mixture in the sublimation process (see Ch. 3.2).

To increase spectral coincidences, one could employ electrodes to tune individual emitters with respect to each other via the Stark effect [185, 194]. Furthermore, M. Colautti *et al.* [195] have recently demonstrated that DBT molecules can be persistently spectrally shifted by intense irradiation. With this method one could tune molecules into resonance without being restricted to a region close to electrodes.

Beyond the measurements detailed in this chapter, it may also be fruitful to investigate the dynamics of the system more closely using intensity correlations. The red-shifted fluorescence emitted from the double-excited state $|e_1 e_2\rangle$ is bunched. The decay of correlations as a function of the time delay τ contains information about the decay via the sub- and superradiant states. This can furthermore be correlated to the emitted resonance fluorescence. Overall, many features of the two molecules coupled via the cavity can be revealed.

6.4 Quantized AC Stark Shift

Analogously to the AC Stark effect in the semiclassical treatment of light-matter interaction (see for example [1, 101]), cavity quantum electrodynamics provides a fully quantum mechanical description of the shift in an emitter's resonance frequency. Without loss of generality[2] we focus on a cavity blue-detuned relative to the emitter $\omega_c > \omega_e$. In the limit of high detuning $\omega_c - \omega_e \gg g$, the state $|n+\rangle$ becomes the state $|g, n\rangle$ and the state $|(n+1)-\rangle$ becomes $|e, n\rangle$ (see Fig. 6.16). The energy difference between them, that is the energy to excite the emitter while leaving the photon number in the cavity constant, is (cf. Eq. 2.21)

$$\begin{aligned} E_{(n+1)-} - E_{n+} &= \hbar\left(n\omega_c + \frac{\omega_c + \omega_e - \Omega_{n+1}}{2} - \left((n-1)\omega_c + \frac{\omega_c + \omega_e + \Omega_n}{2}\right)\right) \\ &= \hbar\left(\omega_c - \frac{1}{2}\left(\Omega_{n+1} + \Omega_n\right)\right) \qquad (6.8a) \\ &= \hbar\left(\omega_e + 2\chi\left(n + \frac{1}{2}\right) + \mathcal{O}\left(\frac{1}{(\omega_e - \omega_c)^3}\right)\right). \qquad (6.8b) \end{aligned}$$

[2] In the case of the opposite detuning $\omega_c < \omega_e$, the states $|n-\rangle$ and $|(n+1)+\rangle$ turn into the states $|g, n\rangle$ and $|e, n\rangle$, respectively. This neither changes the definition of χ nor the frequency shift of the emitter by $2\chi(n + \frac{1}{2})$, but the sign of χ changes, according to its definition in Eq. 6.9.

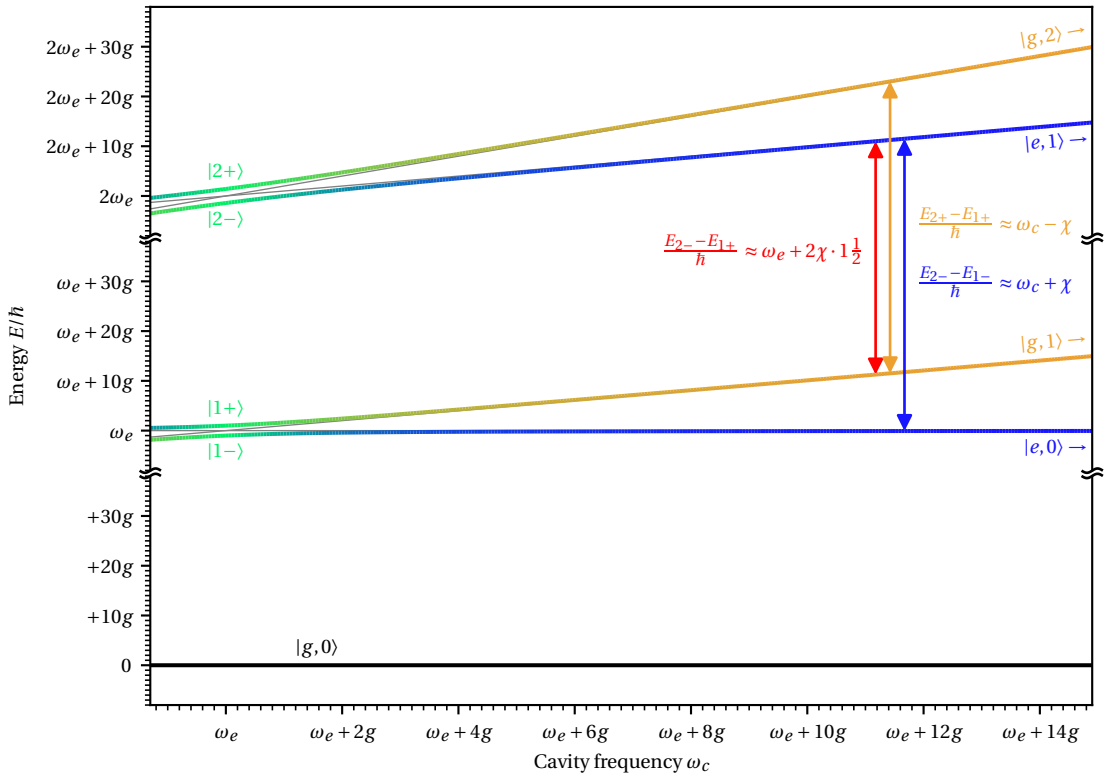

Figure 6.16: Energy levels of a emitter-cavity system (c.f. Ch. 2.3.3). The cavity is far blue-detuned from the emitter. Arrows indicate the transition energies for the emitter while leaving the photon number unaffected (red) and for adding a photon to the cavity while the emitter remains in the ground state (orange) or in the excited state (blue).

Here, we have introduced the dispersive coupling strength as

$$\chi = \frac{g^2}{\omega_e - \omega_c}. \tag{6.9}$$

The resonance frequency of the emitter is shifted by $2\chi\left(n+\frac{1}{2}\right)$ from its bare resonance frequency, depending on the photon number n in the cavity. The red arrow in Fig. 6.16 shows this transition for $n = 1$. At the same time, the cavity resonance frequency is shifted depending on the state of the emitter. If the emitter is in the ground state $|g\rangle$, the energy between n and $n+1$ photons in the cavity is

$$\begin{aligned} E_{(n+1)+} - E_{n+} &= \hbar\left(n\omega_c + \frac{\omega_c + \omega_e + \Omega_{n+1}}{2} - \left((n-1)\omega_c + \frac{\omega_c + \omega_e + \Omega_n}{2}\right)\right) \\ &= \hbar\left(\omega_c + \frac{1}{2}\left(\Omega_{n+1} - \Omega_n\right)\right) = \hbar\left(\omega_c - \chi + \mathcal{O}\left(\frac{1}{(\omega_e - \omega_c)^3}\right)\right). \end{aligned} \tag{6.10a}$$

Hence, the cavity is shifted by $-\chi$ from its bare resonance frequency (see orange arrow in Fig. 6.16). If, instead, the emitter is in the excited state $|e\rangle$, the cavity is shifted by $+\chi$ (blue

arrow in Fig. 6.16):

$$\begin{aligned} E_{(n+1)-} - E_{n-} &= \hbar\left(n\omega_c + \frac{\omega_c+\omega_e-\Omega_{n+1}}{2} - \left((n-1)\omega_c + \frac{\omega_c+\omega_e-\Omega_n}{2}\right)\right) \\ &= \hbar\left(\omega_c - \frac{1}{2}\left(\Omega_{n+1}-\Omega_n\right)\right) = \hbar\left(\omega_c + \chi + \mathcal{O}\left(\frac{1}{(\omega_e-\omega_c)^3}\right)\right) \end{aligned} \tag{6.10b}$$

The latter case (Eqns. 6.10a & 6.10b) is commonly used to infer the state of a superconducting circuit qubit from the shift in the resonance frequency of a dispersively coupled superconducting resonator [196, 197]. The discrete AC Stark shift (Eq. 6.8) has also been measured and could be used to implement quantum gates [198]. For example, the qubit state can be flipped conditionally by applying a π-pulse at frequency $\omega_e + 2\chi\left(m+\frac{1}{2}\right)$. In a general state

$$|\psi\rangle = \sum_{n=0}^{\infty} c_{g,n}\,|g,n\rangle + c_{e,n}\,|e,n\rangle, \tag{6.11}$$

this swaps the $c_{g,m}$ and $c_{e,m}$ coefficients. Furthermore, if the cavity field is in a photon number superposition, as in a coherent state (Eq. 2.48), a measurement of the emitter's resonance frequency collapses the cavity field to a Fock state.

To enable observing the splitting and implementing the gates described, the n-photon resonances must be resolvable, i.e. their splitting 2χ must be larger than their width $\Gamma_n = \frac{1}{2}\left(\gamma + (\bar{n}+n)\kappa\right)$ [199]. The photon-number splitting of the emitter's resonance can be demonstrated in a pump-probe experiment: The pump beam is tuned on resonance with the shifted cavity resonance frequency $\omega_{\text{pump}} = \omega_c - \chi$ and creates a coherent state $|\alpha\rangle$ in the cavity. The weak probe laser then scans around the frequency of the emitter ω_e. Fig. 6.17 shows the

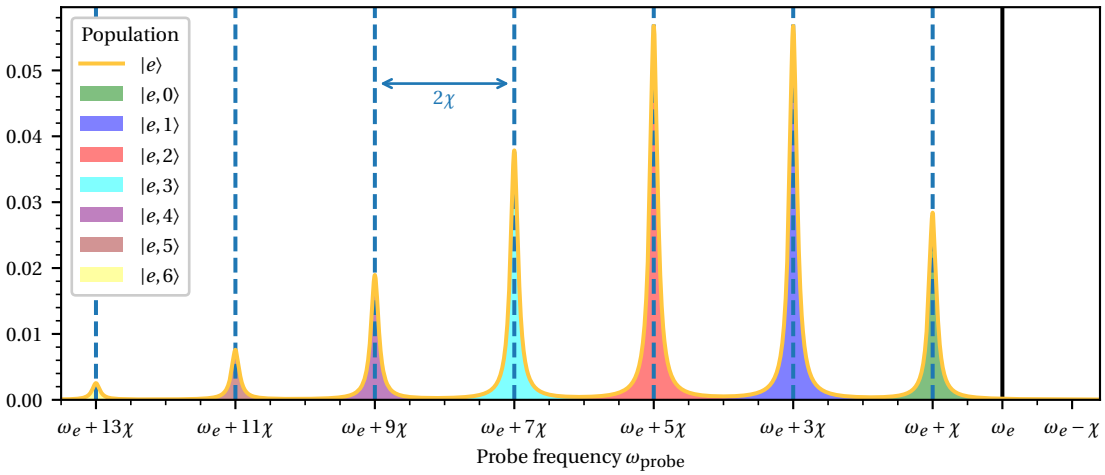

Figure 6.17: The excitation spectrum of an emitter dispersively coupled to a cavity. In this example $\omega_c > \omega_e$, hence $\chi < 0$. Furthermore, $|\omega_e - \omega_c| \gg |\chi|$ and $0.1\,|\chi| = \gamma \gg \kappa$. The pump beam creates a coherent state with a mean photon number $\bar{n} = 2.0$ in the cavity. The dashed blue lines mark the resonance frequencies of the emitter for various photon numbers n.

excited-state population of the emitter as a function of the probe frequency. While there is no resonance at the uncoupled resonance frequency of the emitter ω_e, the probe beam drives transitions at the new resonance frequencies $\omega_e + 2\chi\left(n+\frac{1}{2}\right)$. For a given n, a peak in the population of the state $|e,n\rangle$ attests to the driving of the transition $|g,n\rangle \rightarrow |e,n\rangle$.

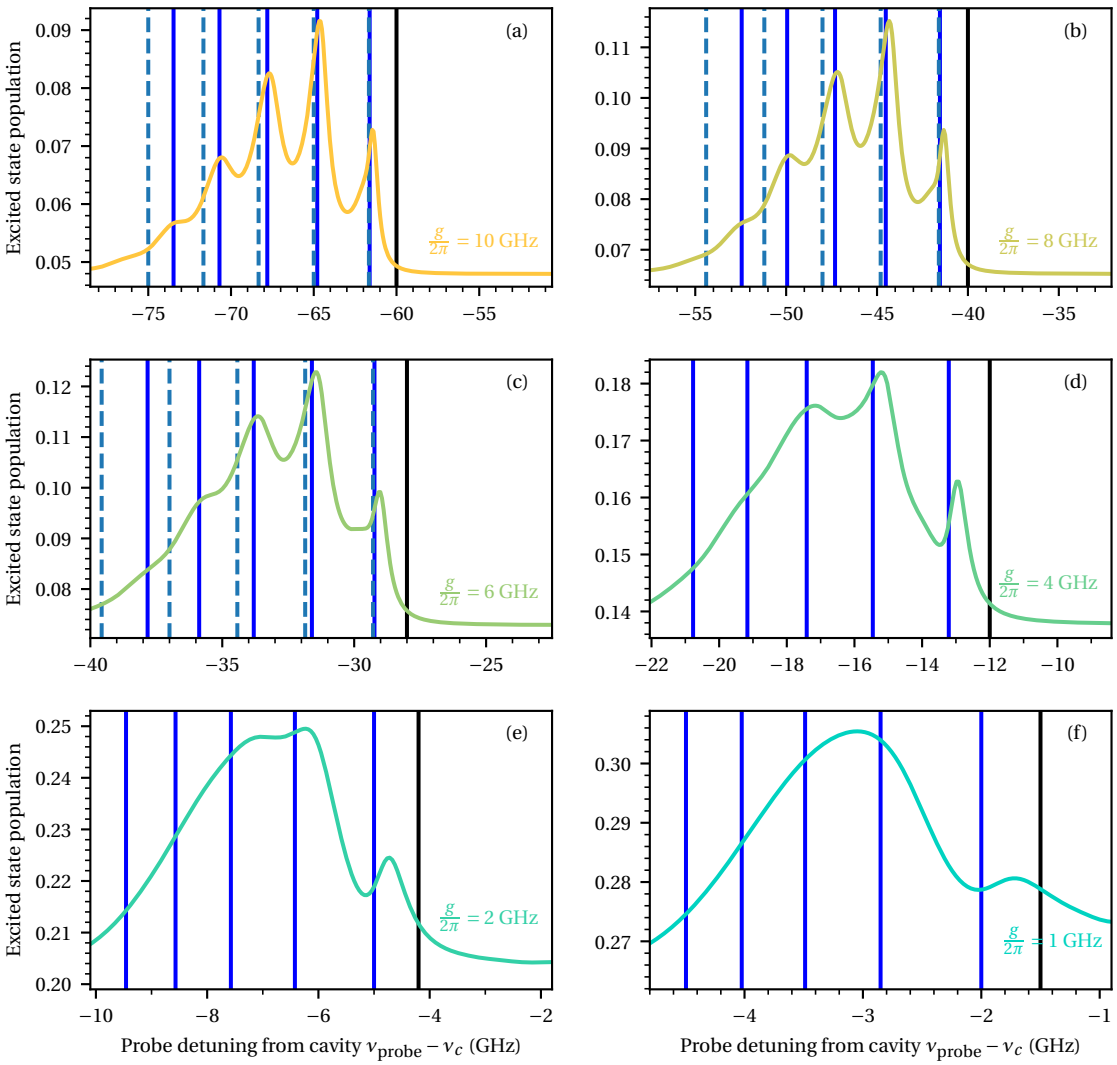

Figure 6.18: The excitation spectrum of an emitter dispersively coupled to a cavity with variable coupling strength g. The dashed lines display the resonances predicted by the dispersive approximation $\omega_e + 2\chi\left(n+\frac{1}{2}\right)$ and the solid lines show the precise frequencies of transitions between polaritons (Eq. 6.8a). The uncoupled emitter resonance frequency ν_e is marked with the black line. In all subplots $\kappa/2\pi = 0.4\,\text{GHz}$ and $\gamma/2\pi = 0.04\,\text{GHz}$. The pump laser creates a coherent state with $\bar{n} = 2.0$ photons in the cavity. Because of the finite detuning $\omega_{\text{pump}} - \omega_e$, the emitter is driven by the pump to some extent. This leads to a probe-frequency independent base excited state population in the spectra, increasing from (a) to (f).

The purpose of Fig. 6.17 is to illustrate the effect with full clarity. While superconducting resonators can exhibit parameters close to this idealized simulation, they are out of reach for resonators at optical frequencies. However, even with lower g/Γ_n, a splitting in the resonances can be observed. Fig. 6.18 shows the excitation spectrum for various parameters, approaching those of our experimental system. By decreasing the detuning $|\omega_e - \omega_c|$, the splitting $|2\chi|$ can be kept high enough to resolve it even with a lower coupling strength g. We note, however, that the lower the detuning, the more hybridized the states (see Eqns. 2.20-2.22). Hence, the spectral peaks do not strictly represent the resonances of the emitter and the cavity, but generally the transition frequency between particular polaritons. We can clearly observe the splitting between the lowest polaritons $|g,0\rangle \rightarrow |1-\rangle$ and the second rung $|1+\rangle \rightarrow |2-\rangle$, even for $\{g,\kappa,\gamma\} = 2\pi \cdot \{1.0, 0.4, 0.04\}$ GHz. Essential to achieving this goal is reducing the cavity decay rate κ, as it is the dominant contribution to the linewidth Γ_n.

With experimental parameters $\{g,\kappa,\gamma\} = 2\pi \cdot \{0.7, 1.28, 0.04\}$ GHz, resembling those in Chapters 4 & 5, the discrete resonances are too broad to be resolved. Nevertheless, it is possible to observe a clear shift and broadening of the overall resonance as a function of the photon statistics inside the cavity [199, 200]. Fig. 6.19 shows excitation spectra for various pump powers.

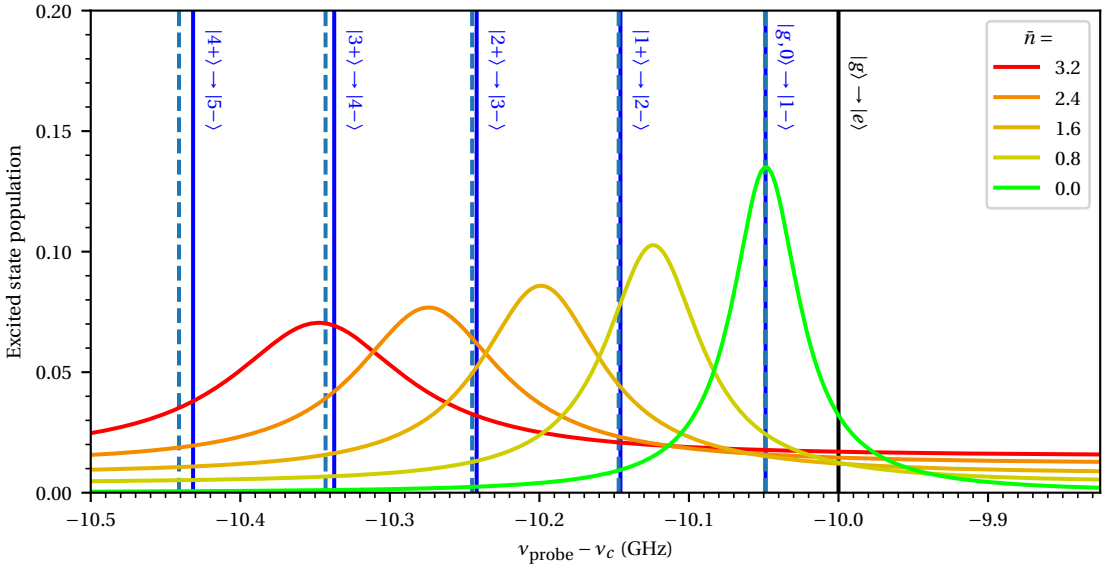

Figure 6.19: The excitation spectrum of an emitter dispersively coupled to a cavity $\{g,\kappa,\gamma\} = 2\pi \cdot \{0.7, 1.28, 0.04\}$ GHz with a detuning of $\nu_e - \nu_c = -10$ GHz. The solid lines show the frequencies of transitions between polaritons (Eq. 6.8a).

Using the extremes of a Q factor of 10^6 and $V = 1.4\,\lambda^3$ as in [201] we would have $\kappa/2\pi = 0.382$ GHz and $g/2\pi = 5.53$ GHz for a molecule in the field maximum with free-space branching ratio $\alpha_{00} = 1/3$ (see Eq. 2.13). This would lie within the regime shown in Fig. 6.18c), where the first three peaks are clearly resolved. Additionally, to separate the excitation of the molecule due to the pump, one could employ a lock-in measurement scheme.

7 General Outlook and Concluding Remarks

In this work, we have provided experimental evidence of the first realization of strong coupling between a single molecule and an optical cavity. The improved efficiency of the inherent photon-number nonlinearity of the molecule made it possible to perform a set of nonlinear optical experiments at intensities corresponding to ~ 1 photon in the cavity. Spectrally tailored dichroic cavity mirrors give us access to the excited state population of the molecule, enabling a whole new class of experiments, some of which we have laid out quantitatively.

The experimental platform is suited to many further applications. Collective light-matter interaction [181, 202] at the transition between quantum and classical physics can be investigated with a number of emitters $2 \leq N \ll 10^{23}$. In particular, a single- or N-molecule laser [203–205] could be realized by incoherently pumping the molecules via a vibrational state $|g, v = 0\rangle \rightarrow |e, v \neq 0\rangle$ while the cavity is resonant with the 00ZPL or a particular $|e, v = 0\rangle \rightarrow |g, v \neq 0\rangle$ transition.

The ability of molecules to generate highly pure [71, 206] and indistinguishable [72] single photons with high quantum yields [207] makes them strong candidates for quantum communication [208], linear optical quantum computation [209] and even redefining the candela [210]. A high-Purcell-factor cavity would enhance all these benefits [211, 212]. A major challenge to the operation of single-photon sources is separating the excitation light from the stream of single photons. This led to the invention of customized excitation protocols, such as phonon-assisted cross-polarization schemes [213]. The energy level scheme of molecules allows one to utilize the vibrational transitions mentioned in the previous paragraph. The excitation light is far blue-detuned from the photons emitted via the 00ZPL and can therefore be filtered out spectrally with high discrimination ratio.

For applications in quantum communication or information processing [214], one could use the long-lived triplet state $|t\rangle$ [75], or switch to a different species of molecules – metal ion complexes [215, 216], which have stable spin-sublevels in their electronic ground states. This would allow for the implementation of equivalent functionality as in other spin-systems with cavity-improved optical transitions such as color centers in diamond [217], quantum dots [218]

and rare-earth ions (REIs) [219]. More generally, microcavities are a platform excellently suited to exploring the properties of various optically active materials, such as carbon nanotubes [220], 2D materials [221–223] and inorganic REI nanocrystals [224].

Appendices

A Acronyms

00ZPL 0-0 zero-phonon line. i, iii, 5, 6, 19, 32, 46, 74–76, 84, 93, 115

AAAS American Association for the Advancement of Science. 86

AOI angle of incidence. 31, 32, 74, 75

AOM acousto-optic modulator. 39, 113

APD avalanche photodiode. 40, 45, 47, 48, 53, 59, 60, 64, 65, 67, 108, 109, 111, 112

DAQ data acquisition. 43, 50, 108

DBR distributed Bragg reflector. 31, 74

DBT dibenzoterrylene. i, iii, 5, 6, 10, 19, 29, 33–36, 38, 39, 73, 75, 82, 84, 88, 115

FIB focused ion-beam. 29–31

FSR free spectral range. 45

FWHM full width at half maximum. 45–48, 59, 68, 70, 115

FWM four-wave mixing. 68–72

GRIN gradient index. 29, 30, 37, 38, 81, 117

HBT Hanbury Brown & Twiss. 40, 64

HWHM half width at half maximum. 60

HWP half-wave plate. 38–40

IRF instrument response function. 48–50, 66, 67

ISC inter-system crossing. 6

LED light-emitting diode. 38, 118

ND neutral density. vi, 38, 40, 54, 113, 114

PAH polyaromatic hydrocarbon. 5

PBS polarizing beamsplitter. 35, 38, 39

PID proportional-integral-differential controller. vi, 39, 42, 113

PSN piezoelectric slip-stick nanopositioner. 36, 37

QuTiP Quantum Toolbox in Python. 21, 25, 26, 110

QWP quarter-wave plate. 38–40, 42

REI rare-earth ion. 94

ROC radius of curvature. 31

sCMOS scientific complementary metal-oxide-semiconductor. 40

SiV silicon vacancy center. 85, 86

TTL transistor-transistor logic. 50

B Vacuum Picture Transformation

The molecule-cavity system evolves according to the Lindblad equation

$$\partial_t \rho = -i\left[\frac{\hat{H}(t)}{\hbar}, \rho\right] + \mathscr{L}_\kappa(\rho) + \mathscr{L}_\gamma(\rho) + \mathscr{L}_{\gamma_{et}}(\rho) + \mathscr{L}_{\gamma_{tg}}(\rho) \tag{B.1}$$

with (see Eq. 2.42)

$$\frac{\hat{H}(t)}{\hbar} = (\omega_e - \omega_L)\,\hat{\rho}_{ee} + (\omega_c - \omega_L)\,\hat{a}^\dagger\hat{a} + g\left(\hat{\sigma}_+\hat{a} + \hat{\sigma}_-\hat{a}^\dagger\right) + \Xi(t)\,\hat{a} + \Xi^*(t)\,\hat{a}^\dagger \tag{B.2}$$

and (see Eq. 2.25c)

$$\mathscr{L}_\kappa(\rho) = \kappa\left(\hat{a}\rho\hat{a}^\dagger - \frac{1}{2}\left(\hat{a}^\dagger\hat{a}\rho + \rho\hat{a}^\dagger\hat{a}\right)\right). \tag{B.3}$$

$\mathscr{L}_\gamma(\rho)$ (see Eq. 2.25b), $\mathscr{L}_{\gamma_{et}}(\rho)$ (see Eq. 2.47a) and $\mathscr{L}_{\gamma_{tg}}(\rho)$ (see Eq. 2.47b) are not considered in this transformation, as they only affect the state of the molecule, not the photonic state.

B.1 Properties of the Displacement Operator

We aim to transform the equation of motion by displacing the photonic part of the density matrix ρ and the photonic operators $\hat{a}$, $\hat{a}^\dagger$ with the amplitude of the coherent $\alpha(t)$ field in the driven empty cavity. The value of $\alpha(t)$ depends on the driving strength of the cavity $\Xi(t)$, as in Eqs. B.12 and B.13. For this, we use the *displacement operator*

$$\hat{\mathscr{D}}(\alpha(t)) = \exp\left(\hat{a}^\dagger\alpha(t) - \alpha^*(t)\hat{a}\right), \tag{B.4}$$

which has the following properties:

$$\hat{\mathscr{D}}^\dagger(\alpha(t))\,\hat{a}\hat{\mathscr{D}}(\alpha(t)) = \hat{a} + \alpha(t) \tag{B.5a}$$

$$\hat{\mathscr{D}}^\dagger(\alpha(t))\,\hat{a}^\dagger\hat{\mathscr{D}}(\alpha(t)) = \hat{a}^\dagger + \alpha^*(t) \tag{B.5b}$$

$$\hat{\mathscr{D}}^\dagger(\alpha(t))\left(\hat{A}\hat{B}\right)\hat{\mathscr{D}}(\alpha(t)) = \hat{\mathscr{D}}^\dagger(\alpha(t))\,\hat{A}\hat{\mathscr{D}}(\alpha(t))\,\hat{\mathscr{D}}^\dagger(\alpha(t))\,\hat{B}\hat{\mathscr{D}}(\alpha(t)) \tag{B.5c}$$

$$\hat{\mathscr{D}}^\dagger(\alpha(t)) = \hat{\mathscr{D}}(-\alpha(t)) \tag{B.5d}$$

$$\hat{\mathscr{D}}^\dagger(\alpha(t))\,\rho\hat{\mathscr{D}}(\alpha(t)) =: \rho_v \tag{B.5e}$$

$$\partial_t\hat{\mathscr{D}}(\alpha(t)) = \hat{\mathscr{D}}(\alpha(t))\left(\left(\hat{a}^\dagger + \tfrac{1}{2}\alpha^*(t)\right)\dot{\alpha}(t) - \dot{\alpha}^*(t)\left(\hat{a} + \tfrac{1}{2}\alpha(t)\right)\right) \tag{B.5f}$$

B.2 Transformation

We apply the displacement operator to each part of the equation of motion and rewrite it in the same form as Eq. B.1.

Evolution of the Vacuum Picture Density Matrix

We first evaluate the temporal derivative of the transformed density matrix ρ_v, as this will be the left-hand side of the transformed equation of motion.

$$\partial_t \rho_v = \partial_t \left(\hat{\mathscr{D}}^\dagger(\alpha(t))\, \rho \hat{\mathscr{D}}(\alpha(t)) \right) \tag{B.6a}$$

$$\begin{aligned} &= \left(\partial_t \hat{\mathscr{D}}^\dagger(\alpha(t)) \right) \rho \hat{\mathscr{D}}(\alpha(t)) \\ &\quad + \hat{\mathscr{D}}^\dagger(\alpha(t)) \left(\partial_t \rho \right) \hat{\mathscr{D}}(\alpha(t)) \\ &\quad + \hat{\mathscr{D}}^\dagger(\alpha(t))\, \rho \left(\partial_t \hat{\mathscr{D}}(\alpha(t)) \right) \end{aligned} \tag{B.6b}$$

We use properties B.5d and B.5f on the first summand and B.5f on the third summand.

$$\begin{aligned} \partial_t \rho_v = &\hat{\mathscr{D}}^\dagger(\alpha(t)) \left(\left(\hat{a}^\dagger - \tfrac{1}{2}\alpha^*(t) \right) (-\dot{\alpha}(t)) - \dot{\alpha}^*(t) \left(\hat{a} - \tfrac{1}{2}\alpha(t) \right) \right) \rho \hat{\mathscr{D}}(\alpha(t)) \\ &+ \hat{\mathscr{D}}^\dagger(\alpha(t)) \left(\partial_t \rho \right) \hat{\mathscr{D}}(\alpha(t)) \\ &+ \hat{\mathscr{D}}^\dagger(\alpha(t))\, \rho \hat{\mathscr{D}}(\alpha(t)) \left(\left(\hat{a}^\dagger + \tfrac{1}{2}\alpha^*(t) \right) \dot{\alpha}(t) - \dot{\alpha}^*(t) \left(\hat{a} + \tfrac{1}{2}\alpha(t) \right) \right) \end{aligned} \tag{B.6c}$$

In the first summand we insert the identity $\hat{\mathscr{D}}(\alpha(t))\hat{\mathscr{D}}^\dagger(\alpha(t)) = \mathbb{1}$ (see B.5c) before ρ and apply definition B.5e. In the third summand we also transform ρ according to B.5e.

$$\begin{aligned} \partial_t \rho_v = &\hat{\mathscr{D}}^\dagger(\alpha(t)) \left(\left(\hat{a}^\dagger - \tfrac{1}{2}\alpha^*(t) \right) (-\dot{\alpha}(t)) - \dot{\alpha}^*(t) \left(\hat{a} - \tfrac{1}{2}\alpha(t) \right) \right) \hat{\mathscr{D}}(\alpha(t))\, \rho_v \\ &+ \hat{\mathscr{D}}^\dagger(\alpha(t)) \left(\partial_t \rho \right) \hat{\mathscr{D}}(\alpha(t)) \\ &+ \rho_v \left(\left(\hat{a}^\dagger + \tfrac{1}{2}\alpha^*(t) \right) \dot{\alpha}(t) - \dot{\alpha}^*(t) \left(\hat{a} + \tfrac{1}{2}\alpha(t) \right) \right) \end{aligned} \tag{B.6d}$$

We then transform $\hat{a}$ and $\hat{a}^\dagger$ in the first summand according to B.5a and B.5b, respectively.

$$\begin{aligned} \partial_t \rho_v = &\left(\left(\left(\hat{a}^\dagger + \alpha^*(t) \right) - \tfrac{1}{2}\alpha^*(t) \right) (-\dot{\alpha}(t)) - \dot{\alpha}^*(t) \left((\hat{a} + \alpha(t)) - \tfrac{1}{2}\alpha(t) \right) \right) \rho_v \\ &+ \hat{\mathscr{D}}^\dagger(\alpha(t)) \left(\partial_t \rho \right) \hat{\mathscr{D}}(\alpha(t)) \\ &+ \rho_v \left(\left(\hat{a}^\dagger + \tfrac{1}{2}\alpha^*(t) \right) \dot{\alpha}(t) - \dot{\alpha}^*(t) \left(\hat{a} + \tfrac{1}{2}\alpha(t) \right) \right) \end{aligned} \tag{B.6e}$$

With some rearrangement of the first summand

$$\begin{aligned} \partial_t \rho_v = &- \left(\left(\hat{a}^\dagger + \tfrac{1}{2}\alpha^*(t) \right) \dot{\alpha}(t) - \dot{\alpha}^*(t) \left(\hat{a} + \tfrac{1}{2}\alpha(t) \right) \right) \rho_v \\ &+ \hat{\mathscr{D}}^\dagger(\alpha(t)) \left(\partial_t \rho \right) \hat{\mathscr{D}}(\alpha(t)) \\ &+ \rho_v \left(\left(\hat{a}^\dagger + \tfrac{1}{2}\alpha^*(t) \right) \dot{\alpha}(t) - \dot{\alpha}^*(t) \left(\hat{a} + \tfrac{1}{2}\alpha(t) \right) \right) \end{aligned} \tag{B.6f}$$

we can merge the first and third summands and write

$$\begin{aligned}\partial_t \rho_v = &\hat{\mathscr{D}}^\dagger(\alpha(t))\left(\partial_t \rho\right)\hat{\mathscr{D}}(\alpha(t)) \\ &- \left[\left(\hat{a}^\dagger + \tfrac{1}{2}\alpha^*(t)\right)\dot{\alpha}(t) - \dot{\alpha}^*(t)\left(\hat{a} + \tfrac{1}{2}\alpha(t)\right), \rho_v\right].\end{aligned} \tag{B.6g}$$

Hence, transforming the left-hand side of the equation of motion B.1 results in

$$\hat{\mathscr{D}}^\dagger(\alpha(t))\left(\partial_t \rho\right)\hat{\mathscr{D}}(\alpha(t)) = \partial_t \rho_v + \left[\left(\hat{a}^\dagger + \tfrac{1}{2}\alpha^*(t)\right)\dot{\alpha}(t) - \dot{\alpha}^*(t)\left(\hat{a} + \tfrac{1}{2}\alpha(t)\right), \rho_v\right]. \tag{B.7}$$

Cavity Decay Term

On the right-hand side of the equation of motion we transform the Hamiltonian part and the cavity decay term $\mathscr{L}_\kappa(\rho)$. For the decay term

$$\begin{aligned}&\hat{\mathscr{D}}^\dagger(\alpha(t))\mathscr{L}_\kappa(\rho)\hat{\mathscr{D}}(\alpha(t)) \\ &\quad = \hat{\mathscr{D}}^\dagger(\alpha(t))\,\tfrac{\kappa}{2}\left(2\hat{a}\rho\hat{a}^\dagger - \hat{a}^\dagger\hat{a}\rho - \rho\hat{a}^\dagger\hat{a}\right)\hat{\mathscr{D}}(\alpha(t))\end{aligned} \tag{B.8a}$$

we transform all occurrences of $\hat{a}$, $\hat{a}^\dagger$ and ρ according to B.5a, B.5b and B.5e

$$\begin{aligned}&= \tfrac{\kappa}{2}\Big(2\left(\hat{a} + \alpha(t)\right)\rho_v\left(\hat{a}^\dagger + \alpha^*(t)\right) \\ &\quad - \left(\hat{a}^\dagger + \alpha^*(t)\right)\left(\hat{a} + \alpha(t)\right)\rho_v \\ &\quad - \rho_v\left(\hat{a}^\dagger + \alpha^*(t)\right)\left(\hat{a} + \alpha(t)\right)\Big)\end{aligned} \tag{B.8b}$$

and expand the products.

$$\begin{aligned}&= \tfrac{\kappa}{2}\Big(2\hat{a}\rho_v\hat{a}^\dagger + 2\hat{a}\rho_v\alpha^*(t) + 2\alpha(t)\rho_v\hat{a}^\dagger + 2\alpha(t)\rho_v\alpha^*(t) \\ &\quad - \hat{a}^\dagger\hat{a}\rho_v - \hat{a}^\dagger\alpha(t)\rho_v - \alpha^*(t)\hat{a}\rho_v - \alpha^*(t)\alpha(t)\rho_v \\ &\quad - \rho_v\hat{a}^\dagger\hat{a} - \rho_v\hat{a}^\dagger\alpha(t) - \rho_v\alpha^*(t)\hat{a} - \rho_v\alpha^*(t)\alpha(t)\Big)\end{aligned} \tag{B.8c}$$

The blue terms form $\mathscr{L}_\kappa(\rho_v)$, the red terms cancel and the green and magenta terms cancel partially.

$$= \mathscr{L}_\kappa(\rho_v) + \tfrac{\kappa}{2}\left(\hat{a}\rho_v\alpha^*(t) + \alpha(t)\rho_v\hat{a}^\dagger - \hat{a}^\dagger\alpha(t)\rho_v - \rho_v\alpha^*(t)\hat{a}\right) \tag{B.8d}$$

We can rearrange this into a commutator.

$$\begin{aligned}&= \mathscr{L}_\kappa(\rho_v) + \tfrac{\kappa}{2}\left(\alpha^*(t)\left[\hat{a}, \rho_v\right] - \alpha(t)\left[\hat{a}^\dagger, \rho_v\right]\right) \\ &= \mathscr{L}_\kappa(\rho_v) + \tfrac{\kappa}{2}\left[\alpha^*(t)\hat{a} - \alpha(t)\hat{a}^\dagger, \rho_v\right]\end{aligned} \tag{B.8e}$$

Hamiltonian Evolution

We use tranformations B.5a, B.5b and B.5e on the Hamiltonian part to obtain

$$\begin{aligned}
&\hat{\mathscr{D}}^{\dagger}(\alpha(t))\left[\frac{\hat{H}}{\hbar},\rho\right]\hat{\mathscr{D}}(\alpha(t)) \\
&\quad=\Big[(\omega_e-\omega_L)\,\hat{\rho}_{ee}+(\omega_c-\omega_L)\left(\hat{a}^{\dagger}+\alpha^*(t)\right)(\hat{a}+\alpha(t)) \\
&\qquad+g\left(\hat{\sigma}_+(\hat{a}+\alpha(t))+\hat{\sigma}_-\left(\hat{a}^{\dagger}+\alpha^*(t)\right)\right) \\
&\qquad+\Xi(t)(\hat{a}+\alpha(t))+\Xi^*(t)\left(\hat{a}^{\dagger}+\alpha^*(t)\right),\rho_v\Big].
\end{aligned} \tag{B.9}$$

Merging the Parts

We then use the transformed parts from Eqs. B.6g, B.8e and B.9 and rearrange them into the form of a Lindblad equation (Eq. B.1).

$$\begin{aligned}
\partial_t\rho_v=&-i\Big[(\omega_e-\omega_L)\,\hat{\rho}_{ee}+(\omega_c-\omega_L)\left(\hat{a}^{\dagger}+\alpha^*(t)\right)(\hat{a}+\alpha(t)) \\
&\qquad+g\left(\hat{\sigma}_+(\hat{a}+\alpha(t))+\hat{\sigma}_-\left(\hat{a}^{\dagger}+\alpha^*(t)\right)\right) \\
&\qquad+\Xi(t)(\hat{a}+\alpha(t))+\Xi^*(t)\left(\hat{a}^{\dagger}+\alpha^*(t)\right),\rho_v\Big] \\
&-\left[\left(\hat{a}^{\dagger}+\tfrac{1}{2}\alpha^*(t)\right)\dot{\alpha}(t)-\dot{\alpha}^*(t)\left(\hat{a}+\tfrac{1}{2}\alpha(t)\right),\rho_v\right] \\
&+\tfrac{\kappa}{2}\left[\alpha^*(t)\hat{a}-\alpha(t)\hat{a}^{\dagger},\rho_v\right] \\
&+\mathscr{L}_{\kappa}(\rho_v)+\mathscr{L}_{\gamma}(\rho_v)+\mathscr{L}_{\gamma_{et}}(\rho_v)+\mathscr{L}_{\gamma_{tg}}(\rho_v).
\end{aligned} \tag{B.10a}$$

We merge the commutators, expand some products

$$\begin{aligned}
=&-i\Big[(\omega_e-\omega_L)\,\hat{\rho}_{ee}+(\omega_c-\omega_L)\left(\hat{a}^{\dagger}\hat{a}+\hat{a}^{\dagger}\alpha(t)+\alpha^*(t)\hat{a}+|\alpha(t)|^2\right) \\
&\qquad+g\left(\hat{\sigma}_+(\hat{a}+\alpha(t))+\hat{\sigma}_-\left(\hat{a}^{\dagger}+\alpha^*(t)\right)\right) \\
&\qquad+\Xi(t)\hat{a}+\Xi(t)\alpha(t)+\Xi^*(t)\hat{a}^{\dagger}+\Xi^*(t)\alpha^*(t) \\
&\qquad-i\hat{a}^{\dagger}\dot{\alpha}(t)-\tfrac{i}{2}\alpha^*(t)\dot{\alpha}(t)+i\dot{\alpha}^*(t)\hat{a}+\tfrac{i}{2}\dot{\alpha}^*(t)\alpha(t) \\
&\qquad+\tfrac{i}{2}\kappa\left(\alpha^*(t)\hat{a}-\alpha(t)\hat{a}^{\dagger}\right),\rho_v\Big] \\
&+\mathscr{L}_{\kappa}(\rho_v)+\mathscr{L}_{\gamma}(\rho_v)+\mathscr{L}_{\gamma_{et}}(\rho_v)+\mathscr{L}_{\gamma_{tg}}(\rho_v).
\end{aligned} \tag{B.10b}$$

and find that some scalar summands only contribute to a global phase and can be removed.

$$
\begin{aligned}
&= -i\Big[(\omega_e-\omega_L)\,\hat{\rho}_{ee} + (\omega_c-\omega_L)\left(\hat{a}^\dagger\hat{a} + \hat{a}^\dagger\alpha(t) + \alpha^*(t)\hat{a}\right) \\
&\qquad + g\left(\hat{\sigma}_+\left(\hat{a}+\alpha(t)\right) + \hat{\sigma}_-\left(\hat{a}^\dagger+\alpha^*(t)\right)\right) \\
&\qquad + \Xi(t)\hat{a} + \Xi^*(t)\hat{a}^\dagger - i\hat{a}^\dagger\dot{\alpha}(t) + i\dot{\alpha}^*(t)\hat{a} \\
&\qquad + \tfrac{i}{2}\kappa\left(\alpha^*(t)\hat{a} - \alpha(t)\hat{a}^\dagger\right), \rho_v\Big] \\
&\quad + \mathcal{L}_\kappa(\rho_v) + \mathcal{L}_\gamma(\rho_v) + \mathcal{L}_{\gamma_{et}}(\rho_v) + \mathcal{L}_{\gamma_{tg}}(\rho_v).
\end{aligned}
\tag{B.10c}
$$

We define the *vacuum picture Hamiltonian* $\hat{H}_v$ from the first part of the above commutator

$$
\partial_t\rho_v =: -i\left[\frac{\hat{H}_v}{\hbar}, \rho_v\right] + \mathcal{L}_\kappa(\rho_v) + \mathcal{L}_\gamma(\rho_v) + \mathcal{L}_{\gamma_{et}}(\rho_v) + \mathcal{L}_{\gamma_{tg}}. \tag{B.10d}
$$

Relation between $\alpha(t)$ and $\Xi(t)$

In this form, the Hamiltonian contains both the cavity driving strength $\Xi(t)$ and the coherent field amplitude $\alpha(t)$, which builds up in the cavity due to the driving. To find the connection between these quantities we compute $\dot{\hat{a}}$ for an empty cavity ($g=0$, $\hat{\rho}_{ee}=0$) in the Heisenberg picture:

$$
\dot{\hat{a}} = i\left[\frac{\hat{H}_v}{\hbar}, \hat{a}\right] + \mathcal{L}_\kappa(\hat{a}) \tag{B.11a}
$$

$$
\begin{aligned}
&= i\Big[(\omega_c-\omega_L)\left(\hat{a}^\dagger\hat{a} + \hat{a}^\dagger\alpha(t) + \alpha^*(t)\hat{a}\right) + \Xi(t)\hat{a} + \Xi^*(t)\hat{a}^\dagger \\
&\qquad - i\hat{a}^\dagger\dot{\alpha}(t) + i\dot{\alpha}^*(t)\hat{a} + \tfrac{i}{2}\kappa\left(\alpha^*(t)\hat{a} - \alpha(t)\hat{a}^\dagger\right), \hat{a}\Big] \\
&\quad + \kappa\left(\hat{a}^\dagger\hat{a}\hat{a} - \tfrac{1}{2}\left(\hat{a}^\dagger\hat{a}\hat{a} + \hat{a}\hat{a}^\dagger\hat{a}\right)\right)
\end{aligned}
\tag{B.11b}
$$

In the commutator, terms with only $\hat{a}$ drop out, because $[\hat{a},\hat{a}]=0$. Using $\left[\hat{a}^\dagger,\hat{a}\right]=-1$ and $\left[\hat{a}^\dagger\hat{a},\hat{a}\right] = \left[\hat{a}^\dagger,\hat{a}\right]\hat{a} = -\hat{a}$, the rest reduces to

$$
\dot{\hat{a}} = -i\left((\omega_c-\omega_L)\left(\tfrac{1}{2}\hat{a}+\alpha(t)\right) + \Xi^*(t) - i\dot{\alpha}(t) - \tfrac{i}{2}\kappa\alpha(t)\right) - \tfrac{\kappa}{2}\hat{a}. \tag{B.11c}
$$

In an empty cavity there is only the coherent field $|\alpha(t)\rangle$. Hence the transformed field operator is $\hat{a}=0$, as is its derivative $\dot{\hat{a}}=0$. Using this, we can eliminate all operators from Eq. B.11c and find that

$$
\begin{aligned}
&0 = (\omega_c-\omega_L)\,\alpha(t) + \Xi^*(t) - i\dot{\alpha}(t) - \tfrac{i}{2}\kappa\alpha(t) \\
\Leftrightarrow\quad &\Xi^*(t) = i\dot{\alpha}(t) + \left(\tfrac{i}{2}\kappa - (\omega_c-\omega_L)\right)\alpha(t)
\end{aligned}
\tag{B.12}
$$

or

$$\Leftrightarrow \quad \alpha(t) = e^{-i(\omega_c-\omega_L)t-\frac{\kappa t}{2}}\left(\alpha(-\infty) - i\int_{-\infty}^{t}\Xi^*(\tau)e^{i(\omega_c-\omega_L)\tau+\frac{\kappa\tau}{2}}\,d\tau\right). \tag{B.13}$$

Simplify the Hamiltonian

We can insert Eq. B.12 and its complex conjugate into the Hamiltonian as defined by Eqs. B.10c and B.10d.

$$\begin{aligned}
\frac{\hat{H}_v}{\hbar} &= \tfrac{1}{2}(\omega_e-\omega_L)\hat{\rho}_{ee} + (\omega_c-\omega_L)\left(\hat{a}^\dagger\hat{a} + \hat{a}^\dagger\alpha(t) + \alpha^*(t)\hat{a}\right) \\
&\quad + g\left(\hat{\sigma}_+(\hat{a}+\alpha(t)) + \hat{\sigma}_-\left(\hat{a}^\dagger+\alpha^*(t)\right)\right) \\
&\quad - \left(i\dot{\alpha}^*(t) + \left(\tfrac{i}{2}\kappa + (\omega_c-\omega_L)\right)\alpha^*(t)\right)\hat{a} + \left(i\dot{\alpha}(t) + \left(\tfrac{i}{2}\kappa - (\omega_c-\omega_L)\right)\alpha(t)\right)\hat{a}^\dagger \\
&\quad - i\hat{a}^\dagger\dot{\alpha}(t) + i\dot{\alpha}^*(t)\hat{a} + \tfrac{i}{2}\kappa\left(\alpha^*(t)\hat{a} - \alpha(t)\hat{a}^\dagger\right)
\end{aligned} \tag{B.14a}$$

$$\begin{aligned}
&= \tfrac{1}{2}(\omega_e-\omega_L)\hat{\rho}_{ee} + (\omega_c-\omega_L)\hat{a}^\dagger\hat{a} + (\omega_c-\omega_L)\hat{a}^\dagger\alpha(t) + (\omega_c-\omega_L)\alpha^*(t)\hat{a} \\
&\quad + g\left(\hat{\sigma}_+(\hat{a}+\alpha(t)) + \hat{\sigma}_-\left(\hat{a}^\dagger+\alpha^*(t)\right)\right) \\
&\quad - i\dot{\alpha}^*(t)\hat{a} - \tfrac{i}{2}\kappa\alpha^*(t)\hat{a} - (\omega_c-\omega_L)\alpha^*(t)\hat{a} \\
&\quad + i\dot{\alpha}(t)\hat{a}^\dagger + \tfrac{i}{2}\kappa\alpha(t)\hat{a}^\dagger - (\omega_c-\omega_L)\alpha(t)\hat{a}^\dagger \\
&\quad - i\hat{a}^\dagger\dot{\alpha}(t) + i\dot{\alpha}^*(t)\hat{a} + \tfrac{i}{2}\kappa\alpha^*(t)\hat{a} - \tfrac{i}{2}\kappa\alpha(t)\hat{a}^\dagger
\end{aligned} \tag{B.14b}$$

All colored terms cancel, simplifying the Hamiltonian to

$$\frac{\hat{H}_v}{\hbar} = \tfrac{1}{2}(\omega_e-\omega_L)\hat{\rho}_{ee} + (\omega_c-\omega_L)\hat{a}^\dagger\hat{a} + g\left(\hat{\sigma}_+(\hat{a}+\alpha(t)) + \hat{\sigma}_-\left(\hat{a}^\dagger+\alpha^*(t)\right)\right). \tag{B.14c}$$

B.3 Coherent Field Strength

For concrete experimental realizations we can calculate $\alpha(t)$. In this thesis we use three different excitation schemes: Single-frequency continuous drive, two-frequency continuous drive and pulsed excitation.

Single-Frequency Excitation

If only one laser beam drives the cavity at constant strength $\Xi^* = \frac{1}{2}\sqrt{I_{\text{in}}\kappa}$, where I_{in} is the rate of photons hitting the cavity, we can use Eq. B.12 without the time-dependence ($\alpha(t) = \alpha$, $\Xi^*(t) = \Xi^*$, $\dot{\alpha}(t) = 0$) and solve for α, giving

$$\alpha = \frac{\Xi^*}{\frac{i}{2}\kappa - (\omega_c-\omega_L)}. \tag{B.15}$$

Two-Frequency Excitation

When two lasers of different frequencies ω_{pump}, ω_{probe} drive the cavity simultaneously, there is no rotating frame, in which $\Xi^*(t)$ is time-independent. To remove the rotating phase from at least one of the beams, we set $\omega_{\text{pump}} = \omega_L$. Then the driving strength is

$$\Xi^*(t) = \Xi^*_{\text{pump}} + \Xi^*_{\text{probe}} e^{-i(\omega_{\text{probe}} - \omega_{\text{pump}})t}. \tag{B.16}$$

We can show that

$$\alpha(t) = \alpha_{\text{pump}} + \alpha_{\text{probe}} e^{-i(\omega_{\text{probe}} - \omega_{\text{pump}})t} \tag{B.17}$$

fulfills Eq. B.12:

$$\begin{aligned}
\Xi^*(t) &= \Xi^*_{\text{pump}} + \Xi^*_{\text{probe}} e^{-i(\omega_{\text{probe}} - \omega_{\text{pump}})t} && \text{(B.18a)}\\
&\stackrel{!}{=} i\dot{\alpha}(t) + \left(\tfrac{i}{2}\kappa - \left(\omega_c - \omega_{\text{pump}}\right)\right)\alpha(t) && \text{(B.18b)}\\
&= i\alpha_{\text{probe}}\left(-i\left(\omega_{\text{probe}} - \omega_{\text{pump}}\right)\right) e^{-i(\omega_{\text{probe}} - \omega_{\text{pump}})t} \\
&\quad + \left(\tfrac{i}{2}\kappa - \left(\omega_c - \omega_{\text{pump}}\right)\right)\left(\alpha_{\text{pump}} + \alpha_{\text{probe}} e^{-i(\omega_{\text{probe}} - \omega_{\text{pump}})t}\right) \\
&= \alpha_{\text{probe}} e^{-i(\omega_{\text{probe}} - \omega_{\text{pump}})t}\left(\left(\omega_{\text{probe}} - \omega_{\text{pump}}\right) + \tfrac{i}{2}\kappa - \left(\omega_c - \omega_{\text{pump}}\right)\right) && \text{(B.18c)}\\
&\quad + \alpha_{\text{pump}}\left(\tfrac{i}{2}\kappa - \left(\omega_c - \omega_{\text{pump}}\right)\right) \\
&= \alpha_{\text{probe}} e^{-i(\omega_{\text{probe}} - \omega_{\text{pump}})t}\left(\tfrac{i}{2}\kappa - \left(\omega_c - \omega_{\text{probe}}\right)\right) && \text{(B.18d)}\\
&\quad + \alpha_{\text{pump}}\left(\tfrac{i}{2}\kappa - \left(\omega_c - \omega_{\text{pump}}\right)\right)
\end{aligned}$$

We can extract α_{pump} and α_{probe} from Eq. B.18d by separating the time-independent terms from those rotating at $e^{-i(\omega_{\text{probe}} - \omega_{\text{pump}})t}$:

$$\begin{aligned}
&\Xi^*_{\text{pump}} = \alpha_{\text{pump}}\left(\tfrac{i}{2}\kappa - \left(\omega_c - \omega_{\text{pump}}\right)\right) && \text{(B.19a)}\\
\Leftrightarrow\quad &\alpha_{\text{pump}} = \frac{\Xi^*_{\text{pump}}}{\tfrac{i}{2}\kappa - \left(\omega_c - \omega_{\text{pump}}\right)} \\
&\Xi^*_{\text{probe}} = \alpha_{\text{probe}}\left(\tfrac{i}{2}\kappa - \left(\omega_c - \omega_{\text{probe}}\right)\right) && \text{(B.19b)}\\
\Leftrightarrow\quad &\alpha_{\text{probe}} = \frac{\Xi^*_{\text{probe}}}{\tfrac{i}{2}\kappa - \left(\omega_c - \omega_{\text{probe}}\right)}
\end{aligned}$$

Pulsed Excitation

If the input is a Gaussian pulse of duration T

$$I_{\text{in}}(t) = \frac{(2A)^2}{\kappa} \exp\left(-\frac{t^2}{2T^2}\right) \tag{B.20}$$

and center frequency ω_L, the driving strength is

$$\Xi^*(t) = \tfrac{1}{2}\sqrt{I_{\text{in}}(t)\kappa} = A\exp\left(-\frac{t^2}{4T^2}\right). \tag{B.21}$$

We can calculate $\alpha(t)$ using Eq. B.13:

$$\begin{aligned}
\alpha(t) &= e^{-i(\omega_c-\omega_L)t-\frac{\kappa t}{2}}\left(\alpha(-\infty) - i\int_{-\infty}^{t}\Xi^*(\tau)e^{i(\omega_c-\omega_L)\tau+\frac{\kappa\tau}{2}}\,d\tau\right) \\
&= -iAe^{-i(\omega_c-\omega_L)t-\frac{\kappa t}{2}}\int_{-\infty}^{t} e^{i(\omega_c-\omega_L)\tau+\frac{\kappa\tau}{2}-\frac{\tau^2}{4T^2}}\,d\tau \\
&= -i\sqrt{\pi}ATe^{-i(\omega_c-\omega_L)t-\frac{\kappa t}{2}+\left(i(\omega_c-\omega_L)+\frac{\kappa}{2}\right)^2}\left(1+\operatorname{erf}\left(\frac{t}{2T}-\frac{\kappa T}{2}-i\left(\omega_c-\omega_L\right)T\right)\right)
\end{aligned} \tag{B.22}$$

We use the same definition of the error function

$$\int_{-\infty}^{t}\exp\left(-\frac{\tau^2}{2T^2}\right)d\tau =: \sqrt{\frac{\pi}{2}}T\left(1+\operatorname{erf}\left(\frac{t}{\sqrt{2}T}\right)\right) \tag{B.23}$$

as the Python implementation in `scipy.special.erf(z)` (version 1.9.0).

C Further Derivations

C.1 Polarization Rotation in a Birefringent Crystal

Without loss of generality, we choose the coordinate system such that the incident laser beam is polarized along the x-axis. Its electric field vector is therefore

$$\vec{E}_{\text{inc}} = \begin{pmatrix} E_{\text{inc},x} \\ 0 \end{pmatrix}. \tag{C.1}$$

When passing twice through a birefringent crystal of thickness d, this vector is transformed according to Eq. 4.9 in [225]

$$\begin{aligned} \vec{E}_{\text{refl}} &= \begin{pmatrix} e^{i\delta}\cos^2\theta + \sin^2\theta & \left(e^{i\delta}-1\right)\sin\theta\cos\theta \\ \left(e^{i\delta}-1\right)\sin\theta\cos\theta & e^{i\delta}\sin^2\theta + \cos^2\theta \end{pmatrix} \vec{E}_{\text{inc}} \\ &= \begin{pmatrix} e^{i\delta}\cos^2\theta + \sin^2\theta \\ \left(e^{i\delta}-1\right)\sin\theta\cos\theta \end{pmatrix} E_{\text{inc},x}, \end{aligned} \tag{C.2}$$

resulting in the polarization vector $\vec{E}_{\text{refl}}$ of the reflected light. θ denotes the angle between the polarization of the incident light and the slow axis of the crystal, and $\delta = 2\pi(n_b - n_a)\frac{2d}{\lambda}$ is the phase difference between the a- and b-polarized parts of the beam accumulated during the propagation through the crystal over a distance $2d$. The x-component of the reflected beam is filtered out by the cross-polarizer; we detect only the intensity of the y-polarized component. This is a fraction

$$\begin{aligned} \frac{I_{\text{refl},y}}{I_{\text{inc}}} &= \frac{\left|E_{\text{refl},y}\right|^2}{\left|E_{\text{inc},x}\right|^2} = \left|\left(e^{i\delta}-1\right)\sin\theta\cos\theta\right|^2 = \left(2\sin\tfrac{\delta}{2}\sin\theta\cos\theta\right)^2 \\ &= \left(2\sin\theta\cos\theta\sin\left(2\pi(n_b-n_a)\frac{d}{\lambda}\right)\right)^2 \end{aligned} \tag{C.3}$$

of the incident intensity I_{inc}.

C.2 Reduction of the Measured $g^{(2)}(\tau)$ Value due to Background

We use the classical definition of $g^{(2)}(\tau)$ based on the time-dependent intensity $I(t)$

$$g^{(2)}(\tau) := \frac{\langle I(t)I(t+\tau)\rangle}{\langle I(t)\rangle^2}. \tag{C.4}$$

The overall intensity has three contributions

$$I(t) = \bar{I}_{\text{sig}} + \Delta I_{\text{sig}}(t) + I_{\text{bkg}}, \tag{C.5}$$

the background I_{bkg}, the mean intensity of the signal $\bar{I}_{\mathrm{sig}}$ and its fluctuations around the mean value $\Delta I_{\mathrm{sig}}(t)$. We can substitute this expansion into the numerator of Eq. C.4:

$$\begin{aligned}\langle I(t)I(t+\tau)\rangle &= \left\langle \left(\bar{I}_{\mathrm{sig}} + \Delta I_{\mathrm{sig}}(t) + I_{\mathrm{bkg}}\right)\left(\bar{I}_{\mathrm{sig}} + \Delta I_{\mathrm{sig}}(t+\tau) + I_{\mathrm{bkg}}\right)\right\rangle \\ &= \left\langle \left(\bar{I}_{\mathrm{sig}} + I_{\mathrm{bkg}}\right)^2\right\rangle + \left\langle \left(\bar{I}_{\mathrm{sig}} + I_{\mathrm{bkg}}\right)\Delta I_{\mathrm{sig}}(t)\right\rangle + \left\langle \left(\bar{I}_{\mathrm{sig}} + I_{\mathrm{bkg}}\right)\Delta I_{\mathrm{sig}}(t+\tau)\right\rangle + \\ &\quad + \left\langle \Delta I_{\mathrm{sig}}(t)\Delta I_{\mathrm{sig}}(t+\tau)\right\rangle \end{aligned} \tag{C.6}$$

We further assume the background to be uncorrelated, i.e. $\left\langle I_{\mathrm{bkg}}^2\right\rangle = \left\langle I_{\mathrm{bkg}}\right\rangle^2 = I_{\mathrm{bkg}}^2$ and uncorrelated with the fluctuations of the signal, i.e. $\left\langle I_{\mathrm{bkg}}\Delta I_{\mathrm{sig}}(t)\right\rangle = I_{\mathrm{bkg}}\left\langle \Delta I_{\mathrm{sig}}(t)\right\rangle$. The separation of the signal into mean $\bar{I}_{\mathrm{sig}}$ and fluctuation $\Delta I_{\mathrm{sig}}(t)$ means that the average value of the fluctuations is zero, i.e. $\left\langle \Delta I_{\mathrm{sig}}(t)\right\rangle = 0$. We can therefore simplify the above expression to

$$\begin{aligned}\langle I(t)I(t+\tau)\rangle &= \left(\bar{I}_{\mathrm{sig}} + I_{\mathrm{bkg}}\right)^2 + \left(\bar{I}_{\mathrm{sig}} + I_{\mathrm{bkg}}\right)\overbrace{\left\langle \Delta I_{\mathrm{sig}}(t)\right\rangle}^{0} + \left(\bar{I}_{\mathrm{sig}} + I_{\mathrm{bkg}}\right)\overbrace{\left\langle \Delta I_{\mathrm{sig}}(t+\tau)\right\rangle}^{0} \\ &\quad + \left\langle \Delta I_{\mathrm{sig}}(t)\Delta I_{\mathrm{sig}}(t+\tau)\right\rangle \\ &= \left(\bar{I}_{\mathrm{sig}} + I_{\mathrm{bkg}}\right)^2 + \left\langle \Delta I_{\mathrm{sig}}(t)\Delta I_{\mathrm{sig}}(t+\tau)\right\rangle. \end{aligned} \tag{C.7}$$

Analogously, we can expand the denominator of Eq. C.4

$$\langle I(t)\rangle^2 = \left\langle \bar{I}_{\mathrm{sig}} + \Delta I_{\mathrm{sig}}(t) + I_{\mathrm{bkg}}\right\rangle^2 = \left(\bar{I}_{\mathrm{sig}} + \left\langle \Delta I_{\mathrm{sig}}(t)\right\rangle + I_{\mathrm{bkg}}\right)^2 = \left(\bar{I}_{\mathrm{sig}} + I_{\mathrm{bkg}}\right)^2. \tag{C.8}$$

Combining the numerator and denominator, the measured $g^{(2)}(\tau)$ is

$$\begin{aligned} g^{(2)}_{\mathrm{meas}}(\tau) &= \frac{\left(\bar{I}_{\mathrm{sig}} + I_{\mathrm{bkg}}\right)^2 + \left\langle \Delta I_{\mathrm{sig}}(t)\Delta I_{\mathrm{sig}}(t+\tau)\right\rangle}{\left(\bar{I}_{\mathrm{sig}} + I_{\mathrm{bkg}}\right)^2} = 1 + \frac{\left\langle \Delta I_{\mathrm{sig}}(t)\Delta I_{\mathrm{sig}}(t+\tau)\right\rangle}{\left(\bar{I}_{\mathrm{sig}} + I_{\mathrm{bkg}}\right)^2} \\ &= 1 + \frac{\frac{\left\langle \Delta I_{\mathrm{sig}}(t)\Delta I_{\mathrm{sig}}(t+\tau)\right\rangle}{\bar{I}_{\mathrm{sig}}^2}}{\frac{\left(\bar{I}_{\mathrm{sig}} + I_{\mathrm{bkg}}\right)^2}{\bar{I}_{\mathrm{sig}}^2}} = 1 + \frac{g^{(2)}_{\mathrm{act}}(\tau) - 1}{\left(\frac{\bar{I}_{\mathrm{sig}} + I_{\mathrm{bkg}}}{\bar{I}_{\mathrm{sig}}}\right)^2} = 1 + \frac{g^{(2)}_{\mathrm{act}}(\tau) - 1}{\left(1 + r_{\mathrm{bg/s}}\right)^2}. \end{aligned} \tag{C.9}$$

Here, we define the background-to-signal ratio $r_{\mathrm{bg/s}} := I_{\mathrm{bkg}}/\bar{I}_{\mathrm{sig}}$. Eq. C.9 can now be rearranged into the form of Eq. 5.8.

C.3 Difference between $G^{(1)}(\tau)$ and $\left\langle \hat{a}^\dagger \hat{a}\right\rangle(t)$

In the simulations of the four-wave mixing experiments, there seems to be a contradiction: While the time-domain simulation (Fig. 5.15) demonstrates clearly visible higher harmonics of the beating signal in the number of cavity photons $\left\langle \hat{a}^\dagger \hat{a}\right\rangle(t)$, in the spectrum $S(\nu)$ computed from the same simulation (Fig. 5.16) the power in the first higher harmonic is $2\frac{1}{2}$ orders of magnitude lower than that of the incident frequency. We can resolve this apparent inconsistency with a calculation of classical fields. Assuming the field in the cavity contains four

frequencies: $\pm\frac{1}{2}\Delta\nu$ and the four-wave mixing frequencies $\pm\frac{3}{2}\Delta\nu$,

$$\begin{aligned} E(t) &= A_0\left(e^{-2\pi i\cdot\frac{1}{2}\Delta\nu t} + e^{2\pi i\cdot\frac{1}{2}\Delta\nu t}\right) + A_{\mathrm{FWM}}\left(e^{-2\pi i\cdot\frac{3}{2}\Delta\nu t} + e^{2\pi i\cdot\frac{3}{2}\Delta\nu t}\right) \\ &= A_0\cos\left(2\pi\cdot\tfrac{1}{2}\Delta\nu t\right) + A_{\mathrm{FWM}}\cos\left(2\pi\cdot\tfrac{3}{2}\Delta\nu t\right). \end{aligned} \tag{C.10}$$

The spectrum $S(\nu)$ is the Fourier transform of $G^{(1)}(\tau)$ (see Ch. 2.4.3).

$$\begin{aligned} G^{(1)}(\tau) &= \lim_{\mathcal{T}\to\infty}\frac{1}{2\mathcal{T}}\int_{-\mathcal{T}}^{\mathcal{T}} E^*(t+\tau)E(t)\,dt \\ &= \lim_{\mathcal{T}\to\infty}\frac{1}{2\mathcal{T}}\int_{-\mathcal{T}}^{\mathcal{T}} \left(A_0^*\cos\left(2\pi\cdot\tfrac{1}{2}\Delta\nu(t+\tau)\right) + A_{\mathrm{FWM}}^*\cos\left(2\pi\cdot\tfrac{3}{2}\Delta\nu(t+\tau)\right)\right) \\ &\qquad\qquad \cdot\left(A_0\cos\left(2\pi\cdot\tfrac{1}{2}\Delta\nu t\right) + A_{\mathrm{FWM}}\cos\left(2\pi\cdot\tfrac{3}{2}\Delta\nu t\right)\right)dt \\ &= \lim_{\mathcal{T}\to\infty}\frac{1}{2\mathcal{T}}\int_{-\mathcal{T}}^{\mathcal{T}} \Big(2\left|A_0\right|^2\left(\cos\left(2\pi\cdot\tfrac{1}{2}\Delta\nu(2t+\tau)\right) + \cos\left(2\pi\cdot\tfrac{1}{2}\Delta\nu\tau\right)\right) \\ &\qquad\qquad + 2A_0A_{\mathrm{FWM}}^*\left(\cos\left(2\pi\cdot\tfrac{1}{2}\Delta\nu(4t+3\tau)\right) + \cos\left(2\pi\cdot\tfrac{1}{2}\Delta\nu(2t+3\tau)\right)\right) \\ &\qquad\qquad + 2A_0^*A_{\mathrm{FWM}}\left(\cos\left(2\pi\cdot\tfrac{1}{2}\Delta\nu(4t+\tau)\right) + \cos\left(2\pi\cdot\tfrac{1}{2}\Delta\nu(2t+\tau)\right)\right) \\ &\qquad\qquad + 2\left|A_{\mathrm{FWM}}\right|^2\left(\cos\left(2\pi\cdot\tfrac{3}{2}\Delta\nu(2t+\tau)\right) + \cos\left(2\pi\cdot\tfrac{3}{2}\Delta\nu\tau\right)\right)\Big)\,dt \\ &= 2\left|A_0\right|^2\cos\left(2\pi\cdot\tfrac{1}{2}\Delta\nu\tau\right) + 2\left|A_{\mathrm{FWM}}\right|^2\cos\left(2\pi\cdot\tfrac{3}{2}\Delta\nu\tau\right) \end{aligned} \tag{C.11}$$

The spectrum

$$S(\nu) = 2\left|A_0\right|^2\left(\delta(\nu-\tfrac{1}{2}\Delta\nu) + \delta(\nu+\tfrac{1}{2}\Delta\nu)\right) + 2\left|A_{\mathrm{FWM}}\right|^2\left(\delta(\nu-\tfrac{3}{2}\Delta\nu) + \delta(\nu+\tfrac{3}{2}\Delta\nu)\right), \tag{C.12}$$

therefore consists of four Dirac Delta functions $\delta(x)$. Hence, the power ratio of the four-wave mixing frequency and the incident frequency is $|A_{\mathrm{FWM}}|^2/|A_0|^2$. In contrast, the photon number expectation value $\langle\hat{a}^\dagger\hat{a}\rangle(t) \sim |E(t)|^2$

$$\begin{aligned} |E(t)|^2 &= \left(A_0^*\cos\left(2\pi\cdot\tfrac{1}{2}\Delta\nu t\right) + A_{\mathrm{FWM}}^*\cos\left(2\pi\cdot\tfrac{3}{2}\Delta\nu t\right)\right) \\ &\quad\cdot\left(A_0\cos\left(2\pi\cdot\tfrac{1}{2}\Delta\nu t\right) + A_{\mathrm{FWM}}\cos\left(2\pi\cdot\tfrac{3}{2}\Delta\nu t\right)\right) \\ &= 2\left|A_0\right|^2\left(1+\cos\left(2\pi\cdot\Delta\nu t\right)\right) \\ &\quad + 2\left(A_0^*A_{\mathrm{FWM}} + A_0A_{\mathrm{FWM}}^*\right)\left(\cos\left(2\pi\cdot\Delta\nu t\right) + \cos\left(2\pi\cdot 2\Delta\nu t\right)\right) \\ &\quad + 2\left|A_{\mathrm{FWM}}\right|^2\left(1+\cos\left(2\pi\cdot 3\Delta\nu t\right)\right) \end{aligned} \tag{C.13}$$

has a frequency component oscillating at twice the beating frequency $2\Delta\nu$ with an amplitude of $2\left(A_0^*A_{\mathrm{FWM}} + A_0A_{\mathrm{FWM}}^*\right)$. The $2\Delta\nu$ component is therefore amplified as in a heterodyne measurement [226].

D Compensation for Temporal Shifts in Acquired Data

In Ch. 3.5.2 we describe a detection scheme in which the vibration of the cavity is recorded alongside the APD signal and the wavemeter reading. If all three signals are synchronous, we can extract cavity transmission spectra for a range of different cavity resonance frequencies ω_c from one dataset. However, due to the finite bandwidth of the balanced photodiode, the error signal is slightly delayed with respect to the APD signal. Since both signals are recorded by the same DAQ card, this delay Δt_{err} is constant across measurements and can therefore be calibrated. In contrast, the delay in the wavemeter reading Δt_{wm} fluctuates between measurements. This is because the wavemeter samples the laser frequency independently of the measurement program. The delay Δt_{wm} depends on the time which elapses between the wavemeter reading the laser frequency and the measurement program querying the reading.

D.1 Calibration of the Error Signal Delay

The calibration measurement for the error signal delay Δt_{err} is sketched in Fig. D.1: The lock and spectroscopy lasers are both tuned within the respective longitudinal cavity modes such that they are resonant at the same cavity length. Then the cavity length is scanned around this double-resonant length while we record the spectroscopy laser transmission

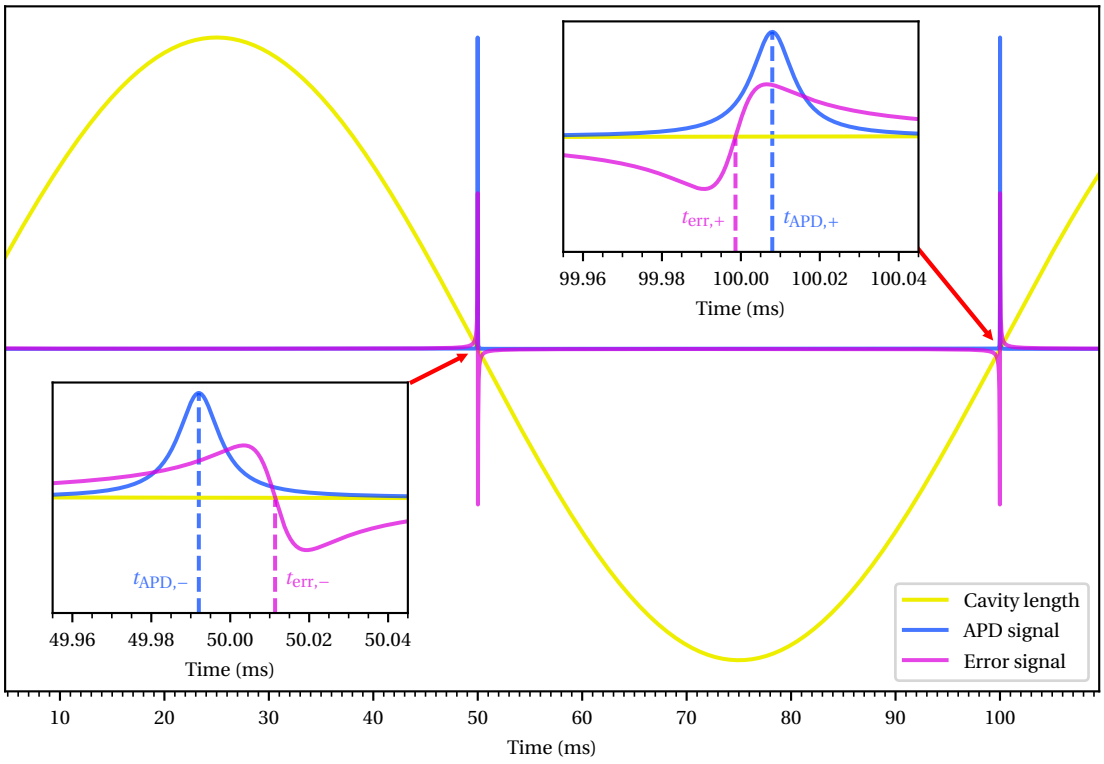

Figure D.1: Calibration of the error signal delay Δt_{err} by scanning the cavity length while recording the cavity transmission with the APD and the error signal.

on the APD and the Hänsch-Couillaud error signal in the same setting as we would do for a regular transmission spectrum. Given the exact simultaneous resonance of the lock and spectroscopy laser, the error signal delay is the difference between measured error signal zero-crossing and transmission peak of the APD signal $\Delta t_{\mathrm{err}} = t_{\mathrm{err}} - t_{\mathrm{APD}}$. Practically, however, the double-resonance is not exact. In Fig. D.1 the APD signal peaks for a slightly longer cavity than the error signal crosses zero. We therefore use the time delays $t_{\mathrm{err},\pm} - t_{\mathrm{APD},\pm}$ on both directions of the cavity scan – increasing (+) and decreasing (−) cavity length. A resonance mismatch changes these delays in opposite directions. Hence, we can extract the pure error signal delay due to acquisition Δt_{err} from the sum

$$\left(t_{\mathrm{err},+} - t_{\mathrm{APD},+}\right) + \left(t_{\mathrm{err},-} - t_{\mathrm{APD},-}\right) = 2\,\Delta t_{\mathrm{err}}. \tag{D.1}$$

By detecting the transmission peaks and the error signal zero-crossings for several hundred scan periods we extract an error signal delay of $\Delta t_{\mathrm{err}} = 5.47 \pm 0.34\,\mu\mathrm{s}$.

D.2 Wavemeter Delay Compensation

One can evaluate the timing of the wavelength reading relative to the APD signal by separating the dataset into ramps of rising/falling laser frequency, as shown in Fig. D.2. In this example, the spectra obtained from rising laser frequency ramps are shifted to lower frequencies, indicating that the wavemeter reading is delayed compared to the APD signal.

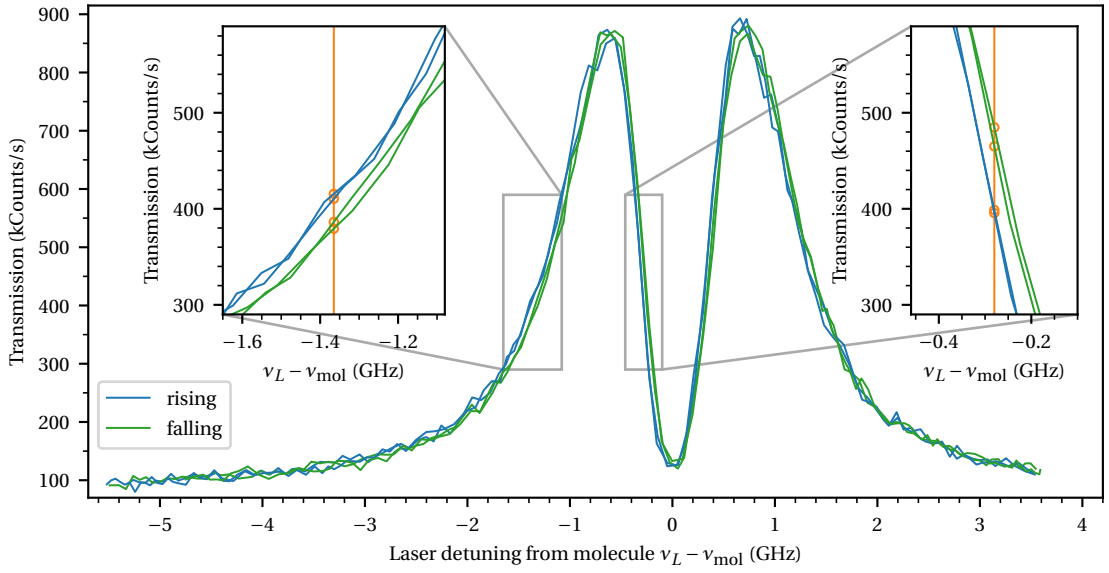

Figure D.2: A relative delay between the wavemeter reading and the APD signal causes a systematic shift between the spectra in which the laser frequency rises/falls.

To correct for this delay, we shift the wavemeter readings relative to the APD signal to minimize the horizontal offset shown in the insets of Fig. D.2. To find the optimal shift very precisely, we divide the dataset into 100 frequency bins and calculate the variance of APD countrates in

each bin. As exemplarily shown by the two vertical orange lines, a systematic shift between the partial spectra from rising/falling ramps causes a high variance, especially in parts of the spectrum with a steep slope. Minimizing the sum over the variances in all 100 spectral bins therefore optimizes the relative shift between the data tracks.

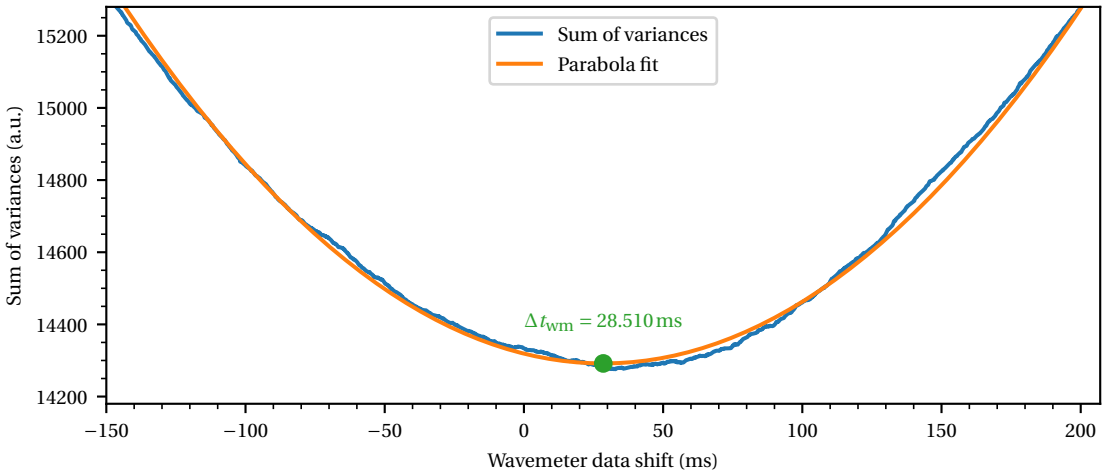

Figure D.3: Shifting the wavemeter data track with respect to the others reveals a minimum variance at $\Delta t_{wm} = 28.510\,\text{ms}$. This is the wavemeter delay for the measurement shown in Fig. D.2.

Fig. D.3 shows the sum of variances as the wavemeter data track is shifted. It exhibits a minimum at a few tens of ms delay. To reduce the influence of "roughness" on the outcome, we obtain the optimal wavemeter delay Δt_{wm} from a parabolic fit. This optimization procedure and its implementation details can be found together with the QuTiP simulations on our internal GitLab [227].

E APD Deadtime Correction

An avalanche photodiode (APD) creates a macroscopic electrical pulse for each absorbed photon. This is made possible by applying a high voltage across a diode, close to its breakdown voltage. If a single photon is absorbed, a single electron-hole pair is created. The charge carriers are accelerated by the high voltage and excite further electron-hole pairs, leading to a macroscopic avalanche. To protect the APD from damage, a quenching circuit is activated. It switches off the high voltage until the avalanche has decayed and the diode is back in its equilibrium state after several tens of nanoseconds. During this so-called *deadtime* T_d no further avalanches can be triggered. Hence, the APD does not respond to a photon absorbed during this time [145].

With a rate of C_{actual} photons absorbed in the APD, we fail to detect on average $C_{\text{actual}} T_d$ photons per deadtime-cycle. As the deadtime is triggered at the rate of detection events C_{det}, the rate of missed photons is

$$C_{\text{miss}} = C_{\text{det}} \left(C_{\text{actual}} T_d \right). \tag{E.1a}$$

Hence, we can reconstruct the actual rate of photons on the APD

$$C_{\text{actual}} = C_{\text{det}} + C_{\text{miss}}. \tag{E.1b}$$

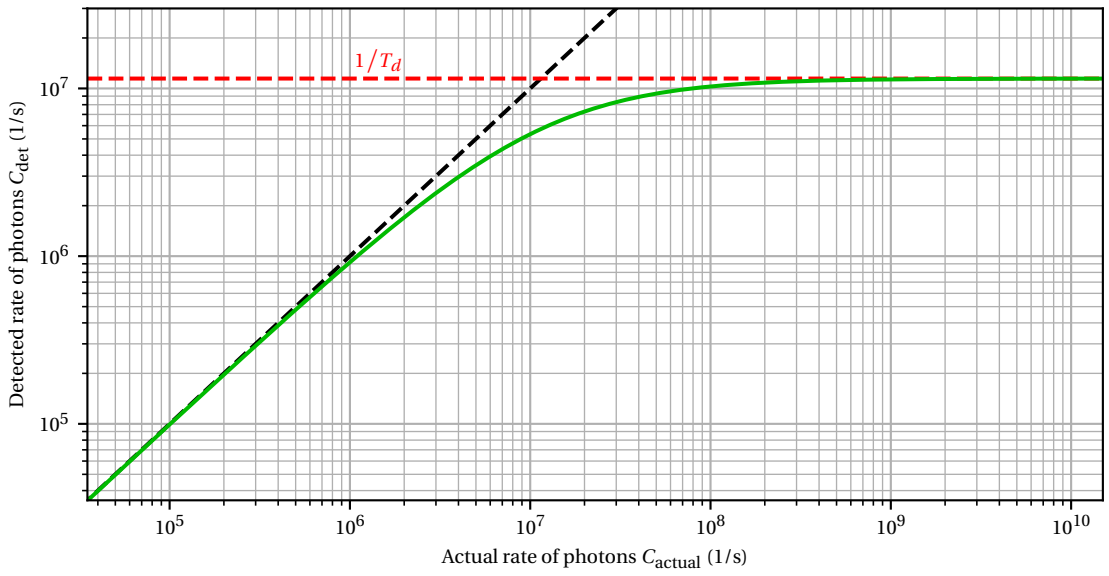

Figure E.1: The detected countrate against the rate of absorbed photons of an APD with deadtime $T_d = 87.3\,\text{ns}$.

Substituting Eq. E.1a into Eq. E.1b and solving for C_{actual} results in the APD deadtime correction formula

$$C_{\text{actual}} = \frac{C_{\text{det}}}{1 - T_d C_{\text{det}}}. \tag{E.1c}$$

Fig. E.1 shows the detected rate C_{det} as a function of the incident rate C_{actual} for a deadtime of $T_d = 87.3\,\text{ns}$. For low rates, the detected rate is equal to the real rate, but they deviate for higher countrates. With detected countrates exceeding 1 MHz in our experiments, we must correct for the APD deadtime in order to obtain accurate measurements.

We can determine the deadtime of the APD used in our experiments by time-tagging its output pulses and computing an autocorrelation histogram (see Fig. E.2). The choice of light source is irrelevant to this measurement. The probability of detecting a second photon with a time delay τ after a first photon is 0 for a few tens of nanoseconds. Zooming in on the sharp rise in coincidences reveals that this deadtime lasts for $T_d = 87.3\,\text{ns}$. The figure also shows a short interval $\tau \in [87.3, 110.9]$ ns of afterpulses, before the APD returns to normal operation.

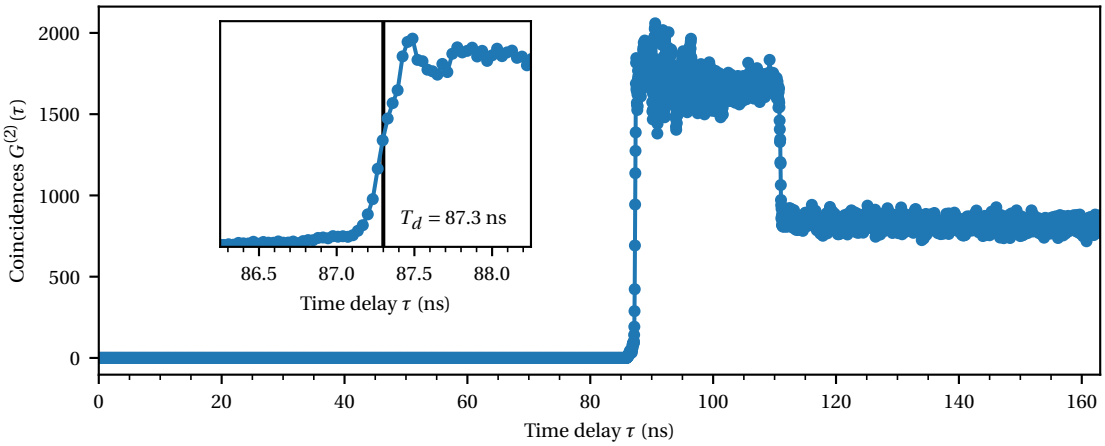

Figure E.2: Coincidence histogram of the APD used in the experiments described in Chapters 4 & 5: Deadtime until $\tau = 87.3\,\text{ns}$, afterpulses until $\tau = 110.9\,\text{ns}$, then normal operation.

F Calibration of Power and Cavity Incoupling Efficiency

We would like to emphasize that the power axes in the nonlinear optical experiments, for example Figs. 5.3 & 5.7, are not inferred *post-hoc* to match the saturation behavior of a single molecule, but result from a careful calibration of the laser power coupled into the cavity. Here, we explain the three steps undertaken to determine the power coupled into the cavity.

F.1 Calibration of the PID Setpoints in the Power Feedback Loops

As explained in Ch. 3.4, each laser beam is power-stabilized by a feedback loop. The signal of a photodiode measuring the power of the laser beam is fed into a PID loop. The PID controls the driving amplitude of an AOM, which in turn changes the power of the beam. We set the laser power using the PID setpoint. To map a given setpoint to power, we measure the laser power in front of the cryostat with a powermeter (Vega, Ophir Optronics Solutions Ltd.) for various PID setpoints. This gives rise to the linear relations shown in Fig. F.1. Since we measure the power outside the cryostat for this calibration, we must additionally multiply it by the transmission through the cryostat windows, namely 87 %.

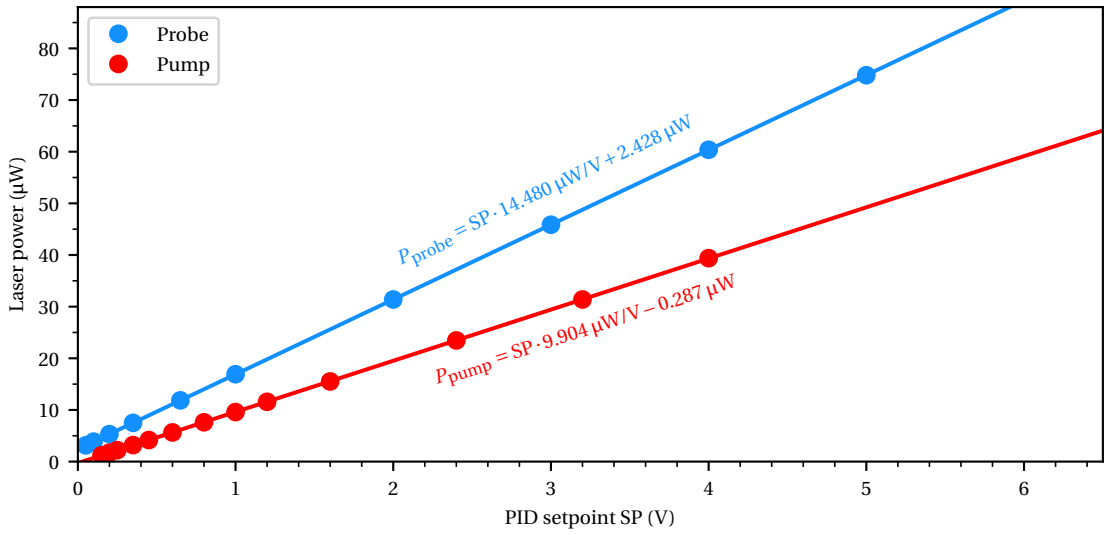

Figure F.1: The background-subtracted power inside the cryostat as a function of the PID setpoint SP for the probe and pump feedback loops.

F.2 Calibration of the ND Filters

After the beam pickoff for the photodiode, we can insert several different ND filters into the laser beam to change the laser power in coarse steps. Their attenuation A_i is given by

$$A_i = \frac{\text{measured laser power with filter } i - \text{background power}}{\text{measured laser power without filter} - \text{background power}}. \tag{F.1}$$

Several ND filters in series allow us to reduce the laser power by up to 9 orders of magnitude.

F.3 Calibration of the Cavity Incoupling Efficiency

Only some of the light which enters the cryostat couples into the cavity mode. This is due to spatial mode mismatch, the polarization mismatch in the cross-polarization scheme (see Ch. 3.4.2) and imperfect reflectivity balance of the two mirrors. We obtain the incoupling efficiencies of the pump η_{pump} and probe beam η_{probe} from the depth of their resonance dips in a reflection spectrum, shown in Fig. F.2. To ensure constant incoupling efficiency across experiments performed on different days, we re-optimize the spatial position of the laser beam every 20 min by scanning the fast steering mirror in front of the $4f$ telecentric system (see setup, Fig. 3.12).

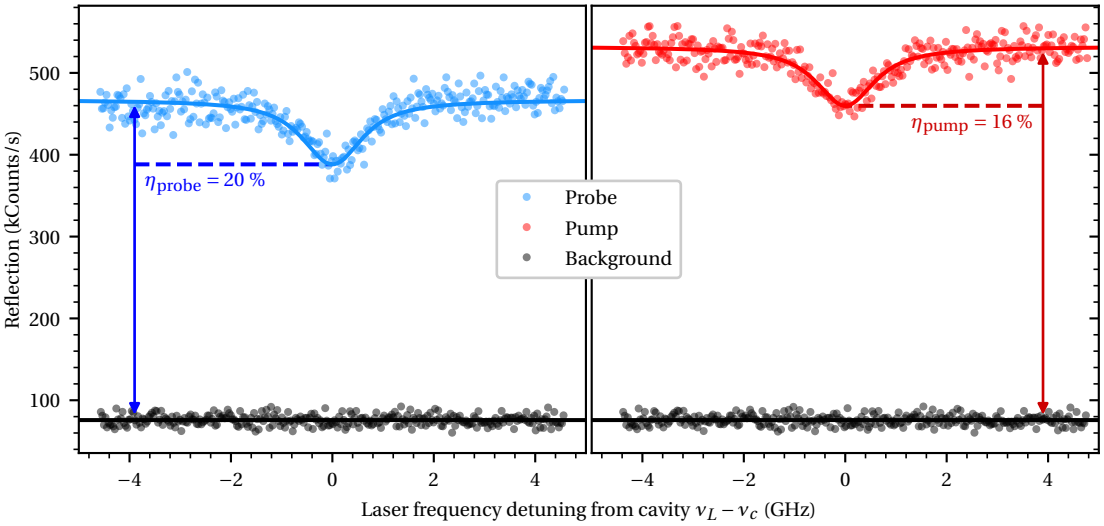

Figure F.2: Measurement of the incoupling efficiencies η of the probe and pump beam.

G Theoretical Expectation of Coupling Strengths

We would like to compare the cavity-emitter coupling strengths we found among molecules ($g < 2\pi \cdot 0.8\,\mathrm{GHz}$) to theoretically expected values. Z. Sadeq *et al.* [102] calculated a transition dipole moment of 13.1 Debye. Assuming a branching ratio of $\alpha_{00} = 1/3$, the dipole moment for the 00ZPL transition is therefore $d_{eg} = \sqrt{\alpha_{00}} \cdot 13.1\,\mathrm{Debye}$. Further assuming a mode volume of $V = 4.4\,\lambda^3$, the coupling strength can reach up to $g = 2\pi \cdot 3.1\,\mathrm{GHz}$ (see Eq. 2.13). Here, we list several factors which can be responsible for the difference between the ideal theoretical value and those experimentally observed.

Firstly, the cavity mode is polarized along the b-axis of the anthracene crystal, whereas the transition dipole moments of individual DBT molecules can be slightly misaligned. A. Nicolet *et al.* [137] find a distribution of 10° FWHM around the b-axis. While a misalignment of 10° only leads to a reduction of g by a factor $\cos 10° \approx 0.98$, we would like to note that cases with a misalignment of 26° have also been observed [228], in which g decreases by 0.90.

Secondly, the transition dipole moment could be lower than the theoretical prediction. The aforementioned amplitude of 13.1 Debye [102] is the result of a Hubbard model simulation and refers to the transition dipole moment of the electronic transition $|S_1\rangle \rightarrow |S_0\rangle$ (see Fig. 2.1), including the vibrational sublevels. Including a local-field correction, this transition dipole moment implies a homogeneous linewidth of $\gamma/2\pi = 40\,\mathrm{MHz}$, which is in line with experimental measurements. In this theoretical calculation, as throughout this thesis, it is assumed that this linewidth is purely due to radiative decay. However, the overall decay rate is the sum of the radiative γ_r and nonradiative γ_nr decay rates, while the transition dipole moment d_{eg} only contributes to the radiative decay rate. At the time of writing, the nonradiative decay rate [229] has not yet been finally determined. M. Musavinezhad *et al.* [207] find the fraction of radiative decay $\eta = \gamma_\mathrm{r} / \left(\gamma_\mathrm{r} + \gamma_\mathrm{nr}\right)$ to lie within $70 \pm 20\,\%$ for DBT in para-dichlorobenzene. Because of the lower transition frequency of DBT in anthracene, η is assumed to be lower, according to the energy gap law [230]. A reduction of the purely radiative linewidth by a factor of $\eta = 50\,\%$ would imply a reduction of the dipole moment, and hence g, by $\sqrt{0.5} \approx 0.71$.

Thirdly, the anthracene crystal changes the mode structure of the cavity. Depending on the crystal thickness, the cavity modes can be air-like or anthracene-like [136]. In the former, the intensity in the air part of the cavity mode is a factor n_b higher than in the anthracene part. In the latter, the intensities in both parts are comparable. Therefore, in an air-like mode, g is a factor of $\sqrt{1/n_b} \approx 0.75$ lower than in an anthracene-like mode. We did not measure the crystal thickness at the position of the cavity mode in the strong coupling experiments. When we removed the sample from the cryostat, an atomic force microscope measurement revealed a thickness between 1.1 µm and 1.3 µm.

Lastly, the field amplitude of the cavity mode in the crystal is not uniform, but follows a spatial distribution, described by the unitless function $\vec{f}(\vec{r})$ in Eq. 2.11. Since we have no control over the position of the molecules within the crystal, we find a random distribution of coupling strengths for a given cavity mode. We can derive an approximate expression

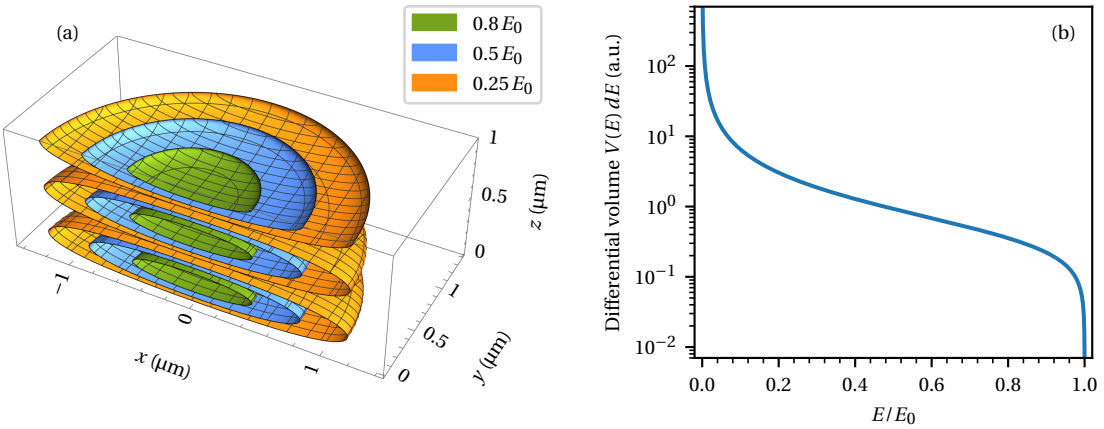

Figure G.1: (a) Equal-field-strength surfaces of a standing-wave Gaussian beam of diameter $w = 1\,\mu\text{m}$. The vertical axis extends over 2½ periods of the standing wave, or over 1¼ wavelengths of $\lambda = 785\,\text{nm}$. (b) The differential volume element $V(E)\,dE$ for the same beam.

for the distribution. The field amplitude has the form of a standing-wave Gaussian beam. Approximating the mode diameter to be constant along the optical axis $w(z) = w_0$, we can write it as

$$E(r,z) = E_0 \left| \sin\left(\frac{2\pi n_b z}{\lambda}\right) \right| \exp\left(-\frac{r^2}{{w_0}^2}\right) \tag{G.1}$$

in cylindrical coordinates (r,z). We can assign surfaces of equal field strength within this mode, as sketched in Fig. G.1a). Molecules within one surface have the same coupling strength to the cavity mode. The probability density for finding a molecule experiencing a field strength in a small interval $[E, E+dE]$ is proportional to the differential volume

$$V(E)\,dE = \frac{\lambda {w_0}^2}{n_b E} \arccos\left(\frac{E}{E_0}\right) dE. \tag{G.2}$$

Fig. G.1b) shows this distribution. Over the majority of the range of possible coupling strengths the probability density decreases proportional to $1/E$, with the arccos term leading to a hard cutoff at the maximal field strength E_0. We have not yet performed a rigorous statistical survey of the distribution of experimentally obtainable coupling strengths. Doing so will provide a more precise estimation of the maximum coupling strength. This in turn will allow us to establish boundaries for systematic reductions of the coupling strengths due to the reasons described above. We would also like to note that the doping concentration varies within a given crystal. In particular a doping gradient along the optical axis would change the probability density for coupling strengths from the differential volume $V(E)\,dE$ in Eq. G.2.

Reducing the coupling strength from the theoretical optimum to the measured values requires the assumption of relatively low values for the four factors elaborated on. It is therefore likely that additional mechanisms contribute to a further reduction.

H Alignment Procedure for the Cryostat Insert

The cryostat insert is aligned outside the cryostat on a duplicate of the landing plate. This chapter documents the full alignment procedure. A regular exchange of the curved/flat mirror, requires only step 8 or 9 respectively, assuming all other components are still aligned. The subfigure labels in Figs. H.1 & H.2 correspond to the following steps:

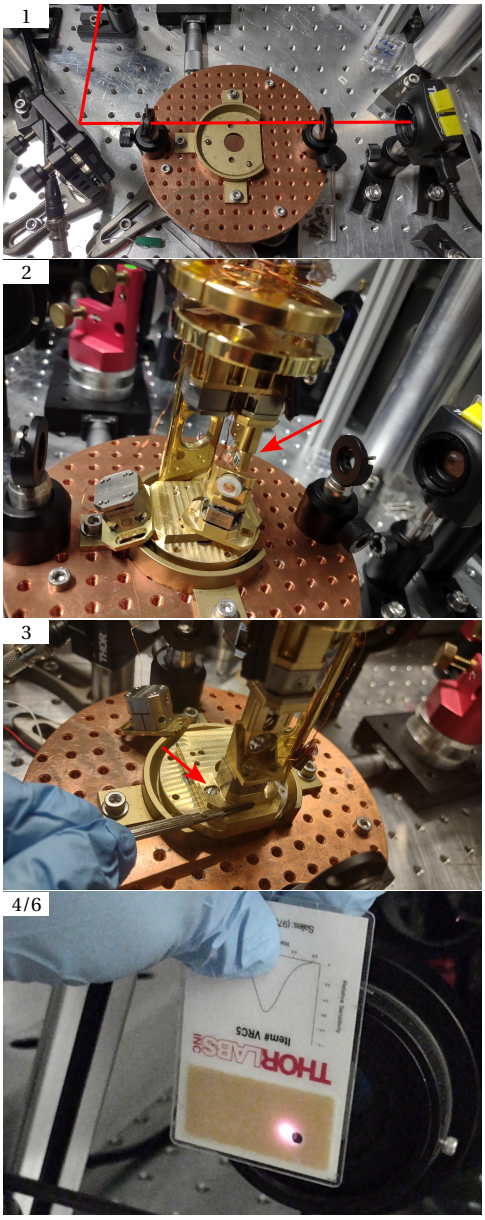

Figure H.1: Cryostat insert alignment.

1. Set the fast steering mirror (see Fig. 3.12) to the center of its movement range, by applying 0 V to the x- and y-inputs. Use a mirror pair to align the laser beam to the two irises defining the optical axis.

2. Mark the position of the beam (for example with a camera). Then, place the cryostat insert on the landing plate and remove every element in the beam path, except for the aspheric lens on the curved mirror side. In Fig. H.1, we additionally removed one of the two pillars connecting the top and bottom parts of the insert. This is not necessary, but simplifies handling. Manually adjust the lateral position of the aspheric lens such that the center of the laser beam coincides with its previous center. If the curved mirror substrate is a GRIN lens (see Ch. 3.1.1), there is no asphere on the curved mirror side and this step can be skipped.

3. Attach the curved mirror assembly to the cryostat insert. When tightening the screws, push the assembly away from the aspheric lens until both screws touch the straight part of the slotted holes. This will serve as a reference when the assembly is removed and brought back. The exact lateral position of the assembly is not relevant at this point.

4. Attach a mirror to the ring piezo of the curved mirror assembly. Loosen the screws holding the mirror mount on the x-attocube. Adjust the orientation of the mount such that the backreflection coincides with the incident laser beam, then re-tighten the screws for the mount.

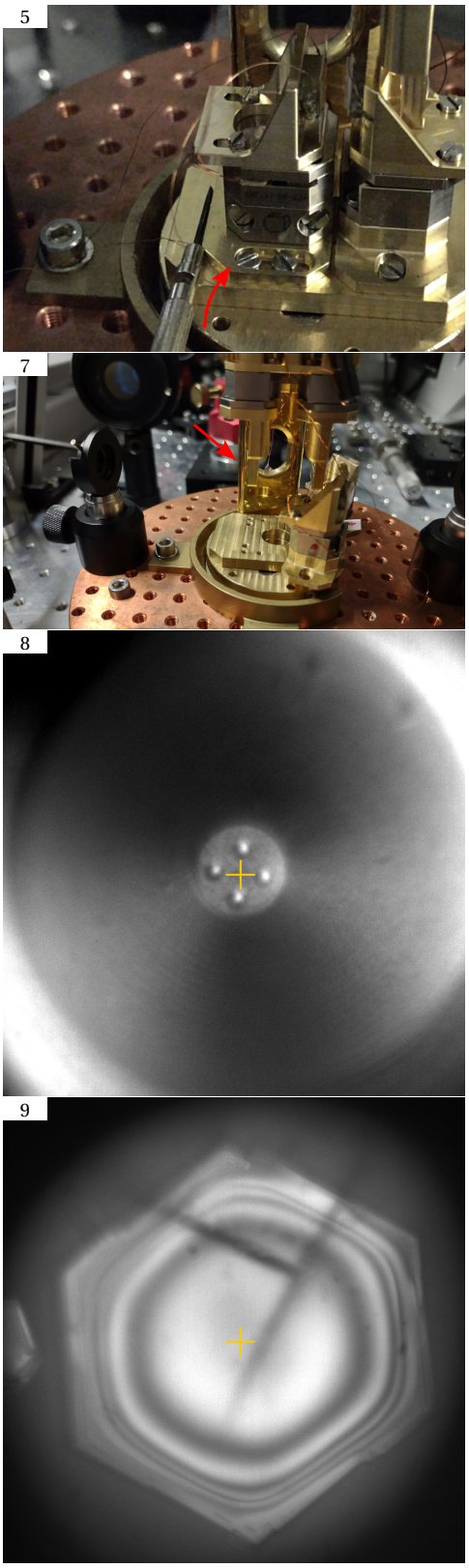

Figure H.2: Cryostat insert alignment.

5. Attach a flat mirror to the ring piezo of the flat mirror assembly and install it in the insert. Here, we create a reference by pushing the assembly towards the curved mirror until the ends of the slotted holes are stopped by the screws.

6. Analogously to step 4, adjust the mount of the flat mirror until the laser beam is reflected onto itself.

7. Remove the mirror assemblies from the beam path and insert the aspheric lens on the flat mirror side. Manually align it such that the laser beam is centered at the same position as in step 2.

8. Reattach the curved mirror assembly using the reference from step 3. Illuminate the curved mirror with the LED shown in Fig. 3.12 and image the substrate of the curved mirror on the camera inside the detection box (Fig. 3.15). Shift the curved mirror substrate laterally with respect to the ring piezo until the image of the pedestal is at the same position as the image of the laser beam.

9. Attach the flat mirror with anthracene crystals (see Ch. 3.2) to the flat mirror assembly and install it in the insert using the reference from step 5. Illuminate the flat mirror and image it on the detection box camera. Shift it laterally with respect to the ring piezo until the desired crystal is imaged to the same position on the camera as the curved mirror.

10. If applicable, reinstall the second pillar. Fasten all electrical connections and ensure they are all located within the cylindrical envelope of the insert. The insert is now ready for insertion into the cryostat.

I Longitudinal Mode Number Estimation in the Cryo Insert

We can estimate the longitudinal mode number q of the cavity in a two-wavelength measurement. We co-couple two lasers at wavelengths λ_1 and λ_2 into the cavity and scan the cavity length around the two fundamental-mode resonances. They are detected by a dip in the reflected power, as in the estimation of the crystal thickness by the polarization mode splitting, see Fig. 3.10. The distance between the two resonances (in terms of voltage applied to the ring piezo V_{piezo}, c.f. Fig. 3.11) for a series of successively increasing longitudinal modes grows approximately linearly, as in Fig. I.1. This allows us to extrapolate the $q = 0$ mode, for which the resonances at λ_1 and λ_2 coincide.

Two issues require consideration here: The phase-shifts upon reflection from the mirrors ϕ_1, ϕ_2 and the Gouy phase, as explained in Ch. 2.2.3. We absorb the reflection phase shifts into an effective mode number q_{eff} [93], such that Eq. 2.7 reads

$$q_{\text{eff}} \cdot 2\pi = 2kL - 2\arcsin\sqrt{\frac{L}{R_0}}. \tag{I.1}$$

To compute the length difference ΔL between the resonances for λ_1 and λ_2 with the same q_{eff}, we must solve Eq. I.1 for L. We are not aware of an analytical solution, so we denote the

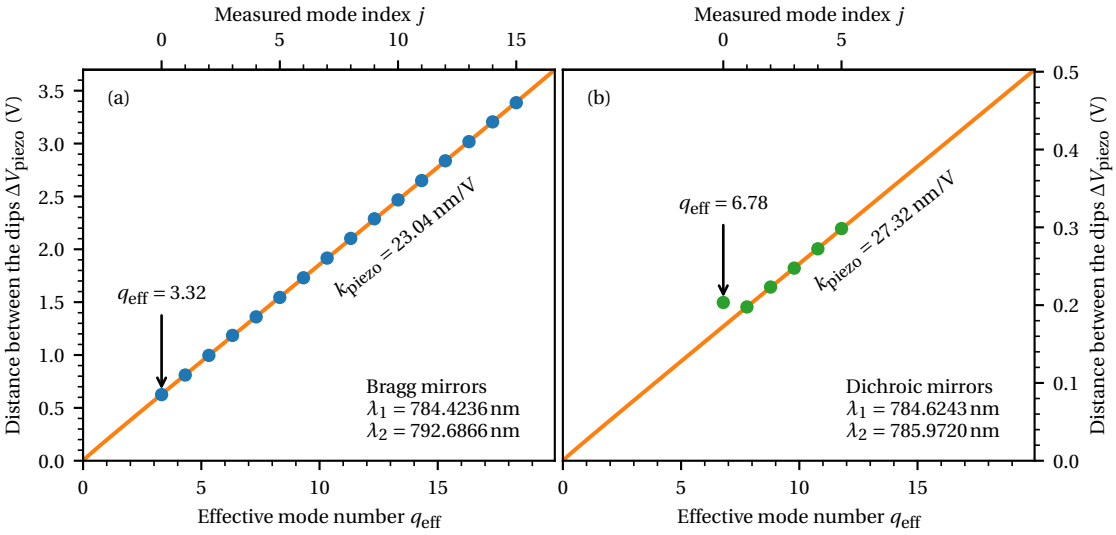

Figure I.1: Estimation of the longitudinal mode number q_{eff} for a cavity with Bragg mirrors (a) and dichroic mirrors (b). The distance between the resonances in the shortest mode in (b) is higher than predicted by the theory. This is because the two mirrors are in mechanical contact. Hence, higher voltages across the piezo ΔV_{piezo} are required to move the same physical distance ΔL. This data point is excluded from the fit. The slight difference in the piezo calibration constants k_{piezo} is due to modifications on the cryostat insert between these two measurements recorded about 1 year apart. We also note that the piezo voltage plotted here is the voltage before a x10 amplifier (MDT693B, Thorlabs Inc.).

numerical solution for a given q_{eff}, k, R_0 as $L(q_{\text{eff}}, \lambda)$. Then, the function fitted to the data is

$$\Delta L(q_{\text{eff}}) = L(q_{\text{eff}}, \lambda_2) - L(q_{\text{eff}}, \lambda_1), \tag{I.2}$$

where ΔL is expressed by the voltage difference on the piezo times its calibration constant $\Delta L = \Delta V_{\text{piezo}} k_{\text{piezo}}$. Similarly, while recording the data, we do not know the effective mode number q_{eff} of the modes, so we parameterize $q_{\text{eff}} = j + q_{\text{offset}}$, where j is the index of the mode in the sequence of scans. The fit therefore delivers the effective mode number of the shortest measured mode q_{offset} as well as the conversion factor between piezo voltage and cavity length change k_{piezo}.

Bibliography

[1] R. W. Boyd, *Nonlinear Optics*, 2nd ed. (Academic Press, London, 2003).

[2] T. H. Maiman, "Stimulated Optical Radiation in Ruby", Nature **187**, 493–494 (1960).

[3] P. A. Franken, A. E. Hill, C. W. Peters, and G. Weinreich, "Generation of Optical Harmonics", Physical Review Letters **7**, 118–119 (1961).

[4] P. D. Maker, R. W. Terhune, and C. M. Savage, "Intensity-Dependent Changes in the Refractive Index of Liquids", Physical Review Letters **12**, 507–509 (1964).

[5] S. E. Harris, M. K. Oshman, and R. L. Byer, "Observation of Tunable Optical Parametric Fluorescence", Physical Review Letters **18**, 732–734 (1967).

[6] D. Magde and H. Mahr, "Study in Ammonium Dihydrogen Phosphate of Spontaneous Parametric Interaction Tunable from 4400 to 16 000 Å", Physical Review Letters **18**, 905–907 (1967).

[7] A. M. Bonch-Bruevich, N. N. Kostin, V. A. Khodovoĭ, and V. V. Khromov, "Changes in the Atomic Absorption Spectrum in the Field of a Light Wave. I.", Soviet Physics JETP **29**, 82–85 (1969).

[8] D. E. Chang, V. Vuletić, and M. D. Lukin, "Quantum nonlinear optics — photon by photon", Nature Photonics **8**, 685–694 (2014).

[9] P. Türschmann, H. Le Jeannic, S. F. Simonsen, H. R. Haakh, S. Götzinger, V. Sandoghdar, P. Lodahl, and N. Rotenberg, "Coherent nonlinear optics of quantum emitters in nanophotonic waveguides", Nanophotonics **8**, 1641–1657 (2019).

[10] I. Gerhardt, G. Wrigge, G. Zumofen, J. Hwang, A. Renn, and V. Sandoghdar, "Coherent state preparation and observation of Rabi oscillations in a single molecule", Physical Review A **79**, 011402 (2009).

[11] F. Schuda, C. R. Stroud, and M. Hercher, "Observation of the resonant Stark effect at optical frequencies", Journal of Physics B: Atomic and Molecular Physics **7**, L198–L202 (1974).

[12] G. Wrigge, I. Gerhardt, J. Hwang, G. Zumofen, and V. Sandoghdar, "Efficient coupling of photons to a single molecule and the observation of its resonance fluorescence", Nature Physics **4**, 60–66 (2008).

[13] J. Hwang, M. Pototschnig, R. Lettow, G. Zumofen, A. Renn, S. Götzinger, and V. Sandoghdar, "A single-molecule optical transistor", Nature **460**, 76–80 (2009).

[14] J. Mertz, C. Xu, and W. W. Webb, "Single-molecule detection by two-photon-excited fluorescence", Optics Letters **20**, 2532 (1995).

[15] T. Plakhotnik, D. Walser, M. Pirotta, A. Renn, and U. P. Wild, "Nonlinear Spectroscopy on a Single Quantum System: Two-Photon Absorption of a Single Molecule", Science **271**, 1703–1705 (1996).

[16] M. Sondermann, R. Maiwald, H. Konermann, N. Lindlein, U. Peschel, and G. Leuchs, "Design of a mode converter for efficient light-atom coupling in free space", Applied Physics B **89**, 489–492 (2007).

[17] N. Lindlein, R. Maiwald, H. Konermann, M. Sondermann, U. Peschel, and G. Leuchs, "A new 4π geometry optimized for focusing on an atom with a dipole-like radiation pattern", Laser Physics **17**, 927–934 (2007).

[18] M. Stobińska, G. Alber, and G. Leuchs, "Perfect excitation of a matter qubit by a single photon in free space", EPL (Europhysics Letters) **86**, 14007 (2009).

[19] M. Arcari, I. Söllner, A. Javadi, S. Lindskov Hansen, S. Mahmoodian, J. Liu, H. Thyrrestrup, E. H. Lee, J. D. Song, S. Stobbe, and P. Lodahl, "Near-Unity Coupling Efficiency of a Quantum Emitter to a Photonic Crystal Waveguide", Physical Review Letters **113**, 093603 (2014).

[20] A. F. Koenderink, "Single-Photon Nanoantennas", ACS Photonics **4**, 710–722 (2017).

[21] M. Trupke, E. A. Hinds, S. Eriksson, E. A. Curtis, Z. Moktadir, E. Kukharenka, and M. Kraft, "Microfabricated high-finesse optical cavity with open access and small volume", Applied Physics Letters **87**, 211106 (2005).

[22] D. Wang, H. Kelkar, D. Martín-Cano, D. Rattenbacher, A. Shkarin, T. Utikal, S. Götzinger, and V. Sandoghdar, "Turning a molecule into a coherent two-level quantum system", Nature Physics **15**, 483–489 (2019).

[23] A. Pscherer, M. Meierhofer, D. Wang, H. Kelkar, D. Martín-Cano, T. Utikal, S. Götzinger, and V. Sandoghdar, "Single-Molecule Vacuum Rabi Splitting: Four-Wave Mixing and Optical Switching at the Single-Photon Level", Physical Review Letters **127**, 133603 (2021).

[24] R. Chikkaraddy, B. de Nijs, F. Benz, S. J. Barrow, O. A. Scherman, E. Rosta, A. Demetriadou, P. Fox, O. Hess, and J. J. Baumberg, "Single-molecule strong coupling at room temperature in plasmonic nanocavities", Nature **535**, 127–130 (2016).

[25] R. J. Thompson, G. Rempe, and H. J. Kimble, "Observation of normal-mode splitting for an atom in an optical cavity", Physical Review Letters **68**, 1132–1135 (1992).

[26] T. Yoshie, A. Scherer, J. Hendrickson, G. Khitrova, H. M. Gibbs, G. Rupper, C. Ell, O. B. Shchekin, and D. G. Deppe, "Vacuum Rabi splitting with a single quantum dot in a photonic crystal nanocavity", Nature **432**, 200–203 (2004).

[27] Y.-S. Park, A. K. Cook, and H. Wang, "Cavity QED with Diamond Nanocrystals and Silica Microspheres", Nano Letters **6**, 2075–2079 (2006).

[28] K. J. Vahala, *Optical Microcavities*, Advanced Series in Applied Physics, Volume 5 (World Scientific Publishing Co. Pte. Ltd., Singapore, 2004).

[29] S. Haroche and J.-M. Raimond, *Exploring the Quantum* (Oxford University Press, Aug. 2006).

[30] E. Schrödinger, "Die gegenwärtige Situation in der Quantenmechanik", Die Naturwissenschaften **23**, 807–812 (1935).

[31] M. Brune, F. Schmidt-Kaler, A. Maali, J. Dreyer, E. Hagley, J. M. Raimond, and S. Haroche, "Quantum Rabi Oscillation: A Direct Test of Field Quantization in a Cavity", Physical Review Letters **76**, 1800–1803 (1996).

[32] A. Imamoğlu, H. Schmidt, G. Woods, and M. Deutsch, "Strongly Interacting Photons in a Nonlinear Cavity", Physical Review Letters **79**, 1467–1470 (1997).

[33] K. M. Birnbaum, A. Boca, R. Miller, A. D. Boozer, T. E. Northup, and H. J. Kimble, "Photon blockade in an optical cavity with one trapped atom", Nature **436**, 87–90 (2005).

[34] C. S. Muñoz, E. del Valle, A. G. Tudela, K. Müller, S. Lichtmannecker, M. Kaniber, C. Tejedor, J. J. Finley, and F. P. Laussy, "Emitters of N-photon bundles", Nature Photonics **8**, 550–555 (2014).

[35] D. A. B. Miller, "Are optical transistors the logical next step?", Nature Photonics **4**, 3–5 (2010).

[36] R. Athale and D. Psaltis, "Optical Computing: Past and Future", Optics and Photonics News **27**, 32 (2016).

[37] J. Touch, Y. Cao, M. Ziyadi, A. Almaiman, A. Mohajerin-Ariaei, and A. E. Willner, "Digital optical processing of optical communications: towards an Optical Turing Machine", Nanophotonics **6**, 507–530 (2017).

[38] P. Minzioni, C. Lacava, T. Tanabe, J. Dong, X. Hu, G. Csaba, W. Porod, G. Singh, A. E. Willner, A. Almaiman, V. Torres-Company, J. Schröder, A. C. Peacock, M. J. Strain, F. Parmigiani, G. Contestabile, D. Marpaung, Z. Liu, J. E. Bowers, L. Chang, S. Fabbri, M. Ramos Vázquez, V. Bharadwaj, S. M. Eaton, P. Lodahl, X. Zhang, B. J. Eggleton, W. J. Munro, K. Nemoto, O. Morin, J. Laurat, and J. Nunn, "Roadmap on all-optical processing", Journal of Optics **21**, 063001 (2019).

[39] S. L. McCall, "Instabilities in continuous-wave light propagation in absorbing media", Physical Review A **9**, 1515–1523 (1974).

[40] H. M. Gibbs, S. L. McCall, and T. N. C. Venkatesan, "Optical Bistability", Optics News **5**, 6 (1979).

[41] C. M. Savage and H. J. Carmichael, "Single atom optical bistability", IEEE Journal of Quantum Electronics **24**, 1495–1498 (1988).

[42] H. M. Gibbs, S. L. McCall, and T. N. C. Venkatesan, "Differential Gain and Bistability Using a Sodium-Filled Fabry-Perot Interferometer", Physical Review Letters **36**, 1135–1138 (1976).

[43] D. Miller, S. D. Smith, and A. Johnston, "Optical bistability and signal amplification in a semiconductor crystal: applications of new low-power nonlinear effects in InSb", Applied Physics Letters **35**, 658–660 (1979).

[44] H. M. Gibbs, S. L. McCall, T. N. C. Venkatesan, A. C. Gossard, A. Passner, and W. Wiegmann, "Optical bistability in semiconductors", Applied Physics Letters **35**, 451–453 (1979).

[45] V. R. Almeida, C. A. Barrios, R. R. Panepucci, M. Lipson, M. A. Foster, D. G. Ouzounov, and A. L. Gaeta, "All-optical switching on a silicon chip", Optics Letters **29**, 2867 (2004).

[46] K. Nozaki, T. Tanabe, A. Shinya, S. Matsuo, T. Sato, H. Taniyama, and M. Notomi, "Sub-femtojoule all-optical switching using a photonic-crystal nanocavity", Nature Photonics **4**, 477–483 (2010).

[47] N. Moroney, L. D. Bino, M. T. M. Woodley, G. N. Ghalanos, J. M. Silver, A. Ø. Svela, S. Zhang, and P. Del'Haye, "Logic Gates Based on Interaction of Counterpropagating Light in Microresonators", Journal of Lightwave Technology **38**, 1414–1419 (2020).

[48] I. L. Chuang and Y. Yamamoto, "Simple quantum computer", Physical Review A **52**, 3489–3496 (1995).

[49] H. J. Kimble, "The quantum internet", Nature **453**, 1023–1030 (2008).

[50] J. L. O'Brien, A. Furusawa, and J. Vučković, "Photonic quantum technologies", Nature Photonics **3**, 687–695 (2009).

[51] Q. A. Turchette, C. J. Hood, W. Lange, H. Mabuchi, and H. J. Kimble, "Measurement of Conditional Phase Shifts for Quantum Logic", Physical Review Letters **75**, 4710–4713 (1995).

[52] M. Mücke, E. Figueroa, J. Bochmann, C. Hahn, K. Murr, S. Ritter, C. J. Villas-Boas, and G. Rempe, "Electromagnetically induced transparency with single atoms in a cavity", Nature **465**, 755–758 (2010).

[53] I. Shomroni, S. Rosenblum, Y. Lovsky, O. Bechler, G. Guendelman, and B. Dayan, "All-optical routing of single photons by a one-atom switch controlled by a single photon", Science **345**, 903–906 (2014).

[54] T. G. Tiecke, J. D. Thompson, N. P. de Leon, L. R. Liu, V. Vuletić, and M. D. Lukin, "Nanophotonic quantum phase switch with a single atom", Nature **508**, 241–244 (2014).

[55] B. Hacker, S. Welte, G. Rempe, and S. Ritter, "A photon–photon quantum gate based on a single atom in an optical resonator", Nature **536**, 193–196 (2016).

[56] S. Daiss, S. Langenfeld, S. Welte, E. Distante, P. Thomas, L. Hartung, O. Morin, and G. Rempe, "A quantum-logic gate between distant quantum-network modules", Science **371**, 614–617 (2021).

[57] D. R. Englund, A. Faraon, I. Fushman, N. Stoltz, P. Petroff, and J. Vučković, "Controlling cavity reflectivity with a single quantum dot", Nature **450**, 857–861 (2007).

[58] D. R. Englund, A. Majumdar, M. Bajcsy, A. Faraon, P. Petroff, and J. Vučković, "Ultrafast Photon-Photon Interaction in a Strongly Coupled Quantum Dot-Cavity System", Physical Review Letters **108**, 093604 (2012).

[59] R. Bose, D. Sridharan, H. Kim, G. S. Solomon, and E. Waks, "Low-photon-number optical switching with a single quantum dot coupled to a photonic crystal cavity", Physical Review Letters **108**, 1–5 (2012).

[60] S. Sun, H. Kim, Z. Luo, G. S. Solomon, and E. Waks, "A single-photon switch and transistor enabled by a solid-state quantum memory", Science **361**, 57–60 (2018).

[61] Z. Luo, S. Sun, A. Karasahin, A. S. Bracker, S. G. Carter, M. K. Yakes, D. Gammon, and E. Waks, "A Spin–Photon Interface Using Charge-Tunable Quantum Dots Strongly Coupled to a Cavity", Nano Letters **19**, 7072–7077 (2019).

[62] A. Sipahigil, R. E. Evans, D. D. Sukachev, M. J. Burek, J. Borregaard, M. K. Bhaskar, C. T. Nguyen, J. L. Pacheco, H. A. Atikian, C. Meuwly, R. M. Camacho, F. Jelezko, E. Bielejec, H. Park, M. Lončar, and M. D. Lukin, "An integrated diamond nanophotonics platform for quantum-optical networks", Science **354**, 847–850 (2016).

[63] C. T. Nguyen, D. D. Sukachev, M. K. Bhaskar, B. Machielse, D. S. Levonian, E. N. Knall, P. Stroganov, R. Riedinger, H. Park, M. Lončar, and M. D. Lukin, "Quantum Network Nodes Based on Diamond Qubits with an Efficient Nanophotonic Interface", Physical Review Letters **123**, 183602 (2019).

[64] M. K. Bhaskar, R. Riedinger, B. Machielse, D. S. Levonian, C. T. Nguyen, E. N. Knall, H. Park, D. Englund, M. Lončar, D. D. Sukachev, and M. D. Lukin, "Experimental demonstration of memory-enhanced quantum communication", Nature **580**, 60–64 (2020).

[65] D. Witthaut, M. D. Lukin, and A. S. Sørensen, "Photon sorters and QND detectors using single photon emitters", EPL (Europhysics Letters) **97**, 50007 (2012).

[66] C. V. Raman and K. S. Krishnan, "The Negative Absorption of Radiation", Nature **122**, 12–13 (1928).

[67] R. Lettow, Y. L. A. Rezus, A. Renn, G. Zumofen, E. Ikonen, S. Götzinger, and V. Sandoghdar, "Quantum Interference of Tunably Indistinguishable Photons from Remote Organic Molecules", Physical Review Letters **104**, 123605 (2010).

[68] F. P. Schäfer, W. Schmidt, and J. Volze, "Organic Dye Solution Laser", Applied Physics Letters **9**, 306–309 (1966).

[69] S. W. Hell and J. Wichmann, "Breaking the diffraction resolution limit by stimulated emission: stimulated-emission-depletion fluorescence microscopy", Optics Letters **19**, 780 (1994).

[70] S. Weisenburger and V. Sandoghdar, "Light microscopy: an ongoing contemporary revolution", Contemporary Physics **56**, 123–143 (2015).

[71] P. Lombardi, M. Colautti, R. Duquennoy, G. Murtaza, P. Majumder, and C. Toninelli, "Triggered emission of indistinguishable photons from an organic dye molecule", Applied Physics Letters **118**, 204002 (2021).

[72] R. Duquennoy, M. Colautti, R. Emadi, P. Majumder, P. Lombardi, and C. Toninelli, "Real-time two-photon interference from distinct molecules on the same chip", Optica **9**, 731 (2022).

[73] C. Toninelli, I. Gerhardt, A. S. Clark, A. Reserbat-Plantey, S. Götzinger, Z. Ristanović, M. Colautti, P. Lombardi, K. D. Major, I. Deperasińska, W. H. Pernice, F. H. L. Koppens, B. Kozankiewicz, A. Gourdon, V. Sandoghdar, and M. Orrit, "Single organic molecules for photonic quantum technologies", Nature Materials **20**, 1615–1628 (2021).

[74] Y. Gu, Z. Qiu, and K. Müllen, "Nanographenes and Graphene Nanoribbons as Multitalents of Present and Future Materials Science", Journal of the American Chemical Society **144**, 11499–11524 (2022).

[75] A. A. L. Nicolet, C. Hofmann, M. A. Kol'chenko, B. Kozankiewicz, and M. Orrit, "Single Dibenzoterrylene Molecules in an Anthracene Crystal: Spectroscopy and Photophysics", ChemPhysChem **8**, 1215–1220 (2007).

[76] J. R. Hill, E. L. Chronister, T.-C. Chang, H. Kim, J. C. Postlewaite, and D. D. Dlott, "Vibrational relaxation and vibrational cooling in low temperature molecular crystals", The Journal of Chemical Physics **88**, 949–967 (1988).

[77] H. Haken and H. C. Wolf, *Molecular Physics and Elements of Quantum Chemistry*, 2nd ed., Advanced Texts in Physics (Springer Berlin Heidelberg, Berlin, Heidelberg, 2004).

[78] J.-B. Trebbia, H. Ruf, P. Tamarat, and B. Lounis, "Efficient generation of near infra-red single photons from the zero-phonon line of a single molecule", Optics Express **17**, 23986 (2009).

[79] J. Bernard, L. Fleury, H. Talon, and M. Orrit, "Photon Bunching in the Fluorescence from Single Molecules: A Probe for Intersystem Crossing", The Journal of Chemical Physics **98**, 850–859 (1993).

[80] W. E. Moerner and L. Kador, "Optical Detection and Spectroscopy of Single Molecules in a Solid", Physical Review Letters **62**, 2535–2538 (1989).

[81] M. Orrit and J. Bernard, "Single Pentacene Molecules Detected by Fluorescence Excitation in a p-Terphenyl Crystal", Physical Review Letters **65**, 2716–2719 (1990).

[82] A. M. Stoneham, "Shapes of Inhomogeneously Broadened Resonance Lines in Solids", Reviews of Modern Physics **41**, 82–108 (1969).

[83] E. A. J. Marcatili, "Bends in Optical Dielectric Guides", Bell System Technical Journal **48**, 2103–2132 (1969).

[84] B. Little, S. Chu, H. Haus, J. Foresi, and J.-P. Laine, "Microring resonator channel dropping filters", Journal of Lightwave Technology **15**, 998–1005 (1997).

[85] I. S. Grudinin, V. S. Ilchenko, and L. Maleki, "Ultrahigh optical *Q* factors of crystalline resonators in the linear regime", Physical Review A **74**, 063806 (2006).

[86] T. Aoki, B. Dayan, E. Wilcut, W. P. Bowen, A. S. Parkins, T. J. Kippenberg, K. J. Vahala, and H. J. Kimble, "Observation of strong coupling between one atom and a monolithic microresonator", Nature **443**, 671–674 (2006).

[87] J. D. Joannopoulos, P. R. Villeneuve, and S. Fan, "Photonic crystals: putting a new twist on light", Nature **386**, 143–149 (1997).

[88] D. Englund, D. Fattal, E. Waks, G. Solomon, B. Zhang, T. Nakaoka, Y. Arakawa, Y. Yamamoto, and J. Vučković, "Controlling the Spontaneous Emission Rate of Single Quantum Dots in a Two-Dimensional Photonic Crystal", Physical Review Letters **95**, 013904 (2005).

[89] J. D. Thompson, T. G. Tiecke, N. P. de Leon, J. Feist, A. V. Akimov, M. Gullans, A. S. Zibrov, V. Vuletić, and M. D. Lukin, "Coupling a Single Trapped Atom to a Nanoscale Optical Cavity", Science **340**, 1202–1205 (2013).

[90] A. Pérot and C. Fabry, "On the Application of Interference Phenomena to the Solution of Various Problems of Spectroscopy and Metrology", The Astrophysical Journal **9**, 87 (1899).

[91] P. Goy, J. M. Raimond, M. Gross, and S. Haroche, "Observation of Cavity-Enhanced Single-Atom Spontaneous Emission", Physical Review Letters **50**, 1903–1906 (1983).

[92] J. P. Reithmaier, G. Sęk, A. Löffler, C. Hofmann, S. Kuhn, S. Reitzenstein, L. V. Keldysh, V. D. Kulakovskii, T. L. Reinecke, and A. Forchel, "Strong coupling in a single quantum dot–semiconductor microcavity system", Nature **432**, 197–200 (2004).

[93] H. Kelkar, D. Wang, D. Martín-Cano, B. Hoffmann, S. Christiansen, S. Götzinger, and V. Sandoghdar, "Sensing Nanoparticles with a Cantilever-Based Scannable Optical Cavity of Low Finesse and Sub-λ^3 Volume", Physical Review Applied **4**, 054010 (2015).

[94] H. A. MacLeod, *Thin-Film Optical Filters*, 3rd ed. (Institute of Physics Publishing, London, Jan. 2001).

[95] G. Rempe, R. Lalezari, R. J. Thompson, and H. J. Kimble, "Measurement of ultralow losses in an optical interferometer", Optics Letters **17**, 363 (1992).

[96] D. Kleckner, W. T. M. Irvine, S. S. R. Oemrawsingh, and D. Bouwmeester, "Diffraction-limited high-finesse optical cavities", Physical Review A **81**, 043814 (2010).

[97] D. V. Karpov and P. Horak, "Cavities with Nonspherical Mirrors for Enhanced Interaction between a Quantum Emitter and Cavity Photons", Physical Review A **105**, 023515 (2022).

[98] J. Benedikter, T. Hümmer, M. Mader, B. Schlederer, J. Reichel, T. W. Hänsch, and D. Hunger, "Transverse-mode coupling and diffraction loss in tunable Fabry–Pérot microcavities", New Journal of Physics **17**, 053051 (2015).

[99] H. Kogelnik and T. Li, "Laser Beams and Resonators", Applied Optics **5**, 1550–1567 (1966).

[100] W. T. Silfvast, *Laser Fundamentals*, 2nd ed. (Cambridge University Press, Jan. 2004).

[101] D. A. Steck, *Quantum and Atom Optics*, revision 0 (2017).

[102] Z. S. Sadeq, R. A. Muniz, and J. E. Sipe, "One- and Two-Photon Absorption Spectra of Dibenzoterrylene", Physical Review Materials **2**, 075202 (2018).

[103] E. T. Jaynes and F. W. Cummings, "Comparison of Quantum and Semiclassical Radiation Theories with Application to the Beam Maser", Proceedings of the IEEE **51**, 89–109 (1963).

[104] M. O. Scully and M. S. Zubairy, *Quantum Optics* (Cambridge University Press, Sept. 1997).

[105] N. Ismail, C. C. Kores, D. Geskus, and M. Pollnau, "Fabry-Pérot Resonator: Spectral Line Shapes, Generic and Related Airy Distributions, Linewidths, Finesses, and Performance at Low or Frequency-Dependent Reflectivity", Optics Express **24**, 16366–16389 (2016).

[106] G. Lindblad, "On the Generators of Quantum Dynamical Semigroups", Communications in Mathematical Physics **48**, 119–130 (1976).

[107] D. Manzano, "A Short Introduction to the Lindblad Master Equation", AIP Advances **10**, 025106 (2020).

[108] H. J. Carmichael, *Statistical Methods in Quantum Optics 2*, Theoretical and Mathematical Physics (Springer Berlin Heidelberg, Berlin, Heidelberg, 2008).

[109] Y. Choi, S. Kang, S. Lim, W. Kim, J.-R. Kim, J.-H. Lee, and K. An, "Quasieigenstate Coalescence in an Atom-Cavity Quantum Composite", Physical Review Letters **104**, 153601 (2010).

[110] A. M. Fox, *Quantum Optics: An Introduction* (Oxford University Press, Oxford, 2006).

[111] D. Kleppner, "Inhibited Spontaneous Emission", Physical Review Letters **47**, 233–236 (1981).

[112] R. G. Hulet, E. S. Hilfer, and D. Kleppner, "Inhibited Spontaneous Emission by a Rydberg Atom", Physical Review Letters **55**, 2137–2140 (1985).

[113] A. Auffèves-Garnier, C. Simon, J.-M. Gérard, and J.-P. Poizat, "Giant Optical Nonlinearity Induced by a Single Two-Level System Interacting with a Cavity in the Purcell Regime", Phys. Rev. A **75**, 053823 (2007).

[114] J. R. Johansson, P. D. Nation, and F. Nori, "QuTiP: An Open-Source Python Framework for the Dynamics of Open Quantum Systems", Computer Physics Communications **183**, 1760–1772 (2012).

[115] J. R. Johansson, P. D. Nation, and F. Nori, "QuTiP 2: A Python Framework for the Dynamics of Open Quantum Systems", Computer Physics Communications **184**, 1234–1240 (2013).

[116] W. H. Press, S. A. Teukolsky, W. T. Vetterling, and B. P. Flannery, *Numerical Recipes*, 3rd ed. (Cambridge University Press, 2007).

[117] B. R. Mollow, "Stimulated Emission and Absorption near Resonance for Driven Systems", Physical Review A **5**, 2217–2222 (1972).

[118] R. J. Glauber, "The Quantum Theory of Optical Coherence", Physical Review **130**, 2529–2539 (1963).

[119] J. W. Goodman, *Statistical Optics*, edited by G. Boreman, 2nd ed. (John Wiley & Sons, Inc., 2015).

[120] H. Pfeifer, L. Ratschbacher, J. Gallego, C. Saavedra, A. Faßbender, A. von Haaren, W. Alt, S. Hofferberth, M. Köhl, S. Linden, and D. Meschede, "Achievements and perspectives of optical fiber Fabry–Perot cavities", Applied Physics B **128**, 29 (2022).

[121] J. Gallego, S. Ghosh, S. K. Alavi, W. Alt, M. Martinez-Dorantes, D. Meschede, and L. Ratschbacher, "High-finesse fiber Fabry–Perot cavities: stabilization and mode matching analysis", Applied Physics B **122**, 47 (2016).

[122] A. Bick, C. Staarmann, P. Christoph, O. Hellmig, J. Heinze, K. Sengstock, and C. Becker, "The role of mode match in fiber cavities", Review of Scientific Instruments **87**, 13102 (2016).

[123] D. Wang, *Coherent Coupling of a Single Molecule to a Fabry-Pérot Microcavity*, Dissertation (Friedrich-Alexander-Universität Erlangen Nürnberg, 2019).

[124] G. K. Gulati, H. Takahashi, N. Podoliak, P. Horak, and M. Keller, "Fiber cavities with integrated mode matching optics", Scientific Reports **7**, 5556 (2017).

[125] J. Orloff, M. Utlaut, and L. Swanson, *High Resolution Focused Ion Beams: FIB and its Applications* (Springer US, Boston, MA, 2003).

[126] Y. Colombe, T. Steinmetz, G. Dubois, F. Linke, D. Hunger, and J. Reichel, "Strong atom–field coupling for Bose–Einstein condensates in an optical cavity on a chip", Nature **450**, 272–276 (2007).

[127] D. Hunger, T. Steinmetz, Y. Colombe, C. Deutsch, T. W. Hänsch, and J. Reichel, "A fiber Fabry–Perot cavity with high finesse", New Journal of Physics **12**, 065038 (2010).

[128] K. Seshan, *Handbook of Thin Film Deposition Techniques: Principles, Methods, Equipment and Applications*, 2nd ed. (Noyes Publications / William Andrew Publishing, Norwich, New York, 2002).

[129] W. Weinstein, "The Reflectivity and Transmissivity of Multiple Thin Coatings", Journal of the Optical Society of America **37**, 576 (1947).

[130] L. Novotny and B. Hecht, *Principles of Nano-Optics*, 1st ed. (Cambridge University Press, 2006).

[131] D. Babic and S. Corzine, "Analytic expressions for the reflection delay, penetration depth, and absorptance of quarter-wave dielectric mirrors", IEEE Journal of Quantum Electronics **28**, 514–524 (1992).

[132] N. Karl, "High Purity Organic Molecular Crystals", in *Organic crystals, germanates, semiconductors*, edited by H. C. Freyhardt (Springer Berlin, Heidelberg, 1980), pp. 1–100.

[133] K. D. Major, Y.-H. Lien, C. Polisseni, S. Grandi, K. W. Kho, A. S. Clark, J. Hwang, and E. A. Hinds, "Growth of optical-quality anthracene crystals doped with dibenzoterrylene for controlled single photon production", Review of Scientific Instruments **86**, 083106 (2015).

[134] I. Nakada, "The Optical Properties of Anthracene Single Crystals", Journal of the Physical Society of Japan **17**, 113–118 (1962).

[135] N. Tomm, A. R. Korsch, A. Javadi, D. Najer, R. Schott, S. R. Valentin, A. D. Wieck, A. Ludwig, and R. J. Warburton, "Tuning the Mode Splitting of a Semiconductor Microcavity with Uniaxial Stress", Physical Review Applied **15**, 054061 (2021).

[136] S. Flågan, *An open Microcavity for Diamond-based Photonics*, Dissertation (Universität Basel, 2021).

[137] A. A. L. Nicolet, P. Bordat, C. Hofmann, M. A. Kol'chenko, B. Kozankiewicz, R. Brown, and M. Orrit, "Single Dibenzoterrylene Molecules in an Anthracene Crystal: Main Insertion Sites", ChemPhysChem **8**, 1929–1936 (2007).

[138] T. Hänsch and B. Couillaud, "Laser frequency stabilization by polarization spectroscopy of a reflecting reference cavity", Optics Communications **35**, 441–444 (1980).

[139] G. F. Franklin, J. D. Powell, and A. Emami-Naeini, *Feedback Control of Dynamic Systems*, 6th ed. (Pearson Higher Education, Inc., Upper Saddle River, New Jersey, 2010).

[140] S. Vadia, J. Scherzer, H. Thierschmann, C. Schäfermeier, C. Dal Savio, T. Taniguchi, K. Watanabe, D. Hunger, K. Karraï, and A. Högele, "Open-Cavity in Closed-Cycle Cryostat as a Quantum Optics Platform", PRX Quantum **2**, 040318 (2021).

[141] M. Pallmann, T. Eichhorn, J. Benedikter, B. Casabone, T. Hümmer, and D. Hunger, "A highly stable and fully tunable open microcavity platform at cryogenic temperatures", (2022).

[142] M. Fisicaro, M. Witlox, H. van der Meer, and W. Löffler, "Active stabilization of an open-access optical microcavity for low-noise operation in a standard closed-cycle cryostat", Review of Scientific Instruments **95**, 33101 (2024).

[143] A. V. Kavokin, J. J. Baumberg, G. Malpuech, and F. P. Laussy, *Microcavities*, 2nd ed. (Oxford University Press, 2017).

[144] PicoQuant, *PicoHarp 300 Data Sheet*.

[145] W. Becker, *The bh TCSPC Handbook*, 8th ed. (Becker & Hickl GmbH, Berlin, Sept. 2019).

[146] A. Giudice, M. Ghioni, R. Biasi, F. Zappa, S. Cova, P. Maccagnani, and A. Gulinatti, "High-rate photon counting and picosecond timing with silicon-SPAD based compact detector modules", Journal of Modern Optics **54**, 225–237 (2007).

[147] D. Najer, *A coherent light-matter interface with a semiconductor quantum dot in an optical microcavity*, Dissertation (Universität Basel, 2019).

[148] L. S. Bishop, J. M. Chow, J. Koch, A. A. Houck, M. H. Devoret, E. Thuneberg, S. M. Girvin, and R. J. Schoelkopf, "Nonlinear response of the vacuum Rabi resonance", Nature Physics **5**, 105–109 (2009).

[149] L. Monniello, C. Tonin, R. Hostein, A. Lemaitre, A. Martinez, V. Voliotis, and R. Grousson, "Excitation-Induced Dephasing in a Resonantly Driven InAs/GaAs Quantum Dot", Physical Review Letters **111**, 026403 (2013).

[150] C. W. Thiel, R. M. Macfarlane, Y. Sun, T. Böttger, N. Sinclair, W. Tittel, and R. L. Cone, "Measuring and analyzing excitation-induced decoherence in rare-earth-doped optical materials", Laser Physics **24**, 106002 (2014).

[151] F. Katsch, M. Selig, and A. Knorr, "Exciton-Scattering-Induced Dephasing in Two-Dimensional Semiconductors", Physical Review Letters **124**, 257402 (2020).

[152] A. Shkarin, D. Rattenbacher, J. Renger, S. Hönl, T. Utikal, P. Seidler, S. Götzinger, and V. Sandoghdar, "Nanoscopic Charge Fluctuations in a Gallium Phosphide Waveguide Measured by Single Molecules", Physical Review Letters **126**, 133602 (2021).

[153] A. Maser, B. Gmeiner, T. Utikal, S. Götzinger, and V. Sandoghdar, "Few-photon coherent nonlinear optics with a single molecule", Nature Photonics **10**, 450–453 (2016).

[154] M. T. Gruneisen, K. R. MacDonald, A. L. Gaeta, R. W. Boyd, and D. J. Harter, "Energy transfer between laser beams propagating through an atomic vapor", Physical Review A **40**, 3464–3467 (1989).

[155] J. H. Shapiro, "Single-photon Kerr nonlinearities do not help quantum computation", Physical Review A **73**, 062305 (2006).

[156] S. Rosenblum, S. Parkins, and B. Dayan, "Photon routing in cavity QED: Beyond the fundamental limit of photon blockade", Physical Review A **84**, 033854 (2011).

[157] M. Heuck, K. Jacobs, and D. R. Englund, "Photon-photon interactions in dynamically coupled cavities", Physical Review A **101**, 042322 (2020).

[158] M. Heuck, K. Jacobs, and D. R. Englund, "Controlled-Phase Gate Using Dynamically Coupled Cavities and Optical Nonlinearities", Physical Review Letters **124**, 160501 (2020).

[159] C. Kurtsiefer, P. Zarda, S. Mayer, and H. Weinfurter, "The breakdown flash of silicon avalanche photodiodes – Back door for eavesdropper attacks?", Journal of Modern Optics **48**, 2039–2047 (2001).

[160] A. Rundquist, M. Bajcsy, A. Majumdar, T. Sarmiento, K. Fischer, K. G. Lagoudakis, S. Buckley, A. Y. Piggott, and J. Vučković, "Nonclassical higher-order photon correlations with a quantum dot strongly coupled to a photonic-crystal nanocavity", Physical Review A **90**, 023846 (2014).

[161] A. Javadi, I. Söllner, M. Arcari, S. L. Hansen, L. Midolo, S. Mahmoodian, G. Kiršanskė, T. Pregnolato, E. H. Lee, J. D. Song, S. Stobbe, and P. Lodahl, "Single-photon non-linear optics with a quantum dot in a waveguide", Nature Communications **6**, 8655 (2015).

[162] A. J. Bennett, J. P. Lee, D. J. P. Ellis, I. Farrer, D. A. Ritchie, and A. J. Shields, "A semiconductor photon-sorter", Nature Nanotechnology **11**, 857–860 (2016).

[163] H. Snijders, J. A. Frey, J. Norman, M. P. Bakker, E. C. Langman, A. Gossard, J. E. Bowers, M. P. van Exter, D. Bouwmeester, and W. Löffler, "Purification of a single-photon nonlinearity", Nature Communications **7**, 12578 (2016).

[164] N. O. Antoniadis, N. Tomm, T. Jakubczyk, R. Schott, S. R. Valentin, A. D. Wieck, A. Ludwig, R. J. Warburton, and A. Javadi, "A chiral one-dimensional atom using a quantum dot in an open microcavity", npj Quantum Information **8**, 27 (2022).

[165] L. Mandel and E. Wolf, *Optical Coherence and Quantum Optics* (Cambridge University Press, Sept. 1995).

[166] H. J. Carmichael, R. Brecha, and P. Rice, "Quantum interference and collapse of the wavefunction in cavity QED", Optics Communications **82**, 73–79 (1991).

[167] R. E. K. Fishman, R. N. Patel, D. A. Hopper, T.-Y. Huang, and L. C. Bassett, "Photon-Emission-Correlation Spectroscopy as an Analytical Tool for Solid-State Quantum Defects", PRX Quantum **4**, 010202 (2023).

[168] N. Tomm, S. Mahmoodian, N. O. Antoniadis, R. Schott, S. R. Valentin, A. D. Wieck, A. Ludwig, A. Javadi, and R. J. Warburton, "Photon bound state dynamics from a single artificial atom", Nature Physics, 1–6 (2023).

[169] G. Floquet, "Sur les équations différentielles linéaires à coefficients périodiques", Annales scientifiques de l'École normale supérieure **12**, 47–88 (1883).

[170] S. Papademetriou, S. Chakmakjian, and C. R. Stroud, "Optical subharmonic Rabi resonances", Journal of the Optical Society of America B **9**, 1182 (1992).

[171] D. Groll, D. Wigger, K. Jürgens, T. Hahn, C. Schneider, M. Kamp, S. Höfling, J. Kasprzak, and T. Kuhn, "Four-wave mixing dynamics of a strongly coupled quantum-dot–microcavity system driven by up to 20 photons", Physical Review B **101**, 245301 (2020).

[172] H. F. Hofmann and S. Takeuchi, "Violation of local uncertainty relations as a signature of entanglement", Physical Review A **68**, 032103 (2003).

[173] K. E. Dorfman, F. Schlawin, and S. Mukamel, "Nonlinear optical signals and spectroscopy with quantum light", Reviews of Modern Physics **88**, 045008 (2016).

[174] S.-H. Huang, T. Dirmeier, G. Shafiee, K. Laiho, D. V. Strekalov, G. Leuchs, and C. Marquardt, "Polarization-entangled photons from a whispering gallery resonator", arXiv:2310.16589 (2023).

[175] C. M. Savage, "Stationary two-level atomic inversion in a quantized cavity field", Physical Review Letters **60**, 1828–1831 (1988).

[176] S. Hughes and H. J. Carmichael, "Stationary Inversion of a Two Level System Coupled to an Off-Resonant Cavity with Strong Dissipation", Physical Review Letters **107**, 193601 (2011).

[177] J. Nobakht, *Design and characterization of a scanning microcavity and potential application toward steady-state inversion of a two-level system*, Master Thesis (Friedrich-Alexander Universität Erlangen-Nürnberg, 2022).

[178] Y.-T. Chough, H.-J. Moon, H. Nha, and K. An, "Single-atom laser based on multiphoton resonances at far-off resonance in the Jaynes-Cummings ladder", Physical Review A **63**, 013804 (2000).

[179] S. S. Shamailov, A. S. Parkins, M. J. Collett, and H. J. Carmichael, "Multi-photon blockade and dressing of the dressed states", Optics Communications **283**, 766–772 (2010).

[180] J. Zirkelbach, M. Mirzaei, I. Deperasińska, B. Kozankiewicz, B. Gurlek, A. Shkarin, T. Utikal, S. Götzinger, and V. Sandoghdar, "High-resolution vibronic spectroscopy of a single molecule embedded in a crystal", The Journal of Chemical Physics **156**, 104301 (2022).

[181] R. H. Dicke, "Coherence in Spontaneous Radiation Processes", Physical Review **93**, 99–110 (1954).

[182] U. Akram, Z. Ficek, and S. Swain, "Decoherence and coherent population transfer between two coupled systems", Physical Review A **62**, 013413 (2000).

[183] C. Hettich, *Coherent Optical Dipole Coupling of Two Individual Molecules at Nanometre Separation*, Dissertation (Universität Konstanz, 2002).

[184] C. Hettich, C. Schmitt, J. Zitzmann, S. Kühn, I. Gerhardt, and V. Sandoghdar, "Nanometer Resolution and Coherent Optical Dipole Coupling of Two Individual Molecules", Science **298**, 385–389 (2002).

[185] J.-B. Trebbia, Q. Deplano, P. Tamarat, and B. Lounis, "Tailoring the superradiant and subradiant nature of two coherently coupled quantum emitters", Nature Communications **13**, 2962 (2022).

[186] C. M. Lange, E. Daggett, V. Walther, L. Huang, and J. D. Hood, "Superradiant and subradiant states in lifetime-limited organic molecules through laser-induced tuning", Nature Physics, 10.1038/s41567-024-02404-4 (2024).

[187] A. Tiranov, V. Angelopoulou, C. J. van Diepen, B. Schrinski, O. A. D. Sandberg, Y. Wang, L. Midolo, S. Scholz, A. D. Wieck, A. Ludwig, A. S. Sørensen, and P. Lodahl, "Collective super- and subradiant dynamics between distant optical quantum emitters", Science **379**, 389–393 (2023).

[188] M. Radulaski, K. A. Fischer, K. G. Lagoudakis, J. L. Zhang, and J. Vučković, "Photon blockade in two-emitter-cavity systems", Physical Review A **96**, 011801 (2017).

[189] A. Blais, A. L. Grimsmo, S. M. Girvin, and A. Wallraff, "Circuit quantum electrodynamics", Reviews of Modern Physics **93**, 025005 (2021).

[190] R. E. Evans, M. K. Bhaskar, D. D. Sukachev, C. T. Nguyen, A. Sipahigil, M. J. Burek, B. Machielse, G. H. Zhang, A. S. Zibrov, E. Bielejec, H. Park, M. Lončar, and M. D. Lukin, "Photon-mediated interactions between quantum emitters in a diamond nanocavity", Science **362**, 662–665 (2018).

[191] J. Majer, J. M. Chow, J. M. Gambetta, J. Koch, B. R. Johnson, J. A. Schreier, L. Frunzio, D. I. Schuster, A. A. Houck, A. Wallraff, A. Blais, M. H. Devoret, S. M. Girvin, and R. J. Schoelkopf, "Coupling superconducting qubits via a cavity bus", Nature **449**, 443–447 (2007).

[192] J. A. Mlynek, A. A. Abdumalikov, C. Eichler, and A. Wallraff, "Observation of Dicke superradiance for two artificial atoms in a cavity with high decay rate", Nature Communications **5**, 5186 (2014).

[193] P. Samutpraphoot, T. Đorđević, P. L. Ocola, H. Bernien, C. Senko, V. Vuletić, and M. D. Lukin, "Strong Coupling of Two Individually Controlled Atoms via a Nanophotonic Cavity", Physical Review Letters **124**, 063602 (2020).

[194] D. Rattenbacher, A. Shkarin, J. Renger, T. Utikal, S. Götzinger, and V. Sandoghdar, "On-chip interference of scattering from two individual molecules", Optica **10**, 1595 (2023).

[195] M. Colautti, F. S. Piccioli, Z. Ristanović, P. Lombardi, A. Moradi, S. Adhikari, I. Deperasinska, B. Kozankiewicz, M. Orrit, and C. Toninelli, "Laser-Induced Frequency Tuning of Fourier-Limited Single-Molecule Emitters", ACS Nano **14**, 13584–13592 (2020).

[196] A. Blais, R.-S. Huang, A. Wallraff, S. M. Girvin, and R. J. Schoelkopf, "Cavity quantum electrodynamics for superconducting electrical circuits: An architecture for quantum computation", Physical Review A **69**, 062320 (2004).

[197] A. Wallraff, D. I. Schuster, A. Blais, L. Frunzio, R. S. Huang, J. Majer, S. Kumar, S. M. Girvin, and R. J. Schoelkopf, "Strong coupling of a single photon to a superconducting qubit using circuit quantum electrodynamics", Nature **431**, 162–167 (2004).

[198] D. I. Schuster, A. A. Houck, J. A. Schreier, A. Wallraff, J. M. Gambetta, A. Blais, L. Frunzio, J. Majer, B. Johnson, M. H. Devoret, S. M. Girvin, and R. J. Schoelkopf, "Resolving photon number states in a superconducting circuit", Nature **445**, 515–518 (2007).

[199] J. Gambetta, A. Blais, D. I. Schuster, A. Wallraff, L. Frunzio, J. Majer, M. H. Devoret, S. M. Girvin, and R. J. Schoelkopf, "Qubit-photon interactions in a cavity: Measurement-induced dephasing and number splitting", Physical Review A **74**, 042318 (2006).

[200] D. I. Schuster, A. Wallraff, A. Blais, L. Frunzio, R.-S. Huang, J. Majer, S. M. Girvin, and R. J. Schoelkopf, "ac Stark Shift and Dephasing of a Superconducting Qubit Strongly Coupled to a Cavity Field", Physical Review Letters **94**, 123602 (2005).

[201] D. Najer, I. Söllner, P. Sekatski, V. Dolique, M. C. Löbl, D. Riedel, R. Schott, S. Starosielec, S. R. Valentin, A. D. Wieck, N. Sangouard, A. Ludwig, and R. J. Warburton, "A gated quantum dot strongly coupled to an optical microcavity", Nature **575**, 622–627 (2019).

[202] Y. Liu, Z. Wang, P. Yang, Q. Wang, Q. Fan, S. Guan, G. Li, P. Zhang, and T. Zhang, "Realization of Strong Coupling between Deterministic Single-Atom Arrays and a High-Finesse Miniature Optical Cavity", Physical Review Letters **130**, 173601 (2023).

[203] D. Meschede, H. Walther, and G. Müller, "One-Atom Maser", Physical Review Letters **54**, 551–554 (1985).

[204] Y. Mu and C. M. Savage, "One-atom lasers", Physical Review A **46**, 5944–5954 (1992).

[205] J. McKeever, A. Boca, A. D. Boozer, J. R. Buck, and H. J. Kimble, "Experimental realization of a one-atom laser in the regime of strong coupling", Nature **425**, 268–271 (2003).

[206] X.-L. Chu, S. Götzinger, and V. Sandoghdar, "A single molecule as a high-fidelity photon gun for producing intensity-squeezed light", Nature Photonics **11**, 58–62 (2017).

[207] M. Musavinezhad, A. Shkarin, D. Rattenbacher, J. Renger, T. Utikal, S. Götzinger, and V. Sandoghdar, "Quantum Efficiency of Single Dibenzoterrylene Molecules in *p*-Dichlorobenzene at Cryogenic Temperatures", The Journal of Physical Chemistry B **127**, 5353–5359 (2023).

[208] N. Sangouard and H. Zbinden, "What are single photons good for?", Journal of Modern Optics **59**, 1458–1464 (2012).

[209] E. Knill, R. Laflamme, and G. J. Milburn, "A scheme for efficient quantum computation with linear optics", Nature **409**, 46–52 (2001).

[210] J. Y. Cheung, C. J. Chunnilall, E. R. Woolliams, N. P. Fox, J. R. Mountford, J. Wang, and P. J. Thomas, "The quantum candela: a re-definition of the standard units for optical radiation", Journal of Modern Optics **54**, 373–396 (2007).

[211] N. Somaschi, V. Giesz, L. De Santis, J. C. Loredo, M. P. Almeida, G. Hornecker, S. L. Portalupi, T. Grange, C. Antón, J. Demory, C. Gómez, I. Sagnes, N. D. Lanzillotti-Kimura, A. Lemaítre, A. Auffeves, A. G. White, L. Lanco, and P. Senellart, "Near-optimal single-photon sources in the solid state", Nature Photonics **10**, 340–345 (2016).

[212] N. Tomm, A. Javadi, N. O. Antoniadis, D. Najer, M. C. Löbl, A. R. Korsch, R. Schott, S. R. Valentin, A. D. Wieck, A. Ludwig, and R. J. Warburton, "A bright and fast source of coherent single photons", Nature Nanotechnology **16**, 399–403 (2021).

[213] A. Javadi, N. Tomm, N. O. Antoniadis, A. J. Brash, R. Schott, S. R. Valentin, A. D. Wieck, A. Ludwig, and R. J. Warburton, "Cavity-enhanced excitation of a quantum dot in the picosecond regime", New Journal of Physics **25**, 093027 (2023).

[214] A. Reiserer, "Colloquium: Cavity-enhanced quantum network nodes", Reviews of Modern Physics **94**, 041003 (2022).

[215] S. L. Bayliss, D. W. Laorenza, P. J. Mintun, B. D. Kovos, D. E. Freedman, and D. D. Awschalom, "Optically addressable molecular spins for quantum information processing", Science **370**, 1309–1312 (2020).

[216] D. Serrano, S. K. Kuppusamy, B. Heinrich, O. Fuhr, D. Hunger, M. Ruben, and P. Goldner, "Ultra-narrow optical linewidths in rare-earth molecular crystals", Nature **603**, 241–246 (2022).

[217] P.-J. Stas, Y. Q. Huan, B. Machielse, E. N. Knall, A. Suleymanzade, B. Pingault, M. Sutula, S. W. Ding, C. M. Knaut, D. R. Assumpcao, Y.-C. Wei, M. K. Bhaskar, R. Riedinger, D. D. Sukachev, H. Park, M. Lončar, D. S. Levonian, and M. D. Lukin, "Robust multi-qubit quantum network node with integrated error detection", Science **378**, 557–560 (2022).

[218] N. Coste, D. A. Fioretto, N. Belabas, S. C. Wein, P. Hilaire, R. Frantzeskakis, M. Gundin, B. Goes, N. Somaschi, M. Morassi, A. Lemaître, I. Sagnes, A. Harouri, S. E. Economou, A. Auffeves, O. Krebs, L. Lanco, and P. Senellart, "High-rate entanglement between a semiconductor spin and indistinguishable photons", Nature Photonics **17**, 582–587 (2023).

[219] M. T. Uysal, M. Raha, S. Chen, C. M. Phenicie, S. Ourari, M. Wang, C. G. Van de Walle, V. V. Dobrovitski, and J. D. Thompson, "Coherent Control of a Nuclear Spin via Interactions with a Rare-Earth Ion in the Solid State", PRX Quantum **4**, 010323 (2023).

[220] T. Hümmer, J. Noe, M. S. Hofmann, T. W. Hänsch, A. Högele, and D. Hunger, "Cavity-enhanced Raman microscopy of individual carbon nanotubes", Nature Communications **7**, 12155 (2016).

[221] L. C. Flatten, L. Weng, A. Branny, S. Johnson, P. R. Dolan, A. A. P. Trichet, B. D. Gerardot, and J. M. Smith, "Microcavity enhanced single photon emission from two-dimensional WSe_2", Applied Physics Letters **112**, 191105 (2018).

[222] C. Gebhardt, M. Förg, H. Yamaguchi, I. Bilgin, A. D. Mohite, C. Gies, M. Florian, M. Hartmann, T. W. Hänsch, A. Högele, and D. Hunger, "Polariton hyperspectral imaging of two-dimensional semiconductor crystals", Scientific Reports **9**, 13756 (2019).

[223] S. Häußler, G. Bayer, R. Waltrich, N. Mendelson, C. Li, D. Hunger, I. Aharonovich, and A. Kubanek, "Tunable Fiber-Cavity Enhanced Photon Emission from Defect Centers in hBN", Advanced Optical Materials **9**, 2002218 (2021).

[224] C. Deshmukh, E. Beattie, B. Casabone, S. Grandi, D. Serrano, A. Ferrier, P. Goldner, D. Hunger, and H. de Riedmatten, "Detection of single ions in a nanoparticle coupled to a fiber cavity", Optica **10**, 1339 (2023).

[225] P. S. Theocaris and E. E. Gdoutos, *Matrix Theory of Photoelasticity*, Vol. 11, Springer Series in Optical Sciences (Springer Berlin Heidelberg, Berlin, Heidelberg, 1979).

[226] H. A. Haus, *Electromagnetic Noise and Quantum Optical Measurements*, Advanced Texts in Physics (Springer Berlin Heidelberg, Berlin, Heidelberg, 2000).

[227] A. Pscherer and M. Meierhofer, *Microcavity analysis functions*, https://gitlab.intranet.mpl.mpg.de/apscher/microcavity-analysis-functions.

[228] D. Wang, H. Kelkar, D. Martin-Cano, T. Utikal, S. Götzinger, and V. Sandoghdar, "Coherent Coupling of a Single Molecule to a Scanning Fabry-Perot Microcavity", Physical Review X **7**, 021014 (2017).

[229] R. Englman and J. Jortner, "The energy gap law for radiationless transitions in large molecules", Molecular Physics **18**, 145–164 (1970).

[230] C. Erker and T. Basché, "The Energy Gap Law at Work: Emission Yield and Rate Fluctuations of Single NIR Emitters", Journal of the American Chemical Society **144**, 14053–14056 (2022).

Acknowledgements

This work would not have been possible without the Max Planck Society, which provided funding for the excellent laboratory equipment. I am very grateful that I was able to do my PhD in the beautiful new building into which the Max Planck Institute for the Science of Light moved in shortly before I started. Not only was the facility brand new and functional, but so was the organisational infrastructure. Maks and Anna swiftly machined every part I needed. Lothar and Oliver explained and repaired many electronic devices and provided help and spare parts for soldering endeavors. Many more "hidden layers" of organisational structure kept the institute running smoothly, such as the purchasing, the HR, the PR and the IT departments.

I would also like to thank Vahid for giving me the opportunity to work in this productive environment, to which he contributed in great parts by judiciously assembling our diversely skilled group. His optimism and insights into the intricacies of research have been invaluable, as have the enriching experiences of group retreats, PhD meetings, and personal career guidance.

My first lab experience was with Emanuel showing me patiently how the setup around the rare-earth-ion project is operated. Yes, I worked with Pr^{3+}:Y_2SiO_5 for the first year of my PhD. Even though we never got to the point where we would put rare-earth doped crystals into a microcavity, this fascinating emitter kept me interested, such that my postdoc in Patrice Bertet's group will be focused on rare-earth ions.

Hrishi and Daqing were the ones who built and introduced me to the microcavity setup and even though the transition period was short, they supported me very well. Even years after they left the group they replied to my emails very quickly. Thank you Daqing for inviting me to Kassel and for the career advice session with you and Kilian Singer.

Right after I started on the microcavity project, Manuel joined for his MSc thesis. These were particularly interesting times with many "aha!" moments as we both figured out how to run these experiments. I would like to thank him for this efficient collaboration. After Manuel, Jahangir joined the project, also as MSc student. He contributed interesting unusual perspectives thanks to his background as theorist. I appreciated the stimulating discussions and wish you great success for the future microcavity experiments. Supervising the internship

students Andreas, Chitres and Leonhard also enriched my experience, teaching me as much as I imparted.

I benefited a lot from the group-internal infrastructure. Jan is a true expert in process technology and made the micromirrors for us. Tobi's management of the experimental framework, including the meticulous organization of optics and care for lasers, electronics, vacuum, and cryo equipment, saved us countless hours. I am very grateful for the co-supervision by Stephan and his helpful tips on experiments, personal development and career planning. I enjoyed physics discussion with him an also the other group members, in particular Alexey, Dominik, Johannes, Burak and Diego.

The whole group has made my days a lot of fun. Whether it was playing kicker, tennis, table tennis, going to the trampoline hall or the Hungry Thursdays. Beyond our group the hBar Omega Student Chapter has broadened my social contacts by giving me the opportunity to attend and organise social events. And of course my family provided continuous support and motivation.

Lastly, but certainly not least, I extend my thanks to everyone contributing to this thesis. Peter's linguistic enhancements elevated the quality of this thesis to align with our high standards. Vahid, Jahangir, Stephan, Alexey, Dominik, Danqing, Ashley and Tim provided valuable feedback.